Structural evolution of massive galaxies in the last 11 Gyr

Fernando Buitrago Alonso

Thesis submitted to the University of Nottingham
for the degree of Doctor of Philosophy, September 2011

Supervisor:	Prof. Christopher J. Conselice (*University of Nottingham*)
External Supervisor:	Dr. Ignacio Trujillo Cabrera (*Instituto de Astrofísica de Canarias & Universidad de La Laguna*)
Deputy Supervisor:	Prof. Alfonso Aragón-Salamanca (*University of Nottingham*)
Examiners:	Dr. Ignacio Ferreras (*University College London*) Dr. Meghan Gray (*University of Nottingham*)

Submitted:	30^{th} September 2011
Examined:	5^{th} December 2011
Final version:	12^{th} April 2012

Dedicated to my uncle Francisco Buitrago de la Torre
and to my friend Gabriel Hortal Benito-Sendín,
and to my family,
and to all my people.

Wandering stars,
for whom it is reserved
the blackness
of darkness
forever?

Portishead - Wandering star

The Cosmos is all that is or ever was or ever will be. Our feeblest contemplations of the Cosmos stir us – there is a tingling in the spine, a catch in the voice, a faint sensation, as if a distant memory, or falling from a height. We know we are approaching the greatest of mysteries.

Initial words in ”Cosmos”, by Carl Sagan

Abstract

This thesis describes the properties and evolution of massive ($M_{stellar} \geq 10^{11} h_{70}^{-2} M_{\odot}$) galaxies at $0 < z < 3$, including their relationship to lower mass systems. Present-day massive galaxies are composed mostly of early-type objects, although it is unknown whether this was also the case at higher redshifts. In a hierarchical assembling scenario the morphological content of the massive population is expected to change with time from disk-like objects in the early Universe to spheroid-like galaxies at present. We first probe this theoretical expectation by compiling a large sample of massive galaxies in the redshift interval 0<z<3. Our sample of 1082 objects is composed of 207 local galaxies selected from the Sloan Digital Sky Survey, plus 875 objects observed with the HST from the POWIR/DEEP2 Survey and the GOODS NICMOS Survey. 639 of our objects have spectroscopic redshifts. Our morphological classification is done in the V-band restframe both quantitatively (using the Sérsic index as a morphological proxy) and qualitatively (by visual inspection). Using both techniques we find a significant change in the dominant morphological class with cosmic time. The fraction of early-type galaxies among the massive galaxy population has changed from ∼20-30% at z∼3 to ∼70% at z=0. Spheroid-like galaxies have been the predominant morphological massive class only since z∼1.

This morphological evolution is so far based on the detailed morphological analysis of these objects, which ultimately rests on the shape of their surface brightness profiles. To explore the consistency of this scenario, we examine the kinematic status of a small subset of these galaxies. We have observed in the H-band 10 massive galaxies at $z \sim 1.4$ with the Integral Field Spectrograph SINFONI at VLT. Our sample of galaxies have been selected purely by their photometric stellar mass without accounting for any morphological criteria a priori, and having [OII] line equivalent widths of $> 15\AA$

to secure their kinematical measurements. Through a 3D kinematical spectroscopy analysis we conclude that half (i.e. $50\pm7\%$) of our galaxies are compatible with being rotationally supported disks in agreement with our previous photometric expectations. This is around a factor of two higher than what is observed in the present Universe for objects of the same stellar mass. Strikingly, the majority of these massive galaxies show clear and fairly large rotational velocity maps, implying that massive galaxies acquire rapidly rotational support and hence gravitational equilibrium. In addition, we have evidence, based on our measured velocity dispersions and imaging, to favour a picture in which minor (and major) mergers are the main driving force behind the evolution of this massive galaxy population.

There is also cumulative evidence showing that the formation process for a number of these massive galaxies occur at even higher redshifts ($z > 5$) and that their morphological features are preserved when observing them in the UV restframe. Hence, we made use of the excellent capabilities of GNS to locate and study massive galaxies beyond $z = 3$ within our imaging and secondly determining whether the strong mass-size relation found for the most massive objects holds as well for lower mass objects. Our findings show the extreme compactness of massive objects at $z > 3$ and only a moderate evolution in size below our $10^{11} M_{\odot}$ mass limit.

Acknowledgements

Once I finished my Physics degree I felt that my family and friends had done 51% of it. The reason why was simple: their love and support. Now, I think the real percentage in my doctorate is 100%. This thesis is meant to be a tribute for many people without their assistance this project would have been impossible to accomplish.

Let me begin with the words you should not pronounce in science: thank you very much indeed to God and María Auxiliadora for everything.

To my family: I do remember the lunch when I said I wanted to go to the Canary Islands to study Astronomy. The sole answer was: 'We already knew it. No problem at all.' No questions. Just live your life to the full. To my parents, Fernando & Ana Luz, and of course my brother Alex, I have no words to express all my love and admiration for them. Enumerating the rest of my family here would be a tough business, so I will just put in words the memories which come to my mind: my uncle Paco giving me hoodies to forget about the cold of Nottingham winter, my cousin Ana coming to our house to have lunch everytime I popped by Spain, my cousin Alberto and his 'Cosmos' Christmas present and his help by phone whenever I faced problems, my cousin Elena and I rushing in Madrid to have lunch together as now our lifes diverged, ... among many other things. [1]

Indeed, now it is time for my supervisors:

To Christopher Joseph Conselice I have to acknowledge firstly the opportunity he offered me of partaking in lots of exciting projects. This was really starting from Cham-

[1] The first version of my family acknowledgements ended up here. My uncle Paco died soon after I showed them to him. I make amends as my uncle was the best and most generous person I have ever met. My thesis and myself as a person are always going to be indebted to you.

pions League. GOODS NICMOS Survey has been a fabulous experience and, I must confess, I was dreaming to participating in something like this since I started reading about Astronomy when I was a child. I really appreciate he always have a minute and an encouraging word for me. But what I remember most is the holidays we had at Salamanca. Thank you Chris!

To Ignacio Trujillo Cabrera, I never imagined even in my weirdest dreams about IAC to have such an amazing person by my side conducting my thesis. Not (only) because of your scientific way of doing things ('Buitrago, te vas a poner muy tenso con lo que te voy a enseñar...'). I state here that I learnt much more from you about life than about science. Your daily example shows the path to follow to many people, Nacho. But I prefer to be with you at night with your dancing Astronomy.

To Alfonso Aragón Salamanca, because as you well know you never treat me as 'secondary' PhD student but as one of your own. I felt like home when you were explaining to me so many key concepts of Astronomy. You told me always the truth and you welcomed me when I was lost, and truly all your advice helped to build me as a person and as a researcher.

And about my friends, I will go through them in chronological order so as not to miss anyone. I shall begin with my Salamanca people. LuisFe was the first person who gave me an Astronomy book when I was nine. So you must feel responsible for what you did. And sorry I have no time, no space (as the Battiato song) to write here how much you have done for me. Thank you to Fran as well, the most international person I ever met. My memories about you guys are just nights out in Berlin! Of course, thinking about good memories I cannot forget by any means that big hug in Palermo train station. David, I hope you will understand at some point how many things you have showed me and how many life lessons I learnt from you. You have really written this science thesis. I am remembering now about Víctor and my first visit to London, with also the first tortilla de patata by Marga. Let alone to mention the visits of Josete, Tamara, Javi and Luis to Nottingham. As my school people are being named, I think I ought to recall the wonderful teachers we had, such as Luis María Rioja or Javier Sanz, who really encouraged us to always look further.

I would like to sincerely thank Javi (Martín-Campo) for all the help he gave me to

settle down in my beginning in Canary Islands. You know you are much more than my official LaTeXand maths advisor. Indeed, thanks to Patri, Nieves, José Miguel and Javi for many nights out (and for checking-in through RyanAir a huge duvet for my bed). Jacob & Cris, thanks a lot for being there when I needed you, you are the best people 'at the other side of the Tormes'. Thanks a lot as well to my 'Bunker' people: Jorge 'el Gran Kaymán' (you are the best!), César, LuisFran, Jody, Manu, Pablo, Esteban, ... And finally to Gabriel, Marta and Mamen. Time flies with you. Let me spare some words to Gabi. Man, I do not know any person more courageous than you, I am proud to be one of your friends. Before the problem, I felt like I had to spend more time with you. Now, even more. I value more your daily example than all the trips around the world you have done (but next Scotland, OK?)[2]. And my dear amigas: Leti & Bea, Xio, Patri (López) and Diana. Many coffees so far, many more to come: thank you for all your support in the tough moments (and your Bolero nights, Einstein papers, ...) Finally, thanks a lot to my Madrid people: Isra, Noe, Rubén (yes, you can), Marta and Fran (sorry, no Alma now, and I promise you we will meet some often from now on).

My Uni people. I must separately acknowledge some of you (you know perfectly the reasons why): Sergio, Javi Truji and Elena. All my love to you. And also to: Alex (how showed so much good music and Jack Daniels), José Manuel, Xose (my coffee and my computer will never be the same), Dani, Javi Ledes, Javi 'Poli', Ángel & Mari Luz, LiFong, Sergio 'Ronaldo', Álvaro, Fer Paes, Vane, Sara, Alberto Pino, my 'Cousin' Carlos, Joche, Aníbal and many others.

And suddenly I found myself living in Canary Islands. And there I found a bunch of wonderful people: Lau (thanks to her I watch 'The Mummy' one thousand times, one for every point she lost), Diego (who showed me the 60s and 70s music), Mirian (best from Avilés, pity she leaves the peas apart), Pedro (who is Minute?), Alba (my favourite partner for watching basketball, and also for drinking out), Maribel (you will never know how much I appreciated your helping hand when I thought everything was over), José Goya (my favourite partner for watching football, haha, and not only for that), Edgar (my philosopher in 'La Resi') and I think I must spare some space for Alberto. You show to all of us the beauty of the Universe and how important

[2]During the writing-up of this thesis, Gabi has passed. My will is not to change a word of what is written, because he deserves it and much more.

is to convey it to the people, not only by telling its wonders, but also make people remember how special they are. I would really want to become one tenth of you in the future. There is no space left to say all the good things to many other friends: Sebas (no Munchkin please), Judit, Inés (thanks a lot for all your computational help and so many good books), Alexander, Tobías, Christoff, Manu, Ariadna, Samu, Paola, Unai, Yoli (OK, from the IAA, but ti voglio bene anyway)... and indeed to my IAC astronomy group (Jesús Varela, Jesús Falcón, Carlinhos, Anna, Javi Navarro ...).

Again, without time to think, I moved to the United Kingdom! However bad my English was at the start, Nottingham was full of amazing guys: my housemates Frank (two years surviving in our house was really a tour-de-force), Alessandra (and Fabio), Karima, Alkistis, Ari and Keith; and then Gustavo, Tony (I will not forget the World Cup final with you), the FIFA guys (Boris - Javi - Daniele), Yara (a thousand thanks for your help for the editing up of this document), Graeme, Mark & Amanda, Markus, Amit, Rob, Will, Ewan, Jonathan, Kate, Evelyn, Dimitri, Bruno, Isma, Ana, Hanni (thanks for your help when I needed it so much) and my office mates: Seb, Neil, Aman, Mitsuo, Steve, Sam, Asa, Ruth, Dani, Vishagan, Stuart, Godfrey, Jamie, Caterina, Sophie, ... and also to all Nottingham postdocs, staff, Phil Parry and Mel Stretton. All the experiences I lived through with you are deep inside of me, I cannot write them, but you know a place in my heart is yours. I must stop for two groups of people. To my ‘coffee club’. Nathan, you are the best person in the world and you always want to do things, I love that. Dani, I say in public what I said to you before in private, I could not survive my PhD in Nottingham without your support. Also a lot of love for my GNS group (forever we will be the GNS guys): the boss (Chris), Super-Amanda (thanks to all your understanding and advices), Ruth (my favourite vegetarian), Alice & Jamie (my little sister and my little brother) and my awesome big bro Asa. As Asa himself would say: you Nottingham guys rock my world!

About my collaborators, I am in debt with Benoît (man, you really helped me beyond the call the of duty) and Alejandro (we overcame that drama week in Nottingham). A big smile for Hugo Messias and Antonio Cava as well. Besides, we had two amazing visitors in the department: José Oñorbe and Kevin Casteels. Indeed, I would like also to acknowledge the non-astronomers: Mandó (‘my lawyer’, a person who cares),

Ioannis (what-a-night!), Dave Kellerman (better than a housemate), Francisco (‘Dr. Cubillos’, big coffees, even bigger drinks together), Jordi (what a pity a Barça supporter is such a nice bloke), Pancho Salinas, Roshana, Britta, Diego, Inma and all the biology bunch. A special space here is saved for Andrea (the Sicily trip was only the beginning...) and to David & Emma (you and your incredible generosity gave me energy to finish all this).

Last but not least, a big thanks to some of my lecturers. Fernando Atrio showed me how to pursue my aim of studying Astronomy and always supported me in this adventure. Paco Anguita pointed out to me than not only Physics is important to comprehend the Cosmos, and the talks of Francisco González de Posada really inspired me. Manolo Collados was more than a tutor for me in Canary Islands. You showed me that it is possible to be a good astronomer and a good person at the same time. Last in this list, but not in my mind, is Prof. Manuel Ledesma Gimeno who recently left us. I owe you tons of encouragement, a deep sense of thrill for science and the happiness to share knowledge with the people. And make them feel special as you did with me. Finally, I acknowledge all the people that indirectly inspired me, in the books I read (Carl Sagan, Isaac Asimov, Stephen Hawking ... and Homer, Cicero, Mark Twain, Miguel Hernández, ...), in the ”concentration” music that has accompanied me in this thesis (Bob Dylan, The XX, Portishead, Marlango, Esclarecidos, the Ethnical Music Compilation by David ...), in the art which nourishs my soul or in any other way.

And this is the most important correction of my thesis. Thanks a lot to my two examiners (Ignacio & Meghan) who make the VIVA very pleasant to me, even when I lost my voice! It truly was a fruitful scientific discussion and they perfectly know that this thesis has benefited a lot from their input, and not only its final stages. Besides, Jim Dunlop gave me plenty of time for taking care about my thesis and publications since I arrived to Scotland, and I am very grateful to him as well.

As Nathan reminded me, we do not have to take for granted all the resources we use in our science: thanks to the public astronomical databases (both for imaging and data) and open source programs which helped me in one way or another during my PhD. `DS9`, `TOPCAT` and the IDL Astronomy Users Library from NASA where specially useful to my work. I am also indebted to STFC and IAC for funding me during this

three-year-ish period. And thanks not only to the British taxpayer but in general to this amazing country which is the United Kingdom, for all the unforgettable experiences I had here.

To all of you, as Soda Stereo would say:

Gracias totales.

Published Work

The material that appear in this thesis is described in a series of publications in several astronomical journals and conference proceedings.

Chapter 2 contents form the body of:

Buitrago F.; Trujillo I.; Conselice C. J., Häußler B. 'Elliptical galaxies have been the predominant morphological massive class only since $z \sim 1$', 2011, MNRAS submitted

while the Sérsic index vs redshift evolution appears as well in

Buitrago F.; Conselice C. J.; Epinat B.; Bedregal A. G.; Trujillo I.; & Grützbauch R. 'Shaping massive galaxies from z=3: merging vs secular evolution', Highlights of Spanish Astrophysics VI, Astrophysics and Space Science Proceedings

Chapter 3 will be promptly submitted to Monthly Notices of the Royal Astronomical Society as:

Buitrago F.; Conselice C. J.; Epinat B.; Bedregal A. G.; Trujillo I.; & Grützbauch R. 'SINFONI/VLT 3D spectroscopy of massive galaxies: Strong rotational support at $z \sim 1.4$', 2012, in preparation

although some Integral Field Unit images and results are already published in the previously mentioned proceedings volume and in

Buitrago F.; Conselice C. J.; Epinat B.; Bedregal A. G.; Trujillo I.; & Grützbauch R. '3D Spectroscopy Unveils Massive Galaxy Formation Modes at High-z', Environment and the Formation of Galaxies: 30 years later, Proceedings of Symposium 2 of JENAM 2010, Astrophysics and Space Science Proceedings

Chapter 4 is still work in progress. However, the characterization of the GOODS NICMOS Survey (GNS) sample and the tables with the individual structural parameters derived by the student for the massive galaxies are in:

Conselice, C. J.; Bluck, A. F. L.; **Buitrago, F.**; Bauer, A. E.; Grützbauch, R.; Bouwens, R. J.; Bevan, S.; Mortlock, A.; Dickinson, M.; Daddi, E.; Yan, H.; Scott, Douglas; Chapman, S. C. and co-authors in alphabetical order, 'The Hubble Space Telescope GOODS NICMOS Survey: Overview and the Evolution of Massive Galaxies at $1.5 < z < 3$', 2010, MNRAS, 413, 80

and we also utilised the results of other works where the student has actively collaborated

Grützbauch, Ruth; Chuter, Robert W.; Conselice, Christopher J.; Bauer, Amanda E.; Bluck, Asa F. L.; **Buitrago, F.**; Mortlock, Alice 'Galaxy properties in different environments up to $z \sim 3$ in the GOODS NICMOS Survey', 2011, MNRAS, 412, 2361

Mortlock A.; Conselice C. J.; Bluck A. F. L.; Bauer A. E.; Grützbauch R.; **Buitrago, F.**; Ownsworth J. 'A Deep Probe of the Galaxy Stellar Mass Functions at $z = 1 - 3$ with the GOODS NICMOS Survey', 2011, MNRAS, 413, 2845

Besides, Appendix A has been presented as the final part of the aforementioned Buitrago et al. 2011 MNRAS submitted.

Contents

List of Figures

List of Tables

Massive galaxies at high redshift

Science is a collaborative enterprise spanning the generations. When it permits us to see the far side of some new horizon we remember those who prepared the way seeing for them also.

Carl Sagan in the fourth Cosmos chapter 'Blues for the red planet'

The electron is a theory we use; it is so useful in understanding the way nature works that we can almost call it real

Richard P. Feynman – Surely you're joking Mr Feynman

Chapter 1

Introduction

1.1 A Universe of Galaxies: our current cosmological view

Most Astronomy theses start with words similar to these written by Aristotle over two thousand years ago:

ΔΙΑ ΓΑΡ ΤΟ ΘΑΥΜΑΣΕΙΝ ΟΙ ΑΝΘΡΩΠΟΙ ΚΑΙ ΝΥΝ ΚΑΙ ΤΟ ΠΡΩΤΟΝ ΗΡΞΑΝΤΟ ΦΙΛΟΣΟΦΕΙΝ, ΕΞ ΑΡΧΗΣ ΜΕΝ ΤΑ ΠΡΟΧΕΛΡΑ ΤΩΝ ΑΤΟΠΩΝ ΘΑΥΜΑΣΑΝΤΕΣ, ΕΙΤΑ ΚΑΤΑ ΜΙΚΡΟΣ ΟΥΤΩ ΠΡΟΙΟΝΤΕΣ ΚΑΙ ΠΕΡΙ ΤΩΝ ΜΕΙΣΟΝΩΝ ΔΙΑΠΟΡΗΣΑΝΤΕΣ, ΟΙΟΝ ΠΕΡΙ ΤΕ ΤΩΝ ΤΗΣ ΣΕΛΗΝΗΣ ΠΑΘΗΜΑΤΩΝ ΚΑΙ ΤΩΝ ΠΕΡΙ ΤΟΝ ΗΛΙΟΝ ΚΑΙ ΑΣΤΡΑ ΚΑΙ ΠΕΡΙ ΤΗΣ ΤΟΥ ΠΑΝΤΟΣ ΓΕΝΕΣΕΩΣ. ('For it is owing to their wonder that men both now begin and at first began to philosophize; they wondered originally at the obvious difficulties, then advanced little by little and stated difficulties about the greater matters, e.g. about the phenomena of the moon and those of the sun and of the stars, and about the genesis of the Universe.' – Aristotle, Metaphysics I, 982b12-24)

We owe the ancient Greeks many things. Arguably the most important one is this: the Universe is knowable. The first recorded scientist/philosopher, Thales of Miletus, dared to say that to understand what is surrounding us we only need to comprehend the

natural phenomena, without any interventions from gods or deities. He and his followers were seeking to find the essence of things, their real constituents, what they called φύσις ('physis'). Hence, our word Physics originally means the quest for knowing the essential nature of all things.

Since then, and even before, a plethora of Cosmologies have been developed. In this context, Cosmology means the description of all the beings which exist. The society we live in is the so called Western world, where the dominant vision of the Universe was based upon the fact that we can describe it by using Mathematics as Galileo[1] stated five centuries ago. Nevertheless, we must not forget contributions from other western cultures like the Arabs (Maimonides, Arzachel, etc.), the Jews (Abraham Zacut, etc.) or from completely different civilizations which inhabited China, India, America, Australia, etc. Everywhere there were people measuring the cycles of the sun, the moon, the stars, the planets. Moreover, the study of these celestial objects (or Astronomy, or Astrophysics as we explained previously) spans from philosophical concepts to Chemistry, Biology or Computer Science. This shared endeavour authentically make it a sort of Humanism, an eclectic science.

Less than a hundred years ago, mankind still believed in a Universe composed solely by the stars and nebulae we could see with our bare eyes or with a small telescope. The astronomers found the celestial objects were part from a larger system, something whose structure is seen at night crossing the sky as a bright strip, called the Galaxy. Again, this word comes from the Greek term κύκλος γαλαξίας ('kyklos galakticos'), which means milky circle, due to its appearance. It looks like a cloud, but a cloud made of stars. Edwin Hubble (Hubble, 1926) resolved stars in other celestial nebulae. Specifically, a special class of variable stars called Cepheids. By a previous study of Henrietta Swan Leavitt, it was known there is a correlation between the luminosity and the variability period of these stars. Consequently Hubble exploited that fact. He realized they were too distant to be members of the Milky Way, establishing that the nebulae that contained these stars were galaxies in their own right as well. From that moment the limits of our Universe have been greatly enlarged, beyond our imagination.

[1] Who knows what he felt when seeing for the first time Jupiter and its satellites with that rudimentary telescope?

Afterwards, it was discovered that the galaxies recede from us at a velocity that is proportional to their distance (Lemaître, 1927; Hubble & Humason, 1931). The conclusion reached was that the very fabric of the Universe, the space-time as Albert Einstein named it, was expanding. Along with it, all the energy and matter are affected by this global process, which 'ruthlessly' stretches the light from the galaxies to longer (and thus redder) wavelengths. Lastly, we realized that this expansion has been accelerated (Riess *et al.*, 1998; Perlmutter *et al.*, 1999). Our fellow galaxies escape from us every second quicker than the previous one. This is happening in the very moment you are reading these lines.

This is the Universe we live in. A place in which we do not know much about the mysterious (dark) components that account for the vast majority of it, a place in which the tiny left-over (which is the baryonic matter or our 'normal' matter) condensed creating the galaxies. From these atoms of baryonic material, the elements that composed our planet Earth such as carbon, oxygen, silicon or iron are mere traces in comparison with the ubiquitous hydrogen or helium, which are the main components of the stars. These stars light up an awe-inspiring Universe filled with planets, black holes, gigantic supernovae explosions and other uncountable wonders. We are overwhelmed by its immensity. It may well be boundless, or surrounded by infinite other Universes, if we pay attention to some string theory renditions.

Someone called the study of galaxies 'Observational Cosmology'. It is truly so. They are the bricks of our cosmic home. Their shapes, their compositions, their colors, their locations are the features which ultimately shape our Universe itself. This is a thesis about these galaxies.

1.2 Galaxies in a ΛCDM framework

We should define the foundations of ΛCDM, which is the current paradigm for galaxy formation and evolution. However, to fully explain the point of this section we ought to dedicate a few sentences to the Big Bang model.[2] This is the current prevailing

[2] As Carl Sagan said: 'If you want to create an apple pie from scratch, you must first create the Universe'.

theory about the origin of the Universe, but as always in science, we must leave open a door to other theories – we may cite past ideas as the Steady State Universe (Hoyle, 1948) or a modern one such as the Ekpyrotic Universe (Steinhardt & Turok, 2002) –. Since the Universe is expanding and cooling the idea that, at some point the in past, it was in an extremely hot and dense state naturally arises. We do not know what was before. We do not know why it started expanding. What we know is that there was no explosion, as space and time themselves arise from that exceptional event.

The Big Bang theory became so successful as it predicts many observables of the primitive Universe, in particular the pattern of the Cosmic Microwave Background (CMB) and the primordial nucleosynthesis. However, there are known issues still unresolved. Why is the curvature of the Universe so close to zero? (The flatness problem) Why is it homogeneous and isotropic at large ($\sim$150 Mpc) scales? (The horizon problem) Why did we not observe any relics from this ancient stage of the Universe (for example magnetic monopoles)? To answer these questions, a mechanism called 'Inflation' (Guth, 1981) was proposed, and it is still a matter of debate. Basically, it consists of a period of exponential expansion of the Universe, which lasts from 10^{-36} to 10^{-34} sec, when the Universe grew by a factor of 10^{43} (Liddle, 2003). Before the Universe was very small and close to the thermodynamic equilibrium. Quantum Physics laws dominated this period, where there were some tiny quantum fluctuations in all the physical quantities due to the Uncertainty Principle. Then Inflation is supposed to take place, spatially amplifying all the primeval perturbations, removing at its end all the theoretical issues enumerated above. For these reasons, although speculative, at the time being it is generally accepted. From this moment onwards the Universe is filled with a fluid of elementary particles.

After approximately 380,000 yr, there occurred the decoupling of matter and radiation. The temperature was low enough to permit electrons to join the atomic nuclei, and the free photons left imprinted the tiny primordial density fluctuations that were at that time, in the form of the Cosmic Microwave Background (CMB; see Figure 1.1). After this preamble, this is the perfect time to introduce the ΛCDM components.

Λ stands for the elusive dark energy which permeates the whole Universe accelerating its expansion which pulls the galaxies and their clusters apart. Its most direct evidence

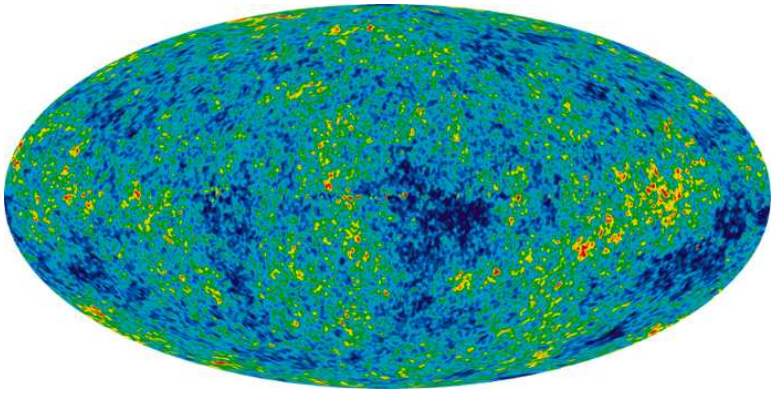

Figure 1.1: 7-year Wilkinson Microwave Anisotropy Probe (WMAP) map of the Cosmic Microwave Background (CMB) seen over the full sky. This image is the internal lineal combination map, which is the combination of the five WMAP frequency maps weighted to minimize the contribution of the galactic foreground. The Cosmic Microwave Radiation was firstly detected by Penzias & Wilson (1965). To measure its temperature fluctuations over the $2.7K$ background (which are of the order of tenths of microkelvin) in a reliable way we had to wait until the COBE satellite observations (Smoot *et al.*, 1992) . When the astronomer George Smoot announced the discovery of these ripples he said it was 'like seeing the face of God'. The map is beautiful in itself as it really is the first light of the Universe. This map shows the CMB temperature fluctuations (linear scale $\pm 200 \mu K$). Credit to WMAP Science Team $http://lambda.gsfc.nasa.gov/product/map/current/m_images.cfm$.

comes from the larger than expected dimming of SNe Type Ia (see references in section 1.1), although attempts to measure the cosmic acceleration are under way using alternative methods like Baryon Acoustic Oscillations and Weak Lensing (for a review and future plans consult Laureijs *et al.*, 2011).

CDM is the abbreviation for Cold Dark Matter. As stated previously, there is evidence for the existence of a larger amount of matter that is invisible. It was initially posited in Zwicky (1933) and since then it has been corroborated by many observables, being perhaps the more famous the non-decaying rotational curves in spiral galaxies (Rubin, Thonnard & Ford, 1978), although other possible explanations for this anomaly remain open as MOND (MOdified Newtonian Dynamics Milgrom, 1983). Dark matter would be composed by the so-called Weak Interactive Massive Particles (WIMPs). Their most likely candidate is the neutralino, which is the lightest stable particle in supersymmetric theories, and large efforts are conducted to detect it. This could be done directly (in principle with the CMS experiment of the Large Hadron Collider) or indirectly (via products of their scattering with atomic nuclei or their annihilation). The term 'cold' comes from the fact that this material moves at non-relativistic velocities at the epoch of matter-radiation decoupling and thus it makes the large-scale structure

of the Universe to grow in a bottom-up manner (Peebles, 1982; Fantin, Merrifield & Green, 2008).

Coming back again to the moment in which the CMB started, we must bear in mind that the places with slight overdensities of matter at that decoupling time were the seeds for structure creation in the next stages of the Universe. The word matter in this context refers principally to dark matter. As it is far more abundant than 'normal' baryonic matter, the gravitational potential wheels traced mostly the DM distribution. The DM particles were clumped into haloes which merge one another in a hierarchical way, i. e. they grow from smaller haloes, dragging with them the baryonic matter. When a sufficient density of this matter was present, it cooled and condensed into the first stars and protogalaxies. Cosmological simulations – as the Millennium Simulation II (Boylan-Kolchin *et al.*, 2009, see Figure 1.2) – have permitted us to visualize the structure of the Universe even at such these early cosmic epochs. These simulations show a filament-dominated large scale structure, hosting inside DM haloes and galaxies in continuous interaction, tailoring a gigantic cosmic web. Gravitational torques provided sufficient angular momentum to create the first galactic disks (Efstathiou & Jones, 1979). Toomre & Toomre (1972) also suggested that elliptical galaxies eventually evolve from major mergers of massive disk galaxies. Galaxy evolution is viewed as a hierarchical merging scenario (Toomre, 1977).

On the contrary, monolithic collapse scenario (Eggen, Lynden-Bell & Sandage, 1962), whereby galaxies are fully assembled at the same time as theirs stars are formed, is not compatible with the evolving number densities of galaxy populations. This is especially important speaking about early-type massive galaxies (van Dokkum *et al.*, 2008), however well this model predicts the chemical enrichment of these galaxies. A high redshift rapid hierarchical formation may mimic the properties of such this formation mechanism.

Cosmological volume simulations including dark matter and baryons are far beyond our currently technology. However, one can trace the merger tree of DM haloes and add a posteriori baryonic Physics recipes or prescriptions. These so-called semi-analytical models have succeed on following the evolution of individual galaxies (e.g. White & Frenk, 1991; Kauffmann, White & Guiderdoni, 1993), reproducing many observables

for late-type and early-type galaxies (De Lucia *et al.*, 2006), unambiguously demonstrating that merging of smaller systems is the cornerstone of galaxy assembly.

Taking a closer glimpse on the primeval galaxies (z$\sim$30-10; Robertson *et al.*, 2010), it is important to realize that they contain the first generation of stars. They must condense out of the neutral intergalactic medium which filled the space. As it was virtually metal-free, these stars were able to accrete enormous quantities of gas and thus it has been theorized they were extremely massive. In fact, they should be very different from present day stars, releasing huge amounts of energy as UV radiation, either produced via nuclear fusion – Population III stars (Tegmark *et al.*, 1997; Greif & Bromm, 2006; Zackrisson *et al.*, 2011) – or perhaps dark matter annihilation – Dark Matter Stars (Spolyar, Freese & Gondolo, 2008; Freese *et al.*, 2010) –. Together with the first QSOs and GRBs, they are thought to ionize the surrounding intergalactic medium. Nevertheless, our knowledge of this process is still limited (Pritchard & Loeb, 2010). Major constraints come from the absorption of UV radiation by hydrogen clouds along the line of sight of distant QSOs (Becker *et al.*, 2001), which tells us that the end of this reionization process occurred at z=6-7 (see Figure 1.3). Thanks to this, we can behold the UV restframe light from the galaxies even when the Universe was 10% of its current age and perhaps even slightly before (McLure *et al.*, 2010; Lehnert *et al.*, 2010; Bouwens *et al.*, 2011). Figures 1.4 and 1.5 aim to explain how the time scale and the spatial scale of the Universe vary with the redshift.

Galaxies at high redshifts do not look the same as at low-z (e.g. Abraham *et al.*, 1996; Conselice, Blackburne & Papovich, 2005; Elmegreen *et al.*, 2005; Delgado-Serrano *et al.*, 2010; Conselice *et al.*, 2011b, with these papers emphasizing the morphological evolution). First indications of this included finding a larger number of blue galaxies at increasing higher redshift in clusters (Butcher & Oemler, 1984), known as the Butcher-Oemler effect. When efficient observational methods to locate galaxies at high redshift were developed more probes were added to address this issue. They were both technical –with the development of CCD cameras– and conceptual –color criteria to select high redshift galaxies, for instance the 'Lyman Break Technique' (Steidel *et al.*, 1996) or the 'BzK method' (Daddi *et al.*, 2004)–. It is worth noting that these detection methods rely on the expected shape of the galaxy SEDs; for instance this 'Lyman

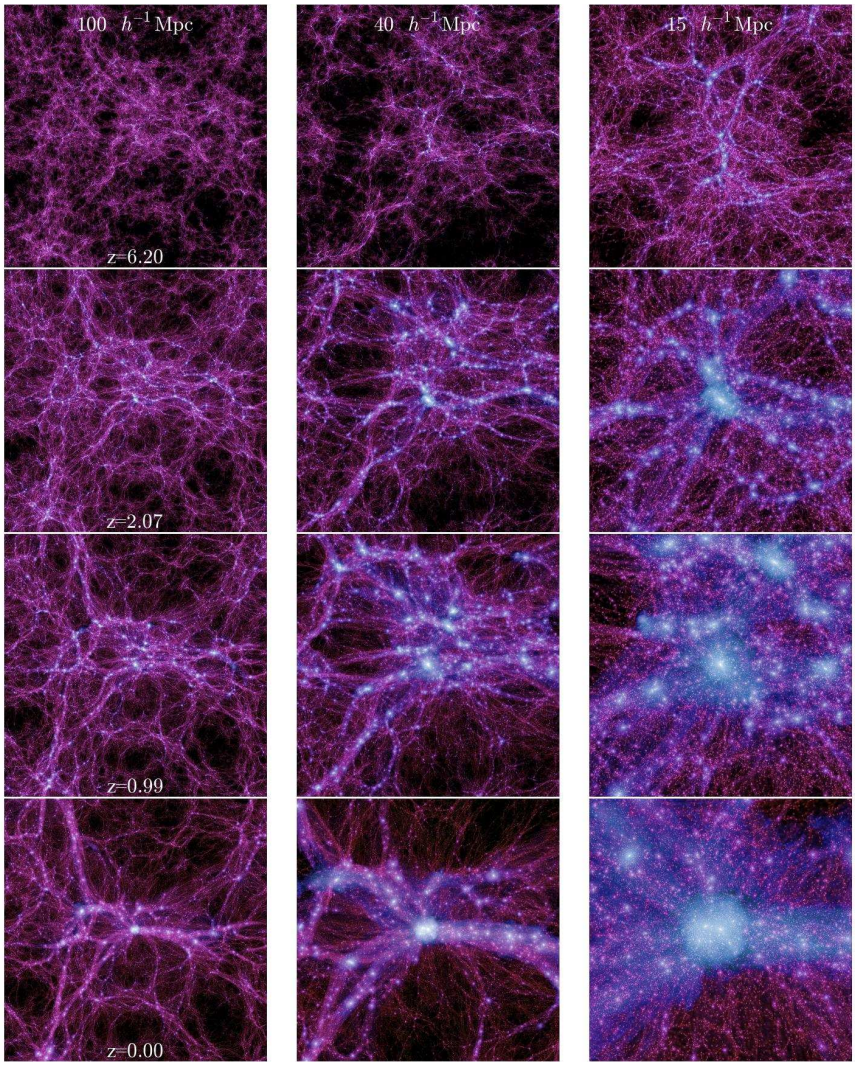

Figure 1.2: In the last 30 years, Astronomy has been revolutionized by numerical simulations. Computers not only speed up scientists' calculations but also enable them to experiment with different laws and initial conditions for astronomical objects. For instance, N-body dark matter simulations such as these series of snapshots from the Millennium Simulation II (spatial resolution $1h_{70}^{-1}kpc$ and mass resolution $6.89 \times 10^6 h_{70}^{-1} M_\odot$) have shown the intricate filamentary pattern of DM aggregates in the large scale structure of the Universe and its evolution through a wide redshift range. Image from Boylan-Kolchin *et al.* (2009).

Break Technique' is based on the fairly flat $G - R$ and extremely red $U - G$ colors for star forming galaxies.

Measurements of star formation indicated its peak was localized around $z \sim 2$ (Lilly *et al.*, 1996; Madau *et al.*, 1996) and also AGN activity reached its maximum by that cosmic time. It has been show as well that, contrary to what happens to dark matter, the baryonic component of galaxies does not share the same 'bottom-up' evolution. This anti-hierarchical scenario was firstly reported as the migration of the peak efficiency of star formation rate from low to high masses as redshift increases (Cowie *et al.*, 1996).

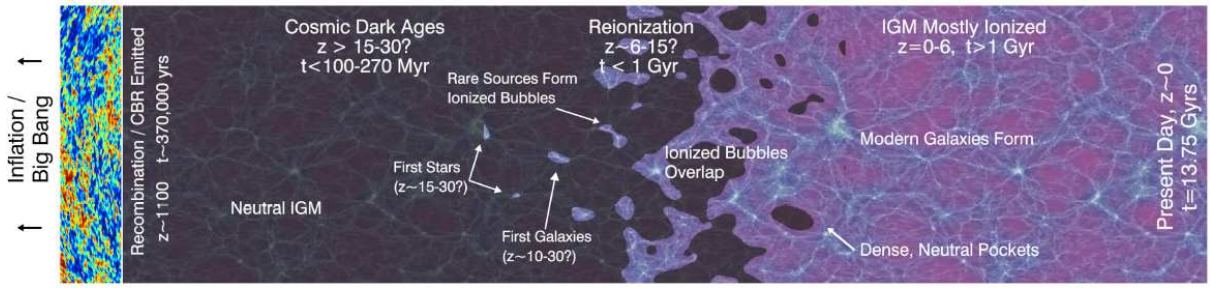

Figure 1.3: Observations at $z > 6$ are hampered by the existence of an ubiquitous haze made by the primordial atoms created after recombination. As stars and galaxies began to condense in it, they emitted huge quantities of UV photons, which created bubbles of ionized material in their surrounding areas. These bubbles grew in number and size, until they overlapped, making the Universe transparent for the restframe UV radiation we collect from the high redshift galaxies. Image from Robertson *et al.* (2010)

Certainly, this is not the only manifestation (Fontanot *et al.*, 2009) of this 'downsizing'. Another observation associated with it which plays an important role in this thesis is the fact that, the more massive a galaxy is, the more rapidly it seems it has assembled its stellar component (Bundy *et al.*, 2006; Pérez-González *et al.*, 2008a).

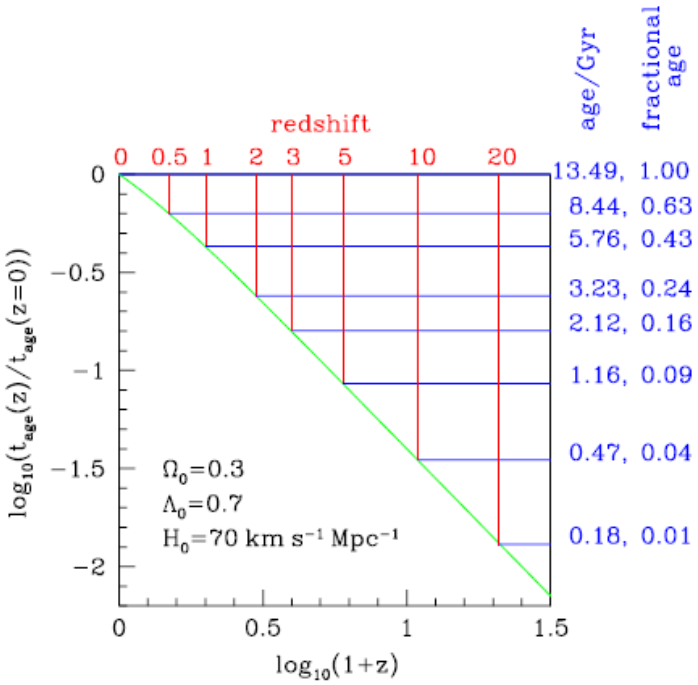

Figure 1.4: This diagram represents the relationship between cosmic or lookback time and redshift in the concordance model, which is a good approximation ($\Omega_0 = 0.3$, $\Lambda_0 = 0.7$, $H_0 = 70 kms^{-1}Mpc^{-1}$) to the most updated cosmological parameters (see Komatsu *et al.*, 2011). It is relevant to include this chart for two reasons: first, our adopted cosmology affects many key parameters in our studies such as masses, distances or surface brightness – see Hogg (1999) for a revision – and secondly, because we sometimes forget that redshift and time are not linearly correlated. As this thesis studies massive galaxy evolution at $0 < z < 3$, the reader can see we are covering 84% of the cosmic time. Image taken from Baugh (2006).

One of the most conspicuous constituents of galaxies is the Super Massive Black Hole (SMBH) which most of them (especially the massive ones) host in their centers (Kormendy & Richstone, 1995; Ueda *et al.*, 2003; Barger *et al.*, 2005; Bluck *et al.*, 2011, to cite some relevant studies). They are thought to be the AGN engines. The mass of this SMBH (which usually ranges between $10^6 - 10^9 M_\odot$) is tightly correlated with the one of the galactic bulge or spheroid (Magorrian *et al.*, 1998) and its velocity dispersion (Ferrarese & Merritt, 2000; Häring & Rix, 2004), regulating how the SMBH growths. This feedback is invoked to explain the quick and efficient quenching of star formation and the sustained lack of cooling in massive galaxies (Granato *et al.*, 2004; Croton *et al.*, 2006). Several issues remain open in this picture as simulations fail to reproduce this from first principles. In order to retrieve the right numbers of objects in the high mass end of the galaxy mass functions, the amount of feedback should be modified accordingly.

As time goes by, galaxies progressively acquire the characteristic features found in the Local Universe. There is a clear bimodality (see Fig. 1.6) in the color distribution of galaxies (Baldry *et al.*, 2004). To produce it, there are several physical processes to take into account. Massive stars are very luminous, especially at bluer wavelengths, but short-lived as well. Once they die, the galaxy quickly migrates to redder colours,

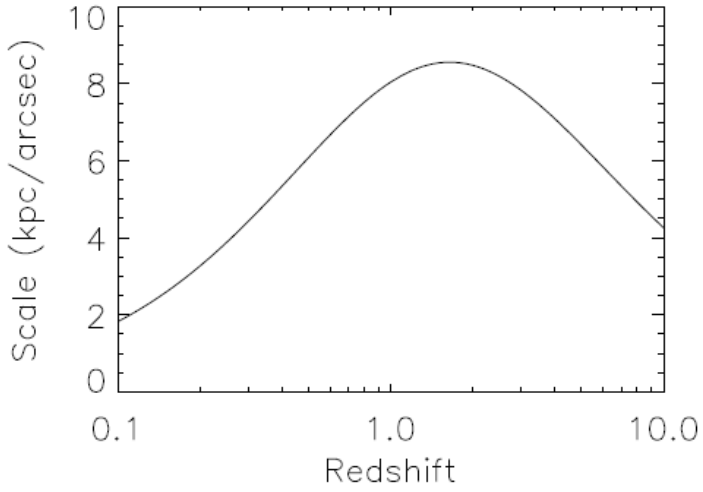

Figure 1.5: Due to the geometry imposed by the adopted cosmological parameters, the angular size of the celestial bodies is not smaller and smaller at increasing redshift/lookback time. In contrast, we reach a maximum point at $z \sim 1.5$, where the scale length is roughly 8.5 kpc arcsec^{-1}. Galaxies above that redshift value appear larger in the sky at increasing redshift, which is a counterintuitive idea. Image taken from Epinat *et al.* (2010).

in a timescale of 1-2 Gyr. Metallicity has also a key role, as more metal-rich stars are redder and dust attenuation is more effective at shorter wavelengths. All this translates – with some environmental influences, see the final paragraph of this section and Faber *et al.* (2007) – in the color-magnitude diagram for galaxies in three separated zones, which are named the blue cloud, the green valley and the red sequence.

The red sequence (see Figure 1.6) is of particular interest for the aim of this thesis, as it is mostly populated by massive galaxies. The small scatter in the color-magnitude diagram (again Figure 1.6, right chart) originates because of two reasons. Firstly, the similar ages on the formation of these objects. This fact has been tested independently by measuring their α-enhancement (the ratio of α elements against iron). As the elements Fe and Cr from delayed supernovae explosions, it is possible to constrain the formation timescale of the stellar populations (Matteucci, 1994; Thomas *et al.*, 2005; Calura & Menci, 2011). Secondly, there is a lack of later episodes of star formation. This relates most probably with the previously mentioned SMBH feedback, making them passively evolving afterwards.

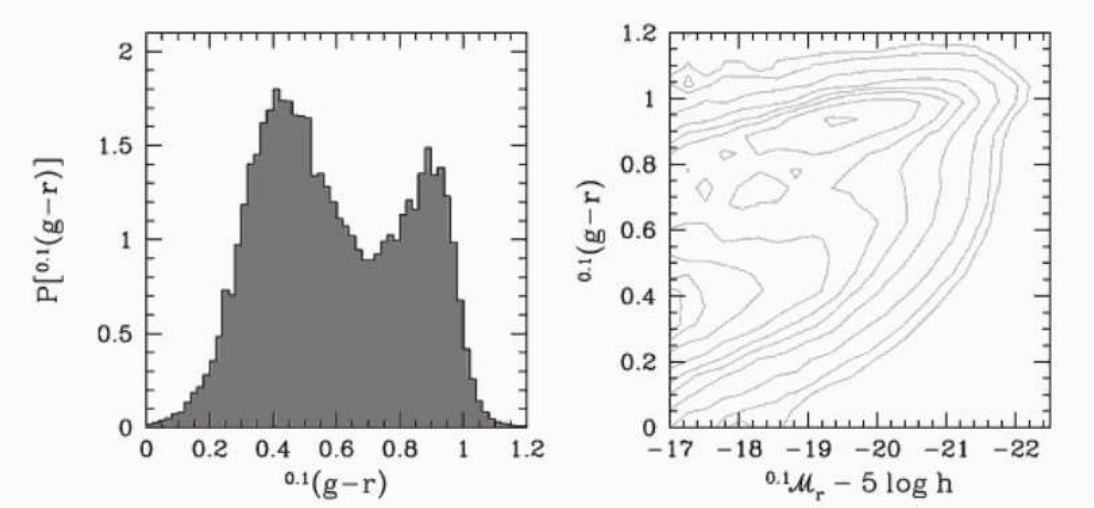

Figure 1.6: The probability density of galaxy colors (left panel) and the galaxy color-magnitude relation (right panel) in the SDSS. $^{0.1}(g-r)$ stands for $(g-r)$ colors which magnitudes have been converted to the same restframe bands at $z = 0.1$. It is easy to notice two peaks in the color distribution, a broad one in the blue part and a narrow red one the red side. Typically, they have been linked with the young and blue late-type galaxies and the old and red early-types. If looking at the color-magnitude chart, the peaks are called blue cloud and red sequence, with the transition zone in between being the green valley. The picture is not straightforward, as one can find blue star-forming ellipticals (Schawinski *et al.*, 2009) and red passive spirals (Masters *et al.*, 2010). Interestingly, brightest (and thus usually the most massive) galaxies appear to be reddest. Image taken from Mo, van den Bosch & White (2010).

Once the galaxies settle into a specific morphology their intrinsic properties establish certain well-defined dependencies, known as the Tully-Fisher relationship – luminosity and maximum rotational velocity; Tully & Fisher (1977) – for late-type galaxies and the Fundamental Plane – effective radius, surface brightness and velocity dispersion; Faber & Jackson (1976); Kormendy (1977) – for early-type galaxies.

Another major debate is the so-called 'nature or nurture' problem, i. e. knowing to what extent the environment of galaxies influences their properties. After the pioneering work of Dressler (1980), it was established that there is a morphological segregation related to the environmental density. A number of plausible mechanisms have been proposed – ram-pressure stripping (Gunn & Gott, 1972), suffocation (Larson, Tinsley & Caldwell, 1980), harassment (Moore *et al.*, 1999) – to facilitate passing from blue star-forming systems which are mainly located in the cluster outskirts to the early-type population which dominates in the cluster core. However, there is not yet a definitive answer about how all the physical agents combine together to reproduce the morphology-density relation, although multiple approaches are devoted to answering this (see for instance Gray *et al.*, 2009; Poggianti *et al.*, 2009; Ferreras, Pasquali & Rogers, 2011).

1.3 The properties of massive galaxies

Hereafter, we will refer to massive galaxies as those with $M_{stellar} \geq 10^{11} h_{70}^{-2} M_{\odot}$. The motivation for this specific mass, although somewhat arbitrary, is that it roughly matches with local Universe values of M_* ($M_{stellar} \sim 7 \times 10^{10} h_{70}^{-2} M_{\odot}$ (Cole *et al.*, 2001), assuming a Salpeter (1955) IMF). In the Press-Schechter formalism (Press & Schechter, 1974) for galaxy mass functions, this parameter is the mass value apart from which the number of galaxies decays exponentially. Massive galaxies are thought to be formed in the high density peaks of the mass distribution in the primitive Universe. They are often the most luminous galaxies at their redshift epoch because of their huge stellar component, thus making their observations excellent test-beds for galaxy formation theories. Furthermore, they may drive the galactic environment around them, being the central objects of galaxy clusters and groups. Several observational works

assure us they are already in place even at early cosmic epochs (Conselice *et al.*, 2007; Pérez-González *et al.*, 2008a; Mortlock *et al.*, 2011), but there is a lack of them in comparison with their theoretically predicted numbers that is not well explained by galaxy formation models (Benson *et al.*, 2003). It is hard to reconcile observations of seemingly massive galaxies at high-z (many of them displaying high star formation rates) with a Universe in which structures grow hierarchically (Baugh, 2006). We must conclude massive galaxies are very interesting objects from either the theoretical and observational point of view, and the fact that they are among the brightest objects at high redshift greatly helps the exploration of their properties and those of the early Universe. We devote this section to the current knowledge (and the lack of it) for massive galaxies.

1.3.1 Are massive galaxies really massive?

We ought to preface this Section 1.3 explaining how stellar masses are computed, as stellar mass is indeed not observable but only the electromagnetic radiation coming from the galaxies. The study of the Spectral Energy Distributions (SEDs), i.e. the flux of the targeted galaxy convolved with various photometric filters, is becoming a standard for obtaining stellar masses and photometric redshifts. For high redshift galaxies, we must rely on this approach for the majority of galaxies, because of the intrinsic faintness of galaxy spectra but also to cover large areas of the sky. This method consists of matching synthetic spectra or empirical galactic templates with the observed photometric fluxes of a given galaxy. Proceeding in such this way, we sample the parameter space defined by the combination of several star formation histories, and different dust and metal contents. There are various models in the literature to conduct this (Fioc & Rocca-Volmerange, 1997; Bruzual & Charlot, 2003; Maraston, 2005, to cite the most known). However, numerous assumptions must been made when making these calculations: parametrization of the star formation histories, IMF shape and dust extinction, to name but a few. There is an ample debate in the extragalactic community about what are the best combinations of parameters to tackle how high-z SEDs should be interpreted. Complicated issues remain open, principally the age-metallicity degeneracy, the universality of the IMF and the Thermally Pulsating Asymptotic Giant

Branch stars (TP-AGB) contribution to the NIR spectra of $\sim$1 Gyr old galaxies.

Muzzin *et al.* (2009) have shown, for a sample of 34 K-selected (and thus massive) galaxies at $z \sim 2.3$, the impact of using different stellar population synthesis codes, dust laws and metallicities. They inferred differences in mass of 0.18 dex between best estimations and the most extreme combination of parameters. This difference is larger (0.3 dex) when using a bottom-light IMF instead a Chabrier (2003) one. No errors in the redshifts were assumed, as they had spectroscopic redshifts. They also confirmed that the addition of Spitzer IRAC photometry substantially improves the results (e.g. Pérez-González *et al.*, 2008b). Summarizing, the quality of the fits remains almost constant through the different codes, although best fit mass values could change by a factor of $\sim$1.5-3 for massive galaxies.

1.3.2 Theories about their formation

The conundrum about their origin is far from being clear. Low redshift studies point out that these objects are the ones which dominate the red sequence and as such, their stellar populations tell us about a short and unique period of huge star formation (Cimatti *et al.*, 2008; Wiklind *et al.*, 2008). Extremely high star formation rates at high-z are necessary to form these objects. There are candidates which match this condition, along with the required stellar mass surface densities and number densities. They are the so-called submillimeter galaxies (Hughes *et al.*, 1998; Blain *et al.*, 2002, selected by flux density $S_{850} > 3$ mJy). They are among the most powerful starbust galaxies in the Universe, reaching sometimes star formation rates as high as 1000 $M_{\odot} yr^{-1}$.

Following this rationale, the formation scenario of massive galaxies would be the following one. Gas rich disks at high-z merge, triggering huge bursts of star formation in timescales of $\sim$0.1 Gyr (Hopkins *et al.*, 2008; Cimatti *et al.*, 2008). The size of the subsequent galactic remnant is inversely proportional to the level of dissipation (Hopkins *et al.*, 2009b; Wuyts *et al.*, 2010). This remnant is also fed by a number of gas rich merging/cold flows, resembling a monolithic collapse (Kereš *et al.*, 2005; Dekel *et al.*, 2009; Oser *et al.*, 2010). Once finished, another prediction of the models is that the resulting galaxy is more flattened that its low redshift massive counterparts (Naab & Trujillo, 2006; Naab, Johansson & Ostriker, 2009).

In order to test all the previous theoretical ideas observationally, Ricciardelli *et al.* (2010) proceeded to look for this kind of galaxies within the GOODS NICMOS Survey (GNS; see Conselice *et al.* (2011a) and Chapter 2 Section 2.2) and GOODS ACS public imaging (Giavalisco *et al.*, 2004). They focused on Michałowski, Hjorth & Watson (2010) sample, which provided them with spectroscopic redshifts and multiwavelength information (masses, star formation rates, SEDs, etc). They found 12 galaxies with a mix of morphologies and sizes, which nevertheless could be accommodated into an evolutionary sequence. They concluded that it was not possible to reject a scenario of these galaxies being likely precursors of the compact massive galaxy population.

1.3.3 On their compactness

In the local Universe, massive galaxies are predominantly (in a proportion of 3:1) early-type objects (Baldry *et al.*, 2004). They harbour old and metal rich stellar populations with abundance ratios resembling those produced by monolithic collapse (Thomas *et al.*, 2005; Ferreras *et al.*, 2009). There exists a clear correlation between mass and size, with the most massive galaxies featuring larger sizes (Shen *et al.*, 2003). Moreover, they are scarce objects, especially at the end of the galaxy mass function (Bernardi *et al.*, 2006; Cimatti *et al.*, 2008).

This last observational hurdle has been overcome since the advent of large NIR extra-galactic surveys in the last years, which have opened a window to locate these objects at high ($z > 1 - 1.5$) redshift. Daddi *et al.* (2005) firstly reported the apparent high compactness of these objects, with sizes $r_e \sim 1.5$ kpc. Subsequent works confirmed those observations (Trujillo *et al.*, 2006a,b, 2007; Longhetti *et al.*, 2007; Zirm *et al.*, 2007; Toft *et al.*, 2007; Cimatti *et al.*, 2008; Buitrago *et al.*, 2008; van Dokkum *et al.*, 2008; Damjanov *et al.*, 2009; Carrasco, Conselice & Trujillo, 2010; Williams *et al.*, 2010; van Dokkum *et al.*, 2010; Cassata *et al.*, 2010, 2011; Trujillo, Ferreras & de La Rosa, 2011; Damjanov *et al.*, 2011; Ryan *et al.*, 2012, among many others). The surface brightness profiles of these objects has been investigated up to very faint ($28 - 29$ mag arcsec^{-2}) limits. It is important to stress that, when talking about compactness, we are referring to the average size of this population (see mass-size relationships in Trujillo *et al.* (2007) or Buitrago *et al.* (2008) where some objects could be found close

to the local mass-size relationship). This detail is a solid probe about there is no bias when measuring galaxy sizes, as we are able to detect both large and small objects at all cosmic distances. It has also been argued about the hypothetical existence of a low surface brightness galaxy population which will be systematically missed in our observations. Deepest images to date – Hubble Ultra Deep Field; Beckwith *et al.* (2006) – do not show any galaxy with these characteristics (Bouwens *et al.*, 2004).

There appear in the literature several claims about the reliability of these results (Valentinuzzi *et al.*, 2010a,b; Mancini *et al.*, 2010). The main concern since the beginning of these investigations resides in the fact that, at large cosmological distances, the surface brightness of the celestial objects drops by $(1+z)^4$. This effect is usually called surface brightness dimming or simply cosmological dimming. Therefore, when discussing the compactness of these objects there may be two major sources of criticism: either the size measurements are wrong as we are missing a large amount of the light in their external parts or stellar mass estimates fail.

To address the first argument, Trujillo *et al.* (2006a) conducted a comprehensive series of comparisons with many observational setups (changing filters, various PSFs/seeing and fixing Sérsic indices) and obtaining a mass-size relationship (and also a luminosity-size one) robust against these changes. It was in agreement with these massive objects

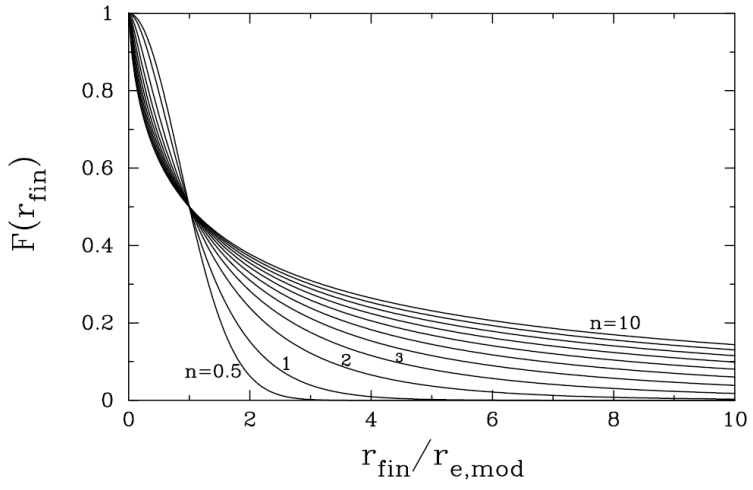

Figure 1.7: Galaxy flux missed according to its Sérsic index model. $F(r_{fin})$ stands for the fraction of the total light missed from a galaxy beyond a radius r_{fin} assuming the galactic surface brightness profile is well-described by a Sérsic function. $r_{e,mod}$ is the effective radius given by the galaxy model. As massive galaxies at high-z are typically observed up to $3-4$ effective radii, on looking at this diagram one can have an idea of the total amount of light missed because of our image noise according to the retrieved Sérsic index. Plot taken from Trujillo, Graham & Caon (2001).

having much smaller sizes than same-mass present-day galaxies. In fact, the first probe on the amount of light lost with the observational conditions parametrizing the galactic luminosity profile as a Sérsic model should be traced back to Trujillo, Graham & Caon (2001). There, the authors show the amount of light missed according to the Sérsic index depending on how far we reach in a galaxy detection (reproduced in Fig. 1.7). The outcome of this figure is that the detection of a galaxy up to 3-4 effective radius (typical HST quality for a massive high-z galaxy) accounts for 80-90% of its total luminosity, for the observed range of Sersic indices of massive galaxies.

Another very useful empirical test was the image stacking in Zirm *et al.* (2007); van Dokkum *et al.* (2008, 2010). We would like to highlight the Figure 1.8 from this last work. Here the exposure-corrected stacked images were created summing the individual images and dividing them by their weight maps (which contained masks for the neighbouring objects). Every galaxy image was normalized by its flux within 75 kpc, and the average flux outside this area was subtracted as well. These were done

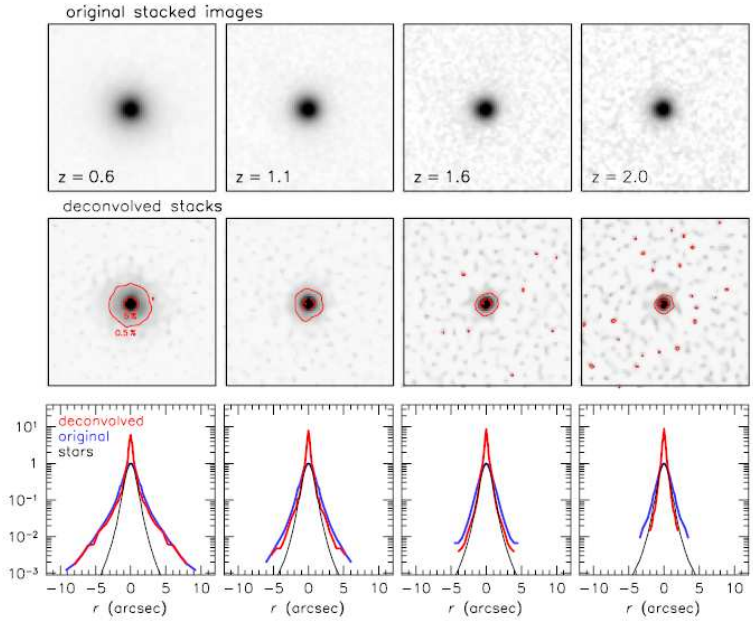

Figure 1.8: *Top row*: We present the stacks of 270 (32+87+73+78) massive galaxies in four redshift bins ($0.2 < z < 0.8$, $0.8 < z < 1.4$, $1.4 < z < 1.8$, $1.8 < z < 2.2$) in van Dokkum *et al.* (2010). The images reach ~ 28.5 mag$_{AB}$ arcsec^{-2} and correspond to ~ 300 hr of total exposure time in a 4m-telescope. *Middle row*: Deconvolved stacks. Lines show the radii where the flux is 5% and 0.5% respectively of the peak flux. We appreciate a significative evolution of low surface features over redshift. *Bottom row*: The blue line denotes the observed surface brightness profiles, red the deconvolved ones, while black is for the stacked image of stars. Again, we are witnessing the development of the galactic wings with decreasing redshift. Image taken from van Dokkum *et al.* (2010).

in order to reliably detect the galactic outskirts and have the same image quality in every redshift bin. Looking at the stacks of massive galaxies at different redshift bins, it is easy to follow how massive galaxies build up their outer regions, in an inside-out fashion.

Surface brightness profiles were also explored for individual objects (see e.g. Carrasco, Conselice & Trujillo, 2010; Szomoru, Franx & van Dokkum, 2012). In this former article, best resolution (to date) NIR images (and hence optical restframe, Figure 1.9) were taken with AO in the K-band ($2.2\mu m$). No hidden low surface brightness component was found, in agreement with previous results.

About derived stellar masses at high redshift, we developed the section 1.3.1. However, we must mention that several works based on massive galaxies' spectroscopy (Cenarro & Trujillo, 2009; Cappellari *et al.*, 2009; Newman *et al.*, 2010; Martinez-Manso *et al.*, 2011) have found velocity dispersions of the order of $\sigma \sim 200\ \mathrm{kms}^{-1}$. This fact

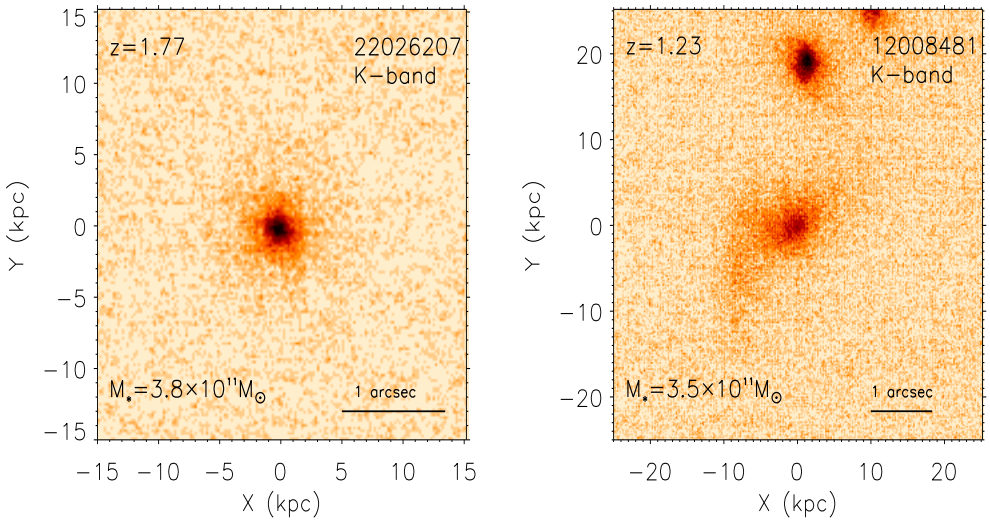

Figure 1.9: *Left side:* State-of-the-art K-band adaptive optics observation for a spheroid-like ($n = 2.54$) massive galaxy at $z = 1.77$, with an effective resolution of ~ 0.15". The object seems to be concentrated in a very small area of the detector. Its surface brightness profile unambiguously confirmed its compactness, reaching a surface brightness limit of $\mu_{crit} \sim 25.5$ K_{AB} arcsec^{-2} which is translated in mass as $10^8 M_{\odot}\mathrm{kpc}^2$. Image taken from Carrasco, Conselice & Trujillo (2010). *Right side:* Another galaxy from the Carrasco, Conselice & Trujillo (2010) adaptive optics massive sample. It is easy to see some differences with the previous image, such as its larger size and the presence of a likely interaction on its eastern (left) side. This disk-like ($n = 1.47$) galaxy has an effective circularized radius of 4.32 kpc. It has been argued that the claimed compactness for this galaxy population is an observational artifact, while some others think all their members are very small. Both extreme views are incorrect, as we certainly observe some large objects. However, the average massive galaxy is much smaller ($r_{e,circ}$=1-2 kpc) than their local Universe counterparts.

reassures us the massive nature of these objects, as these values are similar as those found in local massive galaxies (Hopkins *et al.*, 2009b).

Summarizing all the facts, there are several strong pieces of evidence about the compact nature of massive galaxies at high-z:

- The repeatability of these results using many different telescopes, instruments and observational conditions.
- Their inherent massive nature, assessed through very deep photometry and spectroscopy.
- The disappearance of faint features when stacking galaxies at progressively higher redshifts.
- Similar sizes have been found in different photometric bands, indicating that we are not missing different galactic components (bulge or disk) depending on the passband (Trujillo *et al.*, 2007; Buitrago *et al.*, 2008; Cassata *et al.*, 2010, 2011).
- Indeed, if any light is missed, we lose it as well in the mass estimation, which would lead into even higher masses.

1.3.4 Searching for massive and compact galaxies in the Local Universe

According to some model renditions, a fraction between 1% and 10% of massive compact galaxies could survive intact (in the sense that they would not have experienced important merging events) up to $z = 0$ (with a space density of $\sim 10^{-4}\mathrm{Mpc}^{-3}$ Hopkins *et al.*, 2009b). If we found any of them, our knowledge will broaden considerably as we would have an open window to the high redshift Universe, making possible unprecedented detailed observations for such these objects. Strikingly, in the nearby Universe. Trujillo *et al.* (2009) only found a fraction $< 0.03\%$ of galaxies (NYU Value-Added Galaxy Catalog, Blanton *et al.* (2005), based on SDSS Data Release 6) roughly consistent with their criteria of massive compact galaxies ($M_* \geq 10^{10.8} M_\odot$ and $r_e \leq 1.5kpc$). There were 48 galaxies at $z < 0.2$. 19 were rejected from observational issues (close

to stars, close pairs and edge-on systems) and from the final 29-object sample, their spectra showed ages of ~ 2 Gyr and metallicities $Z \sim Z_{\odot}$. AO imaging for a number of these galaxies is shown in Figure 1.10 (Trujillo, Carrasco & Ferre-Mateu, 2012). Their scarcity was confirmed by Taylor *et al.* (2010); Shih & Stockton (2011). The conclusions we may draw are that these few young objects are incompatible with being descendants of the extremely small and massive galaxies detected at high z, which virtually disappear in the nearby Universe.

Where are the high-z massive galaxies hidden in the local Universe? According to their masses and number densities the most plausible explanation is that they consist of the cores of present day Brightest Cluster Galaxies (Bezanson *et al.*, 2009; Hopkins *et al.*, 2009a). If this affirmation is correct (which most probably is, as the stellar mass present at high z cannot magically vanish), the former question is transformed into: How do these objects evolve to match their low redshift counterparts? Several evolutionary

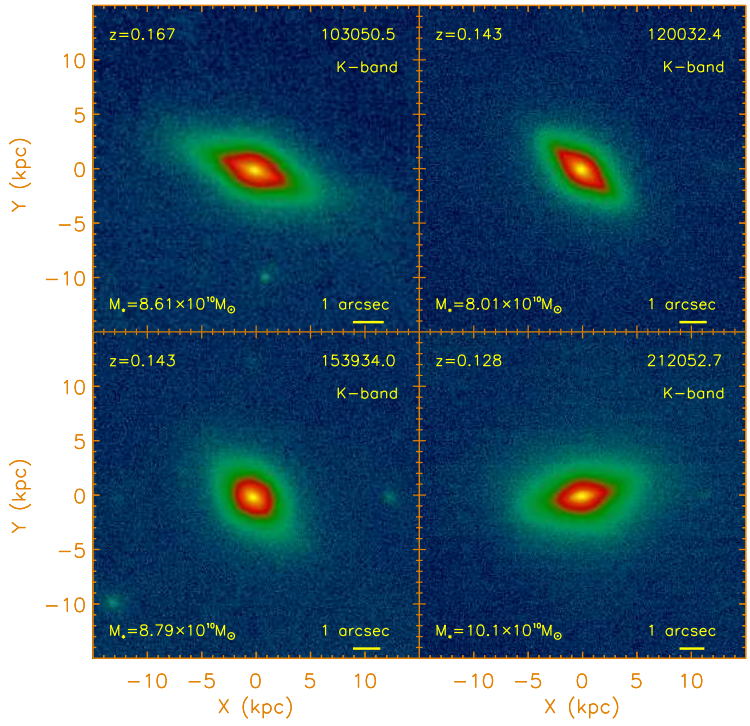

Figure 1.10: Adaptive optics observations in the K-band for compact and local massive galaxies (note the criterion for compact massive objects in this work is $M_* > 10^{10.8} M_{\odot}$ and r_e <1.5 kpc). These are the best resolution NIR images to date of the local compact galaxy population. Sérsic indices are $\sim$ 3. One expects to find a great number of details on these images, owing to the exceptional resolution (pixel scale 0.05 arcsec/pix; effective FWHM 0.2 arcsec) and low redshift. However, being so compact the galaxies are always enclosed in a small number of pixels and their morphology is not perfectly clear. From Trujillo, Carrasco & Ferre-Mateu (2012).

pathways have been advocated as suitable ways to explain the size growth, modifying at the same time the luminosity profiles of these objects into developing the massive ellipticals in the local Universe.

1.3.5 Evolutionary pathways from high to low redshift

Speaking in chronological time, major (similar mass) dry (little gas amount) merging was the first physical agent believed to contribute in this process (Boylan-Kolchin, Ma & Quataert, 2006; Khochfar & Silk, 2006), which have been observed at all cosmological distances (e.g. Patton *et al.*, 2000; Conselice *et al.*, 2003; Conselice, 2006; Conselice, Yang & Bluck, 2009; Bluck *et al.*, 2009; de Ravel *et al.*, 2009; López-Sanjuan *et al.*, 2009a,b, 2010b,a). The size-mass relationship for massive galaxies cannot be explained only with this mechanism, as too few events have been seen to explain it only by themselves (Bluck *et al.*, 2009; Bundy *et al.*, 2009; López-Sanjuan *et al.*, 2010b). To palliate this absence of a process supported by observations able to increase dramatically the galaxy sizes, the AGN puffing up scenario was proposed. In brief, the onset of a SMBH would remove the gas from the central parts of the galaxy (and thus quenching the star formation, which would explain why most massive galaxies in the local Universe are quiescent elliptical galaxies), destabilizing the galaxy inner structure, and returning the whole system to an equilibrium configuration by acquiring a more expanded stellar distribution (Fan *et al.*, 2008, 2010). Trujillo, Ferreras & de La Rosa (2011) suggested this scenario is not compatible with early-type galaxy observations at $z < 1$. According to the puffing up model, there should be an age-dependency on the mass-size relation due to the fact that older galaxies have more possibilities to undergo an AGN phase throughout their 'life'. This effect has not been seen in the ~ 3000-object spectroscopic sample studied in the aforementioned Trujillo, Ferreras & de La Rosa (2011).

Nevertheless, the most promising mechanism following the ΛCDM scenario is minor merging – usually defined as ratio in mass greater than 4:1 – as explained in Bournaud, Jog & Combes (2007); Naab, Johansson & Ostriker (2009). Based on virial theorem assumptions, it is straightforward to show (Naab, Johansson & Ostriker, 2009; Bezan-

son *et al.*, 2009):

$$\frac{r_{1+2}}{r_1} = \frac{M_{1+2}}{M_1} \tag{1.1}$$

(for equal-mass mergers)

$$\frac{r_{1+2}}{r_1} = \left(\frac{M_{1+2}}{M_1}\right)^2 \tag{1.2}$$

(for minor merging, as $M_1 >> M_2$)

The rendition from these formulae is that minor merging is more efficient on growing the galaxy size and it matches better with the low-z masses for massive galaxies. This latter statement has to do with the constraint that imposes that the mass has to grow only mildly with redshift, as most massive galaxies at $z = 0$ surpass the limit of $M_* > 10^{11.5} M_\odot$ very rarely, being the number density for the galaxies at this specific mass $\sim 10^{-4}$ Mpc^{-3} (Bell *et al.*, 2003). Resuming our minor merging discussion, its detection is especially challenging at high redshift, where their tidal features have surface brightness well beyond 30 mag arcsec^{-2} (van Dokkum, 2005). Its observations usually reach ratios of 10:1 in mass or luminosity (López-Sanjuan *et al.*, 2011), with ∼100:1 in case of very deep HST imaging (Bluck *et al.*, 2011). This minor merging must consist of a continuous bombardment with minor objects which should surround the massive ones. These minor satellites will eventually merge with the massive galaxies, providing pristine gas that will feed their star formation. Alternatively, cold gas flows could be accreted from the cosmic web filaments (Kereš *et al.*, 2005; Dekel *et al.*, 2009; Ceverino, Dekel & Bournaud, 2010), retrieving typical star formation rates of $\sim 100 \mathrm{M}_\odot \mathrm{yr}^{-1}$ (Oser *et al.*, 2010).

According to this picture, star formation rates are a pivotal point to understand the evolution of massive galaxies. Various works pointed out that massive galaxies should evolve passively after their formation process, in order to agree with the stellar populations of their local Universe counterparts. By doing so, they must be 'red and dead' objects (Kriek *et al.*, 2006; van Dokkum *et al.*, 2008; Kriek *et al.*, 2009). However, thanks to FIR data, it was soon found that this was not the case (Pérez-González *et al.*, 2008b) but many of these objects should be heavily dust obscured (Viero *et al.*, 2012). Comparing UV and IR star formation indicators confirmed that, also indicating a flat evolution in the star formation of massive galaxies at $1.5 < z < 2.5$. Hence, the physical agent responsible of their star formation quenching should act quickly to match

with their properties in the present day Universe (Twite *et al.*, 2012). It is also important to note that disk-like massive galaxies are the most star forming objects, although spheroids are not completely devoid of star formation (Cava *et al.*, 2010; Viero *et al.*, 2012).

So far our description seems to be closed, but we might inquire ourselves: How all these factors reflect on the galaxy surface brightness profiles? Do disks or spheroids better describe the morphology of these galaxies? Is it possible to check spectroscopically the importance of rotation versus velocity dispersion in setting their gravitational potential?

1.4 Aim of this thesis & its outline

This thesis tries to answer some of these open questions. Our first aim was finishing the largest compilation of massive galaxies at $1.7 < z < 3$ with the goal of characterizing in a statistically meaningful way their size evolution. This is published in Buitrago *et al.* (2008) and it is a perfect introduction to various aspects we will cover throughout the present document.

Figure 1.11 shows the stellar mass-size distribution for that sample. It is clear that, at a given stellar mass, massive galaxies are progressively smaller at higher redshift. Remarkably, none of the galaxies at $z > 1.7$ fall in the mean distribution of the local relation. Moreover, if the stellar masses were overestimated by a factor of two, only two galaxies from the sample would fall in the dispersion of the local relation. To quantify the observed size evolution, in Figure 1.12 is plotted the ratio between the GNS massive galaxy sizes (and Trujillo *et al.* (2007) sample) and the measured sizes of nearby galaxies at the same mass, by using again the SDSS. In light of this diagram, one may conclude that disk-like ($n < 2$) massive galaxies have undergone an increment of a factor of 3 in effective radius since $z = 3$, being a factor of 5 in the case of spheroid-like ($n > 2$) objects. Mean stellar densities reached are comparable to present-day globular clusters. These facts challenge galaxy formation models (Hopkins *et al.*, 2010) and their feedback mechanisms (Silich *et al.*, 2010).

We proceed in different ways to elucidate the nature of massive galaxies at high red-

shift. Chapter 2 is devoted to a photometric description of these objects. We collect a sample of 1082 massive galaxies in the redshift range $0 < z < 3$ investigating their structural parameters and visual morphologies using SDSS imaging (for the objects at $z \sim 0$) and an extensive set of HST imaging (for the high-z population). Following a naive ΛCDM rationale, whereby galaxies follow dark matter in their growth process, one would expect a progressive emergence of an spheroidal population as cosmic time increases due to hierarchical nature of the this paradigm. Although there is indirect proof of this scenario (see e.g. van der Wel *et al.*, 2011; van Dokkum *et al.*, 2011), we conducted a comprehensive series of tests on the morphological nature of massive galaxies at $0 < z < 3$.

To test to what extent this morphological evolution is correct, we need ultimately spectroscopic confirmation. However, traditional long-slit techniques cannot provide us with properties such as rotational velocity, velocity dispersion or metallicity over the spatial extent of the galaxy, and thus accounting for how the mass assembly is taking place. 3D spectroscopy is the solution to this problem, and our study utilising this ob-

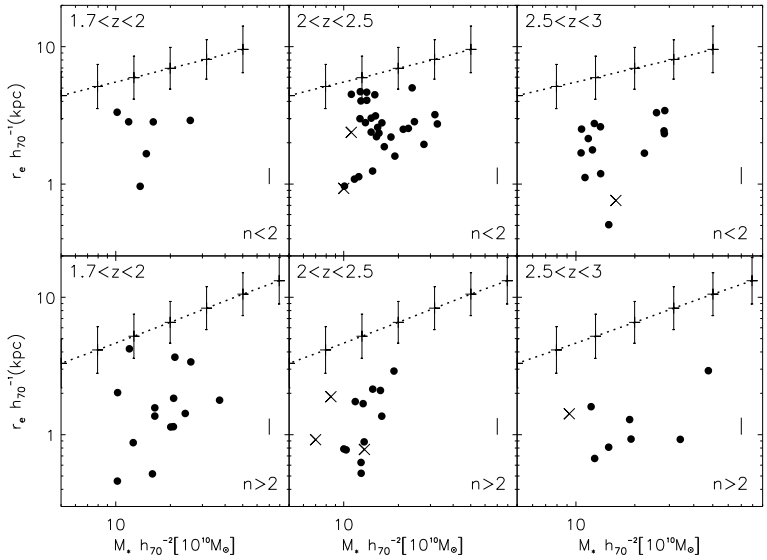

Figure 1.11: The stellar mass-size distribution in Buitrago *et al.* (2008). Top row display the positions of disk-like galaxies ($n < 2$) and the bottom one for spheroid-like galaxies ($n > 2$) Overplotted are the mean and the 1σ dispersion of the distribution of the Sérsic half-light radius of SDSS galaxies as a function of stellar mass (Shen *et al.*, 2003) and the crosses are the galaxies from van Dokkum *et al.* (2008) whose masses have been converted to a Chabrier (Chabrier, 2003) IMF. Typical error in sizes is about 0.3 kpc and it is denoted by the smaller bar at the right side. Uncertainties in stellar masses are ~ 0.2 dex. Image from Buitrago *et al.* (2008).

servational method could be found in Chapter 3 . This relatively novel observational technique is a synergy between photometry and spectroscopy. It is based on the division of the telescope field-of-view in several parts which are afterwards dispersed and rearranged in the initial configuration, producing a final data cube with images of the galaxy at different wavelengths. This is perfect for our purposes as we want to know how the internal velocities of the galaxy relate with its structure. Moreover, the kinematics of massive galaxies is influenced by the physical processes which have an impact in their evolution. Thus, valuable information can be drawn attending to the physical phenomena that are occurring in our sample, evaluating which ones are more significant, such as minor & major merging, AGNs, elusive gas cold flows or a clumpy phase in their formation.

In Chapter 4 we construct the mass-size relationship for the total GOODS NICMOS Survey (GNS) sample. By doing so we aim to figure out the connections between massive galaxies and lower mass systems. So far the only well-known mass-size relation at high-z is the one built using massive galaxies, and our work is an attempt to clarify whether the rest of the galaxies follow a similar size evolution. We also tried to

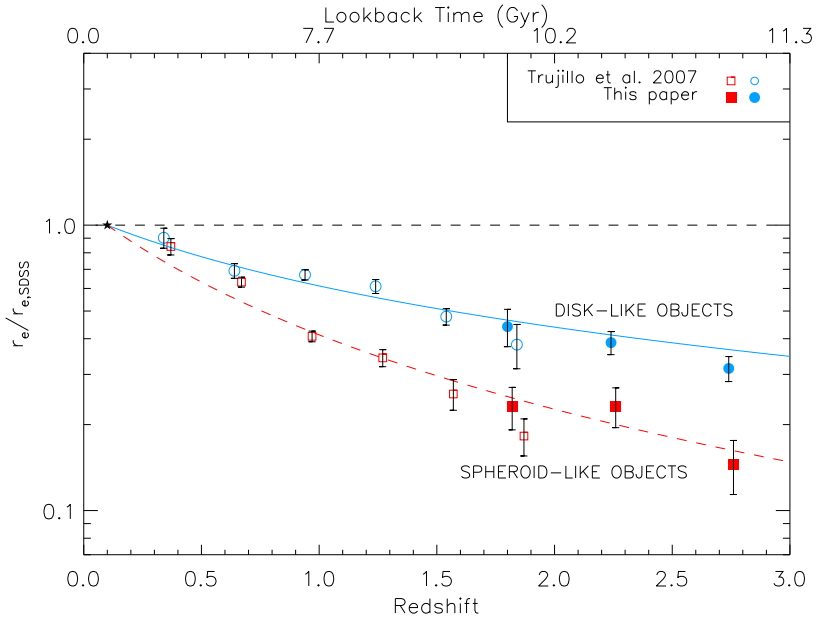

Figure 1.12: Size evolution of massive galaxies with redshift. We plot the ratio between the GNS massive galaxy effective radii and the measured effective radii of nearby SDSS galaxies at the same mass. Circles refer disk-like objects ($n < 2$) while square symbols refer spheroid-like galaxies ($n > 2$). At $0.2 < z < 2$, the points correspond to the massive galaxy sample of Trujillo *et al.* (2007), in which Sersic separation is $n = 2.5$. Error bars are $1 - \sigma$ errors. Image from Buitrago *et al.* (2008).

characterise the massive galaxies at $z > 3$.

We finish this thesis in Chapter 5 with a summary of our results and the description of the future projects we will perform to study in depth the nature of the massive galaxy population. The Appendices provide us with the simulations we did to test the recovery of the structural parameters in our GNS H-band imaging (Appendix A) and a guide of useful abbreviations used (Appendix B).

Throughout this thesis, we use AB magnitudes and adopt a 'concordance' cosmology (H_0=70 km s^{-1}Mpc^{-1}, Ω_λ = 0.7, and $\Omega_{\rm m}$ = 0.3) unless otherwise stated.

Yet it is possible that some bodies, of a nature altogether new, and whose discovery may tend in future to disclose the most important secrets in the system of the universe, may be concealed under the appearance of very minute single stars no way distinguishable from others of a less interesting character, but by the test of careful and often repeated observations.

John Herschel, on creating the Royal Astronomical Society

E pur si muove. (And yet it moves.)

Galileo Galilei, after recanting about his theories

Chapter 2

Morphological change of massive galaxies since $z = 3$

2.1 Introduction

The present-day massive galaxy population is dominated by objects with early-type morphologies (e.g. Baldry *et al.*, 2004; Conselice, 2006). However, it is still unknown whether this was also the case at earlier cosmic epochs. Addressing this question is key in our understanding of the physical processes that drive galaxy evolution, as galaxy morphology is directly linked to the evolutionary paths followed by these objects. In fact, a profound morphological transformation of the massive galaxy population is expected within the currently most favoured galaxy formation scenario, the hierarchical model. For massive galaxies the model predicts a rapid formation phase at $2<z<6$ dominated by a dissipational in-situ star formation fed by cold flows (Oser *et al.*, 2010; Dekel *et al.*, 2009; Kereš *et al.*, 2005) and/or gas rich mergers (Ricciardelli *et al.*, 2010; Wuyts *et al.*, 2010; Bournaud *et al.*, 2011). At the end of this phase, massive galaxies are expected to be more flattened and disk-like than their lower redshift massive counterparts (Naab, Johansson & Ostriker, 2009). After this monolithic-like formation phase, massive galaxies are predicted to suffer a period of intense bombardment by minor satellites (Khochfar & Silk, 2006; Hopkins *et al.*, 2009a; Oser *et al.*, 2010; Feldmann, Carollo & Mayer, 2011) that may eventually transform the original disk-like population into the predominant present-day spheroid-like population.

Although the above scenario is very suggestive of a deep morphological transformation of the massive galaxy population, there is no compelling observational evidence supporting this scenario. However, some recent works suggests that this could be the case (e.g. Van der Wel *et al. 2011*, Cameron *et al.* 2011). To probe this transformation is difficult from the observational point of view due to the scarce number of massive galaxies at high-z. However, the advent of wide area and deep near infrared surveys (e.g. Dickinson, Giavalisco & GOODS Team, 2003; Scoville *et al.*, 2007; Conselice *et al.*, 2011a) have opened the possibilities of exploring a large number of these galaxies up to high redshifts. In this chapter we address, for the first time, the issue of the morphological transformation of massive galaxies using a statistical representative sample of nearly $\sim$1000 galaxies with $M_\star \geq 10^{11} h_{70}^{-2} M_\odot$ obtained from the SDSS DR7 (z$\sim$0; Abazajian *et al.*, 2009), POWIR/DEEP2 (0.2<z<2; Bundy *et al.*, 2006; Conselice *et al.*, 2007) and GNS (1.7<z<3; Conselice *et al.*, 2011a) surveys. We have already conducted a morphological quantitative analysis of the above galaxies in previous papers (Trujillo *et al.*, 2007; Buitrago *et al.*, 2008) where we have provided clear evidence for a significant size evolution for these objects since z$\sim$3. However, a visual classification of these galaxies has been missing. In this chapter we take advantage of the combined power of the visual and quantitative morphological analysis to explore how the morphologies of the massive galaxy population has changed with redshift.

The structure of this chapter is as follows: Section 2.2 is devoted to the data description and its analysis, Section 2.3 presents our main results and in Section 2.4 we discuss them. At the end of this thesis we add an Appendix containing the simulations we have performed to test the accuracy of our structural parameter determination in the GNS. Hereafter, we adopt a cosmology with Ω_m=0.3, Ω_Λ=0.7 and H_0=70 kms^{-1} Mpc^{-1}.

2.2 Data

To accomplish our objectives we need a large number of massive galaxies to be statistically meaningful at all redshifts. Ideally we would also like to study all our galaxies in a similar wavelength range. This is the reason behind our choice of working with several different surveys. The imaging for the local Universe galaxy reference sample

was obtained using the SDSS DR7 (Abazajian *et al.*, 2009) although our sample was selected from the NYU Value-Added Galaxy Catalog (DR6). This catalog includes single Sérsic (1968) fits for 2.65×10^6 galaxies (Blanton *et al.*, 2005), from which 1.1×10^6 galaxies have spectroscopic information. Stellar masses come from Blanton & Roweis (2007), which uses a Chabrier (2003) IMF. We limited our work to all the massive ($M_\star \geq 10^{11} h_{70}^{-2} M_\odot$) galaxies with spectroscopic redshifts up to $z = 0.03$. We have selected this redshift to have a local sample with a number of objects ($\sim$200) similar to the number of galaxies we have in our higher redshift bins. On doing this we assure they are all affected statistically in a similar way, i.e., the statistical errors are similar. By selecting also z=0.03 we guarantee that our galaxies are retrieved from a sample that is complete in stellar mass. One object of the local sample was rejected as we discovered it was a stellar spike. Our final number of local galaxies is 207. We have used the g-band imaging of SDSS to classify visually our local sample.

In the redshift range $0.2 < z < 2$ we utilised the Palomar Observatory Wide-field InfraRed POWIR/DEEP2 survey (Bundy *et al.*, 2006; Conselice *et al.*, 2007). In relation to the imaging used, we restricted ourselves to the ACS I-band coverage in the Extended Groth Strip (EGS). The sample of massive galaxies selected from this survey constitutes the largest sample of massive galaxies in this redshift range published to date. The EGS field (63 Hubble Space Telescope tiles) was imaged with the Advanced Camera for Surveys (ACS) in the V(F606W, 2660s) and I-band (F814W, 2100s). Each tile was observed in 4 exposures that were combined to produce a pixel scale of 0.05 arcsec with a Point Spread Function (PSF) of 0.125 arcsec Full Width Half Maximum (FWHM). The depth reached is $I_{AB} = 27.52\ (5\sigma)$ for point sources, and about 2 magnitudes brighter for extended objects. Complementary photometry in the B, R and I bands was taken with the CFH12K camera at CFHT 3.6-m telescope and in the K_s and J bands with the WIRC camera at the Palomar 5-m telescope.

In total, 421 massive galaxies possess spectroscopic redshifts out of the total 795 in this survey. There were 35 more massive galaxies in the parent sample, but they were excluded as they are identified as AGN and hence they may skew our results. When spectroscopic information was not available, photometric redshifts were calculated for the bright galaxies ($R_{AB} < 24.1$) using ANNZ code (Collister & Lahav, 2004) and BPZ

(Benítez, 2000) for the rest. Accuracy is $\delta z/(1+z) = 0.025$ for $z < 1.4$ massive galaxies, and $\delta z/(1 + z) = 0.08$ for the others (Conselice *et al.*, 2007). Masses were calculated with the method described in (Bundy *et al.*, 2006; Conselice *et al.*, 2007; Trujillo *et al.*, 2007): fitting a a grid of model SEDs constructed from (Bruzual & Charlot, 2003) (BC03) models, parametrizing star formation histories by $SFR \propto exp(-t/\tau)$ (the so-called tau-model) with a range of metallicities and dust contents. To analyze the impact of TP-AGB emission, the same exercise was also performed with Charlot & Bruzual (2007) models, inferring slightly smaller masses ($\sim 10\%$). Combining the total uncertainties with those of the photometric redshifts, errors in the masses could be as high as $\sim 32\%$ for $z > 1.4$ galaxies (Trujillo *et al.*, 2007).

For the highest redshift bins we used the GOODS NICMOS Survey (GNS; Conselice *et al.*, 2011a). The GNS is a large HST NICMOS-3 camera program of 60 pointings centered around massive galaxies at $z = 1.7 - 3$ at 3 orbits depth, for a total of 180 orbits in the F160W (H) band. Each tile (52"x52", 0.203"/pix) was observed in six exposures that were combined to produce images with a pixel scale of 0.1 arcsec, and a PSF of ~ 0.3 arcsec FWHM. The massive galaxies were firstly identified using a series of selection criteria: Distant Red Galaxies from Papovich *et al.* (2006), IRAC Extremely Red Objects from (Yan *et al.*, 2004) and BzK galaxies from Daddi *et al.* (2007). Photometric redshift and masses take advantage of the superb GOODS fields coverage (BVRIizJHK). Basically, they are obtained using BC03 models assuming Chabrier (2003) IMF. As we are probing the optical restframe in these observations, possible effects by TP-AGB stars are minimized. Errors are typically 0.2-0.3 dex. We use spectroscopic redshifts (11) when available (Barger, Cowie & Wang, 2008; Popesso *et al.*, 2009), that agree well with photometric determinations – $\delta z/(1 + z) \sim 0.03$, Buitrago *et al.* (2008) –. This sample is the largest massive galaxies compendium (80 objects) at $1.7 < z < 3$ we are aware of.

2.2.1 Quantitative and visual morphological classification

Once we selected the final sample of objects, the surface brightness distributions of all our galaxies were fit with a single Sérsic model (Sérsic, 1968) convolved with the PSF of the images. The Sérsic model has the following analytical form:

$$I(r) = I_e \exp\left\{-b_n\left[\left(\frac{r}{a_e}\right)^{1/n} - 1\right]\right\}$$

where I_e is the intensity at the effective radius, and a_e is this effective radius along the semimajor axis enclosing half of the flux from the model light profile. The quantity b_n is a function of the radial shape parameter n (called the Sérsic index), which defines the global curvature in the luminosity profile, and is obtained by solving the expression $\Gamma(2n) = 2\gamma(2n, b_n)$, where $\Gamma(a)$ and $\gamma(a, x)$ are, respectively, the gamma function and the incomplete gamma function. We first estimated the apparent magnitudes and sizes of our galaxies using SExtractor (Bertin & Arnouts, 1996) which were then fed as initial conditions to the GALFIT code (Peng *et al.*, 2002, 2010). GALFIT convolves Sérsic $r^{1/n}$ 2D models with the PSF of the images and determines the best fit by comparing the convolved model with the observed galaxy surface brightness distribution using a Levenberg-Marquardt algorithm to minimise the χ^2 of the fit. From our measurements, the sizes were circularized, $r_e = a_e\sqrt{1-\epsilon}$, with ϵ the projected ellipticity of the galaxy.

Before we carried out our fitting we removed neighbouring galaxies using an object mask – as in Häussler *et al.* (2007) –. GALFIT allows the user to exclude pixels from a fit by setting them to a value greater than zero in a 'mask' FITS file. This is done for objects that lay far away from the target galaxy. In the case of very close galaxies with overlapping isophotes, objects were fit simultaneously. Due to the point-to-point variation of the shape of the camera PSF in our images we chose several (non-saturated) bright stars to gauge the accuracy of our parameter estimations. The final values for the structural parameters are the mean of these independent runs (one per each star used as PSF) per object. They are published as part of Trujillo *et al.* (2007) and Conselice *et al.* (2011a). Details on our structural parameter recovery can be found in Appendix A.

In relation to the SDSS imaging, although the NYU catalog already provides us with structural parameters obtained using Sérsic fits to the galaxies, for the sake of consistency with our methodology, we ran GALFIT on the SDSS images of these galaxies to obtain structural parameters. Besides, it is known that the NYU catalog has a systematical underestimation of the Sérsic index, effective radius and total flux, as it is

reported in the simulations performed in Blanton *et al.* (2005) and in the appendix of Guo *et al.* (2009). It occurs mostly for objects with $n > 2$, and it is due to the fact that they are using azimuthally averaged 1D Sérsic profiles instead of more accurate 2D algorithms such as GALFIT, and also because of an overestimation of the local sky noise in dense environments by their pipeline. Our findings agree with this fact, as we find an offset of $26 \pm 2\%$ for the circularised effective radius values of our galaxies and another $14 \pm 3\%$ for the Sérsic indices. (excluding all the galaxies which fall in NYU catalog's fit constraints, which are $n = 5.9033$ and $r_e = 29.7504$ arcsec).

In addition to the quantitative morphological analysis explained above, visual morphological classifications were done for all the galaxies in our sample. To assure a high reliability in our results, the student and his supervisors (FB and IT, with checks by CC) classified visually all the galaxies in an independent way. We divided our sample according to the Hubble classification scheme into spheroid-like objects (E+S0 or early-type), disk-like objects (S or late-type) and peculiar galaxies (either irregular galaxies or ongoing mergers). In Figure 2.1 we show some examples of our classification scheme at different redshifts. Very conspicuous bulge systems were identified as early-type objects. Both E and S0 galaxies are hence included together in the same morphological class. We avoid segregating between E and S0 since, at high-z, it is a difficult task to distinguish between these two types of galaxies, and we prefer to remove this potential source of error. Spiral or late-type morphologies are detected by a central brightness condensation located at the centre of a thin disk containing more or less visible spiral arms of enhanced luminosity. Lastly we joined irregular (unsymmetrical) galaxies and mergers in the same class, again to avoid any misclassification at high-z where the details are more difficult to interpret. We created a series of randomly generated galaxy montages (from Figure 2.2 to Figure 2.10) to show the reader representative examples of the various morphological classes through the different surveys presented in this chapter.

It is not straightforward to asses the robustness of these results based on visual morphologies due to the subjective nature of classifications. At z$\sim$0, we can compare our classification with independent studies. First, we compare our results with the SDSS Bayesian automated morphological classification by Huertas-Company *et al.* (2011).

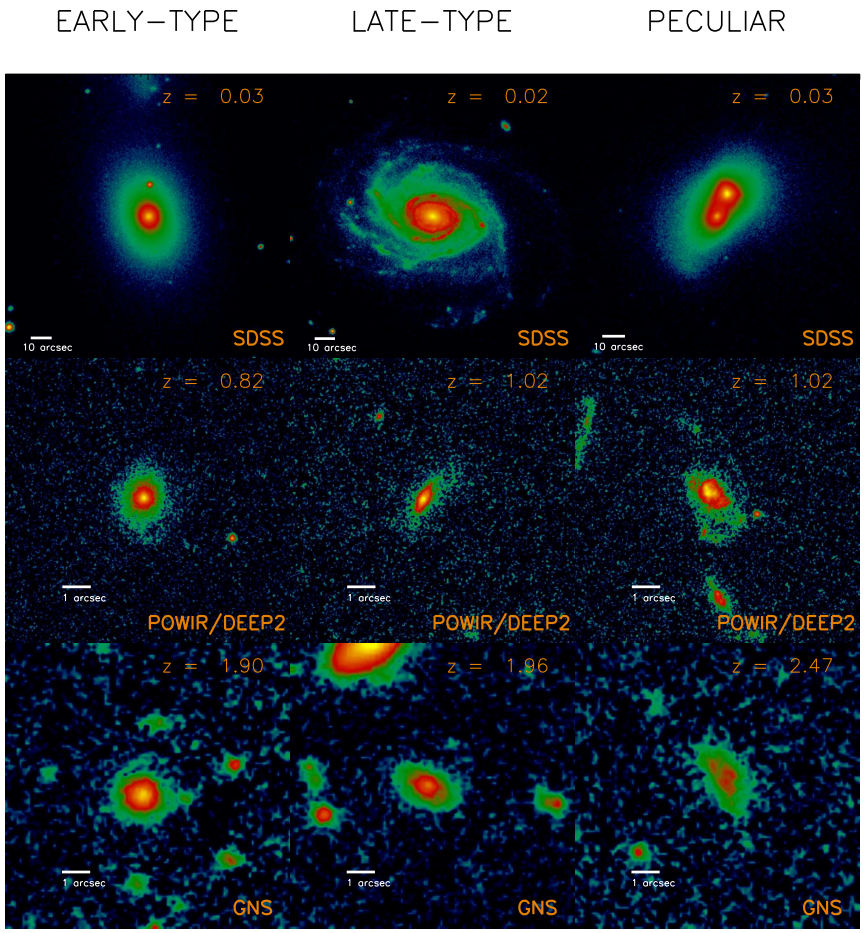

Figure 2.1: Some examples illustrating our morphological criteria (columns) for different galaxies of our sample. Each row shows galaxies of the different surveys. Please note the different scales of each image due to each galaxy redshift (lower left corner); according to the cosmology used in this work, 10 arcsec in SDSS are ~ 6 kpc at z$\sim$0.03, while 1 arcsec in the HST imaging at $z \geq 1$ is ~ 8 kpc. Despite the decrease in angular resolution and the cosmological surface brightness dimming with redshift, the exquisite HST depth and resolution ($\sim$10 times better than ground-based SDSS imaging) allow us to explore the morphological nature of the high-z galaxies. Note that irregulars and mergers are in the same morphological class (peculiars).

There are 190 out of our 207 galaxies in common where can make a direct comparison. They applied support vector machine techniques (Huertas-Company *et al.*, 2008) to associate a probability to each galaxy being E, S0, Sab or Scd. For those galaxies where they have assigned a probability larger than 90% of pertaining to a given class, their neural network agrees with our visual classification for 89% of the early-types and 68% of the late-types. Moreover, all our SDSS local galaxies have been visually classified within the Galaxy Zoo project (Lintott *et al.*, 2011) with similar criteria than ours. We find that 112 out of the 121 galaxies that we classified as early-type are classified as ellipticals by Galaxy Zoo (i.e. $\sim$93%). For spiral galaxies we get 48 out of 62 (i.e. $\sim$77%). Consequently, our local classification seems to be robust.

2.2.2 Potential observational biases

We acknowledge, however, that at higher redshifts visual morphological classification is more controversial for several reasons. First, the cosmological surface brightness dimming may affect the recognition of fainter galactic features and second, the angular resolution is poorer at higher redshift. Nonetheless, the first effect is compensated by the increase of the intrinsic surface brightness of the galaxies due to the higher star formation in the past and the fact that their stellar populations are younger. In relation to the angular resolution, at z=0.03, one arcsec is equivalent to 0.6 kpc, whereas at 1<z<3 it is $\sim$8.0 kpc. Fortunately, the higher resolution imaging used for exploring the morphologies of our high-z galaxies (FHWM is 0.125arcsec [pixel scale 0.05 arcsec/pix] for the ACS camera and 0.3 arcsec/pix [pixel scale 0.1 arcsec/pix] for the NICMOS3 camera) compared to the local ones (FWHM$\sim$1.0-1.5 arcsec [pixel scale 0.396 arcsec/pix]) alleviates this problem, although in general, a smoother surface brightness distribution due to the worse resolution is expected. All these effects, combined, would imply that at higher redshifts there would be a larger number of featureless objects that visually would be confused with early-type galaxies. We will show in the next section that this is the opposite of what we find, giving a stronger support to the results of this chapter.

2.2.3 K-correction study

The K-correction effect is another potential source of error both in the quantitative and visual morphological classification. We have selected our filters at each survey to minimise this effect and observe the galaxies as much as possible in the restframe g-band. Nonetheless, our classification at $1.3 \lesssim z \lesssim 2$ could be compromised by using F814W as this filter is tracing the UV restframe of our targets.

We explore how relevant this effect is by analysing the properties of 24 galaxies with $z<2$ in our sample of the EGS which have also H-band NICMOS imaging. In Trujillo *et al.* (2007) we showed the size difference between the optical and near-infrared for these galaxies (their Fig. 4). We did not find a systematic bias, but a scatter of 32% for these measurements of the effective radius. In relation to the Sérsic index, we find an offset of $30 \pm 9\%$ towards larger indices in the H-band. The difference in the visual morphology between the I and the H-bands shows that 19 galaxies ($79 \pm 18\%$) have the same morphology in the two filters, while only 5 ($21 \pm 9\%$) are catalogued differently.

In addition to this analysis of galaxies in the EGS, we can compare the difference between the I and H band morphologies for those galaxies in the GNS with $1.7<z<2$ (which is the redshift range where our POWIR/DEEP2 and GNS massive galaxy samples were selected to overlap). We use the I-band ACS imaging of the GOODS fields (Giavalisco *et al.*, 2004). This represents the most extreme K-correction for the galaxies we studied in ACS. Post-stamps images for the 20 common galaxies were retrieved from the RAINBOW database[1] (Barro *et al.*, 2011). RAINBOW is an interactive web-based tool to obtain SEDs and images for galaxies within premium CANDELS fields (Grogin *et al.*, 2011). We found that 6 galaxies ($30 \pm 12\%$) were not possible to classify due to the few pixels that correspond to the galaxy in the image, most probably due to dust obscuration (Buitrago *et al.*, 2008; Bauer *et al.*, 2011). For the other 14, 11 ($55 \pm 17\%$) have the same visual morphology while for 3 galaxies ($15 \pm 9\%$) it is different. Regarding the accuracy in retrieving their structural parameters, our GALFIT analysis show that the effective radius and the Sérsic index are recovered without any significant offset, but with a large scatter as in the aforementioned Trujillo *et al.* (2007). On the visual morphologies detected, in the ACS camera, $43 \pm 17\%$ are late-

[1] $https://rainbowx.fis.ucm.es/Rainbow\_navigator\_public/$

types (50 ± 16 in NICMOS), $29 \pm 14\%$ are early-types ($35 \pm 13\%$) and $29 \pm 14\%$ are peculiars ($15 \pm 9\%$). Summarizing, K-correction undoubtedly plays a role, but visual morphologies are robust against these changes within our study.

A number of studies (e.g. Conselice *et al.*, 2011b; Weinzirl *et al.*, 2011) have redshifted local massive galaxies with codes such as FERENGI (Barden, Jahnke & Häußler, 2008) to measure directly the impact of the K-correction and cosmological dimming in the galaxy images. Despite this method intends to take all the systematics into consideration, its efforts are inherently hampered by the impossibility of determining the luminosity evolution history for a given galaxy. As we will explain on Section 2.3, we carried out extensive simulations to measure to what extent we are able to reliably retrieve the galaxy structural parameters, which it is an alternative unbiased way to probe whether we are missing a certain parameter space region on the massive galaxy properties.

Finally, some authors argue about the convenience of performing double Sérsic fits (fixing the disk component to $n = 1$ and the bulge to $n = 4$, or allowing variations in this bulge Sérsic index). This bulge-to-disk decomposition is undoubtedly a better description of the galaxy luminosity profile. However, one needs sufficient signal-to-noise ratio in the images to obtain meaningful results, i.e., adequate χ^2 values in the fits. We must note that our images (except SDSS ones) do not permit such exercise. Besides, utilizing single Sérsic models makes possible comparisons among our sample's galaxies and with the vast majority of works in the literature.

2.2.4 Axis ratios

Finally, we can conduct a further test to quantify the robustness of our visual classification, namely to explore the axis ratio distribution of our objects. The axis ratio distribution of local disk galaxies has a mean value of $\sim$0.5 (Ryden, 2004). On the other hand, the axis ratio distribution of the nearby E/S0 population is known to peak at around 0.7-0.8 (Ryden, Forbes & Terlevich, 2001). In Table 2.1 we show the mean axis ratio for our different galaxy population as a function of redshift. We find that the objects that are visually classified as early-type galaxies have a typical axis ratio of $\sim$0.7 (independent of their redshift). This is similar to the values found in the local

Universe. Also, for galaxies visually classified as disks, the axis ratio is independent of the redshift with an average b/a$\sim$0.55. Again, our value is in good agreement with the expectation from the local Universe. This test reinforces our idea that the visual classification that we are doing is accurate.

2.3 Results

The evolution of the morphologies of the galaxies with redshift can be addressed in two different ways: quantitative (exploring how the structural parameters have changed with time) and qualitative (probing how the visual appearance has evolved with redshift). In the local Universe, the structural properties of the massive galaxies (mainly its light concentration) can be linked with their appearance. In particular, as a first approximation one can identify disk or late-type galaxies with those galaxies having lower values of the Sérsic index (n$\sim$1; Freeman, 1970) and early-type galaxies with those having a profile resembling a de Vaucouleurs (1948) shape (n$\sim$4). This crude segregation based on the Sérsic index was shown to work reasonably well by Ravindranath *et al.* (2004). Whether this equivalence also holds at higher redshift is not clear, and in this chapter we explore this issue.

In Fig. 2.11, we show the Sérsic index distribution for our different visually classified morphological types as a function of redshift. The mean value as well as the width of the distribution is listed on Table 2.1. At all redshifts, massive galaxies identified visually as late-types show low values of the Sérsic index. This reinforces the idea that the stellar mass density distributions of rotationally supported systems are close to an exponential profile. However, the distribution of the Sérsic index for these late-type galaxies shows a tail towards larger values. This is normally interpreted as the result of the bulge component. In fact, the excess of light caused by the bulge at the center of the disk will increase the value of this concentration parameter when the galaxies are fitted just using a single Sérsic model. Interestingly, we observe that at higher redshift the prominence of this tail of higher Sérsic indices decreases for the late-type galaxies. One could be tempted to interpret this result as a result of the disappearance of prominent bulges at higher redshifts. However, a detailed exploration of this issue is beyond

the scope of this study. In the same figure, we show the distribution of the Sérsic index for massive galaxies visually classified as early-types. We see that at low redshift, the distribution of Sérsic indices for these galaxies predominantly show large values of concentration as expected. Up to z$\sim$1.5 there is a peak around n$\sim$4-6 (see also Table 2.1). A general trend is also observed: there is a progressive shift towards lower and lower Sérsic index values as redshift increases. The reason for that shift could be double: either it is real (produced by a decrease in the tail of the surface brightness distribution of the spheroid galaxies at higher redshift) or it is artificial (produced by a bias at recovering large Sérsic index values).

To explore this last possibility we have conducted extensive simulations to check whether there is any bias on the recovery of the Sérsic index. In the case of the POWIR sample the simulations are fully explained in Trujillo *et al.* (2007). We did not find any significant trend in either the sizes or the concentration of the galaxies (see their Fig. 3) but for a slight underestimation of $\sim 20\%$ in the Sérsic index of the very faint $I_{AB} > 24$ spheroid-like galaxies. A similar analysis has been conducted now for the galaxies in the GNS sample. The results are comprehensively explained in the Appendix at the end of this thesis. We find that for objects with disk-like surface brightness profiles (i.e $n_{input}<2.5$), both sizes and Sérsic indices are recovered with basically no bias down to our limiting explored H-band magnitude. However, by increasing the input Sérsic index we find biases in the determination of the sizes and n. For a galaxy with $n_{input}\sim4$ and H=22.5 mag (our typical magnitude within the GNS catalogue), the output effective radii are $\sim 10\%$ smaller and output Sérsic indices are $\sim 20\%$ smaller than our input galaxies. The results of these simulations show that the decrease in the Sérsic index we observe from z$\sim$2.5 to z=0 for the spheroid-like population (which is around a factor of $\sim$2) can not be explained as a result of the bias on recovering the Sérsic index.

We can now use the output of our simulations (H_{output}, $r_{e,output}$ and n_{output}) to estimate the intrinsic (input) values of our sample and provide a more accurate representation of the evolution of the Sérsic indices at high-z. In Figure 2.11, we already implement these corrections for GNS and also for the POWIR/DEEP2 using the results of the Trujillo *et al.* (2007) simulations. Even after the corrections are applied the trend

we observe towards lower Sérsic indices at higher redshifts is maintained. In fact, the corrections are minor (see in Figure 2.12 the uncorrected values). We use these corrections in the rest of the chapter. The interpretation of the histograms of Fig. 2.11 is in the next section. In relation to the distribution of the Sérsic index for the galaxies we classified as interacting or irregulars, we see a large spread.

Many studies (e.g. Shen *et al.*, 2003; Barden *et al.*, 2005; McIntosh *et al.*, 2005; Trujillo *et al.*, 2006b) have used n=2.5 as a quantitative way to segregate between early and late-type galaxies. We explore, using this criteria, how the percentages of the different types of massive galaxies evolve with redshift. This is shown in Fig. 2.13 A. That figure clearly indicates that the fraction of massive galaxies with lower Sérsic index values has dramatically increased at higher redshift. If the association between the Sérsic index and the global morphological type that holds at low redshift also applies at high-z this would imply that massive galaxies at the high-z Universe were mostly late-type (disk) galaxies. However, there is no guarantee that such an association holds at all redshifts. For this reason, we explore the evolution of the fraction of different galaxy types with redshift using the visual morphologies (see Fig. 2.13 B). We find that the population of visually classified massive disk galaxies remains almost constant with (if any) a slight increase with redshift. The most dramatic changes are associated with the early-type and irregular/mergers classes. The fraction of visually classified E/S0 galaxies has increased by a factor of 3 since z$\sim$3 to now, whereas a reverse situation is seen for the irregular/merging galaxies. This latter fact agrees with merging becoming more important in massive galaxy evolution at increasing redshift (Conselice, Yang & Bluck, 2009; Bluck *et al.*, 2009). One of the most important outcomes of Fig. 2.13 is that the E/S0 type has been the dominant morphological fraction of massive galaxies only since z$\sim$1.

The number density of massive galaxies has significantly changed since z$\sim$3 (e.g. Rudnick *et al.*, 2003; Pérez-González *et al.*, 2008a; Mortlock *et al.*, 2011; Conselice *et al.*, 2011a) with a continuous increase in the number of these objects in the last $\sim$11 Gyr. In order to probe the emergence of the different galaxy types explored in this chapter we have estimated the comoving number density evolution of each class. To do this, we have used the Schechter fits to the stellar mass functions provided by Pérez-González

et al. (2008a, their Table 2). We have integrated these functions for all massive objects with $M_{stellar} \geq 10^{11} h_{70}^{-2} M_{\odot}$. We have later multiplied those numbers by the fractions we have estimated for the different classes of galaxies explored in this work. We show the comoving number density evolution in Fig. 2.13 C & D. The number density of both disk-like and spheroid-like massive galaxies, according to their Sérsic index, has changed with time. This evolution is particularly significant for spheroid-like objects, which are now a factor of $\sim$10 more numerous per unit volume than at z$\sim$2. The number of massive disks has also increased as cosmic time progresses, but at a lower rate than spheroid galaxies. Finally, the comoving number density of massive irregular/merging galaxies has very mildly grown (if any) in the last $\sim$11 Gyr.

2.4 Discussion

The evidence collected in the previous section suggests that there is a strong evolution in the morphological properties (both quantitative and qualitative) of the massive galaxy population. At high redshift, in agreement with the theoretical expectation, the dominant morphological classes of massive galaxies are late-types and peculiars. Consequently, the morphology that better represents the majority of these galaxies at a given epoch has dramatically evolved as cosmic time increases. Two effects could play a role explaining this significant change on the dominant morphological class. On one hand, the galaxies that are progressively been added into the family of massive objects (i.e. by the merging of less massive galaxies) can be incorporated with already spheroidal morphologies. On the other hand, the already old massive galaxies can also evolve towards spheroidal morphologies due to frequent mergers. For instance, frequent minor mergers (López-Sanjuan *et al.*, 2010b; Kaviraj, 2010; López-Sanjuan *et al.*, 2011, Bluck *et al.* 2011) experienced by the massive galaxy population will destroy existing stellar disks and also would be responsible for the appearance of long tails in their luminosity profiles. This scenario could explain why the evolution towards spheroid-like morphologies is stronger when we use the Sérsic index n instead of the visual classification. In fact, the surface brightness of nearby massive ellipticals are well described with large Sérsic indices due to their bright tails or envelopes. These wings, however, seem to disappear at higher and higher redshifts just leaving the inner

(core) region of the massive galaxies (Bezanson *et al.*, 2009; Hopkins *et al.*, 2009a; van Dokkum *et al.*, 2010; Carrasco, Conselice & Trujillo, 2010). The disappearance of these tails is also connected with the dramatic size evolution reported in previous works (see e.g. Trujillo *et al.*, 2007). Consequently, it is not only that the typical morphology of the massive galaxy population is changing with redshift but also that there is progressive build-up of their tails making the morphological evolution appears more dramatic when we use the Sérsic index instead of the visual classification as a morphological segregator.

If we were just using the information contained in the change of the fraction of morphological types with redshift we would be tempted to explain the morphological evolution as being just a consequence of a transformation from one class to another, however, the evolution in the number density of all the classes suggests a more complex scenario. In fact, one of the results we can conclude from the evolution of the number densities of all the galaxy classes is that high-z massive disk-like galaxies cannot be the only progenitors of present-day massive spheroid-like galaxies. They are just simply not enough in number to explain the large increase of the number density of elliptical galaxies at low redshifts.

All the morphological classes (maybe with the exception of irregular/merging galaxies) have increased their number densities with cosmic time. This emergence of massive galaxies is more efficient (by a factor $\sim$2) for creating spheroid-like galaxies than disk-like objects from z$\sim$1 to now. The reason why the formation of elliptical galaxies is more efficient at recent times than it was in the past has been theoretically linked to a lower availability of gas during the merger phases that are creating new galaxies (Khochfar & Silk, 2006, 2009; Eliche-Moral *et al.*, 2010; Shankar *et al.*, 2011).

2.5 Summary

Using a large compilation of massive ($M \geq 10^{11} h_{70}^{-2} M_{\odot}$) galaxies ($\sim$1100 objects) since z$\sim$3 we have addressed the issue of the morphological change of this population with time. We have found that there is a profound transformation in the morphological content of massive galaxies during this cosmic interval. Massive galaxies were typi-

Table 2.1: Mean structural parameters for visually classified massive ($M_\star > 10^{11} h_{70}^{-2} M_\odot$) galaxies at 0<z<3

Early-type galaxies						
Redshift Range	Number of galaxies	Survey	Effective radius (kpc)	Sérsic index	Axis ratio (b/a)	Mean stellar mass ($10^{11} h_{70}^{-2} M_\odot$)
0-0.03	133	SDSS	7.15 ± 1.56	4.83 ± 1.19	0.74 ± 0.13	1.26 ± 0.22
0.2-0.6	44	POWIR	4.77 ± 2.14	5.57 ± 1.46	0.71 ± 0.15	1.51 ± 0.45
0.6-1.0	184	POWIR	3.52 ± 1.87	5.13 ± 1.41	0.67 ± 0.19	1.78 ± 0.69
1.0-1.5	104	POWIR	2.06 ± 1.07	4.39 ± 1.32	0.63 ± 0.19	1.70 ± 0.51
1.5-2.0	30	POWIR	1.31 ± 0.73	3.97 ± 1.38	0.65 ± 0.17	1.56 ± 0.37
1.7-3.0	25	GNS	1.30 ± 0.55	2.73 ± 0.96	0.68 ± 0.11	1.58 ± 0.42
Late-type galaxies						
Redshift Range	Number of galaxies	Survey	Effective radius (kpc)	Sérsic index	Axis ratio (b/a)	Mean stellar mass ($10^{11} h_{70}^{-2} M_\odot$)
0-0.03	67	SDSS	8.44 ± 3.28	2.71 ± 1.19	0.60 ± 0.22	1.21 ± 0.14
0.2-0.6	26	POWIR	5.39 ± 2.20	2.62 ± 1.28	0.50 ± 0.25	1.40 ± 0.30
0.6-1.0	124	POWIR	4.91 ± 2.21	1.86 ± 0.98	0.54 ± 0.21	1.53 ± 0.49
1.0-1.5	95	POWIR	4.81 ± 2.17	1.53 ± 0.87	0.57 ± 0.23	1.58 ± 0.41
1.5-2.0	42	POWIR	3.88 ± 1.60	1.20 ± 0.73	0.50 ± 0.20	1.61 ± 0.49
1.7-3.0	34	GNS	2.55 ± 1.18	1.38 ± 0.62	0.54 ± 0.18	1.55 ± 0.50
Peculiar galaxies						
Redshift Range	Number of galaxies	Survey	Effective radius (kpc)	Sérsic index	Axis ratio (b/a)	Mean stellar mass ($10^{11} h_{70}^{-2} M_\odot$)
0-0.03	7	SDSS	8.39 ± 2.22	3.17 ± 0.61	0.72 ± 0.13	1.16 ± 0.13
0.2-0.6	8	POWIR	4.93 ± 2.43	4.95 ± 2.04	0.56 ± 0.23	1.16 ± 0.08
0.6-1.0	42	POWIR	4.16 ± 2.35	3.05 ± 2.40	0.56 ± 0.20	1.65 ± 0.49
1.0-1.5	58	POWIR	3.83 ± 1.71	1.96 ± 1.62	0.61 ± 0.18	1.65 ± 0.51
1.5-2.0	30	POWIR	2.53 ± 1.68	1.70 ± 1.36	0.53 ± 0.26	1.81 ± 0.68
1.7-3.0	21	GNS	2.45 ± 1.04	1.69 ± 1.31	0.61 ± 0.18	1.44 ± 0.34

cally disk-like in shape at $z \gtrsim 1$ and elliptical galaxies have been only the predominant massive class since that epoch. The fraction of early-type morphologies in massive galaxies has changed from ∼20-30% at z∼3 to ∼70% at z=0 (see Figure 2.13).

We have addressed the morphological transformation of the massive galaxies using a quantitative (based on GALFIT fits to the surface brightness distribution of the galaxies) and a qualitative (visual classification) approach. Both analyses agree on a clear morphological change in the dominant morphological class with time. In particular, the quantitative approach, which uses the Sérsic index as a morphological segregator, shows that the number of galaxies with low Sérsic index at high-z was higher than in the present day Universe. We interpret this as a consequence of two phenomena: a decrease in the number of early-type galaxies at higher redshift plus an intrinsic decrease of the Sérsic index values of those elliptical galaxies at earlier cosmic times due to the loss of their extended envelopes.

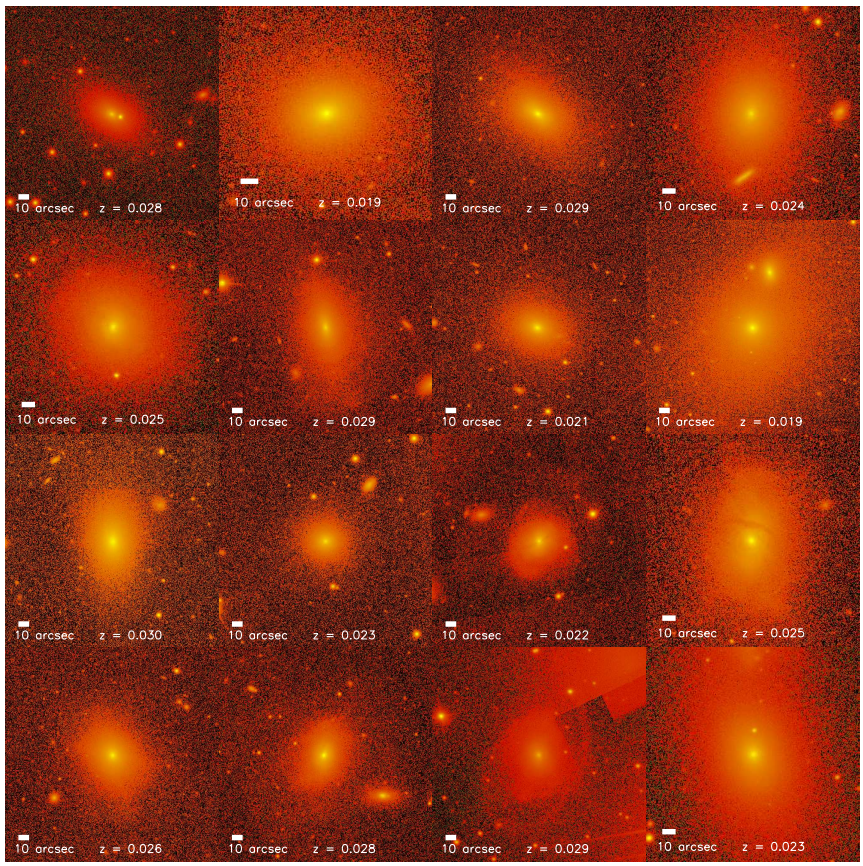

Figure 2.2: Randomly generated sample of SDSS early-type galaxies.

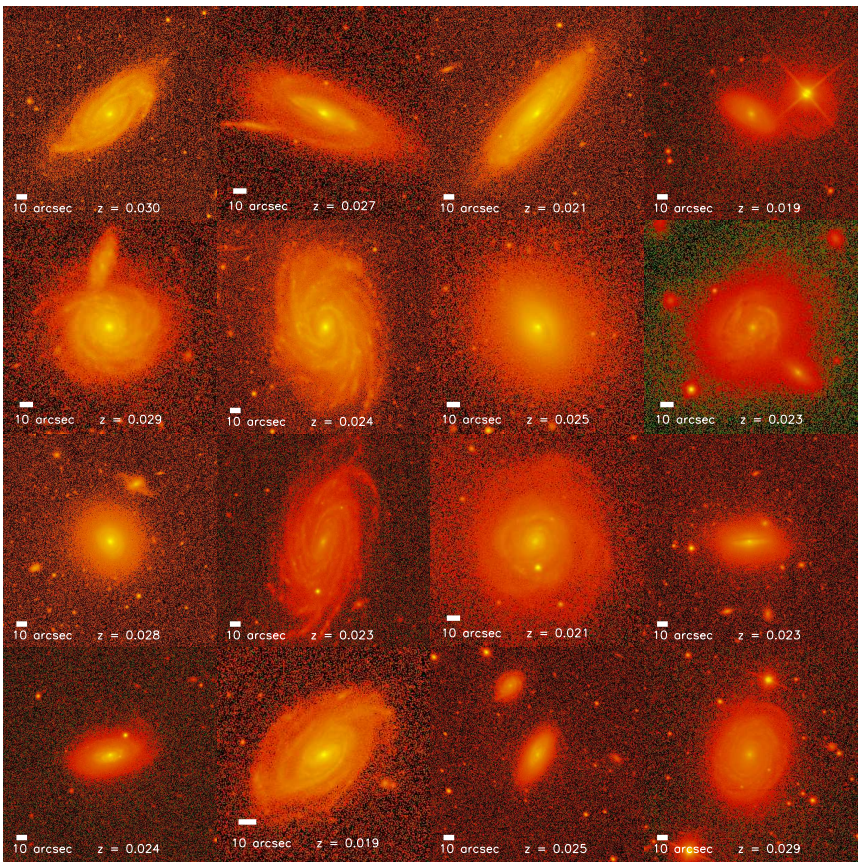

Figure 2.3: Randomly generated sample of SDSS late-type galaxies.

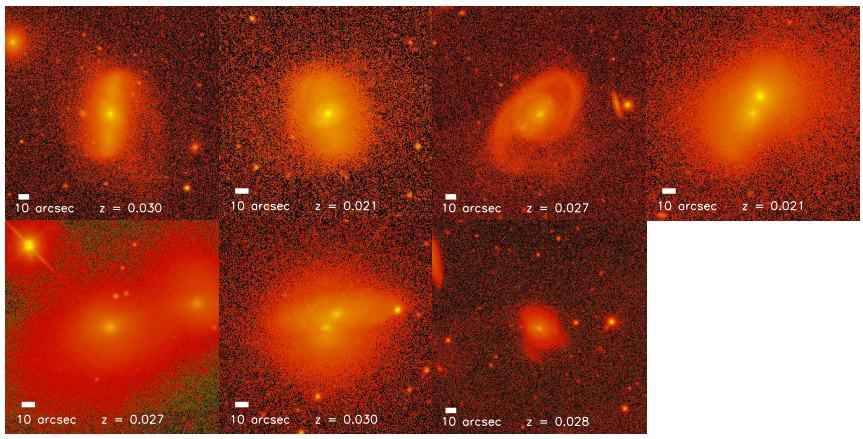

Figure 2.4: Randomly generated sample of SDSS peculiar galaxies.

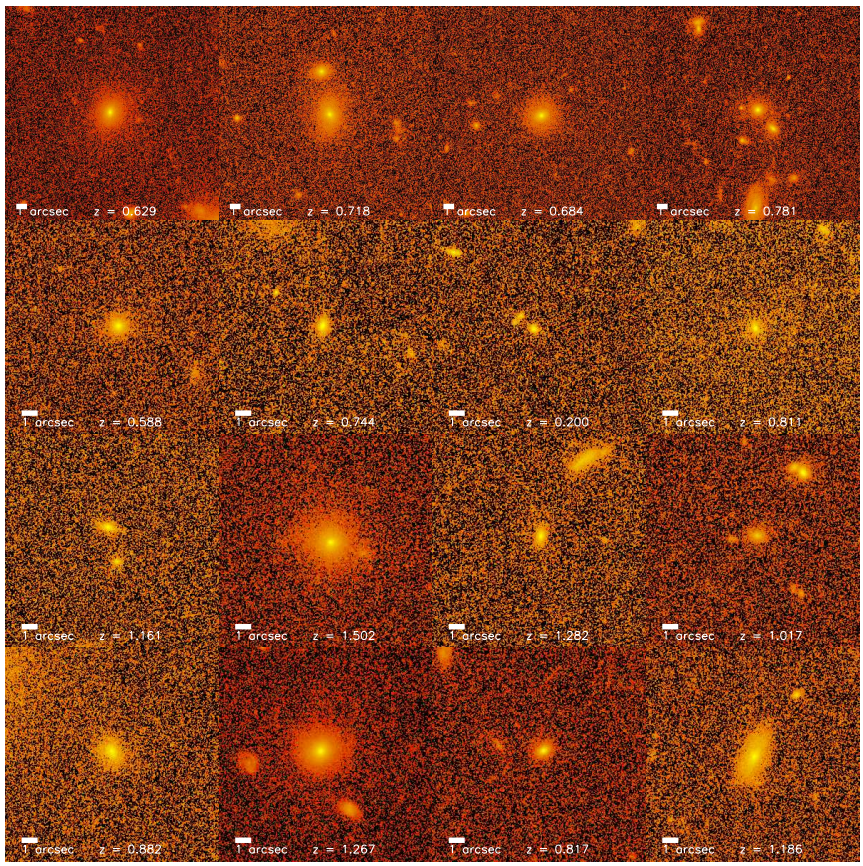

Figure 2.5: Randomly generated sample of POWIR/DEEP2 early-type galaxies.

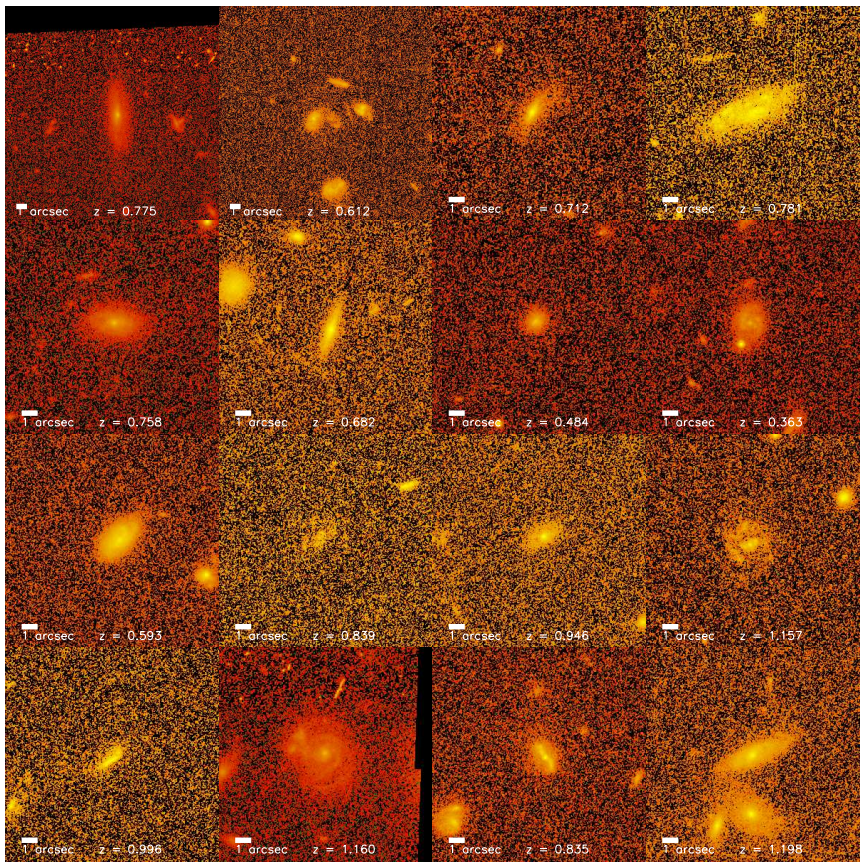

Figure 2.6: Randomly generated sample of POWIR/DEEP2 late-type galaxies.

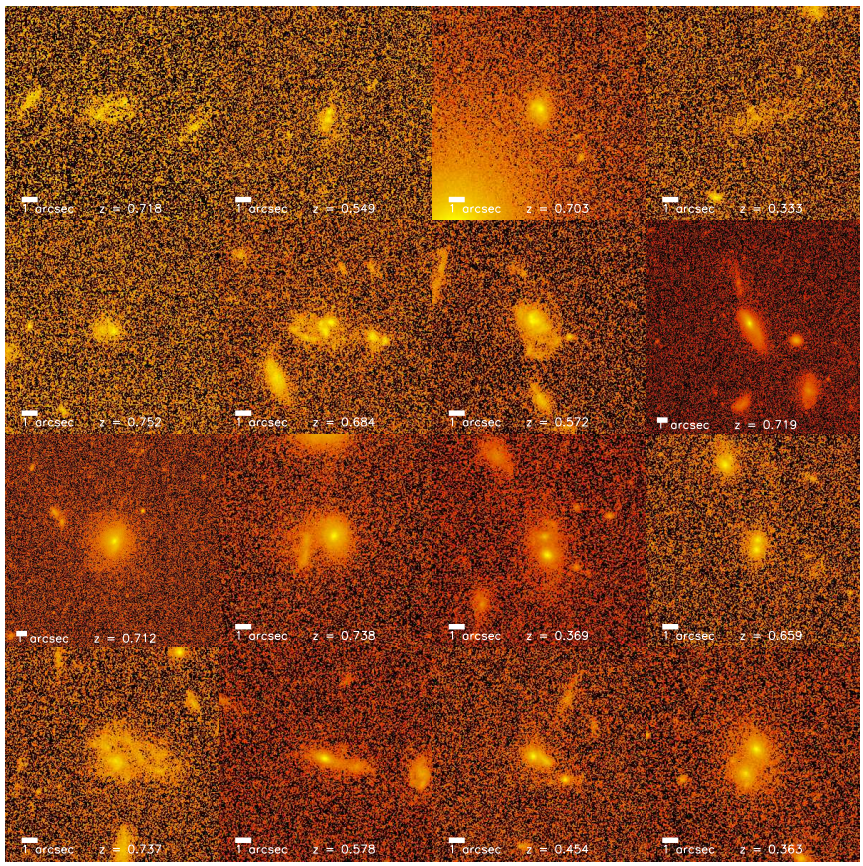

Figure 2.7: Randomly generated sample of POWIR/DEEP2 peculiar galaxies.

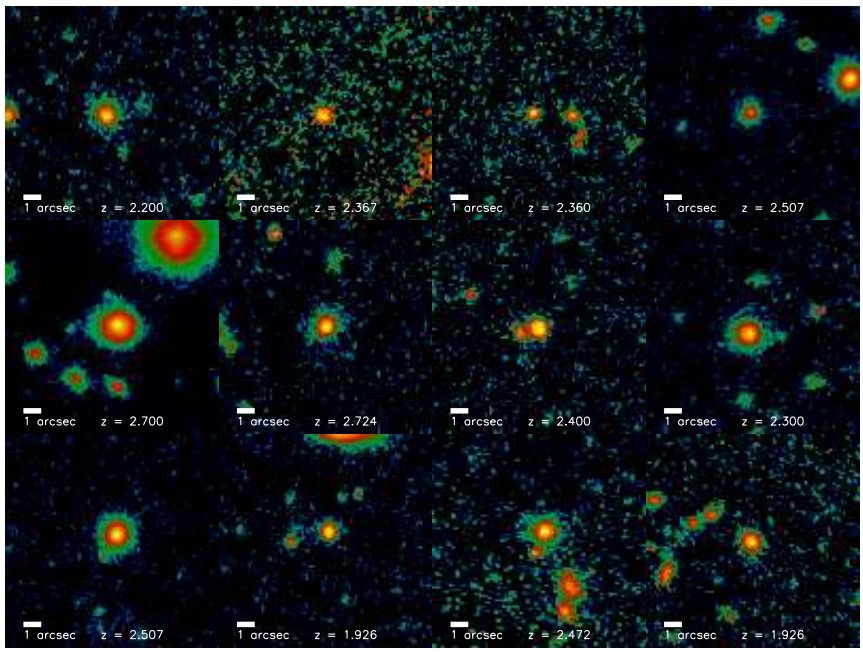

Figure 2.8: Randomly generated sample of GNS early-type galaxies.

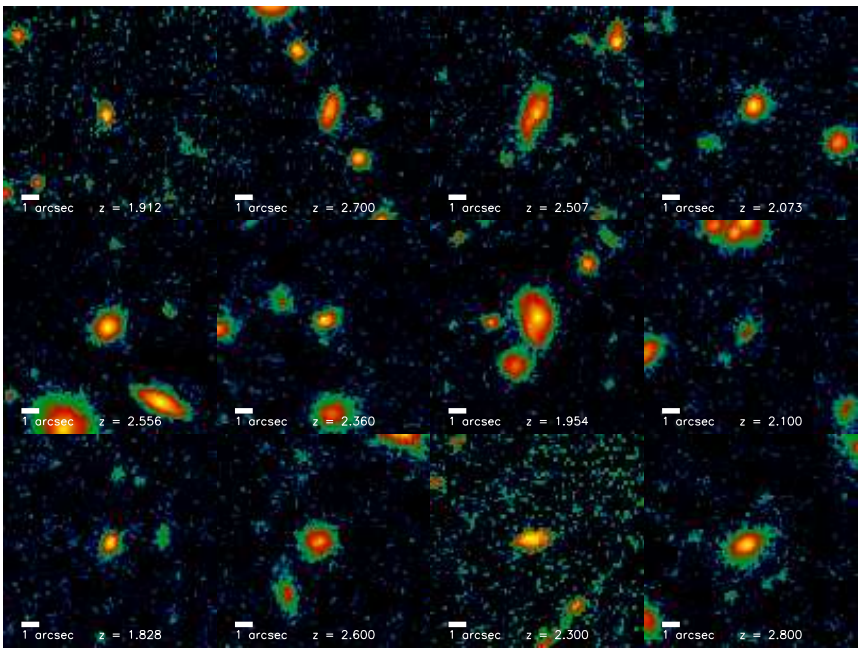

Figure 2.9: Randomly generated sample of GNS late-type galaxies.

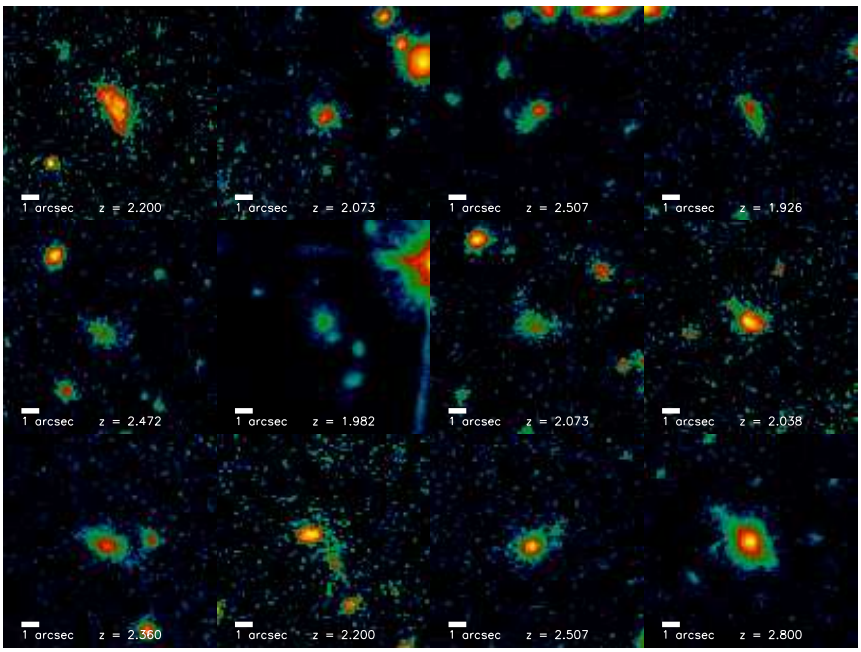

Figure 2.10: Randomly generated sample of GNS peculiar galaxies.

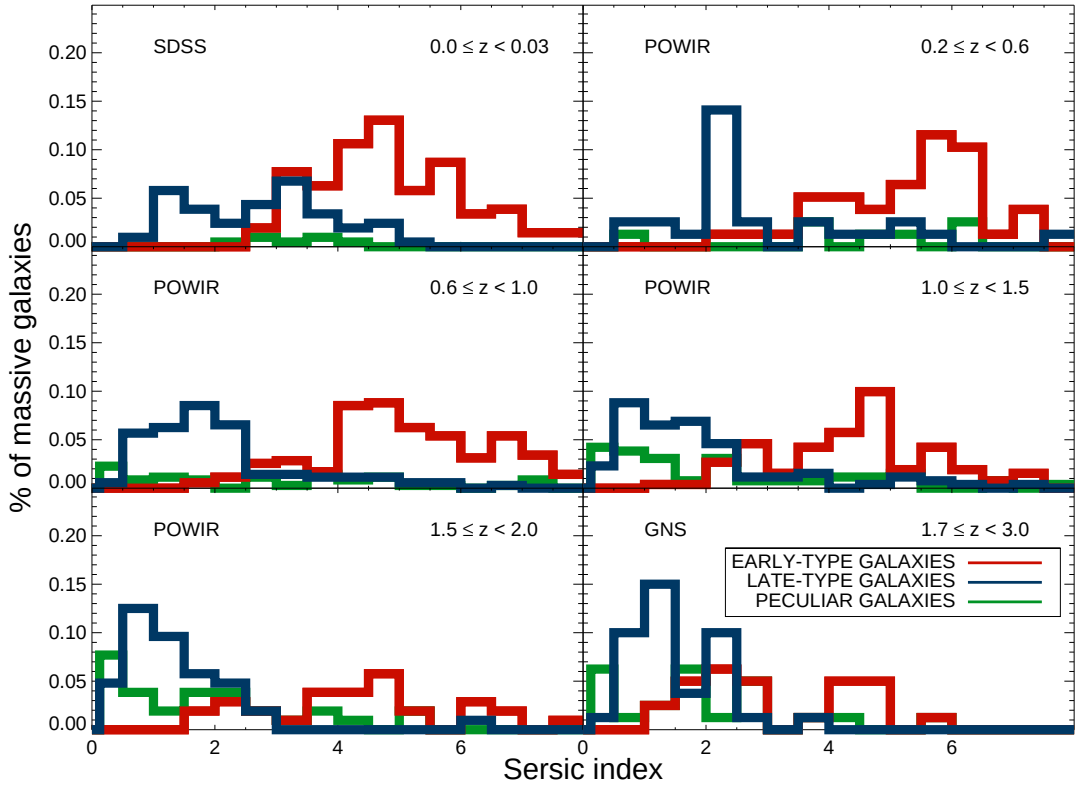

Figure 2.11: Sérsic index distribution of massive ($M_\star \geq 10^{11} h_{70}^{-2} M_\odot$) galaxies at different redshift intervals. The Sérsic indices of the individual galaxies have been corrected following the simulations presented in Trujillo *et al.* (2007, POWIR) and the Appendix A. Color coding is related with visual morphology: blue for late-type galaxies, red for early-type galaxies and green for peculiar (irregulars/mergers) galaxies. For our SDSS sample, the Sérsic index of disky objects are mainly located between 1<n<3 but for some galaxies extend up to $n = 5$. Conversely, the Sérsic index of spheroid galaxies starts at n∼3 and then peaks at n∼5. The distributions of the Sérsic index steadily shift to lower values at increasing redshift with the high Sérsic index values progressively disappearing.

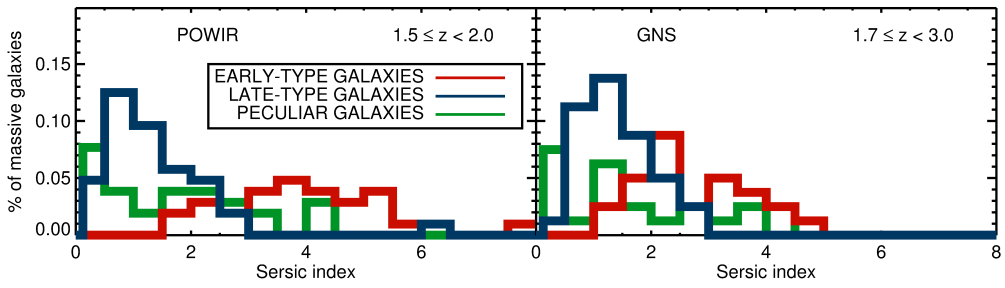

Figure 2.12: These are the highest redshift histograms of the Figure 2.11, showing the observed Sérsic indices values, without any a posteriori correction based on Trujillo et al. (2007) or our current GNS simulations (Appendix A). The more noticeable change is seen for the GNS data, where it is very conspicuous the non-existence of any large ($n > 4.62$) Sérsic index. The difference between these histograms and the ones presented in Figure 2.11 is small.

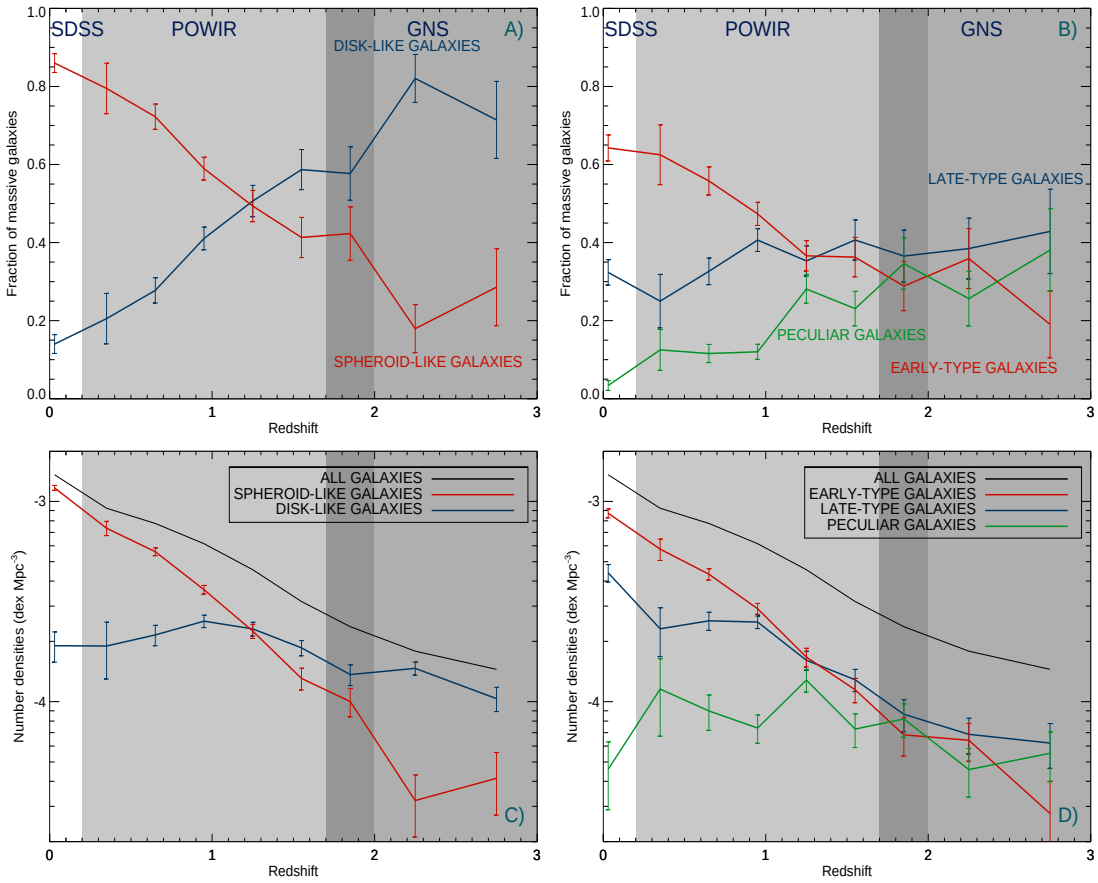

Figure 2.13: Panel A): Fraction of massive ($M_* \geq 10^{11} h_{70}^{-2} M_\odot$) galaxies showing disk-like surface brightness profiles ($n < 2.5$) and spheroid-like ones ($n > 2.5$) as a function of redshift. Different color backgrounds indicate the redshift range expanded for each survey: SDSS, POWIR/DEEP2 and GNS. Error bars are estimated following a binomial distribution. Sérsic indices are corrected by Trujillo *et al.* (2007) and Appendix A simulations. Panel B): Same as Panel A) but segregating the massive galaxies according to their visual morphological classification. Blue color represents late type (S) objects and red early type (E+S0) galaxies, while peculiar (ongoing mergers and irregulars) galaxies are tagged in green. Panel C): Comoving number density evolution of massive galaxies split depending on the Sérsic index value. The solid black line corresponds to the sum of the different components. Panel D): Same as panel C) but segregating the massive galaxies according to their visual morphological type.

Sein Gesicht scheint nicht männlich oder kindlich, sondern irgendwie tausendjährig, irgendwie zeitlos. Tiere können so aussehen oder Bäume, oder Sterne. (His face seems not manly or child-like, but somehow millenary, somehow timeless. Animals could look like that, or trees, or stars.)

Hermann Hesse in 'Demian'

Can we actually 'know' the Universe? My God, it's hard enough finding your way around in Chinatown.

Woody Allen

Chapter 3

Spectroscopic confirmation of the rotational support of massive galaxies at $z = 1.4$

3.1 Introduction

Massive ($M_{stellar} \geq 10^{11} h_{70}^{-2} M_{\odot}$) galaxies represent a challenge to the dominant ΛCDM paradigm as many of their observables (such as number densities, SFRs, sizes, mass growth or merging histories) are not well reproduced in galaxy evolution models (e.g. Benson *et al.*, 2003; Baugh, 2006; Conselice *et al.*, 2007). Interestingly, the most massive galaxies are nearly all in place at high-z (e.g. Conselice *et al.*, 2007; Pérez-González *et al.*, 2008a; Mortlock *et al.*, 2011) and their high luminosities allow us to track them throughout a wide redshift range. As such, many studies focused on these massive galaxies, trying to comprehend the evolutionary paths between systems seen at low and high redshift. In the present day Universe, they are mainly (but not only, see Panel B Figure 2.13 Chapter 2) composed of elliptical galaxies which feature large sizes and harbour red, old and metal-rich stellar populations (Baldry *et al.*, 2004; Thomas *et al.*, 2005). Conversely at $z \sim 2$, massive galaxies show ~ 5 times smaller sizes than their local counterparts (e.g. Daddi *et al.*, 2005; Trujillo *et al.*, 2006a,b, 2007; Buitrago *et al.*, 2008; Carrasco, Conselice & Trujillo, 2010; van Dokkum *et al.*, 2010;

Cassata *et al.*, 2010; Trujillo, Ferreras & de La Rosa, 2011), a variety of star formation histories (Cava *et al.*, 2010; Viero *et al.*, 2012; Bauer *et al.*, 2011) and differing morphologies (Cameron et al. 2011, Van der Wel et al. 2011, van Dokkum et al. 2011, Chapter 2 of the present thesis), suggesting huge dynamical transformations for this galaxy population since $z \sim 2$.

To explain this dichotomy, simulations predict that primeval massive galaxies are remnants of very dissipative mergers (Wuyts *et al.*, 2010; Bournaud *et al.*, 2011, see also Ricciardelli et al. 2009) which afterwards suffer a combination of frequent minor merging events (Bournaud, Jog & Combes, 2007; Naab, Johansson & Ostriker, 2009) and dry major mergers (Khochfar & Silk, 2006). Following this rationale, it is natural to expect a size increment and the modification of other structural properties. However it is hard to constraint the merger history, especially when dealing with faint galactic companions. Another physical mechanism that may contribute to this picture is the existence of cold gas flows, which will feed the massive galaxies with pristine gas to support large star formation rates of $\sim 100 M_{\odot}\mathrm{yr}^{-1}$ (Dekel *et al.*, 2009; Oser *et al.*, 2010). These cold streams create turbulent and unstable disks which will fragment into star-forming clumps that gradually migrate to the galactic center developing their bulge component (Ceverino, Dekel & Bournaud, 2010).

Observationally, most of the information regarding these massive galaxies comes from large and deep NIR surveys, which aim to probe galaxy evolution during the last 10 Gyr. The data gathered so far favours a picture in which late-type and clumpy/interacting objects are more common at high-z, due to the higher gas fractions for these systems (Erb *et al.*, 2006; Tacconi *et al.*, 2010) and higher merging rates (Conselice *et al.*, 2007; Bluck *et al.*, 2009; López-Sanjuan *et al.*, 2010b,a). Ultimately, we would ideally like to rely on spectroscopic information to fully test and characterize all the processes involved in galaxy assembly. However, even for massive (and thus very often luminous) galaxies, it is very expensive in observational time to obtain high signal-to-noise spectra. From the tens of massive galaxies studied so far at $z > 1.5$ with traditional long-slit techniques (Kriek *et al.*, 2006; Cimatti *et al.*, 2008; Newman *et al.*, 2010; Onodera *et al.*, 2010; van de Sande *et al.*, 2011) there is some agreement on the high velocity dispersion values of these objects, reassuring their inherent massive nature

even at such early cosmic times (Cenarro & Trujillo, 2009; Cappellari *et al.*, 2009).

Integral field spectroscopy (aka 3D spectroscopy) is presently a well-establish technique which can enhance greatly our understanding of massive galaxies, both at low-redshift (Cappellari *et al.*, 2011; Sánchez *et al.*, 2012) and at high-redshift (Law *et al.*, 2009, Förster-Schreiber et al. 2009 –hereafter F-S09–, Epinat et al. 2009 –hereafter E09–). On the one hand, it measures the rotational and the velocity dispersion support (currently from gaseous kinematics) for a galaxy, and thus provides us with profound physical information on characteristics of the total galaxy system (both baryonic and dark matter components). On the other hand, the possibility of having spatially-distributed spectral information helps us addressing the question of how morphology and galaxy assembly are linked. State-of-the-art studies show a kinematic mixture at high-z (Genzel *et al.*, 2008; Nesvadba *et al.*, 2008; Shapiro *et al.*, 2009; Cresci *et al.*, 2009; Law *et al.*, 2007, 2009; Wright *et al.*, 2007, 2009; Bouché *et al.*, 2010; Lemoine-Busserolle & Lamareille, 2010; Gnerucci *et al.*, 2011, Epinat et al. 2012) , with a high percentage of objects displaying large ordered rotational motions, and also fairly large velocity dispersions. Uncovering the origin of these motions is difficult as it is hard to separate kinematically merging systems from more turbulent clumpy phases of galaxy formation (e.g. Förster Schreiber *et al.*, 2011b).

We stress in this chapter the importance of massive galaxies at high redshift as potential targets for integral field spectroscopy because of their relative compactness (which make them easy to observe even with a small field-of-view) and the current lack of spectra for this galaxy population. Ideally, absorption lines would be the best indicators to examine their stellar populations (e.g. Bedregal *et al.*, 2009). Nevertheless, Hα emission line analysis is usually preferred due to its relative ease of study. However by using Hα one must be cautious when interpreting the derived kinematics, since this ionized gas may not be coupled with the stellar component in the galaxy. Although there is a good correlation between gas emission and broadband imaging (Förster Schreiber *et al.*, 2011a) it is important to keep in mind that this comes from ionized gas, which is collisional and dissipative. Hence the Hα emission may exhibit complicated morphologies and kinematics which will ultimately be related to what extent the galaxy at study is relaxed. The SAURON survey (de Zeeuw *et al.*, 2002) and

the more recent ATLAS^{3D} survey (Cappellari *et al.*, 2011) have opened a new perspective on this topic, whereby they classify early-type galaxies as slow and fast rotators depending on the degree of angular momentum they show. Fast rotators have been found to host disks made up of gas and stars which contain a range of the galactic mass fraction (Krajnović *et al.*, 2008). Massive fast rotators appear to have large reservoirs of hot gas which is co-rotating with the stellar component (Falcón-Barroso *et al.* 2006, Davis *et al.* 2011).

We present in this chapter 8m-telescope VLT observations of massive galaxies using the SINFONI integral field spectroscopy instrument. Our sample comprises 10 objects at $z \sim 1.4$, whose redshift choice is a trade-off between high redshift and having a sample selected by stellar mass. Nevertheless, this redshift is of particular importance in the development of massive galaxies in particular, and galaxies in general, as it nearly coincides with the star formation and quasar activity peak, apart from being the most likely period at which massive galaxies switch their morphologies from late to early types (see Chapter 2). We discuss the Hα derived kinematic properties for this sample and interpret these findings in the context of massive galaxy formation.

This chapter is structured as follows: Section 3.2 describes the data reduction and subsequent analysis, Section 3.3 shows each individual galaxy, explaining in a detailed way its particularities and how each massive galaxy is related with the total sample, Section 3.4 discusses what the different probes of 3D spectroscopy offer towards characterizing the rotation dominated nature of these objects, and in Section 3.5 we present the conclusions of our study. We name the galaxies in our sample with the prefix POWIR followed by a number, instead of the numeric code in the parent survey, as it is easier to use these numbers throughout the chapter (please note there is not a POWIR9 galaxy). These numbers are written in the plots instead of symbols for the reader to locate and understand the properties of individual galaxies. We assume the following cosmology: H_0=70 km s^{-1}Mpc^{-1}, Ω_λ = 0.7, and $\Omega_{\rm m}$ = 0.3, and use AB magnitude units unless otherwise stated.

Table 3.1: Observational data for our massive galaxy sample

Name	POWIR ID	RA(J2000) (hours)	DEC(J2000) (degrees)	z	logM log ($h_{70}^{-2}M_{\odot}$)	K_s mag Vega magnitudes	Observ. night	Integration time sec	(S/N)	Seeing ”
(1)	(2)	(3)	(4)	(5)	(6)	(7)	(8)	(9)	(10)	(11)
POWIR1	32007614	23 : 30 : 58.2	00 : 02 : 27.5	1.374	11.23	18.24	$21 - Jun$	5400	3	0.58
POWIR2	32073051	23 : 31 : 08.2	00 : 06 : 38.5	1.396	11.02	18.65	$04 - Sep$	5400	3	0.52
POWIR3	32015443	23 : 29 : 59.2	00 : 09 : 20.8	1.384	11.16	18.47	$08 - Aug$	2700	3	0.65
POWIR4	32015501	23 : 30 : 12.2	00 : 06 : 03.8	1.394	11.41	17.97	$31 - Jul$	2700	2	0.58
POWIR5	32021317	23 : 29 : 58.5	00 : 10 : 07.1	1.382	11.33	18.26	$20 - Jul$	5400	2	0.55
POWIR6	32021394	23 : 29 : 45.4	00 : 09 : 08.4	1.375	11.52	17.90	$01 - Jul$	5400	3	0.48
POWIR7	32029850	23 : 31 : 02.4	00 : 16 : 52.6	1.396	11.34	18.26	$19 - Jul$	5400	2	0.63
POWIR8	32037003	23 : 30 : 13.8	00 : 20 : 17.0	1.400	11.02	18.38	$01 - Jul$	5400	3	0.42
POWIR9	–	–	–	–	–	–	–	–	–	–
POWIR10	32100059	23 : 30 : 57.8	00 : 01 : 15.0	1.389	11.10	18.71	$20 - Jul$	5400	3	0.55
POWIR11	32100778	23 : 30 : 41.7	00 : 14 : 55.2	1.393	11.09	18.34	$08 - Aug$	2700	2	0.65

Notes. (1) Name of the galaxy (2) Name of the galaxy in the parent POWIR/DEEP2 survey (3) Right ascension (4) Declination (5) Spectroscopic redshift from our SINFONI observations (6) Stellar mass from the parent POWIR/DEEP2 survey (7) K_s-band magnitude from the parent POWIR/DEEP2 survey (8) Date of the observations, all done in 2007 (9) Integration time (10) Signal-to-noise ratio threshold (see S/N per pixel map in Fig. 3.3 - 3.24) above which we show the spaxels' value in the kinematical maps (11) Seeing as derived from the SINFONI telluric standards observed.

3.2 Data and analysis

3.2.1 Observations

The parent sample where our target galaxies are selected comes from the Palomar Observatory Wide InfraRed survey (POWIR; Bundy *et al.*, 2006; Conselice *et al.*, 2007). This survey covers a 1.53 deg^2 area in the K$_s$ and J bands down to $K_{Vega} = 21$ and $J_{Vega} = 23.5$. This imaging consists of 75 WIRC camera pointings, with a pixel scale of $0.25”/\mathrm{pix}$. In the K$_s$ band 30-s exposures were taken, for total 1-2h integration time per pointing, and with typical seeing value of $0.7 - 1”$. In addition, optical coverage was imaged with the 3.6m Canada-France-Hawaii Telescope (CFHT) using the CFH12K camera in the B, R and I bands. The R-band depth is $R_{AB} = 25.1$, with similar results for the other two bands (see Coil *et al.*, 2004a, for more details). Both Palomar and CFHT images were analysed using $2”$ diameter apertures. Stellar masses were derived with the photometric techniques discussed in Bundy *et al.* (2006) using a Chabrier (2003) IMF. Basically, our stellar mass computational method consists of fitting a grid of model SEDs constructed from Bruzual & Charlot (2003) stellar populations synthesis models using a number of star formation histories. It turns out that parameters such as metallicity, e-folding time or age are not as well constrained as stellar mass due to various degeneracies. The final error in stellar mass was measured as 0.2-0.3 dex, i.e. roughly a factor of two (Bundy *et al.*, 2006; Conselice *et al.*, 2007;

Grützbauch *et al.*, 2011b).

Spectroscopic redshifts were measured by the DEEP2 Redshift Survey (Coil *et al.*, 2004b) using the DEIMOS spectrograph (Faber *et al.*, 2003) at the Keck II telescope. Spectra were obtained with a resolution of $R \sim 5000$ within the wavelength range $6500 - 9100\mathring{A}$. Redshifts were measured comparing templates to the data. One was an artificial emission line spectrum with a velocity dispersion value coincident with the instrumental broadening (60 km/s). The second was a signal-to-noise ratio absorption dominated spectrum obtained averaging thousands of SDSS galaxies. A χ^2 minimization was applied between data and templates, giving as a result the most 5 likely redshifts for human inspection. We only utilised those in which two or more lines were identified. See Coil *et al.* (2004b) or the most updated Newman *et al.* (2012) for more information. Masses were derived using spectroscopic redshifts when available.

With all these data at hand, our final choice of galaxies to observe was not based on a selection using colours, morphologies or sub-mm flux as many others have done. Instead our sample is solely selected by stellar mass and those galaxies with large [O II] equivalent widths ($> 15\mathring{A}$). This last fact might signify that we are more likely investigating star forming systems. However, this is a necessary requirement to robustly assess our galaxies' kinematic features and it is not unusual as this galaxy population show high star-formation independently of their luminosity profile, and nearly all massive galaxies at this epoch have some star formation (e.g. Pérez-González *et al.*, 2008b; Cava *et al.*, 2010; Viero *et al.*, 2012). We also took special care in our final selection to ensure that none of our galaxies' Hα lines were situated close to any OH sky emission lines, based on the atlas from Rousselot *et al.* (2000), which would potentially hamper our results.

Our group was granted 20 hours of observing time in service mode with the NIR (1.1-2.45 μm) 3D-spectrograph SINFONI (Eisenhauer *et al.*, 2003; Bonnet *et al.*, 2004) at ESO-VLT located at the Cassegrain focus of UT4-Yepun. This instrument has four different configurations depending on the observed band (J, H, K and H+K), with three possible pixel scales (8"×8" –seeing limited mode–, 3"×3" and 0.8"×0.8" –adaptive optics mode–). The SINFONI field of view is sliced into 32 slices. Each one of them is imaged onto 64 pixels of the detector. Thus one obtains 32×64 spatial pixels (aka

spaxels), providing a coverage of 2048 spectral pixels for every one of them. Our observations were conducted during 9 nights from June to September 2007 – ESO run ID 079.B-0430(A) –. SINFONI was used in seeing limited mode and thus with a spatial sampling of $0.125" \times 0.25"$. Due to the redshifts of our sample of galaxies ($z \sim 1.4$) we choose to observe them in the H-band (1.45 - 1.85 μm) in order to map the Hα emission. The spectral resolution ($R \sim 3000$) allows us to disentangle any minor sky emission lines close to our target line without problems. Our observational strategy was the so-called 'butterfly pattern' or 'on-source dithering', by which the galaxy is set in two opposite corners of the detector to remove sky background using contiguous frames in time. For several galaxies in our sample (POWIR4, POWIR5 and POWIR7) the galaxies were not correctly placed in the two corners of the detector but only in its center, reducing the final integration time by half of its total nominal value (1h 30min) and thus reducing the final signal-to-noise ratio by a factor of $\sqrt{2}$. Even in these cases, exquisite SINFONI sensitivity permitted us to detect the emission from all our objects. Images were dithered by $0.3"$ in order to minimize instrumental artifacts when the individual five minute observations were aligned and combined together. PSF and telluric stars were also observed along with each galaxy for calibration purposes. However, no flux calibration was attempt as our aim was to focus only in the kinematical properties of our sample. Measured PSFs are listed in Table 3.1, for a mean seeing of 0.56 arcsec.

3.2.2 Data reduction & Observed kinematical maps

The ESO-SINFONI pipeline version 2.5.0 (Modigliani *et al.*, 2007; Mirny *et al.*, 2010) was utilised in order to reduce our data. In brief, this pipeline subtracts sky emission lines (using algorithms by Davies (2007), corrects the image using darks and flat-fields, spectrally calibrates each individual observation and reconstructs all the information into a final datacube. The recipe used for this purpose was sinfo_rec_jitter, which was fed exclusively with the master files provided by ESO. All of these processes were performed separately for each individual exposure. Afterwards the two datacubes were combined into a single one by using the recipe sinfo_utl_cube_combine. We always used the pipeline parameter *product-density = 3* (which retrieves the most detailed

possible outputs), *objnod-scales_sky = true* (to perform a subtraction of the median value at each wavelength and thus remove the sky more efficiently) and *skycor.rot-cor = true* (to remove the contribution of any rotational OH transitions).

The final datacube was spatially smoothed using a sub-seeing Gaussian core (FWHM=2 pixels) to increase the signal-to-noise without affecting our data interpretation. We analyse this datacube with IDL routines we constructed. Basically, we located the Hα line in each spaxel according to the known spectroscopic redshift of the target galaxy, and then fit a Gaussian profile, taking into account the sky spectrum weighting its contribution with the help of the routines `mpfit` and `mpfitfun` (Markwardt, 2009). Radial velocity maps were computed using the relativistic velocity addition law:

$$V_{spaxel} = \frac{(z_{spaxel} - z_{cen})}{1 + z_{cen}} c \tag{3.1}$$

where z_{spaxel} and z_{cen} are the redshifts for a given spaxel and for the kinematical center of the galaxy, respectively. From the Hα line width, we computed velocity dispersion maps, subtracting the instrumental broadening which was measured from sky lines. Our routines produced other outputs for every galaxy: an Hα line flux map, a [NII] $\lambda\lambda 6583 \mathring{A}$ flux map, a signal-to-noise per spaxel and a continuum map. For the final outcome, we used the spectral information in the range $1.5 - 1.7 \mu m$, i.e., all the H-band except its borders where the information is noisier. We then fit a linear function to the galaxy spectrum in this wavelength range in order to account for the existence of a continuum emission and its possible variation within this wavelength range. Our continuum maps (top right panels in the first set of each galaxy maps; from Figure 3.3 to Figure 3.24) show the integral of the fitted mathematical function. All our objects have continuum emission which we compare to the ionized gas emission, which in principle only tells us about the areas of star formation in each galaxy. As such, comparing the peak of the emission and the continuum gives us insights of how well Hα , and hence star formation, traces the underlying older stellar population. One caveat to this is a known problem (ironically with unknown origin; B. Epinat private communication) with the SINFONI detector, where there appears stripes of flux in the data after coadding high numbers of spectral pixels. One can see them for instance in the contin-

uum maps of Fig. 3.3 (lower part of the galaxy) and Fig. 3.7 (white stripe on the top of the galaxy). This effect prevents us from making a total continuum flux measurement, but does not affect qualitatively the fact that we can locate where the maximum of the continuum is in the detector.

3.2.3 Data modelling

We recover the kinematical parameters for each galaxy in our sample by fitting a model to the velocity field obtained from our SINFONI datacubes. To perform this task we assume that the galaxies from our sample are described kinematically as rotating disk systems with a symmetric rotation curve. For this method we utilised the formalism and programs developed in E09. The full theoretical description of this method is in Epinat *et al.* (2010), where the authors also conducted a comparison with local galaxies to asses the reliability of their method. Essentially this consists of a χ^2 minimization between the observed data and a given high resolution model convolved to our pixel scale and seeing conditions. We chose the flat rotation curve parametrization used by Wright *et al.* (2007, 2009) as suggested in Epinat *et al.* (2010) from the study of local galaxy velocity fields projected at high redshift:

$$V(r) = V_t \frac{r}{r_t} \tag{3.2}$$

when $r \leq r_t$ and

$$V(r) = V_t \tag{3.3}$$

otherwise. In the above equations V_t is the value for the plateau in the rotation curve and r_t is the radius at which the plateau is reached. The model contains seven parameters : the center (x_c and y_c), the systemic redshift (or velocity), the inclination of the disk, the position angle of the major axis and the two rotation curve parameters. Note that the fit to these simple formulas are done by considering the associated error map for the velocity field.

As shown and discussed in Epinat *et al.* (2010), due to the reduced spatial information of our data and due to some degeneracy in the models, the center and the inclination are the parameters that are the least constrained. We thus fixed the center to the spaxel with the maximum flux in the continuum maps (as we expect it is a better proxy for the

stellar component kinematics) as well as the inclination, reducing to four the number of free parameters of our model. In rotating disk models there is a degeneracy between rotation velocity and inclination (its sine) that could only be solved using very high resolution data. As a result the inclination is the major source of uncertainty for determining the actual rotation velocity. Given the photometric quality of our POWIR parent sample imaging, it is difficult to constrain this parameter with a high certainty. We used GALFIT (Peng *et al.*, 2010) surface brightness fits for our sample in order to into account the large Point Spread Function (PSF) of our images. We also use bright, non-saturated stars within our imaging to create a model PSF. The output inclination was then utilised as input for our velocity modelling.

Once the best fit for the rotational velocity was obtained, we also computed a model velocity dispersion map. To calculate this we take into account the width of the Hα line due to the unresolved velocity gradient. The intrinsic velocity dispersion is obtained after subtracting in quadrature the velocity dispersion model map from the observed one. To facilitate comparison with other samples and to discuss each galaxy as a whole, we computed the integrated velocity dispersion value, weighting the value of every spaxel by an amount inversely proportional to their squared error ($1/\text{error}^2$). From this we obtain a measure of the overall velocity dispersion of the galaxy. Results from the models are listed in Table 3.2 and their kinematical maps are in the montages in Figures 3.1 and 3.2.

In addition, we look for any possible correlation between the inclination and the main kinematical parameters, namely the rotational velocity, the integrated velocity dispersion and V_{max}/σ. This was performed using the maximum/integrated values for each galaxy and the ones inferred within their effective radii (see Section 3.4.1). We have also computed the Pearson correlation coefficient in each case (bottom right corner of every chart), that it is always consistent with no correlation. This is a strong indication that our kinematical parameters are measured without any significant bias.

3.3 Individual galaxy observations

In this section we present a detailed description of each massive galaxy within our survey. The description of the galaxy maps are detailed in the captions of the maps belonging to the first galaxy, in Figure 3.3 and 3.4. Each explanation begins with the comparison between the parent POWIR/DEEP2 K_s band imaging and their resemblance to Hα flux images from SINFONI. Then we comment the different features of the H-band continuum, radial velocity (and its model), observed velocity dispersion (and the inferred velocity dispersion after removing the beam smearing), signal-to-noise and error maps. In our maps, north is up and east is left, and we show not the whole field-of-view but the spaxels where the galaxy images overlap in the two opposite corners of the detector. The model maps are discussed at the end of this section. Hα contours are overlapped in all of the maps (with decrements of 10% in flux between adjacent contours), in order to facilitate the reader to know which spaxels belong to the galaxies. It is noteworthy to tell both POWIR and SINFONI have the same astrometry, but the SINFONI resolution after dithering is a factor of 2 better. The axes show sizes both in kpc and arcsec. The kinematical centers used for our models are located in the spaxels with the maximum flux in the continuum maps, and are highlighted by a cross. In the kinematical maps, the coloured spaxels shown are all above a certain threshold (usually 3, 2 for the weakest galaxy detections) in signal-to-noise which is written in Table 3.1, Column (S/N). The signal-to-noise is computed as the intensity of fitted line over the standard deviation of the residual spectrum, with both signal and noise weighted by the sky contribution around the Hα wavelength. However, this threshold was not applied for the continuum maps, in order to understand where in the galaxy the Hα emission originates (see Section 3.2.2). Finally, we attempted to quantify the existence of AGN sources within our sample compiling the $[NII]/$Hα ratio summing up the contributions of all the galaxies' spaxels (see Table 3.3). For POWIR1, 3 and 7 we do not find anything conclusive as the $\lambda\lambda 6583\mathring{A}$ [NII] line is located over OH sky lines. The results of the analysis of this ratio, as well as other results, are described in each galaxy subsection.

3.3.1 POWIR1

The maps belonging to this galaxy are Figures 3.3 and 3.4. This galaxy, albeit a clear detection, is a very compact system both in the K_s band and in the Hα image. The explanation for this is in its inclination, which is the highest of the sample. When looking at the continuum image other features appear. There is a flux stripe in its right side which is spurious as it has no counterpart in the POWIR imaging and its shape and extension makes it an impossible object to exist. However, we notice two blobs which seem real because they have an angular size comparable with the seeing of this observation, although it is certainly strange they do not have any Hα emission. The fainter one, in the northern part of the galaxy, may help us understand why the galaxy shows large values of the velocity dispersion close to it, as this may signal a minor merging event. Conversely, the brightest spot in the south west of the continuum image of the galaxy is not associated with any Hα emission and it does not cause any significative distortion of the main galaxy. Kinematical models show a regular rotational gradient and a fairly high (~ 70 km/s) velocity dispersion. Although it is tentative to identify this galaxy as a merger, we prefer to classify it as very inclined disk galaxy, because of its large rotational velocity and ordered velocity field without any substantial disruption.

3.3.2 POWIR2

The maps belonging to this galaxy are Figures 3.5 and 3.6. The Hα flux map covers in this case the whole of the galaxy. The continuum center and Hα center are well aligned. The Hα map peaks in the center, and there is also a very bright group of spaxels located in the north west part of the galaxy. This sharp feature is most probably caused by a cosmic ray not totally removed by the reduction pipeline. The galaxy looks slightly asymmetrical in its southern part. But overall we can state that this galaxy looks like a relaxed and ordered system. Hα line lies in a spectral region far away from any sky line and thus the [NII] line is clearly identified, giving a ratio of $[NII]/\mathrm{H}\alpha = 0.494$. As a matter of fact, this 1:2 ratio between Hα and [NII] is preserved even within the external spaxels, being this an AGN hint. We consider this system as an early disk-like galaxy

or spheroid with a disk, as its large velocity dispersion and the low importance of the rotational velocity on setting its gravitational support as the low V_{max}/σ ratio reveal. A full discussion on these considerations is described in the next section. Nevertheless, the interpretation as a disk galaxy is favoured at the light of the strong velocity gradient.

3.3.3 POWIR3

The maps belonging to this galaxy are Figures 3.7 and 3.8. Both K_s and continuum maps show an elongated structure with a diagonal shape from left to right parts of the detector. Hα contours do not exactly overlap the galaxy continuum and none of the brightest Hα spots coincide with it. The Hα center and the continuum center are located in different places. Regarding the continuum, we rely on its center location (it is clear its position) but not on the shape as it may be affected by the aforementioned flux stripes in the continuum maps. This is a clear case of disturbed object, but it is remarkable that even in this case, the rotational field is quite clear. The lack of any neighbouring galaxy and stretched shape are evidence for an ongoing merger. With the data we have we cannot add anything to this discussion. It is important to stress that this is one of the galaxies which was observed half of the integration time in the detector and for this reason it does not have a well-defined shape, and taking all the available probes into account we define it as disturbed.

3.3.4 POWIR4

The maps belonging to this galaxy are Figures 3.9 and 3.10. If one looks either at the K_s band map or at the continuum map a bright galaxy appears, and by its eastern side a very elongated arc-shaped feature in Hα , which has some very weak continuum as well. In this case, it seems that the emission comes from a minor object whose gas has been stripped or conversely a fan of stars coming from the main object. The Palomar image also shows this feature, indicating that the merging interpretation is favoured. Our kinematics are thus inferred for the Hα visible object which, at the light of the facts, was not the primary target of our observations. We find a rotational velocity field but not large (maybe because its non-massive nature) and a comparatively big

velocity dispersion consistent with its interacting nature. Its morphology is clumpy, disentangling at least two clumps on it. We catalog it as disturbed/merging galaxy.

3.3.5 POWIR5

The maps belonging to this galaxy are Figures 3.11 and 3.12. By looking at its flux images, this galaxy appears as a blob with a tail in its upper part. Its Hα emission extends over the K_s image and the continuum image. The maximum rotational velocity is very high, as is the velocity dispersion, and thus the dynamical mass is the second largest in our sample. This might be related with a contribution from a sky line in the redder part of the spectrum. The pipeline is meant to remove OH sky lines, but there are sometimes (as in this case) residuals. When the Hα line and the sky line are close to each other it becomes very hard for our IDL programs to disentangle them, increasing somewhat the final results. It is impossible to quantify with certainty this effect although it is not dominant as our routines were able to resolve the gradient in the radial map. We find $[NII]/\mathrm{H}\alpha = 0.602$, which is puzzling as it is a large ratio and we note that the [NII] is detectable all over the galaxy spaxels, and not just concentrated in the center, as we will expect for a standard AGN emission. The properties of this object cannot be perfectly explained as a disk-like object and, despite the limitations of our information, we classify this galaxy as a perturbed rotator.

3.3.6 POWIR6

The maps belonging to this galaxy are Figures 3.13 and 3.14. This is the brightest galaxy in our POWIR imaging. The Hα appearance of the galaxy is largely different from either the continuum or the K_s band. Remarkably, we do not detect Hα emission in the central area, appearing as a hole in the Hα flux map and four knots or clumps surrounding it. This hole overlaps with the center of the K_s and continuum images. Similar cases are seen in Epinat *et al.* (2010), for example the local galaxy UGC04820, which has a ring morphology in Hα , produces the same kind of kinematical maps after redshifting it at $z = 1.7$ than ours. This is typically found in early-type spiral galaxies. The clumps are also conspicuous in the velocity dispersion map. Both theoretical

expectations and recent works agree in their existence (Förster Schreiber *et al.*, 2011b, and references therein). We identify four of them in the Hα map, which match the velocity dispersion enhancements. Another piece of evidence to reassure us in our view of a star-forming disk is that it is strongly rotationally supported ($V_{max}/\sigma = 4.88$ and $V_{max} = 214$ km s^{-1}).

3.3.7 POWIR7

The maps belonging to this galaxy are Figures 3.15 and 3.16. In this case, one of the images of the galaxy fell in the borders of the SINFONI detector. This is the reason why its low signal-to-noise for all its spaxels. However, K_s POWIR/DEEP imaging, Hα and continuum maps overlap well, and show a slight distorted and clumpy galaxy. Rotation seems to play an important role in the support of the galaxy (with $V_{max}/\sigma = 6.88$), but the low signal-to-noise prevents us from drawing accurate conclusions. Its [NII] line is coincident with an OH sky line, impelling any analysis about it. Because of its irregular shape, we classify this is a perturbed galaxy.

3.3.8 POWIR8

The maps belonging to this galaxy are Figures 3.17 and 3.18. Our best seeing (0.42 arcsec) observations are for this system, where we retrieve a very clear disk, even when the continuum map displays a faint spurious flux strip. A bulge component in the center could be present, as the central region is very bright in both Hα and K_s imaging, and displays a large velocity dispersion of $\sigma \sim 130$ km/s. This agrees with the renditions of the anisotropy plot (which will be explained in the next section), as it occupy a locus close to the local fast rotators. However, its rotational support is very strong ($V_{max}/\sigma = 4.60$). Its dynamical mass is very large ($6.63 \times 10^{11} M_{\odot}$) and reliably measured due to its clear velocity gradients, which identification was helped by the excellent seeing of this object's observation. We classify this galaxy as a rotating disk.

3.3.9 POWIR10

The maps belonging to the main galaxy are Figures 3.19 and 3.20, while the secondary object appears in Figures 3.21 and 3.22. We present two different set of figures for this galaxy. Our K_s and continuum images show two galaxies. Most of the flux in these two maps comes from the object in the southern part of the image, although Hα emission is mainly found in the galaxy located in the north. This system has some similarities with POWIR4, specifically in that most of the Hα emission does not come from the main galaxy. For this reason Hα kinematical parameters listed on the tables are related with the object identified as the non-massive galaxy, as kinematics could only be reliably retrieve from it. As a matter of fact, we found strong emission at the [NII] wavelength for the central spaxels of this object in the south part of the detector. This makes us suspect that, given it is a point source, this system harbours an AGN on its center, and the Hα emission at its sides might be outflows of material coming out from it. As said previously, we surprisingly found another galaxy in the map, for which we can see a hint of continuum and very clear kinematics. Due to its distortion/clumpiness, the high velocity dispersions present in the southern part and of course since Hα is detected at the same wavelength as the AGN object, we classify this system as a merger. Due to the low values in the kinematical velocities for this second galaxy we think the photometrical mass is only derived for the AGN.

3.3.10 POWIR11

The maps belonging to this galaxy are Figures 3.23 and 3.24. This is a clearly detected galaxy which was only observed half of the total integration time. However, K_s and continuum images clearly show an extended galaxy, in agreement with the Hα emission. It is most probably close to being face-on, as its inclination is 30°. The signal-to-noise decreases in its right side because of the presence of a sky line at the same side of the spectrum where the Hα line is found, and as consequence our algorithms give less statistical importance to these Hα detections. Nevertheless, the rotational velocity gradient is easy to observe in the whole galaxy and this was the reason behind setting $S/N = 2$ as a threshold for the galaxy maps, as we know that even in

the faint outskirts what we are detecting is the Hα line. Overall, this galaxy presents a disturbed discoidal shape and a couple of bright Hα spots or clumps in its central part. The absence of clear merger events makes us conclude that this is a disk, although rather perturbed or turbulent, as indicated by its fairly low V_{max}/σ ratio.

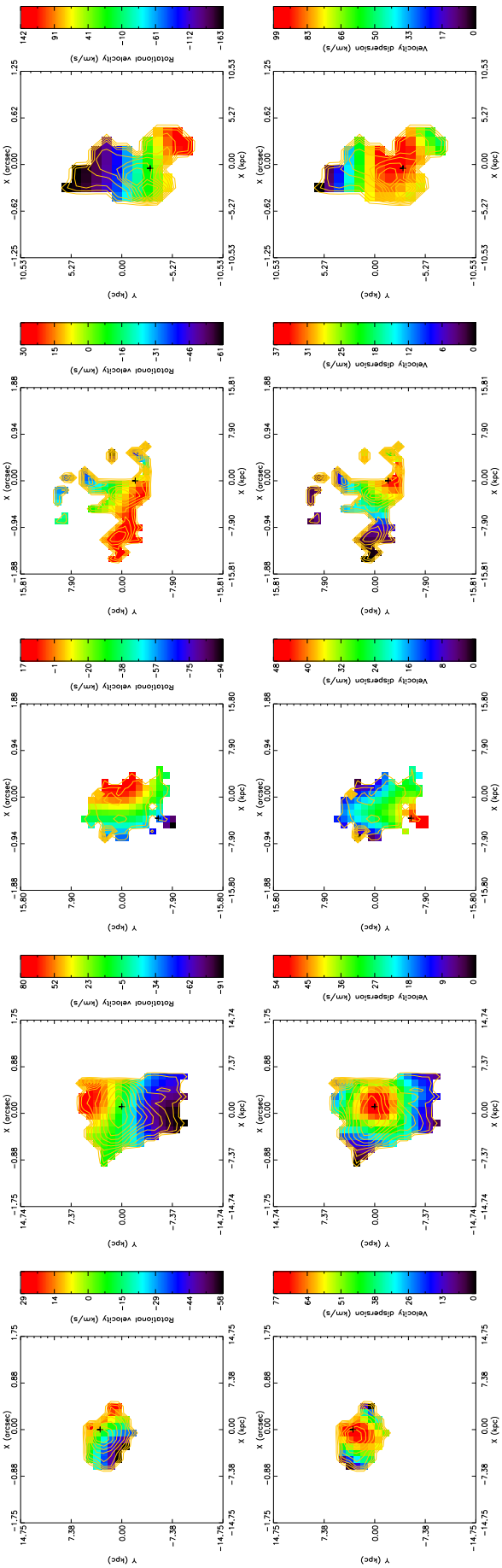

Figure 3.1: Montage with the kinematical models. First row are the rotational velocity maps, and the second the velocity dispersion. From left to right, the columns are POWIR1, POWIR2, POWIR3, POWIR4, and POWIR5. Please note that the descriptions of these figures are written at the beginning of Section 3 and in the first galaxy montages' description (Figures 3.3 and 3.4) as we display there all the different maps we performed for the first galaxy from our sample.

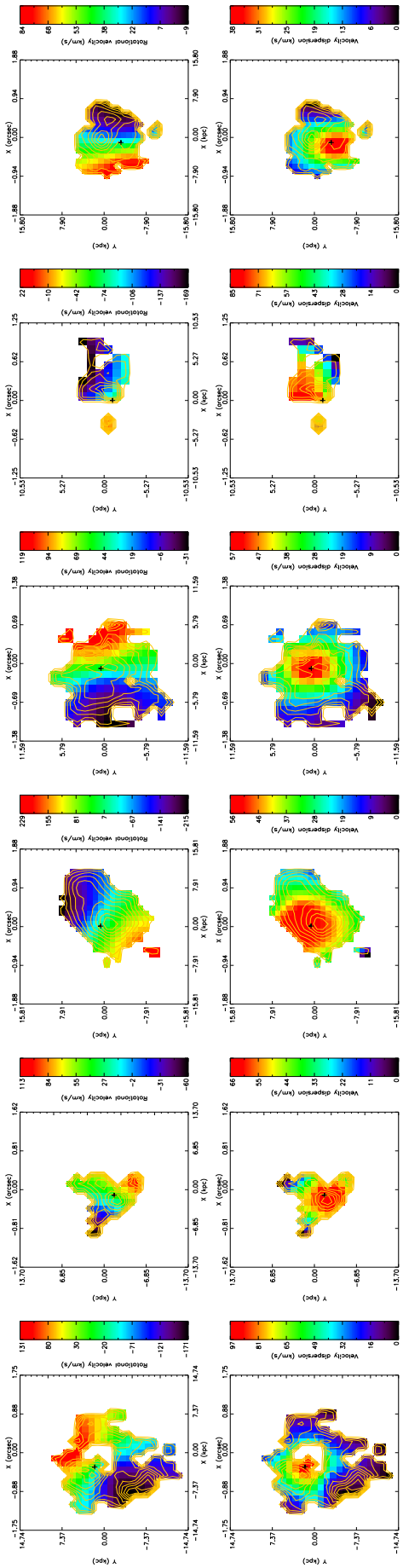

Figure 3.2: Montage with the kinematical models for the rest of the massive galaxies not plotted in the previous Figure 3.1 . First row are the rotational velocity maps, and the second the velocity dispersion. From left to right, the columns are POWIR6, POWIR7, POWIR8, POWIR10 (non-massive galaxy), POWIR10 (massive galaxy) and POWIR11.

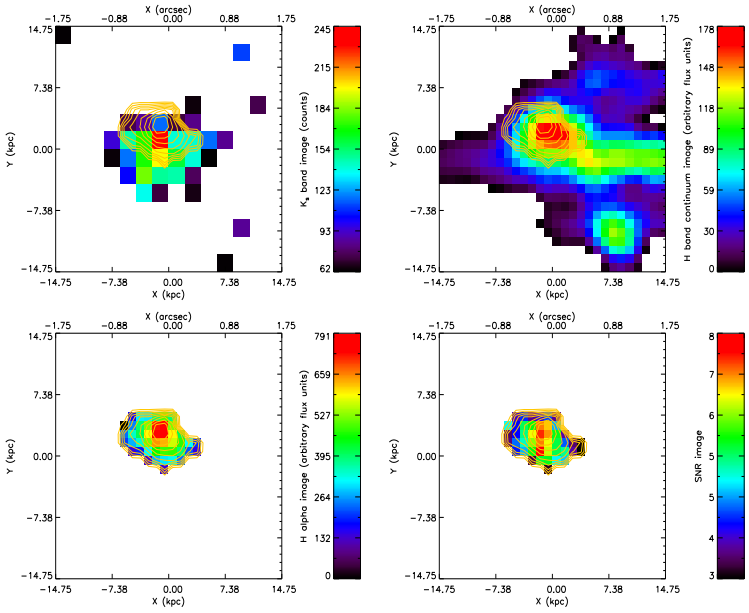

Figure 3.3: From left to right, from top to bottom: K_s POWIR survey image of the galaxy, H-band SINFONI continuum image, SINFONI Hα flux image and signal-to-noise map for every spaxel. Hα contours are overlapped in all the maps (with decrements of 10% in flux between adjacent contours) in order to facilitate the reader to know which spaxels belong to the galaxies. The axes show sizes both in kpc and arcsec. All the rest of the first montages of every galaxy in our sample are performed the same way as these. POWIR1 – Disk-like galaxy. *Comments:* Two neighbouring objects in the continuum image. The central galaxy is very compact due to its high inclination.

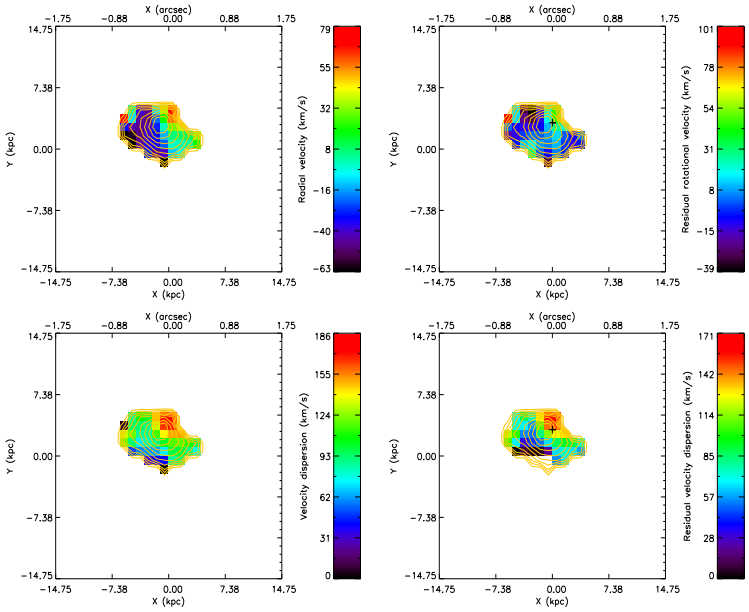

Figure 3.4: From left to right, from top to bottom: observed radial velocity map, residual rotational velocity map (after substracting quadratically the rotational velocity model from Figure 3.1 in this case, otherwise Figure 3.2), observed velocity dispersion map and residual velocity dispersion map (after substracting quadratically the rotational velocity model from Figure 3.1 in this case, otherwise Figure 3.2). contours and axes are the same as in the previous montage. A cross appears in the place we set our galaxy center (see beginning of Section 3.3 for an explanation). All the rest of the second montages of every galaxy in our sample are performed the same way as these. POWIR1 – Disk-like galaxy. *Comments:* Clear Hα line in all the spaxels above the signal-to-noise threshold, velocity dispersion enhancement due to minor merging.

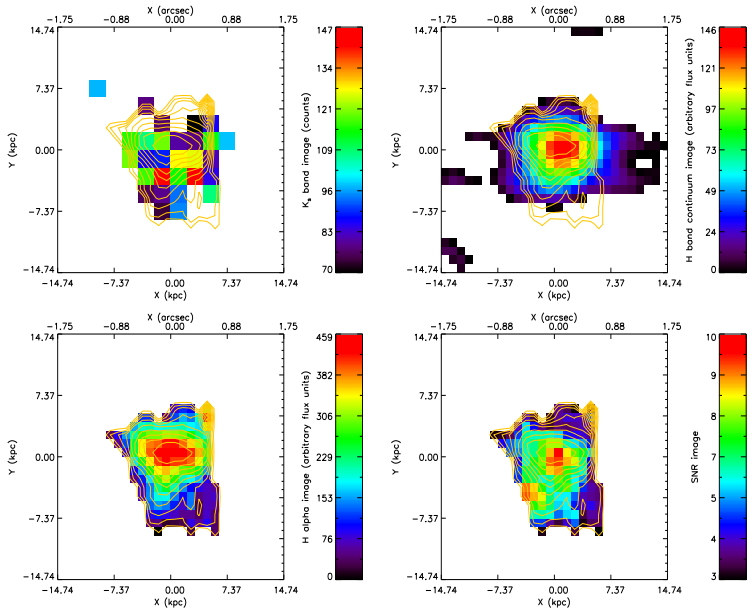

Figure 3.5: POWIR2 – Disk-like galaxy. *Comments:* Very extended Hα emission. Very clear Hα detection, with an elongation and a signal-to-noise enhancement in the lower part, arguably because of a merging episode.

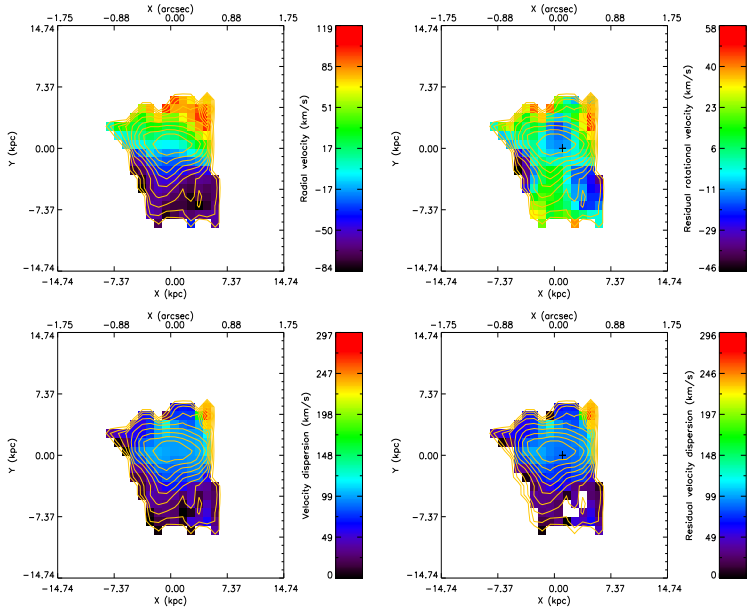

Figure 3.6: POWIR2 – Disk-like galaxy. *Comments:* The group of spaxels in the top right displays high velocity dispersion are an artifact, but not the high values in its center. This latter feature points towards the development of a spheroidal component.

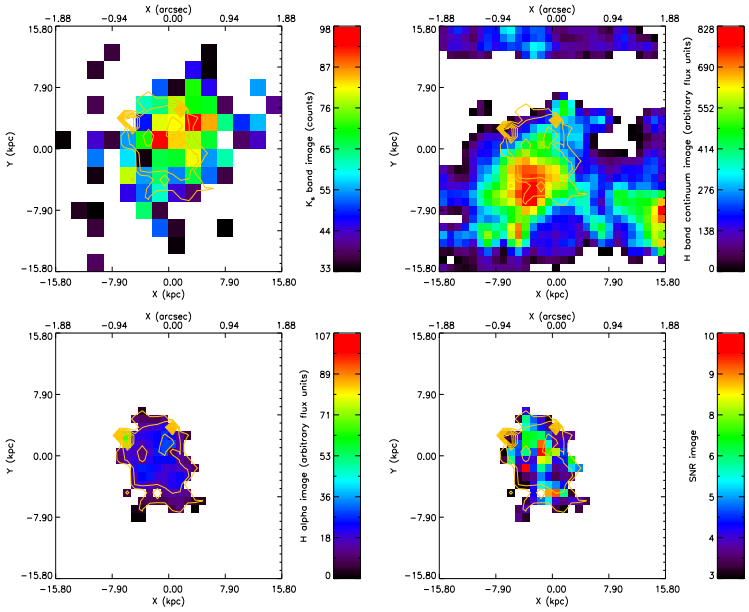

Figure 3.7: POWIR3 – Merging/Interacting galaxy. *Comments:* K_s and continuum images are vaguely related but not with the Hα map. Most probably this is an ongoing merger, and this would explain its elongated shape.

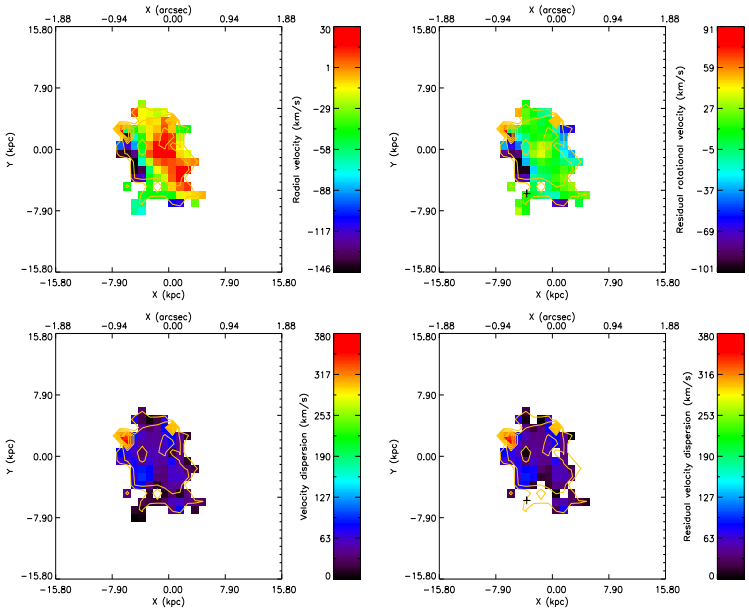

Figure 3.8: POWIR3 – Merging/Interacting galaxy. *Comments:* Rotation is found, it shows complex kinematics, as expected for its interacting nature.

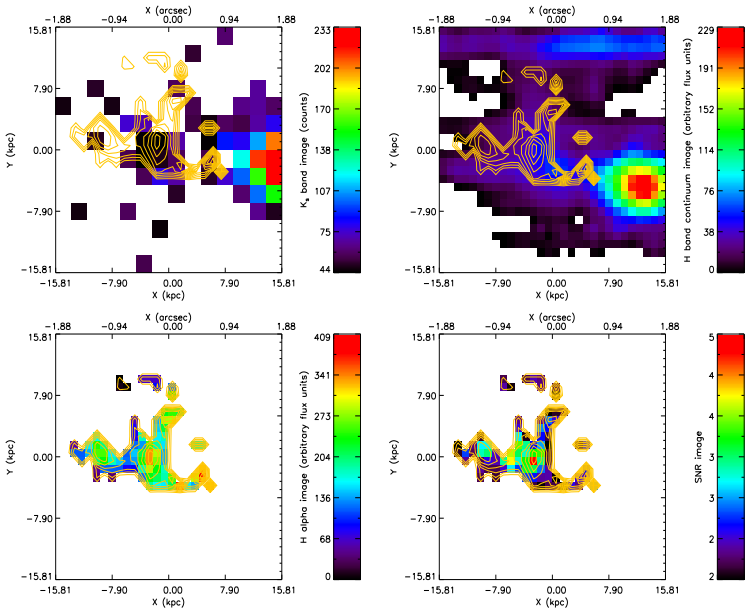

Figure 3.9: POWIR4 – Merging/interacting galaxy. *Comments:* Both K_s and continuum maps show a bright object located at the right side of the Hα detection. We interpret this as the massive galaxy (which is devoid of Hα emission) is interacting with another object, whose gas is being stripped or very perturbed.

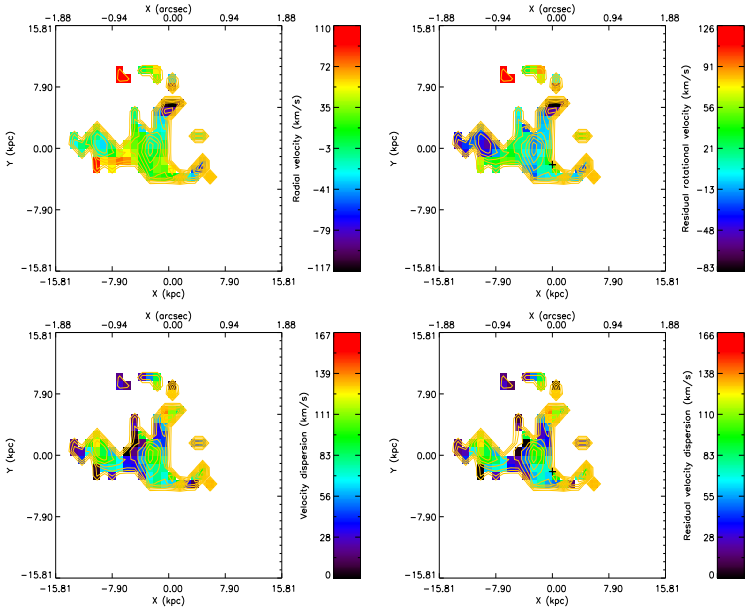

Figure 3.10: POWIR4 – Merging/interacting galaxy. *Comments:* For the Hα detection, which is the non-massive galaxy, non-neglectable values of rotation and velocity dispersion are retrieved.

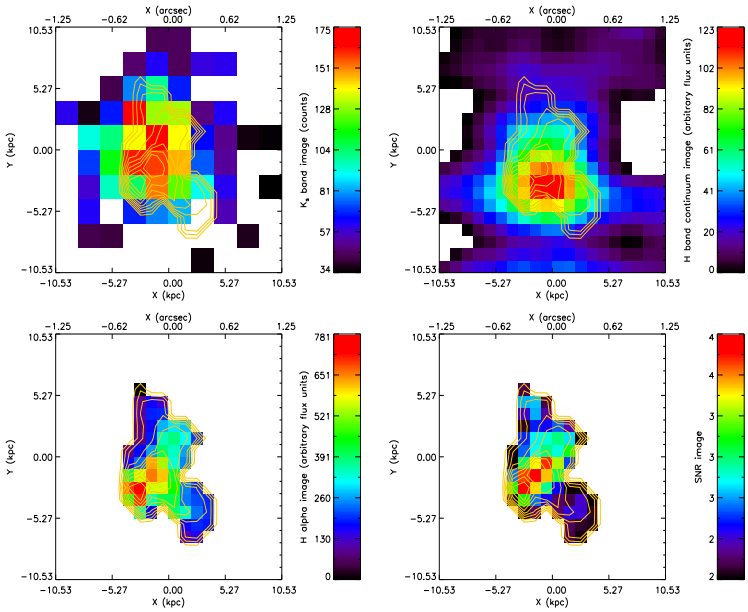

Figure 3.11: POWIR5 – Perturbed rotator. *Comments:* K_s , continuum and Hα overlap in the same place, showing a galaxy slightly elongated in its top part.

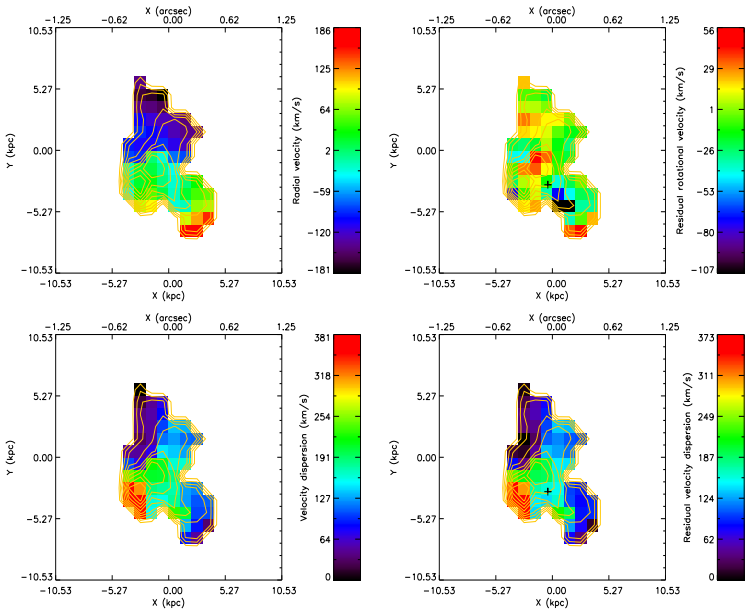

Figure 3.12: POWIR5 – Perturbed rotator. *Comments:* High radial velocity values. Velocity dispersion might be affected by a close sky line, increasing slightly its actual value.

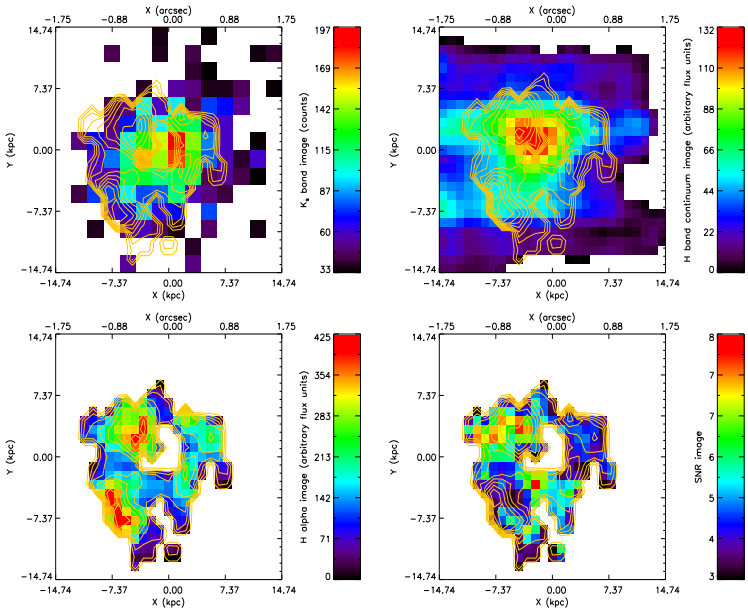

Figure 3.13: POWIR6 – Disk-like galaxy. *Comments:* This ring pattern in the Hα image was observed before in low redshift late galaxies (see Epinat et al. 2010).

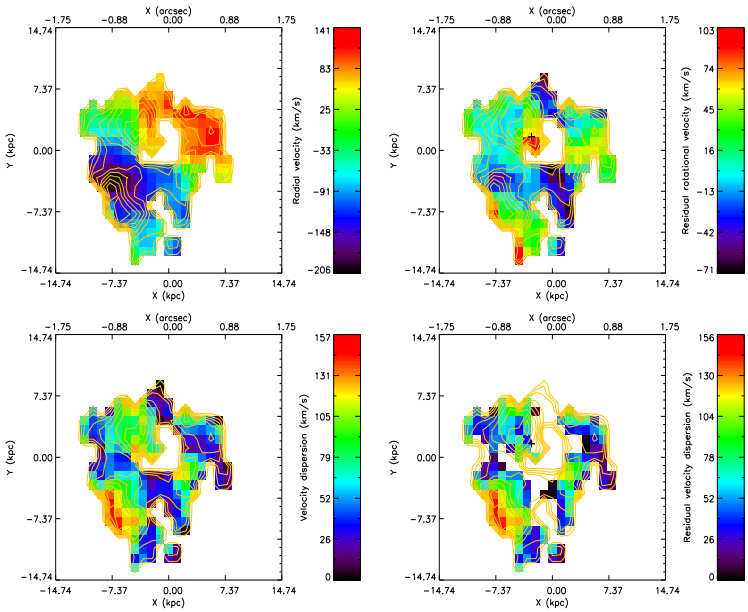

Figure 3.14: POWIR6 – Disk-like galaxy. *Comments:* We identify four different clumps in Hα and the velocity dispersion map.

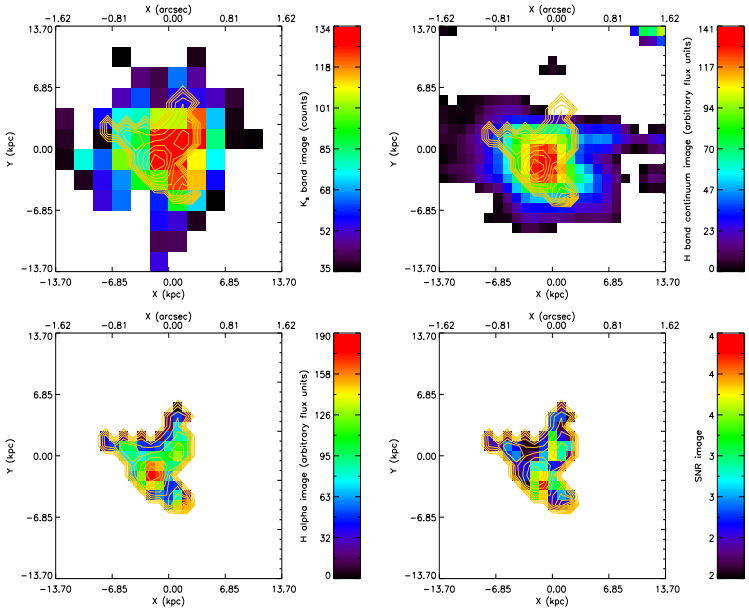

Figure 3.15: POWIR7 – Perturbed rotator. *Comments:* K_s , Hα and continuum maps overlap well. This galaxy was not observed half of the integration time but was set in the border of the detector, which explains its low signal-to-noise detection.

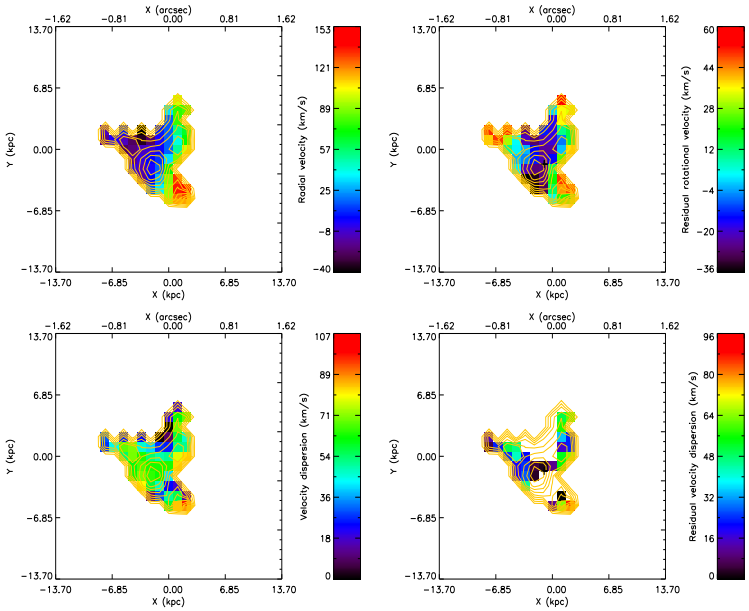

Figure 3.16: POWIR7 – Perturbed rotator. *Comments:* Slightly disturbed morphology, with a possible clumpy structure.

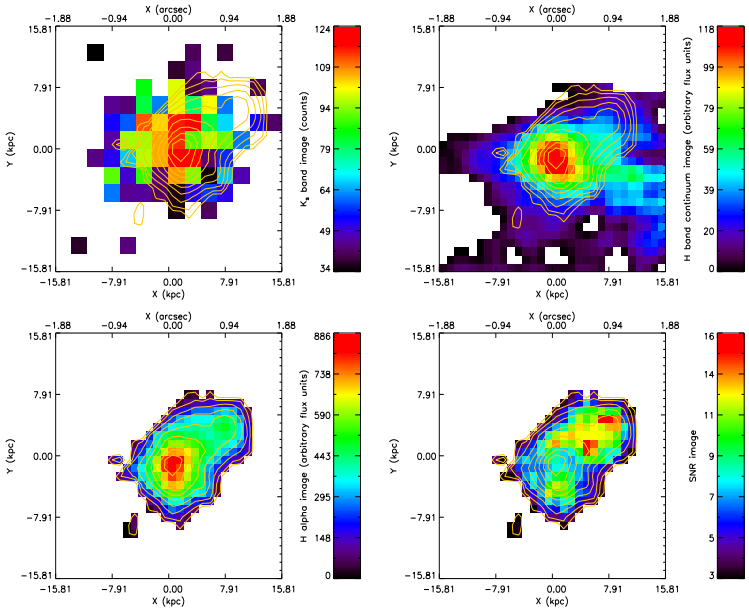

Figure 3.17: POWIR8 – Disk-like galaxy. *Comments:* Clear and extended disk in all the images.

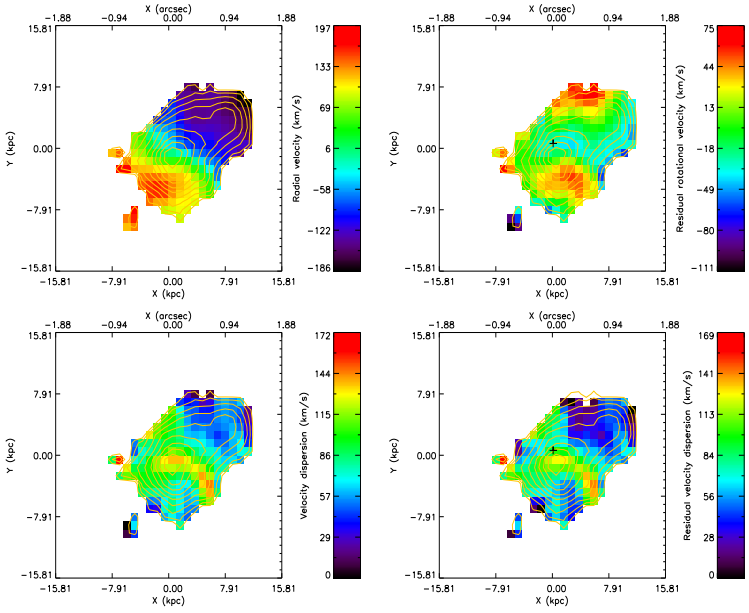

Figure 3.18: POWIR8 – Disk-like galaxy. *Comments:* High radial velocity values, with a large velocity dispersion in its center, which is a hint of a bulge component.

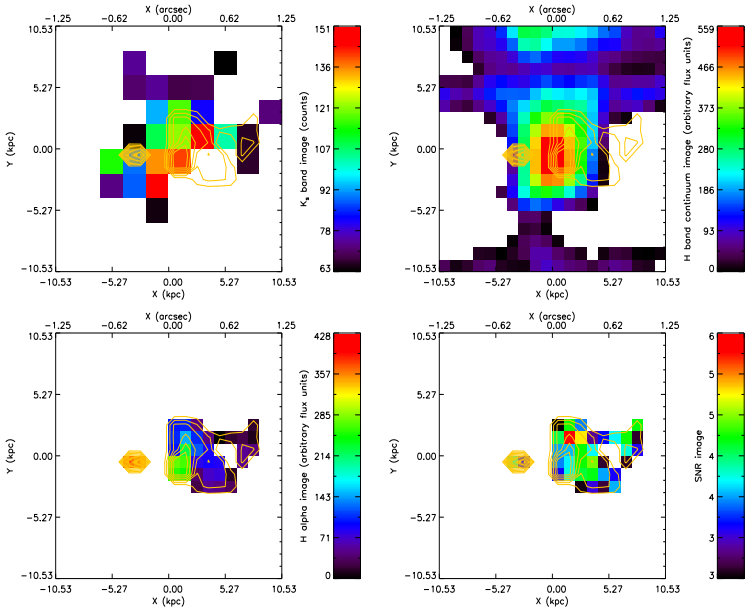

Figure 3.19: POWIR10 – Merging/interacting object. *Comments:* Similar case as POWIR4. Here we can see the main object, which has another blob in its upper part. As most of the continuum and K_s signal come from this main object, we identify it as the massive galaxy. It shows high [NII] values in its centers, indicative of its AGN nature. The Hα detections at its sides might be related with gas outflows.

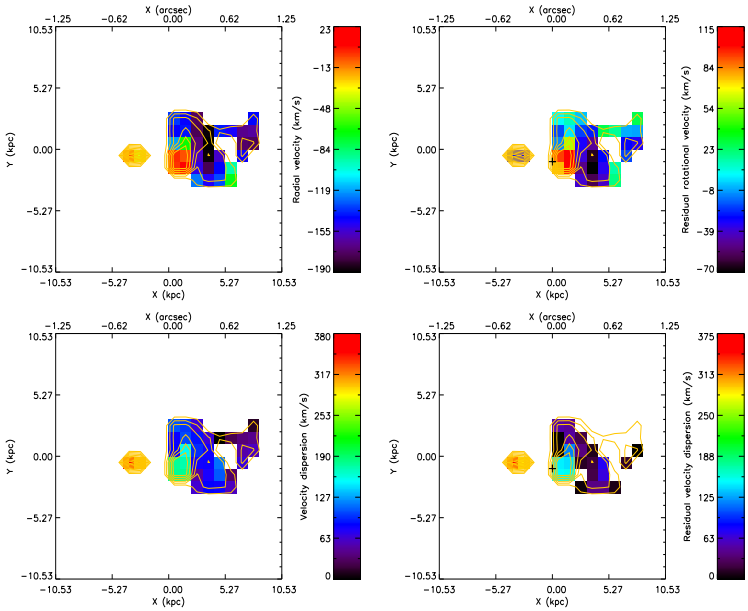

Figure 3.20: POWIR10 – Merging/interacting object. *Comments:* Messy kinematics, we cannot infer anything conclusive.

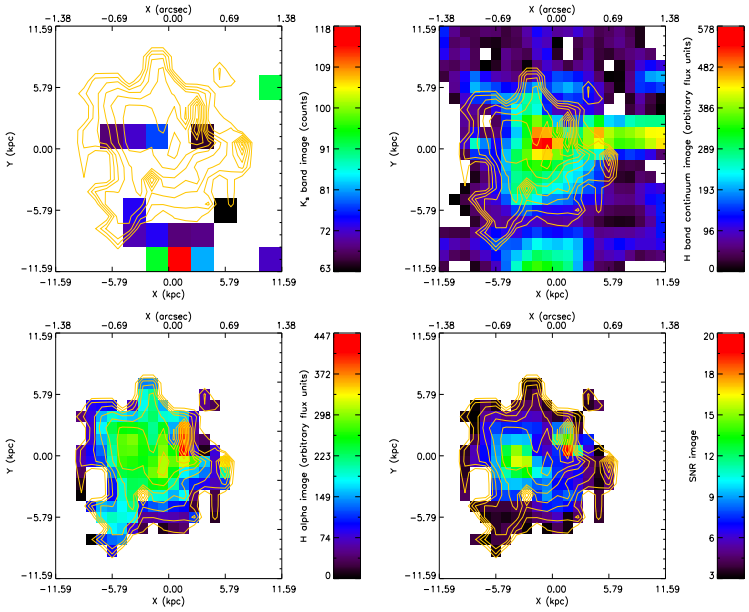

Figure 3.21: POWIR10 – Merging/interacting object. *Comments:* This is the galaxy which was at the top of the previous AGN object. It is a large, at least in the Hα map.

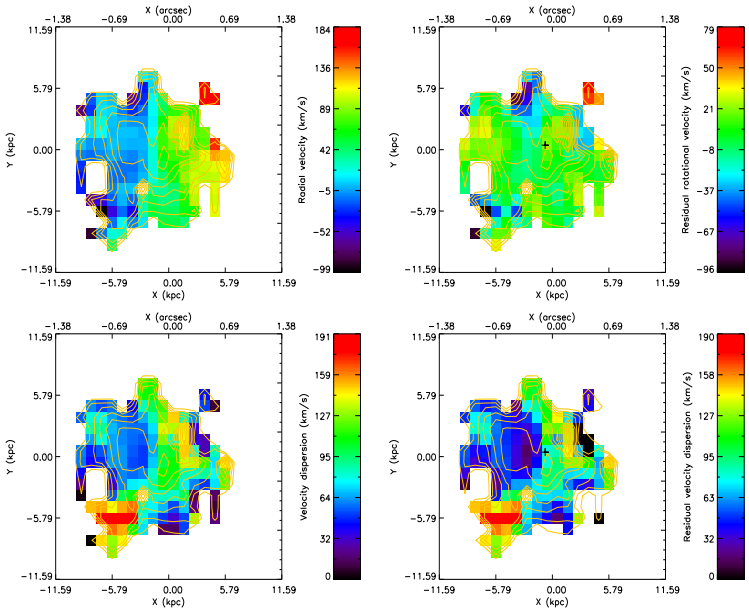

Figure 3.22: POWIR10 – Merging/interacting object. *Comments:* Its radial and velocity dispersion values are not very high, suggesting it is not as massive as its partner galaxy. There is a velocity dispersion enhancement in the lower part, where the two galaxies are connected/interacting.

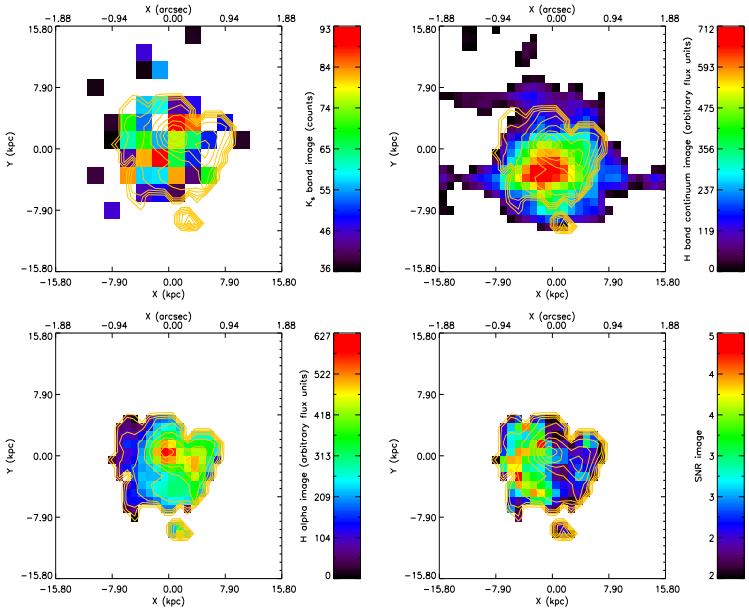

Figure 3.23: POWIR11 – Disk-like object. *Comments:* Close agreement between K_s , continuum and Hα . Low signal-to-noise because of the observational problems. This is the galaxy with the lowest inclination in our sample.

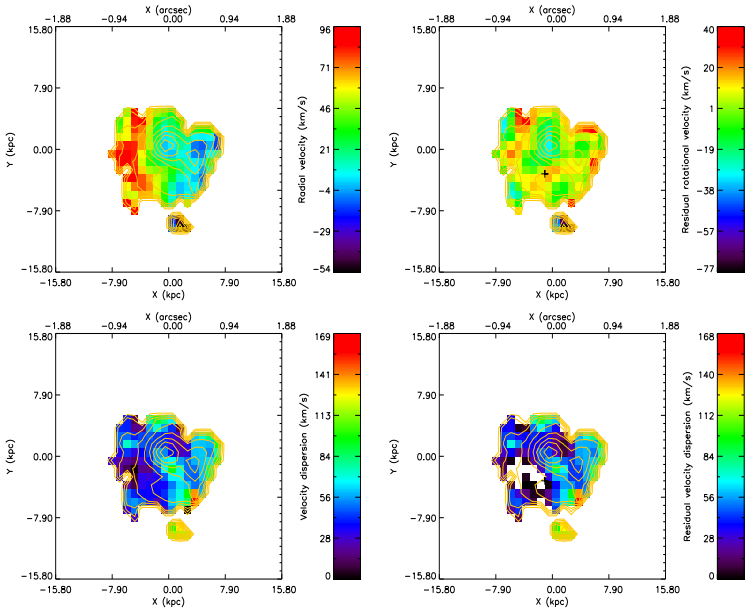

Figure 3.24: POWIR11 – Disk-like object. *Comments:* Clear velocity gradient as Hα is clearly detected in all the coloured spaxels.

3.4 Results

3.4.1 Kinematical classification

Previous studies of high redshift galaxies connecting photometry and spectroscopy have demonstrated that these systems are more clumpy/irregular and have higher velocity dispersions than local galaxies (Förster Schreiber *et al.*, 2011a, and references therein). There are several attempts in the literature to establish a kinematical classification of high-z galaxies relying on Hα kinematics (Flores *et al.*, 2006; Law *et al.*, 2009; Cresci *et al.*, 2009; Förster Schreiber *et al.*, 2009; Epinat *et al.*, 2009; Gnerucci *et al.*, 2011, Epinat et al. 2012). All of them roughly agree that there are three basic kinematical classes, which may be linked with the morphological nature of each galaxy. First, rotating disks have been observed, showing well-defined and regular rotational velocity gradients that are larger than their velocity dispersion. Usually these systems are large in size. Ongoing mergers are also clearly distinguished, not only by disentangling two or more components but also through a chaotic velocity pattern, and local increments in the velocity dispersion. Finally, objects which do not fit in any of the previous categories are tagged as perturbed rotators, which are probably more similar to early type systems due to a high velocity dispersion in comparison with the maximum rotational velocity.

Before characterising our sample according to these criteria, we should enumerate several caveats that might affect our interpretation of the data. Firstly, behind this classification there is the disk-like assumption in the modelling. This will not be an accurate model when dealing with mergers or pure spheroidal galaxies. Arguably, this has an impact in our sample as massive galaxies in the local Universe are predominantly elliptical (e.g. Baldry *et al.*, 2004). However, at the redshift of our observations ($z \sim 1.4$), we would expect to have a morphological mixture (van Dokkum *et al.* 2011 or see this thesis Chapter 2). To the best of our knowledge, only disk models have been considered when dealing with high-z 3D spectroscopy observations. This is based on that fact these disk models – for a review on them, please go to (Epinat *et al.*, 2010) – work reasonably well for the previous star forming selected samples (Genzel *et al.*, 2008; Cresci *et al.*, 2009). Investigating how to take into consideration a bulge/spheroidal

component into the modelling is certainly a necessary future path of study, as evolved galaxies are present at high-z (Kriek *et al.*, 2006) and the advent of increasing quality data will permit more detailed studies. Finally, we must remember we are looking at the gas emission and not at the total stellar component. Performing a preliminary visual classification, we firstly noticed that the Hα emission extends over all of the K_s and continuum images for most cases, which is difficult to reconcile with the possibility of being spheroid-like objects, specially when Hα emission is usually linked with present star formation. As stated in the introduction, the existence of gas disks within elliptical galaxies has been reported in the past (Falcón-Barroso *et al.* 2006, Krajnović *et al.*, 2008; Oosterloo *et al.*, 2010) but their sizes (hundreds of parsecs) are much smaller than our current gas disks which span the galactic size.

We focus now on the individual properties of the sample, which has been discussed in detail in Section 3.3. POWIR6 is recognized as a late-type galaxy. POWIR1, 2 and 8 show clear rotational gradients. Although the centers of the latter two display fairly large velocity dispersions. But in both E09 and F-S09 these were indicators of typical disks galaxies which are developing a bulge component. We classify the three of them as disk-like galaxies, primarily based in their large and regular rotational velocity gradients. POWIR4 and 10 are classified as interacting objects. In fact, in both cases the Hα emission originates (although there is a very weak detection in POWIR10 for the main object) from spaxels that do not belong to the target galaxy. Hence we discern two separate galaxies interacting in our SINFONI data. The photometric data information has been derived for the main objects, which we identify as the massive objects in the K_s band imaging, while the Hα detection comes from the secondary galaxies. We exclude the latter from the plots as they are not massive galaxies, but we derived kinematics for them to understand which physical processes are taking place in the merger. Little can be said about the two massive and main objects: POWIR4 is completely devoid of Hα emission, while POWIR10 looks like a point source with a strong [NII] line in its center, that suggests it host an AGN. POWIR3 is an object which may be in this category as well. This K_s and continuum images do not match with the Hα emission, whose map is quite irregular. The rest of the objects are more difficult to catalog visually. We must bear in mind that 2 out of the 3 other objects were observed half of the integration time because our 'on-source dithering' problem. Either

POWIR5, 7 and 11 have relaxed morphologies in the K_s and continuum bands while Hα shows, as expected, a more complicated pattern. POWIR11 is different, despite the observational issues. It has an easily distinguishable and large in size rotational field, which fits better the disk object classification. The other two galaxies are catalogued as perturbed rotators.

In low redshift studies, the V_{max}/σ vs. ε diagram (also called the anisotropy plot; Figure 3.26; with the ellipticity $\varepsilon = 1-$ axis ratio) is a classical tool to measure elliptical galaxies' kinematics (Illingworth, 1977; Bender, Saglia & Gerhard, 1994; Cappellari *et al.*, 2007; Emsellem *et al.*, 2011). We created this plot with our sample's data as an exercise, as massive galaxies at low-z are ellipticals in the majority and this is a good test to shed light into the nature of our sample. If our sample clearly departs from the locus occupied by ellipticals we may accept it as a good indication about their distinct nature. The disk modelling has no important impact regarding this plot, as it only corrects the measured velocity by more realistic values breaking the degeneracies introduced by the inclination and the beam smearing at high-z. This is of course not necessary at low-z due to the high resolution of the observations. However, the plotted parameters used in this relation usually are measured at one effective radius distance from the galaxy center. To palliate our uncertainty on this, we computed effective radii in our sample using the relation published in Buitrago *et al.* (2008) for massive disk-like galaxies (to be consistent with our modelling), extrapolated to each galaxy's redshift. Then we computed V_{max}/σ in the closest aperture to the calculated effective radius, as to calculate velocity dispersions we need an integer number of spaxels around our kinematical center. All the information used is tabulated in Table 3.4. We add low redshift galaxies from ATLAS^{3D} Survey (Emsellem *et al.*, 2011). Note that their kinematics are obtained for the stellar component and that not all their masses fulfill our definition of massive galaxy ($M_* > 10^{11} M_\odot$). Nevertheless the comparison makes sense as their sample is composed of some of the most massive galaxies in the nearby Universe. Our results tell that, although uncertainties are huge (also for the ellipticity, due to the coarse resolution of our images), we find that all of the massive galaxies at high-z lay above the line defined by

$$\left(\frac{V}{\sigma}\right) \approx 0.890\sqrt{\frac{\varepsilon}{1-\varepsilon}} \tag{3.4}$$

which is the minimal rotational approximation to the isotropy line optimized for integral-field kinematic observations (Binney, 2005; Cappellari *et al.*, 2007). This reveals the high level of rotational support for these massive galaxies in the high-z Universe, especially when comparing with slow rotators that are the most massive galaxies nearby. It is interesting as well that both POWIR2 and POWIR8 are close the isotropy line. Both galaxies show a clear disk with a velocity dispersion enhancement in the center, which we identify as a hint of a bulge component. Possibly these galaxies are beginning to fall into the early-type group due to secular evolution. But due to their total V_{max}/σ (the ones not derived within one effective radius) and rotational velocity fields we acknowledge them as more similar to disk dominated galaxies.

Perhaps, for high redshift studies where the information is not so detailed, it is more meaningful to plot the rotational velocity versus the velocity dispersion as in Figure 3.27. We use the maximum rotational velocity from our models and the $1/\text{error}^2$ velocity dispersion for our sample, and we supplemented it with SINFONI observed massive galaxies with published modelling information available, coming from the SINS sample (galaxies Q2343-BX610, D3a-6004,D3a-6397, D3a-15504 from F-S09). The Spectroscopic Imaging survey in the Near-infrared with SINFONI (SINS; F-S09) is very useful for our purposes as it is the largest survey at high-z ($1.3 < z < 2.6$) using SINFONI, consisting of 62 rest-UV/optically selected sources through a variety of methods, targeting mainly their Hα and [NII] emission lines. As one can see, all the galaxies in Figure 3.27 exhibit $V_{max}/\sigma > 1$, in most cases larger than 2.4. We constructed as well the histogram of the Figure 3.27. The dashed part corresponds to the galaxies that are not part of our sample. Although the number statistics are poor, all the massive galaxies plotted show rotational velocities which exceed their computed central velocity dispersions, in most of the cases by a large factor. Interestingly the objects from the SINS survey have V_{max}/σ ratios which exceed ours. One possible explanation is that, as these objects are selected by their star-formation, they are later types than our sample. Again, this fact would be evidence for massive galaxies have settled down by $z \sim 1.4$ and developing a bulge component, as suggested by the anisotropy plot.

3.4.2 Dynamical masses

Integral field spectroscopy can be used to explore the dark matter content in our sample. To achieve this aim we computed dynamical masses combining the information coming from the rotational velocity and the velocity dispersion maps using the formula (from E09)

$$M_{dyn} = M_\theta + M_\sigma = \frac{V_{max}^2 R_{last}}{G} + \frac{\sigma^2 R_{last}^3}{G h^2} \tag{3.5}$$

where M_θ describes the mass enclosed up to a radius R_{last} and M_σ is called the asymmetric drift correction (Meurer *et al.* 1996) by which one takes into account the velocity dispersion/random motions support within the galaxy. All the terms are described in Table 3.3 except h, which is the gas surface density disk scale length described by a Gaussian function, whose expression is $h = (2ln2)^{-1/2} r_e$. Our assumptions are that both M_θ and r_e are for disk-like systems, as explained in Section 3.4.1. The outcomes of this calculation are plotted in Figure 3.28. Two lines are drawn on it: the solid one is the 1:1 reference, while the dashed line is the local relationship ($M_{dyn}/M_* = 1.68$ is the average ratio for SDSS galaxies) coming from van de Sande *et al.* (2011). In principle, one would expect all galaxies to populate the region above the solid 1:1 line, as their dynamical mass would have to account for the baryonic mass plus the dark matter component. This does not happen for all the objects in our sample. There are a number of reasons which may explain this disagreement. First, we must not forget that this mass originates from the ionised gas dynamics which may depart from the values obtained from the stellar measurements. Secondly, our calculations account for the mass within R_{last}, i.e., the maximum Hα radius, which is smaller than the apertures where the stellar masses has been measured and also smaller than the typical radius used in other works such F-S09 to obtain this parameter. Our dynamical masses would grow if we correct them by these effects. Adding both contributions would make our dynamical masses larger. Besides, Martinez-Manso *et al.* (2011) claimed a possible overestimation on the stellar masses we are utilising from Bundy *et al.* (2006). If confirmed, our dynamical masses would be in better agreement with the new stellar masses. To try to understand better the origin of these dynamical masses, we performed a plot of the relative contributions of each term of in the formula in the Figure 3.29. The galaxy 220584167 from E09 is plotted, correcting its two contributions to

the total mass to match our Chabrier IMF. This shows us the location of a confirmed massive rotating disk (according to E09) in this chart. Interestingly, this galaxy is the most rotation dominated object ($M_\theta/M_\sigma = 18$ and $V_{max}/\sigma = 5.9$) of that sample. Apart from the anomalous POWIR7, the contribution for the velocity dispersion term is quite important for all our sample, making its addition mandatory to retrieve correct dynamical mass estimations of high-z galaxies.

3.4.3 Tully-Fisher relation

The Tully-Fisher Relation (TFR) links the maximum rotational velocity of spiral galaxies with their luminosity or stellar mass (Tully & Fisher, 1977; Fernández Lorenzo *et al.*, 2009, this last one for a comprehensive update). It has also been extended to S0 galaxies (e.g. Bedregal, Aragón-Salamanca & Merrifield, 2006) and early-type galaxies in general (e.g. Davis *et al.*, 2011). Modern investigations focus on finding and understanding any evolution in its slope, intercept or both (Bamford, Aragón-Salamanca & Milvang-Jensen, 2006). It is a powerful scaling relation which accounts for how the stellar mass and the dark matter content are related (Conselice *et al.*, 2005). Several attempts to determine it with SINFONI integral-field Hα spectroscopy have been performed. Cresci *et al.* (2009) found a slope consistent with the Bell & de Jong (2001) $z \sim 0$ relationship, while in E09 the scatter is higher, especially for those galaxies with the lower rotational velocity values.

We attempt to shed some light into this TFR for our sample of massive galaxies at high redshift. The number of objects is not high and their morphological nature is not perfectly constrained, but it is an useful indicator that relates the mass and the rest of kinematical properties of a given galaxy sample. We show the K_s band TFR for our sample of galaxies in Fig. 3.30 using the maximum rotational velocity retrieved in our modelling. As we did in the previous plots, we add SINFONI Hα measurements for the massive galaxies in the SINS survey (F-S09, with a detailed TFR study in the aforementioned Cresci *et al.* (2009)). The solid line account for the local ($z \sim 0.2 - 0.3$) K_s band POWIR/DEEP2 relationship in Fernández Lorenzo *et al.* (2010), being the crosses the objects studied in that article. Please note that the relationship was inferred by inversely weighting the errors of the galaxies in the fit. Overall, our results

are similar to E09, as POWIR2 and 11 display the lowest rotational velocities plotted (note that POWIR4 and 10 have also very small ones, but they do not appear in the figures as the Hα detections in those two cases correspond to the non-massive galaxies which are interacting with the main ones). Whereas for POWIR2 this constitutes a further indication of its departure from a pure disk system, the interpretation is not so obvious for POWIR11, when looking also at the anisotropy plot (Fig. 3.26). We attribute this to the fact that this is the object with lowest inclination in our sample, and subsequently it is more difficult to constrain this parameter which affects to the rotational velocity determination.

The number of galaxies in our sample and their selection prevent us from drawing any significative conclusion about a possible evolution of the TFR over resdshift. Cresci *et al.* (2009) and E09 would be the only direct comparison to our data due to the similarities with our sample. However we should bear in mind the consequences of finding an evolution in this scaling relation. There is a widespread consensus about the intercept change in the B-band, although the works differ in the the value. Vogt *et al.* (1996, 1997) found $\Delta M_B \leq -0.4$ at $z = 0.5$. Ziegler *et al.* (2002) and Böhm *et al.* (2004) obtained $\Delta M_B \sim -1$ at $z = 1$. These last two articles also claimed a change in the slope of the relationship, whereby the most massive galaxies follow the local TFR but the less massive were brighter in the past. This slope change is more controversial, however well it agrees with the luminosity evolution due to higher SFR at high-z.

There are a number of other works in other bands (e.g. Giovanelli *et al.*, 1997; Masters, Springob & Huchra, 2008) and simulations (van den Bosch, 2000; Tonini *et al.*, 2011). Returning to NIR K-band TFR, Conselice *et al.* (2005) did not find evolution at $0 < z < 1.2$. Likewise Fernández Lorenzo *et al.* (2010), although they found a change in luminosity for the B, V and R bands. It is noteworthy that there are other works with the GIRAFFE instrument using IFUs. They showed contradictory results (Flores *et al.*, 2006; Puech *et al.*, 2008), probably owing to the different local relations assumed.

The stellar mass or baryonic TFR (using stellar mass instead of luminosity) has been claimed to be a better proxy for the galaxy mass assembly. We show this for our sample in Fig. 3.31. The solid line is the local relationship found by Bell & de Jong (2001) corrected to our Chabrier IMF, while the dashed line is the derived stellar mass TFR

at $z \sim 2.2$ in Cresci *et al.* (2009). We also add the disk galaxies from Conselice *et al.* (2005), separating their sample between $z \leq 0.7$ and $z > 0.7$ as they did. There is a close resemblance with Fig. 3.30. We can see that all the galaxies occupy similar loci, indicating our disk assumption for the galaxy is not a bad one. In order to disentangle better the disordered motions of the gas we follow the prescriptions in Kassin *et al.* (2007), where they used the parameter $S_{0.5} = \sqrt{(0.5 * V_{max}^2) + \sigma^2}$, arguing that the scatter in the TFR is tighter when taking into account the contribution in the velocity dispersion. We show this relation in Fig. 3.32, plotting the highest redshift ($0.925 < z < 1.2$) relation inferred in Kassin *et al.* (2007). Again, galaxies with lower rotational velocity values are the ones that are further apart from the fiducial relationship revealing that their properties are more difficult to match with the assumption of simply a disk-like nature.

3.5 Discussion & Conclusions

We present a SINFONI study of a sample of massive galaxies ($M_{stellar} \geq 10^{11} h_{70}^{-2} M_{\odot}$) at $z \sim 1.4$ selected by stellar mass in order to understand the kinematics/secular motions of this galaxy population and furthermore constrain their rotational nature. This is a matter of debate after recent photometrical studies – van der Wel *et al.* 2011, this Thesis Chapter 2 – and Hα detections for massive galaxies at $1 < z < 1.5$ in the 3D-HST Survey (van Dokkum *et al.* 2011), being our work an attempt to clarify the diversity of properties these galaxies display and whether they are better described kinematically by a disk-like or spheroidal population.

We carefully chose 10 massive galaxies at $z \sim 1.4$ with available deep Keck spectroscopy and K_s band imaging from the POWIR/DEEP2 survey. VLT/SINFONI H-band observations (with a spatial sampling of $0.125" \times 0.25"$ and a spectral resolution of $R \sim 3000$) with a very good (0.56 arcsec) seeing, enabled us to build Hα kinematical maps. We adjusted rotating disk models on the velocity fields that allowed to derive rotation velocities and correct the velocity dispersion maps from beam smearing. Hence we try to minimize potential sources of errors as the uncertainty in the galaxies' inclination or the broadening of the spectral lines by velocity shear.

A very reasonable question we may ask ourselves is whether we could generalize our conclusions to the whole massive galaxy population at $z = 1.4$. Our sample was selected by its mass and [OII] luminosity. Both Hα and [OII] emission come from ionized gas by star formation activity in HII regions. However [OII] is more sensitive on the metallicity, but their luminosities are correlated both at low and high redshift (Tresse *et al.*, 2002). Simple 'downsizing' arguments tell us that the massive galaxy population are quenched soon in cosmis history terms, being most of this galaxies devoid of any star formation in the local Universe. Hence, is our sample unusual because of the fact of having Hα emission at $z = 1.4$? To the best of our knowledge, there is no work that address this question directly. Twite *et al.* (2012) sample is not as massive as ours and not complete in mass. The Hi-redshift(z) Emission Line Survey – HiZELS; Geach *et al.* (2008) – probes with narrow-band filters thin redshift slides ($\Delta z = 0.03$) on looking specially for Hα emission. In the Figure 4 of their work Sobral *et al.* (2011), the authors plotted the number of detections at $z = 0.84$ according to the mass. For massive ($M_{stellar} \geq 10^{11} M_{\odot}$) galaxies, the fraction of massive galaxies detected are $\sim 15\%$ (having equivalent widths greater than $\sim$15 Å, which typically translates into star formation rates of 5-10 $M_{\odot} yr^{-1}$; P. Best private communication). Our galaxies are also selected with equivalent widths greater than this threshold. One would expect this fraction to increase at $z = 1.4$, but how much?

The series of works which deal with star formation for massive galaxies (Pérez-González *et al.*, 2008b; Cava *et al.*, 2010; Williams *et al.*, 2010; Bauer *et al.*, 2011; Viero *et al.*, 2012). Their main outcome is that massive galaxies are star forming objects (both using SFR and SSFR arguments) at $z > 1.5$. This is specially true for disky galaxies. Looking at our data, we find five of these objects, and another 2 or 3 suffering interactions which most probably trigger star formation and hence Hα emission. Consequently, it is hard to state to what extent our sample is 'typical' in comparison with the full population of massive galaxies at their redshift range. Certainly the way they are selected, albeit as general as possible, obey to the fact that, for observing them, a certain amount of star formation is necessary and thus probably constraining them to a subset of the total population. Although a level of star formation is expected, our conclusions should be taken carefully, as they may be only applicable to non-passive massive galaxies. Hopefully, future mass complete spectroscopic surveys will unveil

the relation between star formation rates - Hα emission - mass.

The massive galaxies in our sample show remarkably ordered (as has been seen before in star-forming less-massive 3D spectroscopy samples at high redshift) rotational velocity gradients and also high velocity dispersions. All galaxies from our sample show $V_{max}/\sigma > 1$, where this ratio in most of cases is greater than 2.4, with velocity dispersion values around $60 - 70$ kms^{-1}. This is at odds with local Universe counterparts which either display $V_{max}/\sigma < 1$ (e.g. Emsellem *et al.*, 2011) for early-type galaxies or $V_{max}/\sigma > 10 - 20$ (e.g. Dib, Bell & Burkert, 2006) in case of spirals. We agree with previous high redshift 3D spectroscopy studies –E09, Law *et al.* (2009), F-S09– such that, at high redshift, galaxy formation and evolution is a more turbulent process because of the larger amounts of cold gas involved, which at the same time leads to higher star formation rates than in the present day Universe. Major merging is indeed occurring (see for instance POWIR4 or POWIR10 galaxies). However most of the gas should be accreted either via minor merging, whose hints are found in multiple galaxies of our sample, or cold gas flows along cosmic web filaments.

The main difference between our sample and previous published datasets (such as MASSIV, LSD/AMAZE or SINS surveys) lies in its high stellar mass selection ($M_{stellar} \geq 10^{11} h_{70}^{-2} M_{\odot}$). Observationally, we notice that our sample consists of quite regular velocity fields showing high rotation. As stated in E09 when discussing their disk galaxies, this fact implies that the most massive disks seem to be stable objects even at early cosmic times. We present here the largest sample of kinematical maps for massive galaxies at high redshift. In addition, we gathered other galaxies in the literature selected by its mass without taking into account any other a priori criteria. Strikingly, the conclusions remain the same. Moreover, less-massive galaxies (Law *et al.*, 2007; Wright *et al.*, 2007; Epinat *et al.*, 2009; Förster Schreiber *et al.*, 2009, 2011a) contain a high percentage of clumpy or distorted objects. We conclude that massive galaxies acquire more rapidly a morphology and gravitational equilibrium than less-massive objects, accounting for what we call a morphological downsizing. Their high masses protect them from being perturbed and are key for understanding their eventual development, via either merging or secular evolution, whereby they progressively join the observational properties of the massive galaxies in the nearby Universe. Future NIR

high resolution photometry over larger samples of massive galaxies shall contribute to corroborate this scenario. They should be the basis of surveys taking advantage of new generation integral field spectrographs which will increase by a high factor the number of galaxies with available kinematical information.

Table 3.2: Modelled kinematical parameters of our sample

Name	Velocity dispersion km s^{-1}	Max. rotational velocity km s^{-1}	V_{max}/σ	Vel. disp. in r_e km s^{-1}	Max. rot. vel. in r_e km s^{-1}	$(V_{max}/\sigma)_e$	Inclination $^\circ$ (degrees)	Classification
(1)	(2)	(3)	(4)	(5)	(6)	(7)	(8)	(9)
POWIR1	70 ± 41	236 ± 19	3.37 ± 0.29	71 ± 40	236 ± 15	3.32 ± 0.21	80	D
POWIR2	72 ± 30	117 ± 16	1.63 ± 0.24	89 ± 7	117 ± 9	1.31 ± 0.09	64	D
POWIR3	42 ± 26	170 ± 25	3.96 ± 0.62	18 ± 29	76 ± 19	4.27 ± 1.14	65	I
POWIR4	71 ± 30	95 ± 35	1.34 ± 0.50	74 ± 22	95 ± 13	1.28 ± 0.17	60	I
POWIR5	131 ± 60	313 ± 28	2.40 ± 0.22	172 ± 66	313 ± 37	1.82 ± 0.21	48	P
POWIR6	43 ± 35	214 ± 29	4.88 ± 0.69	38 ± 32	214 ± 28	5.63 ± 0.75	57	D
POWIR7	20 ± 23	141 ± 27	6.88 ± 1.42	17 ± 22	141 ± 26	8.16 ± 1.58	63	P
POWIR8	60 ± 23	278 ± 27	4.60 ± 0.47	87 ± 18	99 ± 21	1.14 ± 0.24	61	D
POWIR10	59 ± 26	113 ± 18	1.92 ± 0.32	53 ± 22	114 ± 10	2.13 ± 0.19	60	I
POWIR11	45 ± 23	111 ± 15	2.43 ± 0.36	24 ± 22	111 ± 10	4.53 ± 0.46	31	D

Notes. (1) Name of the galaxy (2) '1/error^2'-weighted integrated velocity dispersion from the modelled velocity dispersion after removing the beam smearing (3) Maximum rotational velocity from our rotational velocity modelling (4) Maximum rotational velocity over velocity dispersion ratio (5) '1/error^2'-weighted integrated velocity dispersion from the modelled velocity dispersion within oen effective radius after removing the beam smearing (6) Maximum rotational velocity at effective radius from our rotational velocity modelling (7) Maximum rotational velocity over velocity dispersion ratio at one effective raidus (8) Inclination as measured from GALFIT analysis. Note that for POWIR4 and POWIR10 values are fixed to 60°, as we show the values for the Hα well detected objects, that in those cases are not the targeted massive galaxies (9) Final kinematical classification for our massive galaxies: D for rotating Disks, I for Interacting galaxies and P for perturbed rotators.

Table 3.3: Masses inferred for our sample & N2 calibrator

Name	Stellar mass $10^{10}h_{70}^{-2}M_\odot$	Dynamical mass $10^{10}h_{70}^{-2}M_\odot$	Mass enclosed in effective radius $10^{10}h_{70}^{-2}M_\odot$	Asymmetric drift correction $10^{10}h_{70}^{-2}M_\odot$	N2 calibrator	Notes about N2 calibrator
(1)	(2)	(3)	(4)	(5)	(6)	(7)
POWIR1	17.10	9.71	6.86	2.85	-	OH line over $[NII]6584\AA$ wavelength
POWIR2	10.45	30.57	2.97	27.60	-0.31	
POWIR3	14.34	16.60	6.94	9.66	-	OH line over $[NII]6584\AA$ wavelength
POWIR4	25.73	10.87	1.87	9.00	-0.59	
POWIR5	21.21	54.86	19.82	35.05	-0.22	
POWIR6	33.55	19.58	12.95	6.63	-0.31	OH sky line residual increases this ratio
POWIR7	22.08	3.94	3.42	0.51	-	OH line over $[NII]6584\AA$ wavelength
POWIR8	10.36	66.28	21.96	44.32	-0.60	
POWIR10	12.69	15.98	2.67	13.31	-0.33	The value for the massive galaxy is N2 = -0.15
POWIR11	12.38	8.77	2.35	6.42	-0.38	

Notes. (1) Name of the galaxy (2) Stellar mass from the parent POWIR/DEEP2 survey (3) Dynamical mass, as calculated in section 3.2 (4) Enclosed mass term, as calculated in section 3.2 (5) Assymetric drift correction, as calculated in section 3.2 (6) N2 calibrator as in Queyrel *et al.* (2009) (7) Observational notes

Table 3.4: Radii used in our calculations

Name	Model radius ”	Model radius kpc	Hα maximum radius ”	Hα maximum radius kpc	Effective radius kpc	Pixels taken	Radius taken kpc
(1)	(2)	(3)	(4)	(5)	(6)	(7)	(8)
POWIR1	0.12	1.05	0.62	5.26	3.36	3.5	3.68
POWIR2	0.12	1.05	1.10	9.27	2.59	2.5	2.63
POWIR3	0.70	5.90	1.22	10.30	3.06	2.5	2.63
POWIR4	0.12	1.05	1.05	8.83	4.18	3.5	3.69
POWIR5	0.43	3.64	1.03	8.68	3.77	3.5	3.68
POWIR6	0.16	1.35	1.44	12.10	4.81	4.5	4.74
POWIR7	0.12	1.05	0.88	7.41	3.85	3.5	3.69
POWIR8	0.88	7.43	1.44	12.17	2.58	2.5	2.63
POWIR10	0.12	1.05	1.06	8.90	2.87	2.5	2.63
POWIR11	0.12	1.05	0.97	8.19	2.83	2.5	2.63

Notes. (1) Name of the galaxy (2) Radius of our kinematical model in kpc (3) Radius of our kinematical model in arcsec (4) Hα maximum extent in kpc (5) Hα maximum extent in arcsec (6) Effective radius as calculated by the disk-like relation for massive galaxies in Table 2 of Buitrago *et al.* (2008) (7) Pixels taken as effective radius according to previous column (note that the 0.5 is added as we start from the kinematical center). (8) Equivalent in kpc of the previous column.

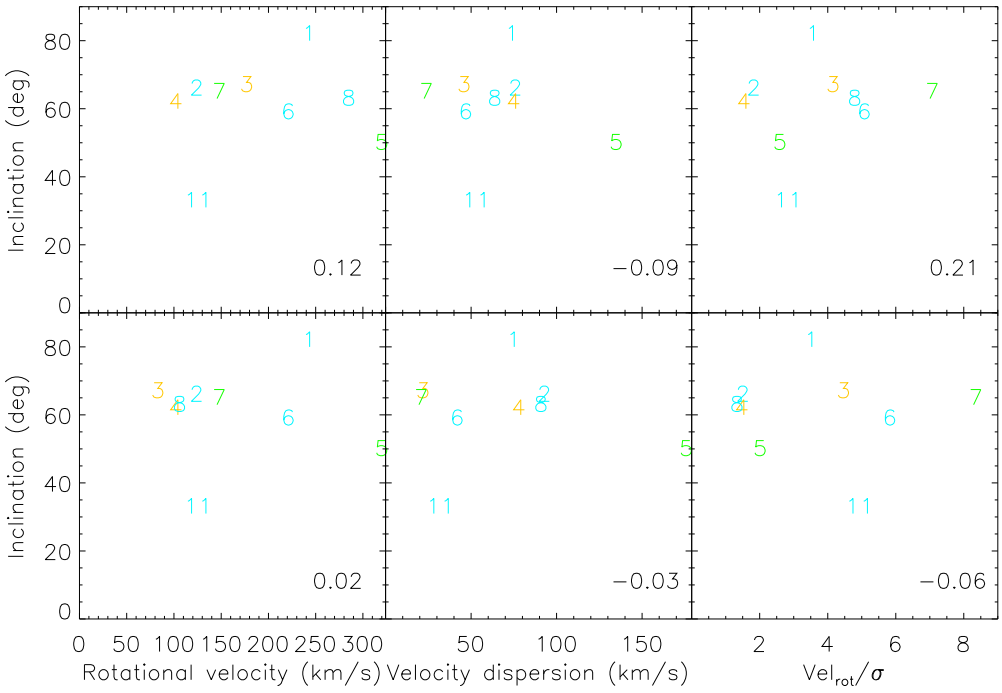

Figure 3.25: Inclination vs rotational velocity, velocity dispersion and V_{max}/σ for the maximum/integrated values for each galaxy (top row) and within their effective radii (bottom row). Galaxies are represented by their respective numbers, having the following color coding: blue for disk-like galaxies, green for perturbed rotators and yellow for interacting galaxies. Pearson correlation coefficients for each galaxy appear in the bottom right corners. In light of these plots, the fact about we do not find any correlation indicates there is no bias on obtaining the kinematical data for our sample.

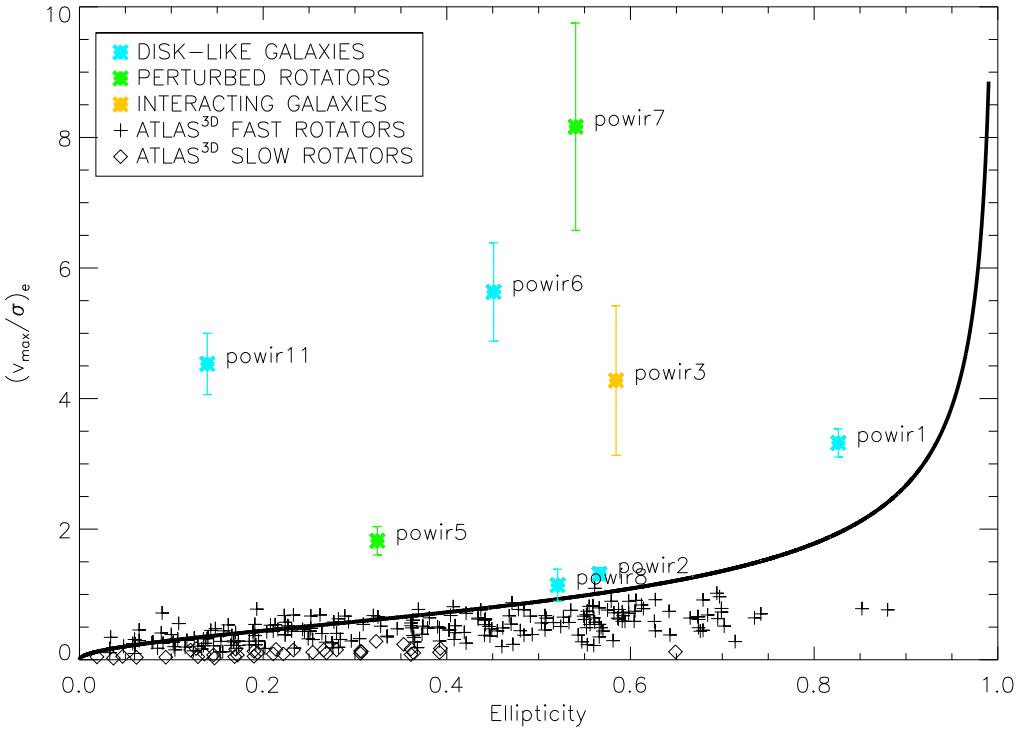

Figure 3.26: (V_{max}/σ,ε) diagram for massive ($M_{stellar} \geq 10^{11} h_{70}^{-2} M_{\odot}$) galaxies in our sample. Apart from them, we supplemented the figure with published values in Emsellem *et al.* (2011). These galaxies at low-z are early-type galaxies studied as part of the ATLAS^{3D} survey (Cappellari *et al.*, 2011). Ellipticities for our sample were measured in the K-band imaging of POWIR/DEEP2 survey using GALFIT and thus taking into account the PSF of our imaging. The continuous line defines the ideal oblate rotator with isotropic stellar velocity distribution for integral field studies (Binney, 2005; Cappellari *et al.*, 2007). Uncertainties are large but it is clear that massive galaxies at $z \geq 1.4$ depart from velocity dispersion dominated objects.

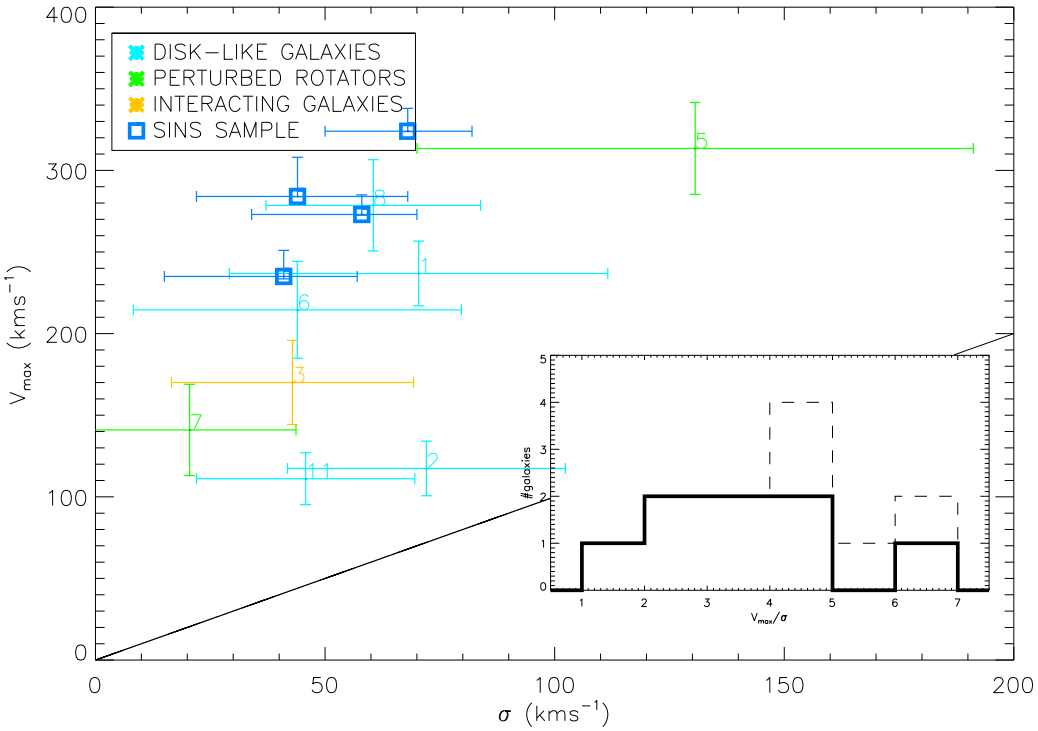

Figure 3.27: Maximum rotational velocity inferred from our modelling versus the '1/error^2' velocity dispersion after correcting it from beam smearing. Numbers depict each one of the massive galaxies from our sample, whereas the blue squares come from the SINS sample (F-S09). We also attach the histogram of the V_{max}/σ of our massive galaxies with and without F-S09 galaxies (solid or dashed histogram respectively). For all these massive galaxies $V_{max}/\sigma > 1$, as they lay above the 1:1 solid line, with most of them showing ratios even greater than 2.4 which corroborates their gravitational support. The fact that SINS objects lay in the upper part of this plot is evidence about they are purer disks than our objects. We conclude our sample constitutes a more independent and almost solely selected by mass sample.

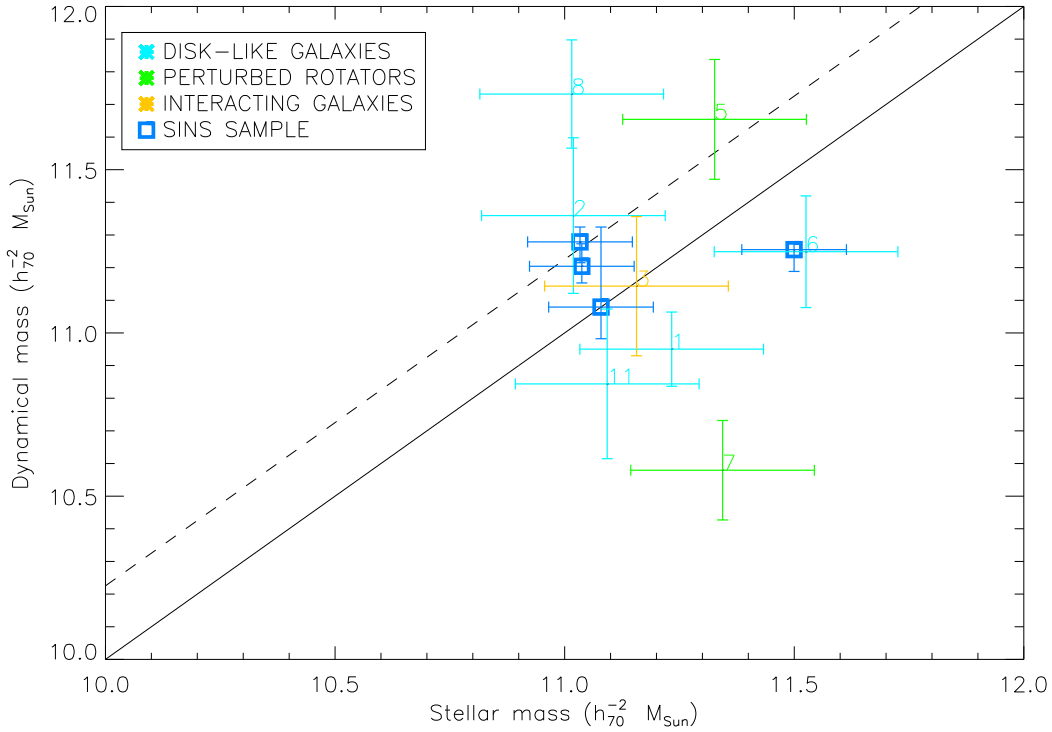

Figure 3.28: Comparison between the inferred dynamical mass and the photometric stellar mass of our galaxies. The dynamical mass was obtained using the enclosed mass estimation due to the rotational velocity and adding the contribution of the velocity dispersion using the asymmetric drift correction (Meurer *et al.*, 1996). However this is not true for the four objects corresponding to the SINS survey where the estimations are performed assuming the isotropic virial estimation (see section 9.6 in F-S09). The number of each galaxy is plotted, to better understand the properties of every galaxy. The solid line is the 1:1 relationship, while the dashed line is the local relationship for local SDSS galaxies in van de Sande *et al.* (2011). Assuming good (albeit with 0.2-0.3 dex errors) stellar mass calculations, the difference in mass may relate with the fact that what we measure is the ionized gas content in our galaxies and not the overall baryonic matter contribution.

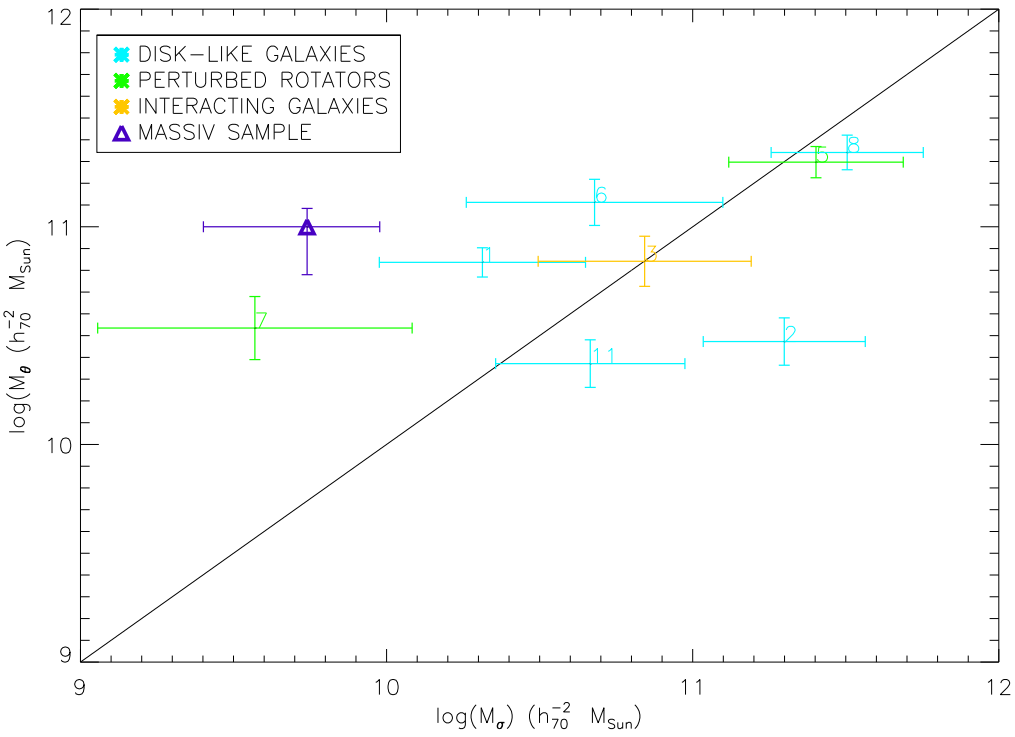

Figure 3.29: Relative importance of the two terms which contribute to the dynamical mass. The number of each galaxy is plotted, to better understand the properties of every galaxy. The solid line shows the 1:1 relation for convenience. Note that the SINS objects do not appear in this plot as their dynamical mass were calculated in a different manner than ours. We add the most massive galaxy in E09 (MASSIV sample (Contini et al. 2012); changing its masses accordingly to our Chabrier IMF). There is a mix of disky and perturbed galaxies which prevents us from splitting their populations using this plot.

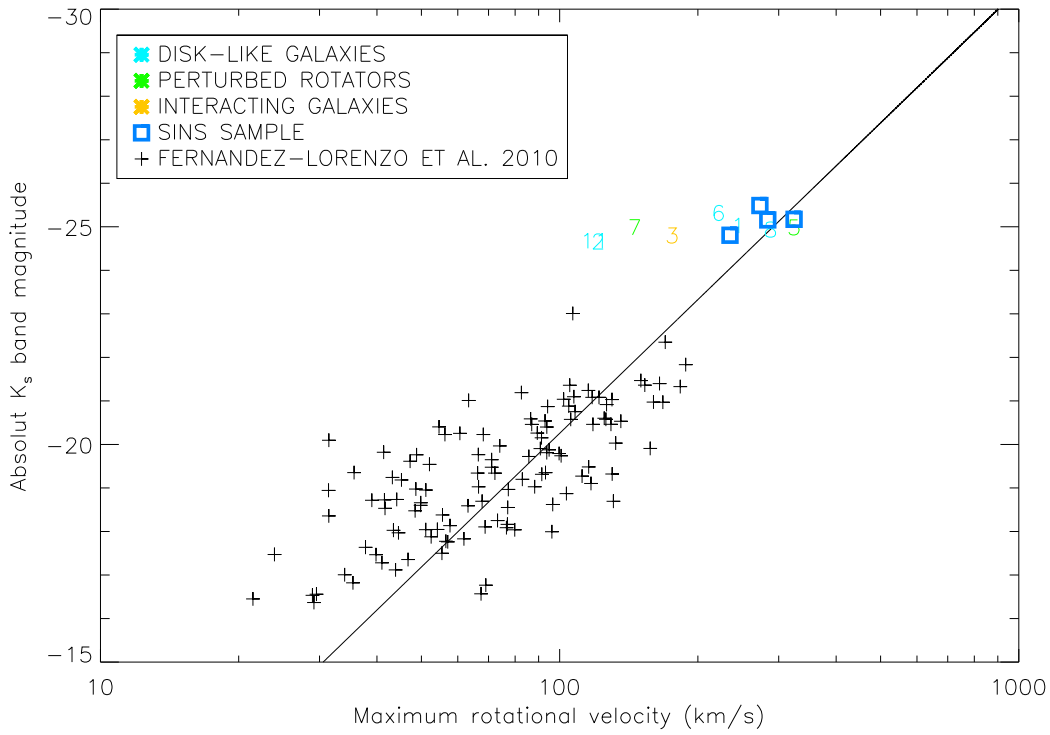

Figure 3.30: Tully-Fisher relation with K_s absolute luminosity for our massive galaxies at high redshift. The number of each galaxy is plotted, to better understand the properties of each galaxy throughout this chapter. Symbols have the same meaning as in previous plots. The solid line comes from Fernández Lorenzo *et al.* (2010), and it is the local ($z \sim 0.2 - 0.3$) Tully-Fisher relation derived for POWIR K_s band galaxies (which the small crosses). This relationship was inferred by weighting the importance of every point by its errors. Galaxies displaying the lowest rotational velocity values are the ones that depart more from the local relation.

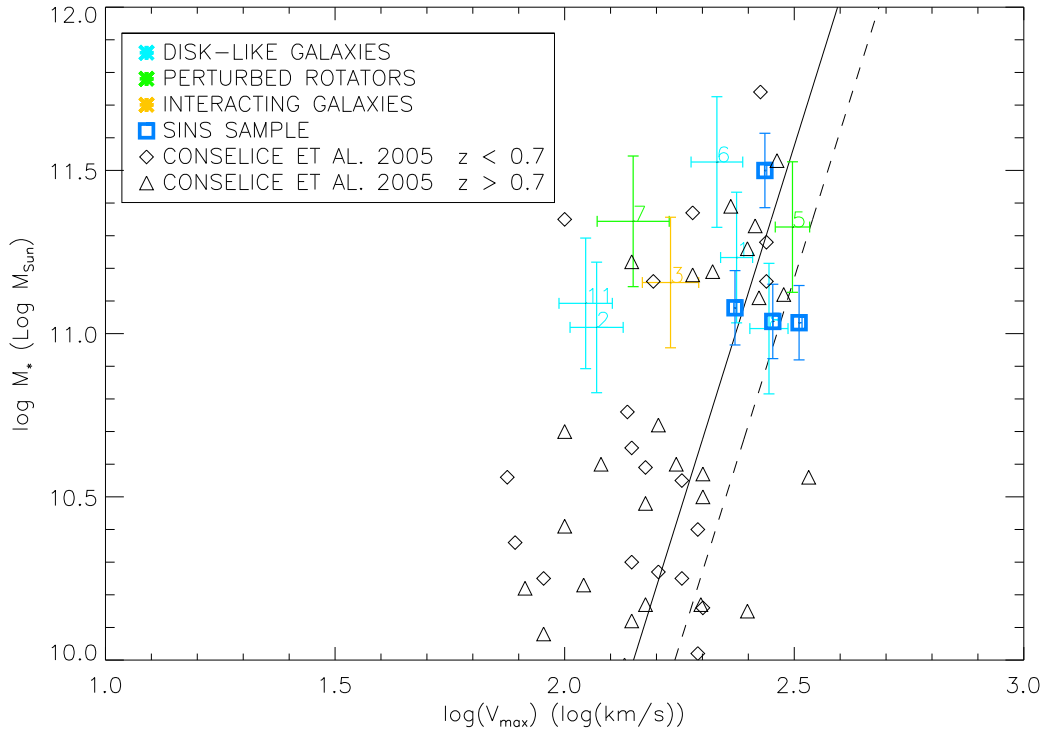

Figure 3.31: Baryonic or stellar mass Tully-Fisher relation for our massive galaxies at high redshift. The number of each galaxy is plotted, to better understand the properties of each galaxy throughout the paper. The solid line is the local relationship from Bell & de Jong (2001) and the dashed line is the $z = 2.2$ Tully-Fisher relationship derived in Cresci *et al.* (2009) for SINS galaxies. We also add it with the disk galaxies from Conselice *et al.* (2005), separating their sample between $z \leq 0.7$ and $z > 0.7$ to better comprehend any possible redshift evolution.

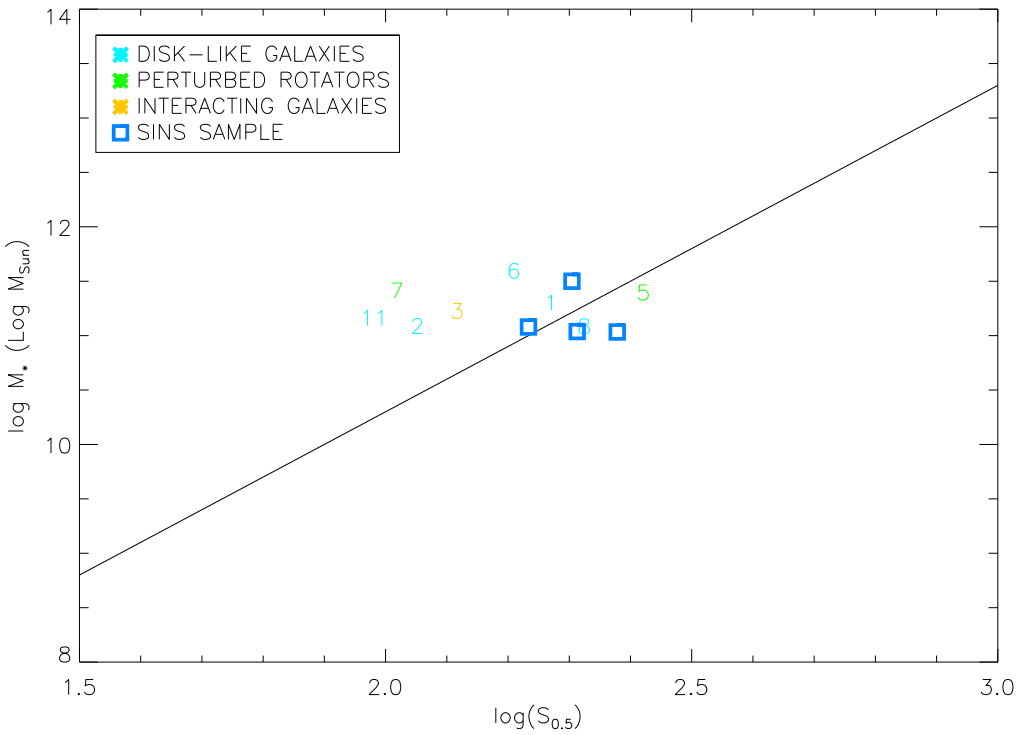

Figure 3.32: Kassin *et al.* (2007) Tully-Fisher relation. On that work, the authors develop the $S_{0.5}$ parameter, which is $S_{0.5} = \sqrt{(0.5 * (v_{max}^2)) + \sigma^2}$. They argue this accounts for the non ordered motions of the gas and also the scatter of its Tully-Fisher relation is smaller. The solid line represents the relation they found in their closest redshift bin to our data ($0.925 < z < 1.2$). Each massive galaxy symbol is its number in our sample, to better understand their properties throughout the plots. The scatter in our galaxies is still large, showing that the objects further away from the Kassin relationship cannot be solely describe as disk-like galaxies.

Antes programar era un arte, ahora es todo marketing.

(Before programming was art, now is just marketing.)

Paco Menéndez, speaking about 'The Abbey of Crime'

Es que no hay nada mejor que imaginar,

la Física es un placer.

Y es que no hay nada mejor que formular,

escuchar y oír a la vez.

Espacio y tiempo juegan al ajedrez.

(There is nothing better than imaging,

Physics is a pleasure.

And there is nothing better than formulating,

hearing and listen at the same time.

Space and time are playing chess together.)

Nacha Pop – 'Una décima de segundo'

Chapter 4

Full GNS structural parameter determination and the size-mass relationship extended at all masses

4.1 Introduction

In the local Universe there is a strong correlation between galaxy mass and size, with the most massive galaxies displaying larger sizes (see e.g. Shen *et al.*, 2003). Multiple studies in the recent years (Daddi *et al.*, 2005; Trujillo *et al.*, 2006b, 2007; Cimatti *et al.*, 2008; Buitrago *et al.*, 2008; van Dokkum *et al.*, 2008; Damjanov *et al.*, 2009, among many others) find the fact that massive galaxies ($M_{stellar} \geq 10^{11} h_{70}^{-2} M_{\odot}$) at high-z ($2 \leq z \leq 3$) are on average remarkably smaller (a factor of 4-5 for spheroids, and a factor of $\sim$3 for disks) than their local counterparts. The origin of this apparent evolution in size for this galaxy population is not clear, but it is not completely unexpected, as this resembles a formation through gas-rich and dissipative mergers (e.g. Wuyts *et al.*, 2010). K-correction effects and cosmological dimming hamper the detection of low surface brightness features that ultimately could alter the estimation of the sizes of high-z objects (Valentinuzzi *et al.*, 2010a,b; Mancini *et al.*, 2010) although many observational tests have been conducted in order to assess their reliability (Trujillo *et al.*, 2006b; Muzzin *et al.*, 2009; van Dokkum *et al.*, 2010).

However, there is a significant lack of studies which specifically explore whether this strong evolution in the mass-size relationship holds for less massive galaxies. Massive galaxies, although scarce, are often very luminous objects, which helps in their detection at high redshift. This is not true when working with lower mass objects. Very deep and high resolution surveys in the NIR wavelength range are thus necessary to characterize them, allowing comparisons with the local Universe. The GOODS NICMOS Survey is the perfect tool to address all these questions, because of its extraordinary depth – ~ 2 magnitudes deeper than any ground-based observations (Retzlaff *et al.*, 2010; Conselice *et al.*, 2011a) – and good resolution (~ 0.3 PSF FWHM).

Another very interesting question regarding galaxy sizes and structural parameters' determination for massive galaxies is the evidence of similar sizes both at the UV and optical restframe. Trujillo *et al.* (2007) studied 24 galaxies at $0.2 < z < 2$ in the Extended Groth Strip observed in both the HST ACS i-band and in the HST NICMOS H-band finding no systematic biases between these two bands. Buitrago *et al.* (2008) worked with GOODS imaging for all (80) their massive galaxies at $1.7 < z < 3$ both in ACS (Giavalisco *et al.*, 2004) and NICMOS (Conselice *et al.*, 2011a). In this case, 49 objects were not detected because of dust obscuration (Bauer *et al.*, 2011). For the remaining objects a good correlation was found between the sizes measured in both bands, with a small possible bias towards smaller sizes (4$\pm$6%) in the H-band compared to the $z-$band measurements.

More recently, HST WFC3 confirmed these results in the HUDF. Cassata *et al.* (2010) selected 6 massive and passive galaxies at $1.3 < z < 2.4$. These galaxies have a very weak morphological K-correction between a variety of bands (z in ACS; Y, J and H in WFC3). This was later confirmed in Cassata *et al.* (2011), with a larger sample of 563 massive ($M_* \geq 10^{10} M_\odot$ in this case), passive (SSFR $< 10^{-2}$ Gyr^{-1}) and morphologically selected spheroidal galaxies at $0 < z < 2.5$. Summarizing, all these probes point towards a tentative conclusion, which is that one could have a good idea of massive galaxy structural parameters using the UV restframe. This idea is attractive for us because we stopped analysing the sizes of massive galaxies at redshift $z = 3$ in our previous work Buitrago *et al.* (2008). We did this as we wanted to always utilise V-band restframe imaging to provide a direct comparison with the local

Universe measurements. Secondly, we were aware that at $z > 3$ the contribution of the cosmological $(1+z)^4$ dimming is very important. Despite this, we are encouraged to make one step further having all the previous caveats in mind, looking at the sizes in the UV restframe of $z > 3$ massive galaxies using NIR deep observations.

This chapter is based in the GNS parametric analysis of the full GOODS NICMOS Survey, linking the observational properties of $M_* > 10^{10} - 10^{11} M_\odot$ galaxies and the less massive population at high-z. Note as well that the photometry used in this chapter differs from Chapter 1, as we are using now photometric masses and redshifts derived for the whole GNS sample, and not the subset of massive objects detections in which the survey was based. All the details for these two determinations can be found in Conselice *et al.* (2011a), and their respective catalogs can be downloaded from the GNS webpage

$http://www.nottingham.ac.uk/astronomy/gns/$

The structure of this chapter is as follows: Section 4.2 describes our data, the GOODS NICMOS Survey (GNS), and Section 4.3 deals with their analysis and which galaxies enter in the final study. Section 4.4 presents our results. In Section 4.5 we explain our conclusions. On what follows, we adopt a cosmology with Ω_m=0.3, Ω_Λ=0.7 and H_0=70 kms^{-1} Mpc^{-1}.

4.2 The GOODS NICMOS Survey description

Our sample of galaxies originates from the Great Observatories Origins Deep Survey (GOODS) North and South fields (Dickinson, Giavalisco & GOODS Team, 2003) and are imaged as part of the GOODS NICMOS Survey (GNS; PI C. Conselice). The GNS is a large HST NICMOS-3 camera program of 60 pointings centered around massive galaxies at $z = 1.7 - 3$ at 3 orbits depth, for a total of 180 orbits in the F160W (H) band covering 43.7 arcmin^2 (roughly one sixth of the GOODS fields). Each tile ($51.2" \times 51.2"$, $0.203"$/pix) was observed in six exposures that were combined to produce images with a pixel scale of $0.1"$, and a PSF of $\sim 0.3"$ FWHM. The details of the data reduction procedure are discussed in Magee, Bouwens & Illingworth (2007). We optimize our pointings to obtain as many high-mass $M_* > 10^{11}$ $M_\odot$ galaxies as possi-

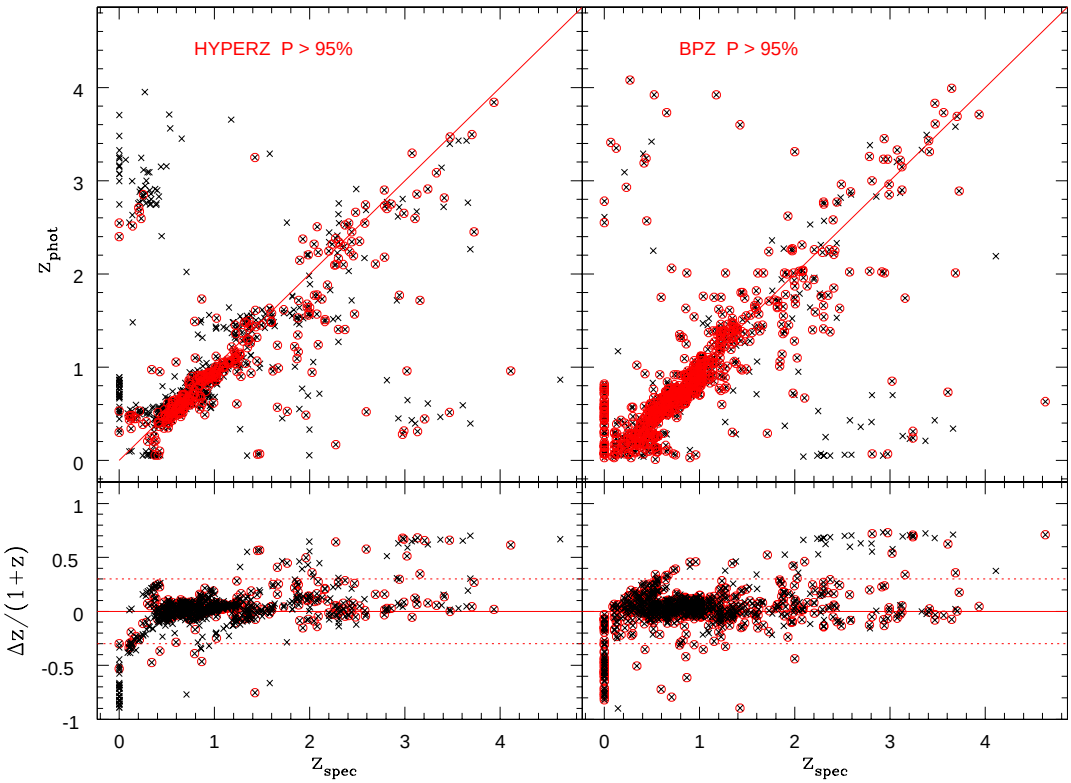

Figure 4.1: Comparison between our photometric and spectroscopic redshifts (for a total 16% of our sample). Apart from our HYPERZ derived redshifts, we checked our measurements using the Bayesian-approach code BPZ (Benítez, 2000). The former one was chosen due to its slightly better treatment of outliers on setting low probabilities for their redshifts. Black crosses stand for all redshifts, while red circled points denote high probability redshifts (P $>$ 95 %). The dashed lines show our limit for catastrophic outliers: $|\Delta z/(1+z)| > 0.3$. Image taken from (Grützbauch *et al.*, 2011a).

ble, with the selection of these targets described in Conselice *et al.* (2011a). Limiting magnitude reached is $H \sim 26.8(5\sigma)$.

A total of 8298 objects were detected within GNS imaging running SExtractor, using a 2σ detection threshold above the background noise and a minimum of 3 adjacent pixels with values above this threshold. We then constructed a master catalog gathering B, V, i and z ACSv2.0 data products for them. GOODS ACS survey (Giavalisco *et al.*, 2004) probes sources down to a 5σ limiting AB magnitude of $z \sim 27.5$. We found a systematic offset of 0.3" between our NICMOS astrometry and ACS one. Then masses and photometric redshift were computed with this set of BVizH filters. We restricted ourselves to this 5 bands in order to obtain the highest fidelity photometry and not to be affected by zero-point random or systematic errors, or background noise and confusion if utilising Spitzer ancillary data.

Photometric redshifts were derived using a χ^2 minimization procedure with the program HYPERZ (Bolzonella, Miralles & Pelló, 2000). Details can be found in Conselice *et al.* (2011a); Grützbauch *et al.* (2011a). In brief, synthetic spectra were constructed with the Bruzual & Charlot (2003) evolutionary code. Five templates were used, corresponding to the spectral types E, Sa, Sc and Im, plus a single starburst model. The reddening law comes from Calzetti *et al.* (2000). Due to the premium coverage of the GOODS fields, several spectroscopic releases were available: the FIREWORKS compilation in the GOODS-S field (Wuyts *et al.*, 2008) and Barger, Cowie & Wang (2008) in GOODS-N. Photometric redshifts are in good agreement with the available spectroscopic ones, for a total of 906 galaxies with both. Defining $\Delta z/(1+z) \equiv (z_{spec} - z_{phot})/(1+z_{spec})$, sources in the GOODS-N field have an $\langle \Delta z/(1+z) \rangle = 0.027$, with a scatter of $\sigma = 0.04$ (222 out of 537 galaxies with $P > 95$ percent). Sources in the GOODS-S field show similar values: $\langle \Delta z/(1+z) \rangle = 0.043$ and $\sigma = 0.04$ (134 of 369 with $P > 95$ percent). A visual comparison between the photometric and spectroscopic redshifts can be found in Figure 4.1 – taken from (Grützbauch *et al.*, 2011a) –.

Stellar masses were inferred with a method which consists of fitting a grid of model SEDs constructed from (Bruzual & Charlot, 2003) stellar population synthesis models, with a variety of star formation histories. We use an exponentially declining model to characterise the star formation history, with various ages, metallicities, and dust contents used for different models. A Salpeter IMF (Salpeter, 1955) was utilised on this process. Typical errors are 0.2-0.3 dex. To test this on our galaxy sample, we utilised the newer Bruzual and Charlot (2011, in prep) models, finding that on average that stellar masses were smaller by < 0.07 dex. As this number is much smaller than our typical uncertainties we conclude that it has not a significant impact in our sample.

The photometric redshift and masses we present here differ from the ones in the Chapter 2 (on the morphologies of massive galaxies). There we utilised the detections from previous photometric studies (see Buitrago *et al.*, 2008; Conselice *et al.*, 2011a, for the full description). Not all the galaxies previously considered as massive retain with the new photometry their status. For the coincident 68 objects, we show in Figures 4.2 and 4.3 a comparison of their properties. Redshifts are compatible with similar results

(a measured offset of $5 \pm 18\%$ towards larger values using the previous photometry) although masses do not agree that well ($32 \pm 71\%$, again larger for the old values). The difference in mass is due to the different set of filters used, as galaxies with similar redshifts in the old and new photometry display similar scatter and mean in the mass determination.

4.3 Structural parameter determination and object selection

We examine the light profiles of the galaxies within our sample with a single Sérsic model (Sérsic, 1968) to compare our size estimations with previous works. We utilised SExtractor (Bertin & Arnouts, 1996) and GALFIT (Peng *et al.*, 2002, 2010). All the procedure is detailed in Chapter 2 Section 2.2.1. Our measured sizes are circularized, $r_e = a_e\sqrt{1-\epsilon}$, with ϵ the projected ellipticity of the galaxy. This factor $1-\epsilon$ is the axis ratio of the fit.

An important point in our study is the characterization of the NICMOS3 PSF. Due to the point-to-point variation of the shape of the PSF in our images we select five (non-saturated) bright stars to gauge the accuracy of our parameter estimations. The final effective radii (as well as the rest of the structural parameters) are the 5σ outlier-resistant mean of these five independent runs (one per each star used as PSF) per object. We conducted exhaustive simulations on the recovery of the structural parameters within our imaging. They are described in the Appendix A. Our program was executed for the whole sample of 8298 galaxies. 1371 of them fell in the GALFIT constrains we imposed, namely effective radius values between 0.1 and 20 kpc and Sérsic indices between 0.1 and 9.9. The main reason for the non-realistic values in their fit is their faintness (being their median magnitude $H_{AB} = 25.1$). For 1010 galaxies our mass determination failed, and they were excluded from subsequent analysis. Our algorithms could not provide a mass for these objects as they were detected only in the H-band imaging. We also rejected galaxies with stellar masses smaller than $10^6 M_\odot$ (another 113). Moreover, we visually inspected all the galaxies in the sample, and discarded objects whose fit were not meaningful. 91 detections were associated with stars or stellar

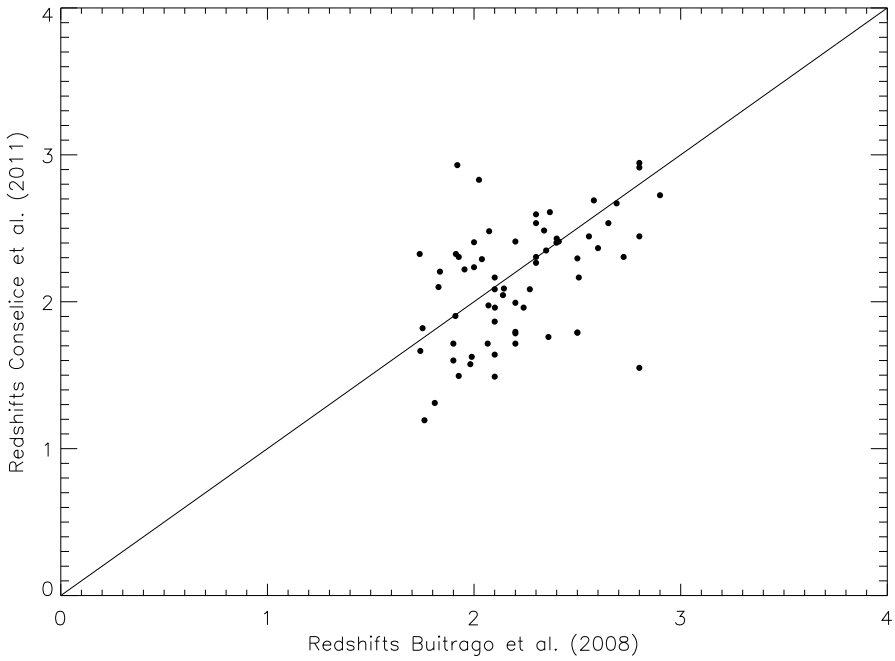

Figure 4.2: Comparison between the redshifts used in Buitrago *et al.* (2008) (the ones in Chapter 2) and the ones derived in the total GNS sample – see Conselice *et al.* (2011a) –. The solid line is the 1:1 reference. Spectroscopic redshifts where in used in both samples when available.

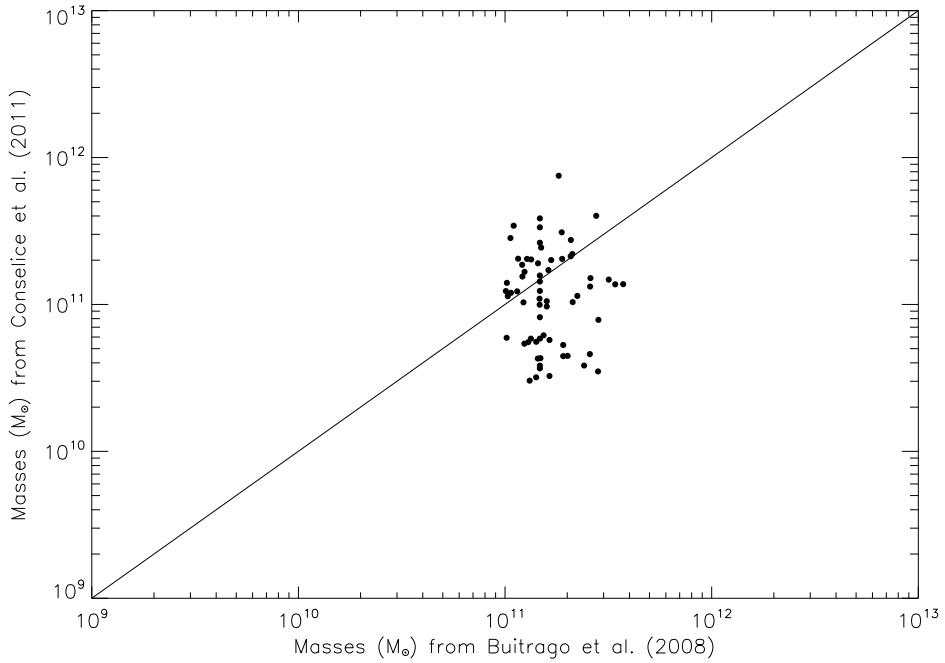

Figure 4.3: Comparison between the masses used in Buitrago *et al.* (2008) (the ones in Chapter 2) and the ones derived in the total GNS sample – see Conselice *et al.* (2011a) –. The solid line is the 1:1 reference. Masses computed with spectroscopic redshifts where in used in both samples when available.

spikes that do not enter in our analysis. 185 galaxies lay too close the pointing borders and thus they were strongly affected by drizzling defects, being not considered as well. Finally, galaxies with known defects in their photometric data or their images were removed, as galaxies close to stars or with non-sense values in their detection catalogs (47 more). In total, our size analysis encompasses 5481 galaxies, which are more than two thirds of the GNS sample. Out of these, 866 posses spectroscopic redshifts and masses (16%). Summarizing, our sample was carefully selected, accounting for every bias we could think of.

4.4 Results

4.4.1 Mass-size relationship at $0 < z < 5$ in the H-band

We present the mass-size relationship for disk-like galaxies ($n < 2.5$; Figure 4.5 and Table 4.1) and spheroid-like galaxies ($n > 2.5$; Figure 4.6 and Table 4.2) as done in Shen *et al.* (2003). In that article, the authors analysed the size distribution of galaxies, both in luminosity and mass, splitting their sample according to the Sérsic index in order to have a crude automatic estimation which can be linked with the visual morphology (Ravindranath *et al.*, 2004, and see also the Chapter 2). Our figures are divided in 8 redshift bins, covering intervals of 0.5 in redshift each one, but the last two ($3 < z < 4, 4 < z < 5$). Blue points are the means (obtained with a 5σ outlier-resistant determination) for the following mass intervals: $10^8 M_\odot < M_* < 10^9 M_\odot$, $10^9 M_\odot < M_* < 10^{10} M_\odot$, $10^{10} M_\odot < M_* < 10^{11} M_\odot$ and $> 10^{11} M_\odot$. Mass intervals with less than three objects are not considered due to the intrinsic statistical uncertainties. Error bars represent the standard deviation of the means.

The solid lines are the SDSS local size-mass relations (Shen *et al.*, 2003) corrected to match our Salpeter IMF. This was done by multiplying by a factor of 1.7 (0.23 dex), as they used a Chabrier (2003) IMF. We note that Shen *et al.* (2003) relationships are built using only the most massive galaxies, especially for spheroid-like objects, and hence they do not cover the entire range of masses studied in this work; their mass ranges are 8×10^9 – $1 \times 10^{12} M_\odot$ for spheroid-like objects and 5×10^8 – $1 \times 10^{12} M_\odot$

for disk-like objects. To quantify the observed size evolution, we calculate the ratio between the sizes we measure, and the measured sizes of nearby galaxies at the same mass, by using the SDSS results (Shen *et al.*, 2003). Local radii come from the r'-band, which is nearly equivalent to the V-band rest-frame at $z \sim 0.1$, the mean redshift of the galaxies in SDSS. As such, this is better suited to match the restframe light of galaxies at $1.5 < z < 3$.

Both disk-like and spheroid-like objects show smaller radii at higher z. This trend is easier to see for the disks. We attribute this to the fact that our statistics are better constrained for low Sérsic index objects, as disk-like are more numerous than spheroid-like galaxies (1614 vs 3885 objects). Another effect which of course plays a major role is the K-correction. Whereas in the first redshift bin we are looking at the NIR resftrame, we are in the UV regime for the last one, as the central wavelength in the H-band (1600 nm) corresponds to 1600 nm/(1+z) restframe wavelength at every redshift. Lastly, cosmological $(1+z)^4$ dimming is hampering our detections largely at the highest redshifts. This has been quantified in Conselice *et al.* (2011a); Mortlock *et al.* (2011). In Figure 1 of Mortlock *et al.* (2011) (reproduced in this chapter as Figure 4.4), the magenta lines show the theoretical detection limits of the NICMOS3 camera, calculated for the mass-to-light ratios of a maximally old stellar populations and combining it with the limiting magnitude of the survey and the luminosity distance for each redshift bin. Nevertheless, looking at the same plot it would be more accurate to take the first value (the higher in mass) of the red points, which are the data affected by incompleteness. These incompleteness limits are then $10^{8.5} M_{\odot}$ at $1 < z < 1.5$, $10^{9} M_{\odot}$ at $1.5 < z < 2.5$ and $10^{9.5} M_{\odot}$ at $2.5 < z < 3.5$. Finally, there is a steady drop in the number densities of massive galaxies at high-z (Conselice *et al.*, 2007; Pérez-González *et al.*, 2008a; Conselice *et al.*, 2011a). As a result, for $z > 3$ the mix between incompleteness and decreasing number densities produce smaller number statistics in our study.

We attempted a number of different approaches to clarify the mass-size relations for the different objects that compose our sample. Figures 4.7 and 4.8 show the evolution of the mean radius of galaxies within the same mass range versus redshift. Note that for spheroid-like objects only $M_{*} > 10^{10} M_{\odot}$ objects are displayed, to be consistent with

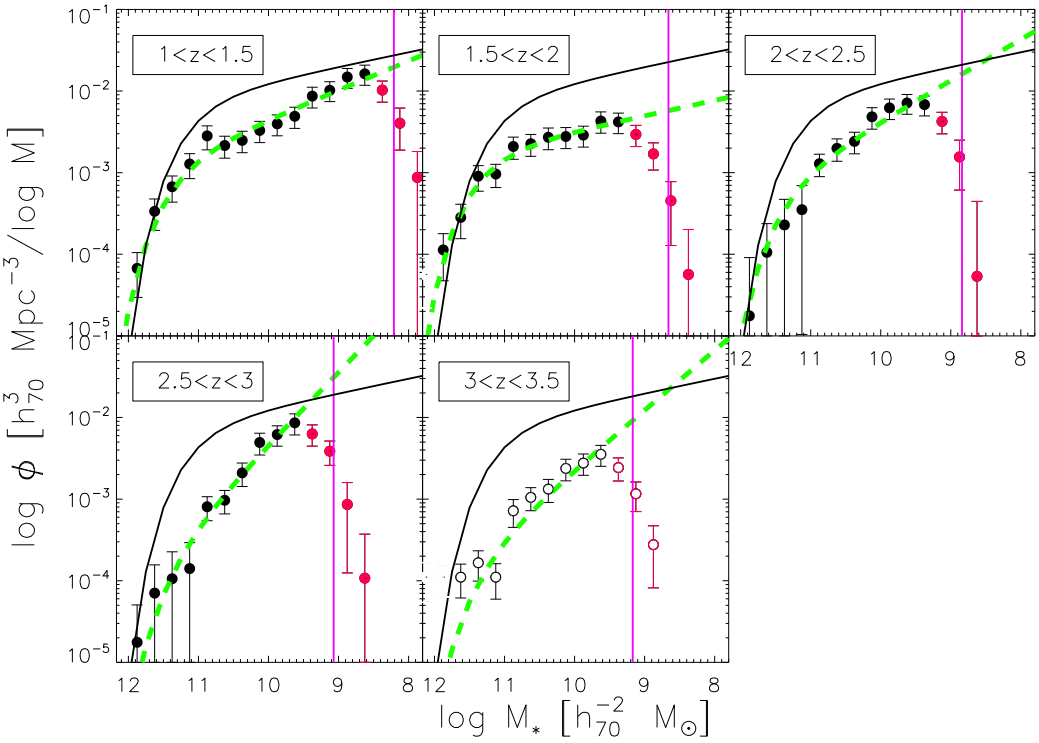

Figure 4.4: Mass functions of the GNS with increments of 0.5 in redshift between consecutively bins from $z = 1$ to $z = 3.5$. Black points are the data which has been fitted with a Press-Schechter function (Press & Schechter, 1974) that it is depicted by the green dashed line. Last redshift bin points are open circles because they were not included in the analysis of the parent paper Mortlock *et al.* (2011). Vertical pink lines represent the theoretical mass limits of the GNS survey and the red points are the ones affected by incompleteness. The solid black curve is the fiducial local mass function in Cole *et al.* (2001). Image taken from (Mortlock *et al.*, 2011).

the Shen *et al.* (2003) local study. We did not display the first redshift bin results as the volume probed by the GNS at these redshifts is too small to have accurate statistical interpretations. Our results are in agreement with similar mass-size relations found in the local Universe, where more massive objects have larger sizes. This is somewhat less clear at $z > 3$, where galaxies display similar sizes almost independently of their masses, although we would need a larger number of galaxies and more careful inspection of every object to confirm this. In relation with the more massive ($M_* \geq 10^{11} M_\odot$) galaxies, while at low redshift they fit with the previous description, they drastically change at $z > 1.5$, displaying average radii smaller than lower mass objects. This agrees well with the results of Trujillo *et al.* (2007); Buitrago *et al.* (2008) (dashed lines), although we notice a small shift for disk-like objects due to the low number statistics.

Relative changes in size in comparison with the SDSS sample at all the masses are

shown in Figures 4.9 and 4.10. It seems that, at least for disk-like galaxies, there is a general trend towards smaller radii at high redshift (again, we always bear in mind the caveats in our interpretation, but this decrease is noticeable at even low redshifts). However, massive galaxies are systematically shifted to lower relative size values, as it has been reported many times for the massive galaxy population (e.g. Trujillo *et al.*, 2006b, 2007; Buitrago *et al.*, 2008).

Indeed our statistics are better constrained for those redshifts where the number of objects is larger. Although this number of objects is written in Tables 4.1 and 4.2, we show it graphically in the montage of the Figure 4.11. As expected, intermediate mass objects ($10^9 M_\odot < M_* < 10^{11} M_\odot$) at $0.5 < z < 1.5$ are the most numerous objects in the GNS survey. We must also stress that GNS was specifically designed to probe the high mass end of the galaxy mass function at $z > 1.5$, having a total overdensity of 3.05 (Conselice *et al.*, 2011a) of these galaxies than a blank field survey. This feature helps overcome the problem of their scarcity, allowing us to obtain meaningful results for this mass range ($M_* \geq 10^{11} M_\odot$) as well as the others.

In both Table 4.1 ant Table 4.2 there is an extra column with the comparison with previous photometrical masses and redshifts used for studying the massive galaxy population at $1.7 < z < 3$ in our previous article Buitrago *et al.* (2008). As stated in the introduction of this chapter, we are dealing with newly photometric values derived not only for the massive galaxies but for all the galaxies within our imaging. We chose to work with them for the sake of consistency, as we wanted the photometry to be the same throughout the sample to allow comparisons between the various mass and redshift bins. The impact of this fact in the sample consists of the reduction in the number of objects which fulfill the condition of massive ($M_* \geq 10^{11} M_\odot$) in the previously mentioned redshift range. The final column in the tables – called $M_* \geq 10^{11} M_\odot (B08)$ – shows how our new results compare with the old ones. Note also that the Sersic index separation value between disk-like and spheroid-like galaxies were 2 instead of 2.5 in Buitrago *et al.* (2008). Nevertheless, looking at the same time to all the results for massive galaxies we see the same statistical trends for the previous and the new photometric values within the error bars. We noticed the sizes for disk-like galaxies are on average 28% larger with the previous results. This is probably due to the fact

that the new photometry retrieves less massive galaxies and thus our statistics are less constrained for these objects. The difference between the published values in Table 1 of Buitrago *et al.* (2008) and in the tables of this chapter for the old photometry are based on the fact that here we show the mean values of the effective radii, whereas in the article the chosen statistical value was the median. It is noteworthy that the previous photometry was chosen up to $z = 3$, and as a result there are no complementary values for the photometric masses and redshifts for galaxies beyond that limit.

4.4.2 Comparison with other mass-size relationships in the literature

This is the first attempt, to the best of our knowledge, whereby the size-mass relationship has been analyzed for the full range of masses of the galaxies within a survey. Conclusions must be drawn with caution, as our sample is not complete at all masses and redshifts, and also cosmological variance effects are not fully understood due to the patchy nature of GNS.

However, for massive galaxies, there are a number of examples in the literature. These works differ on the various criteria they used on splitting galaxy types, and thus helping claiming justifications for their compactness at high-z. Here we will cite some of the most relevant works.

Saracco, Longhetti & Andreon (2009) investigated 32 morphologically classified early-type galaxies at $1 < z < 2$ observed with the HST NICMOS3 camera in the H-band. They divided their sample between young and old ETGs (mean difference in age $\sim 1.5 - 2$ Gyr). All the compact objects were members of the old population. Newer analyses utilizing the same criteria failed to obtain similar results, and using larger samples of massive galaxies (Trujillo, Ferreras & de La Rosa, 2011, McLure *et al.* 2012 in preparation).

Williams *et al.* (2010) studied the size evolution for ∼30000 massive (in this case $M_* \geq 6 \times 10^{10} M_\odot$) galaxies, splitting them according to their colors and their passive/star forming nature. The latter method was the most successful one, and the threshold value they chose was SSFR = $0.3/t_H$, where t_H is the age of the Universe at

a given redshift. SSFR, i.e., the star formation efficiency seems to be a very promising mechanism to shed light into this problem. Nevertheless, largest changes are always related with mass. The less massive galaxies in their sample (between $M_* \geq 6\times10^{10}M_\odot$ $M_* \geq 6 \times 10^{10}M_\odot$) have milder evolution in size that the $> 10^{11}M_\odot$ galaxies. They parametrized it by $r_e \propto (1+z)^a$, $a \sim -0.7$ for the former, $a \sim -1.3$ for the latter; while Buitrago *et al.* (2008) reports -0.82 for massive disk-like galaxies and -1.48 for massive spheroid-like galaxies.

Finally, some authors tried to link the size-mass relationship with the environmental influence (Gutiérrez *et al.*, 2004; Maltby *et al.*, 2010; Valentinuzzi *et al.*, 2010a,b). There are tantalizing hint about low-mass disks suffering from a slight decrease in their sizes in denser environments, although it is not clear the role the environment play in this context. This is especially the case for high-z observations, where no relation has been found between sizes and local densities of neighbouring galaxies (Grützbauch *et al.*, 2011a).

Future exploration of the parameter space defined by mass - size - SSFR - Sérsic index happens to be key to understand the mass-size relationship and its departures for specific kinds of galaxies. Moreover, it offers an alternative way to constrain at which point the star formation quenching of massive galaxies takes place. The problem for these studies to be achieved is based on the fact that high-z low-mass and complete samples of galaxies with reliable star SFRs are challenging as they require very deep observations with high-quality ancillary data. Steps are being taken in this direction, with ongoing wide ($> 1\ deg^2$) and deep NIR surveys as UltraVISTA (McCracken *et al.* 2012 in preparation, Buitrago *et al.* 2012 in preparation).

4.4.3 Massive galaxies at $z > 3$

To explore the sizes of massive galaxies at $z > 3$ is extremely challenging. Interestingly, the actual time to build up any high mass system was very limited, as the age of the Universe was less than 2 Gyr. In total, according to our detection criteria and our photometrical estimations, we detect 11 massive galaxies ($M_* \geq 10^{11}M_\odot$) at $z > 3$. Eight ($73 \pm 24\%$) are disk-like ($n < 2.5$) and 3 ($27 \pm 16\%$) are spheroid-like ($n > 2.5$) galaxies. These percentages fit remarkably well on the fraction of massive galaxies at

$z > 2$ segregated depending on their Sérsic indices (see Chapter 2 Figure 3). Their size-mass relationship in comparison with the Shen *et al.* (2003) local sample can be found in images 4.12 (disks) and 4.13 (spheroids).

We also tried to assign a visual morphology to them (knowing the difficulties this task entails) in the UV restframe. Five ($45 \pm 20\%$) are classified as irregular/peculiar galaxies (out of which 4 were are also consistent visually with a disky nature rather than a spheroid), 4 ($36 \pm 18\%$) as disks without disturbances and there are 2 ($18 \pm 13\%$) spheroidal galaxies. These results are in agreement with what was previously reported in Chapter 2.

Little work has been devoted to investigate galaxies as the ones in this section in the literature. Wiklind *et al.* (2008) studied 11 candidates for massive ($0.5\text{-}5 \times 10^{11} M_{\odot}$) galaxies at $4.9 < z < 6.5$ (with one redshift confirmed spectroscopically). Remarkably, these galaxies were already old, having stellar population ages between 0.2 and 1.0 Gyr. Their half light radii were always smaller than 2 kpc and 7 of them had Spitzer MIPS detections at $24 \mu m$. Recently, (Willott *et al.*, 2012) focused on Lyman Break Galaxies (with smaller masses, $\sim 10^{10} M_{\odot}$) at $z \sim 6$ discovering that 20 galaxies on their sample were partially resolved in their ground-based data. According to their renditions this fact implies we are witnessing a merging phase in these very high redshift objects. Interestingly, the only galaxy in their sample with CANDELS/WFC3 observations had an effective radius is 0.49 kpc in the H-band. For the 6 galaxies with imaging in the ACS I-band filter they could tell a multiple component nature.

4.5 Summary & Conclusions

We performed a quantitative structural parameters' determination for the total GOODS NICMOS Survey galaxy sample. The total number of galaxies that were analysed fitting Sérsic surface brightness profiles was 8298. A careful by-eye selection and an automatic process to reject bad photometric data detections (by which we eliminated one third of the objects) was carried out in order to asses the reliability of our sample.

We constructed a size-mass relation for $M_* > 10^8 M_{\odot}$ galaxies at $0 < z < 5$, both for disk-like ($n < 2.5$) and spheroid-like ($n > 2.5$) objects. Sizes are parametrized

as circularized effective radii. We find that more massive galaxies have larger sizes independent of redshift, and there is also a general decrement of sizes with redshift. Most massive ($M_* \geq 10^{11} M_\odot$) galaxies are the largest at the lowest redshifts but then they are quickly shifted towards much smaller sizes. The evolution of lower mass objects is not so pronounced. We note, however, that our method suffers from several limitations. In the first place, there are severe K-corretion effects among our different redshift bins as we are restricted ourselves to H-band imaging. Secondly, it is also very significant the impact of the cosmological dimming at the highest redshifts ($z > 3$) probed by our sample.

We have explored how massive galaxies look at $z > 3$. Based on recent photometrical renditions (Trujillo *et al.*, 2007; Buitrago *et al.*, 2008; Cassata *et al.*, 2010, 2011) we expect $M_* \geq 10^{11} M_\odot$ galaxies to have luminosity profiles which do not differ very much between their optical and UV restframe. We found 11 massive galaxies, being 8 of them disk-like and 3 spheroid-like galaxies. Their median sizes are $36 \pm 4\%$ and $16 \pm 13\%$ of their local SDSS massive counterparts respectively. In comparing this with the results in the Figure 2 and the Table 1 of Buitrago *et al.* (2008), it seems we have reached a plateau in the size evolution. This could be explained by the huge mean stellar densities of these systems, comparable to present day globular clusters. Perhaps this represents a limit for the stellar mass densities of galactic objects (Hopkins *et al.*, 2010).

On assigning visual morphologies to the massive galaxies at $z > 3$, 5 looked like irregular/peculiar galaxies (4 of them compatible with a disky nature as well), 4 were disks and 2 spheroidal. We must stress once again that it is remarkable that massive galaxies resemble disks at high-z, which is very differently as their low-z appearance as large early-type galaxies. Secondly, there are often perceived distortions and minor features in these galaxies (which are very conspicuous in 5 of them), barely above the sky noise level. Possibly they are related with minor merging or related processes. Improvements in the resolution and sensitivity (such as the ongoing HST CANDELS survey) are necessary to fully characterise what is happening in these cases. Future steps in the present work will be studying ACS imaging for the $z < 1.5$ galaxies and accessing to K-band images for $z > 3$ objects. Both of them will improve our analysis

as they remove greatly K-correction issues. Much better statistics would be achieved by adding new spectroscopic data available in the GOODS fields (Balestra *et al.*, 2010; Cooper *et al.*, 2011).

Table 4.1: Sizes for disk-like ($n < 2.5$) objects

	$10^8 - 10^9 M_\odot$	$10^9 - 10^{10} M_\odot$	$10^{10} - 10^{11} M_\odot$	$> 10^{11} M_\odot$	$> 10^{11} M_\odot (B08)$
$0 < z < 0.5$					
$r_e(kpc)$	1.43 ± 1.04	1.88 ± 1.52	2.18 ± 1.06	$- \pm -$	$- \pm -$
$r_e/r_{e,SDSS}$	0.92	0.86	0.64	$-$	$-$
number	124	55	19	1	0
$0.5 < z < 1$					
$r_e(kpc)$	1.25 ± 0.81	1.68 ± 0.91	2.14 ± 1.22	$- \pm -$	$- \pm -$
$r_e/r_{e,SDSS}$	0.80	0.77	0.63	$-$	$-$
number	750	351	112	1	0
$1 < z < 1.5$					
$r_e(kpc)$	1.00 ± 0.72	1.51 ± 0.85	2.10 ± 1.12	2.13 ± 1.11	$- \pm -$
$r_e/r_{e,SDSS}$	0.65	0.69	0.62	0.30	$-$
number	336	242	103	7	0
$1.5 < z < 2$					
$r_e(kpc)$	0.93 ± 0.58	1.23 ± 0.72	2.10 ± 1.11	2.52 ± 1.34	2.42 ± 0.83
$r_e/r_{e,SDSS}$	0.60	0.56	0.61	0.36	0.34
number	31	150	111	17	6
$2 < z < 2.5$					
$r_e(kpc)$	1.08 ± 0.66	1.20 ± 0.80	1.94 ± 0.95	1.97 ± 0.99	2.82 ± 1.15
$r_e/r_{e,SDSS}$	0.70	0.55	0.57	0.28	0.40
number	31	256	98	17	28
$2.5 < z < 3$					
$r_e(kpc)$	0.69 ± 0.71	0.99 ± 0.62	1.95 ± 0.99	1.45 ± 0.95	2.11 ± 0.80
$r_e/r_{e,SDSS}$	0.45	0.46	0.57	0.21	0.30
number	25	237	65	4	14
$3 < z < 4$					
$r_e(kpc)$	0.71 ± 0.57	0.77 ± 0.58	1.32 ± 0.76	1.34 ± 0.35	$- \pm -$
$r_e/r_{e,SDSS}$	0.46	0.35	0.39	0.19	$-$
number	9	117	53	4	0
$4 < z < 5$					
$r_e(kpc)$	$- \pm -$	0.88 ± 0.73	1.04 ± 0.95	$- \pm -$	$- \pm -$
$r_e/r_{e,SDSS}$	$-$	0.40	0.31	$-$	$-$
number	0	31	23	2	0

Table 4.2: Sizes for spheroid-like ($n > 2.5$) objects

	$10^8 - 10^9 M_\odot$	$10^9 - 10^{10} M_\odot$	$10^{10} - 10^{11} M_\odot$	$> 10^{11} M_\odot$	$> 10^{11} M_\odot (B08)$
$0 < z < 0.5$					
$r_e(kpc)$	1.14 ± 1.04	2.86 ± 2.91	1.53 ± 0.81	$- \pm -$	$- \pm -$
$r_e/r_{e,SDSS}$	6.86	4.75	0.70	$-$	$-$
number	16	6	9	0	0
$0.5 < z < 1$					
$r_e(kpc)$	0.82 ± 0.78	1.16 ± 0.94	2.44 ± 1.77	6.30 ± 3.43	$- \pm -$
$r_e/r_{e,SDSS}$	4.94	1.92	1.12	0.79	$-$
number	238	33	49	5	0
$1 < z < 1.5$					
$r_e(kpc)$	0.64 ± 0.63	1.26 ± 0.92	1.81 ± 1.21	2.23 ± 1.60	$- \pm -$
$r_e/r_{e,SDSS}$	3.83	2.09	0.83	0.28	$-$
number	215	33	20	8	0
$1.5 < z < 2$					
$r_e(kpc)$	0.82 ± 0.87	1.03 ± 0.93	1.97 ± 1.51	1.96 ± 0.80	1.81 ± 1.12
$r_e/r_{e,SDSS}$	4.97	1.72	0.90	0.25	0.23
number	33	46	21	7	14
$2 < z < 2.5$					
$r_e(kpc)$	0.42 ± 0.43	0.90 ± 0.80	1.01 ± 0.59	0.96 ± 0.37	1.41 ± 0.73
$r_e/r_{e,SDSS}$	2.53	1.49	0.46	0.12	0.18
number	38	103	18	3	11
$2.5 < z < 3$					
$r_e(kpc)$	0.49 ± 0.47	0.97 ± 0.97	1.64 ± 0.89	0.99 ± 0.54	1.04 ± 0.31
$r_e/r_{e,SDSS}$	2.94	1.62	0.75	0.12	0.13
number	28	131	5	4	7
$3 < z < 4$					
$r_e(kpc)$	0.77 ± 0.70	0.57 ± 0.62	1.27 ± 1.03	$- \pm -$	$- \pm -$
$r_e/r_{e,SDSS}$	4.63	0.95	0.58	$-$	$-$
number	7	85	24	1	0
$4 < z < 5$					
$r_e(kpc)$	$- \pm -$	0.40 ± 0.44	1.29 ± 1.58	$- \pm -$	$- \pm -$
$r_e/r_{e,SDSS}$	$-$	0.67	0.59	$-$	$-$
number	0	31	14	0	0

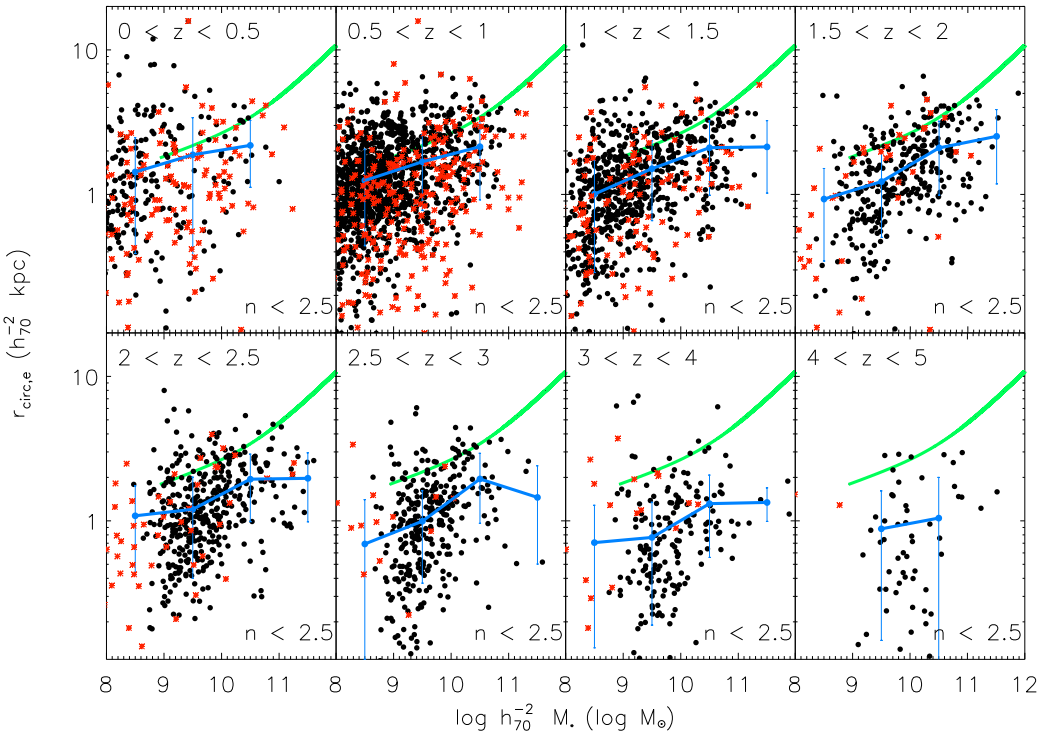

Figure 4.5: Size-mass relationship for disk-like ($n < 2.5$) objects at $0 < z < 5$. Error bars account for the standard deviation on the mean size. Green solid line is local SDSS relation in Shen *et al.* (2003). Black dotes denote the galaxies with photometric redshifts, while red asterisks are the ones having spectroscopic redshifts.

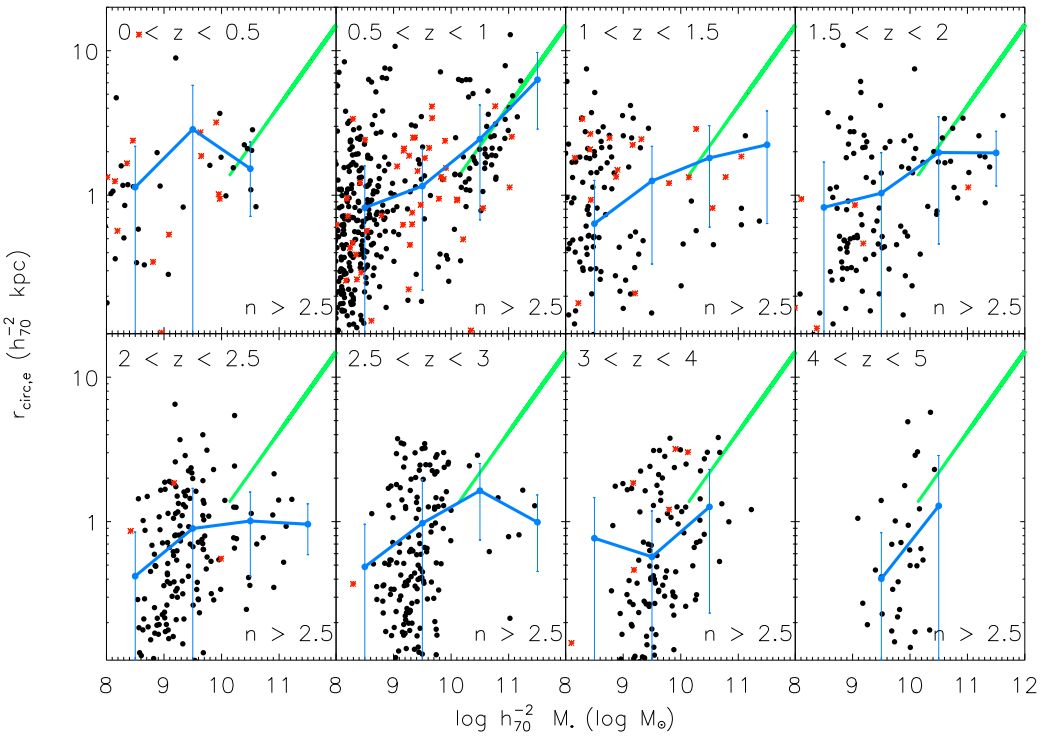

Figure 4.6: Size-mass relationship for spheroid-like ($n > 2.5$) objects at $0 < z < 5$. Error bars account for the standard deviation on the mean size. Green solid line is local SDSS relation in Shen *et al.* (2003). Black dotes denote the galaxies with photometric redshifts, while red asterisks are the ones having spectroscopic redshifts.

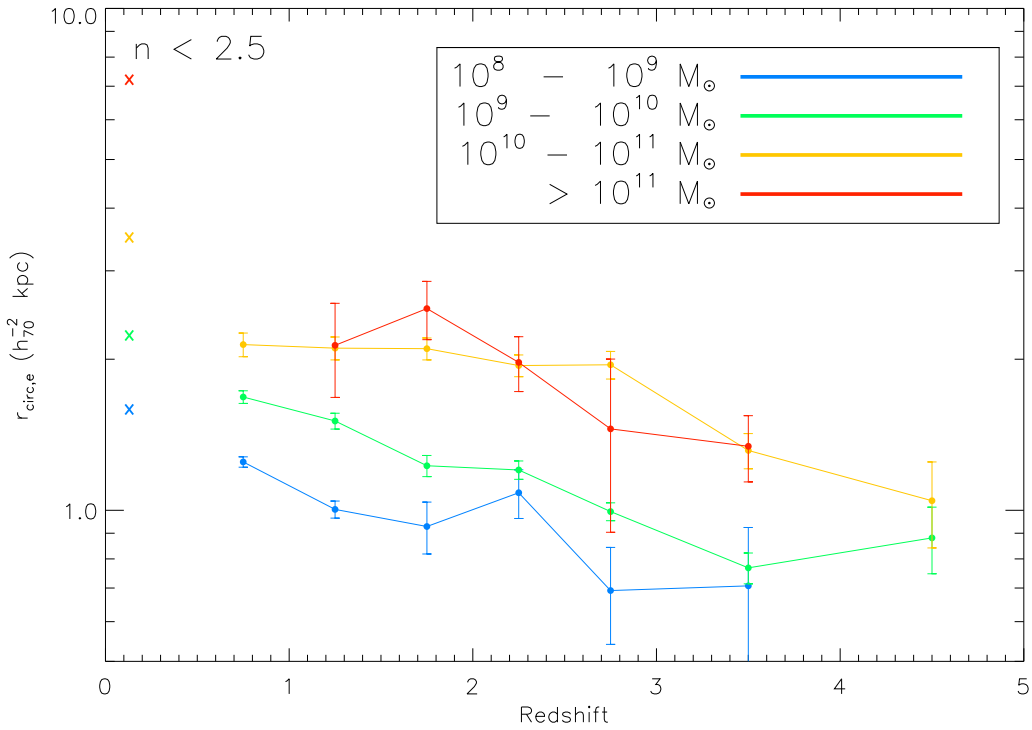

Figure 4.7: Evolution of galaxy sizes with redshift for disk-like ($n < 2.5$) galaxies. Errors bars are the uncertainty of the mean ($\sigma/\sqrt{(N-1)}$, being σ the standard deviation and N the total number of galaxies for each point). Crosses mark the sizes in the local (median redshift $z = 0.1$) sample of Shen *et al.* (2003) for masses in the middle point of each mass interval.

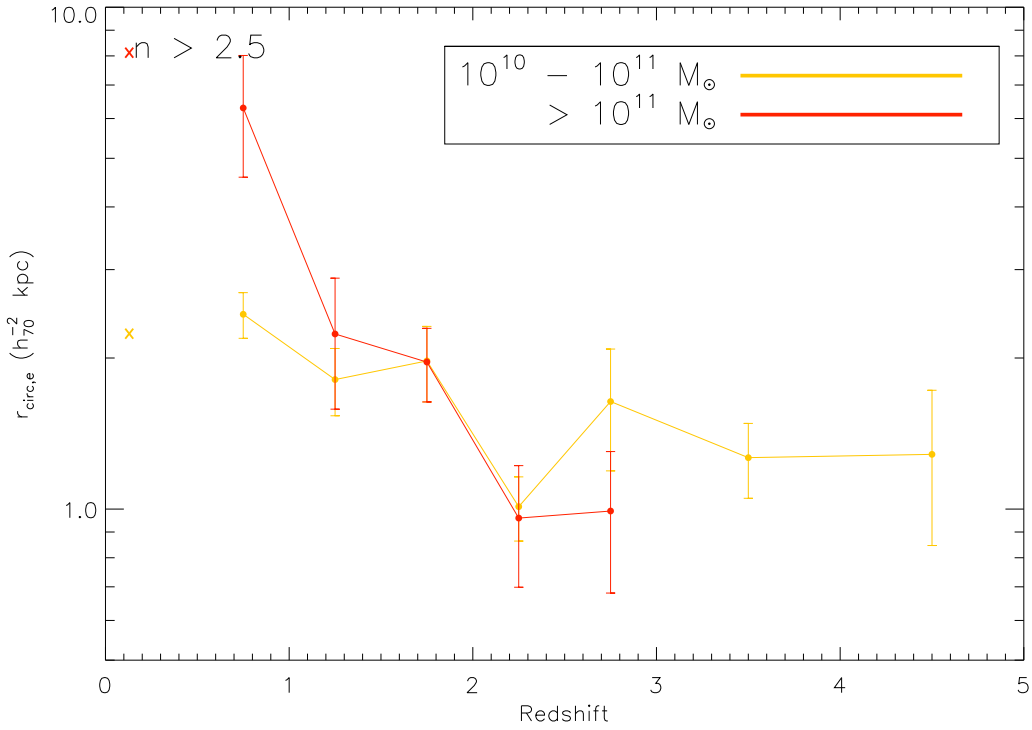

Figure 4.8: Evolution of galaxy sizes with redshift for spheroid-like ($n > 2.5$) galaxies. Errors bars are the uncertainty of the mean ($\sigma/\sqrt{(N-1)}$, being σ the standard deviation and N the total number of galaxies for each point). Crosses mark the sizes in the local (median redshift $z = 0.1$) sample of Shen *et al.* (2003) for masses in the middle point of each mass interval.

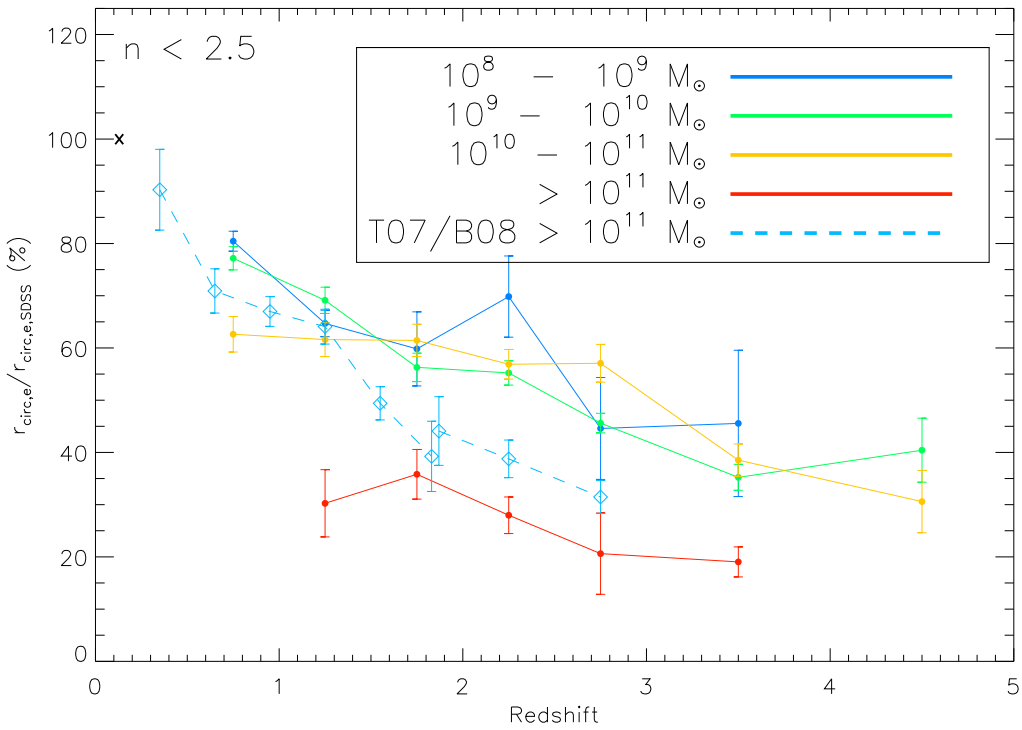

Figure 4.9: Evolution of galaxy sizes with redshift in comparison with local SDSS reference sample (Shen et al. 2003) for disk-like ($n < 2.5$) galaxies. Plotted is the ratio between the mean size and the local size in the middle point of the mass interval. The dashed lines correspond to the median sizes of galaxies in Trujillo *et al.* (2007) (T07) and Buitrago *et al.* (2008) (B08) with respect to the sizes of SDSS. The cross refers to the fact that SDSS local reference at $z = 0.1$ is 100% of the relative sizes for all the mass ranges.

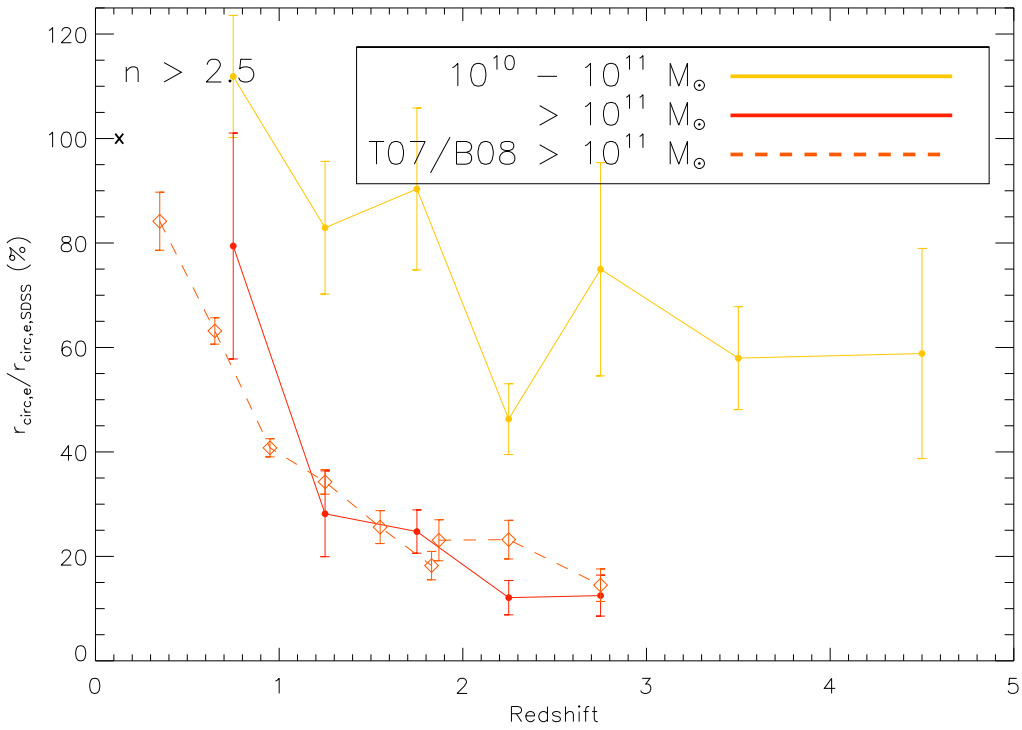

Figure 4.10: Evolution of galaxy sizes with redshift in comparison with local SDSS reference sample (Shen et al. 2003) for spheroid-like ($n > 2.5$) galaxies. Plotted is the ratio between the mean size and the local size in the middle point of the mass interval. The dashed lines correspond to the median sizes of galaxies in Trujillo *et al.* (2007) (T07) and Buitrago *et al.* (2008) (B08) with respect to the sizes of SDSS. The cross refers to the fact that SDSS local reference at $z = 0.1$ is 100% of the relative sizes for all the mass ranges.

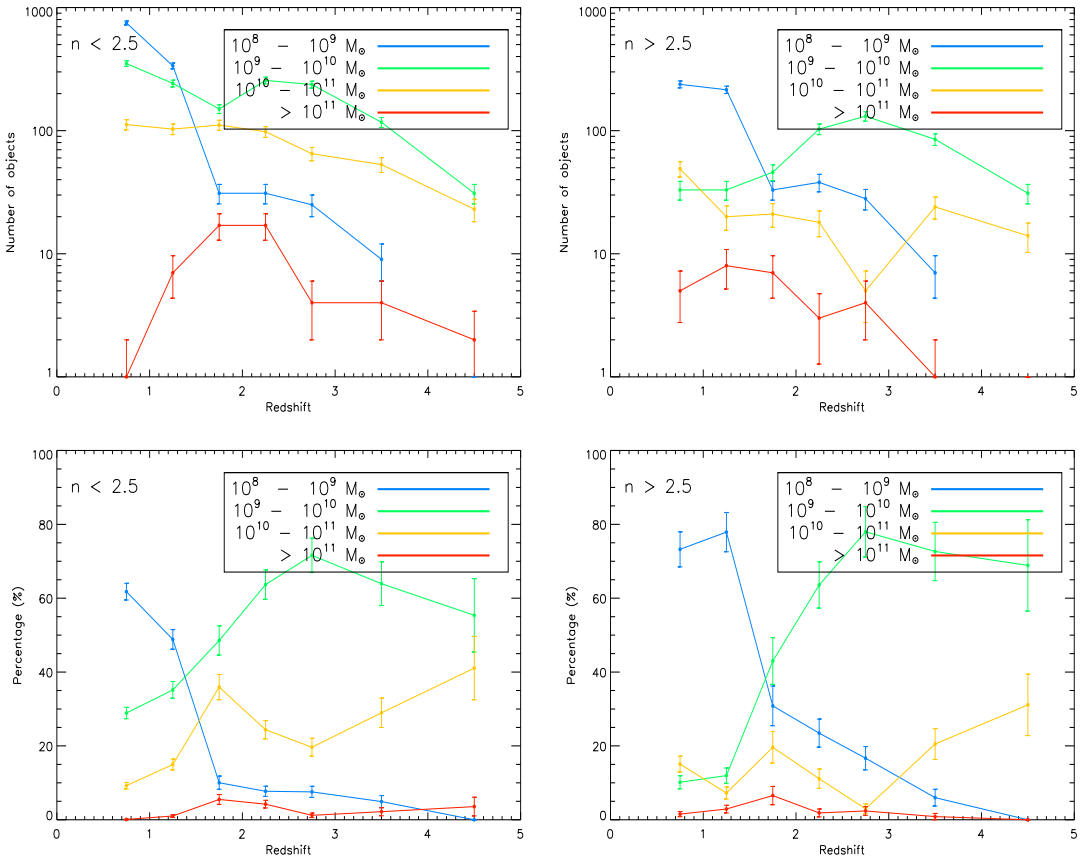

Figure 4.11: From left to right, from top to bottom: Number of galaxies in every redshift bin for disk-like ($n < 2.5$) galaxies. Number of galaxies in every redshift bin for spheroid-like ($n > 2.5$) galaxies. Percentages per redshift bin of disk-like ($n < 2.5$) galaxies with different masses. Percentages per redshift bin of spheroid-like ($n > 2.5$) galaxies with different masses. Note that the lines always link sets of galaxies in the same mass range. Error bars are Poissonian.

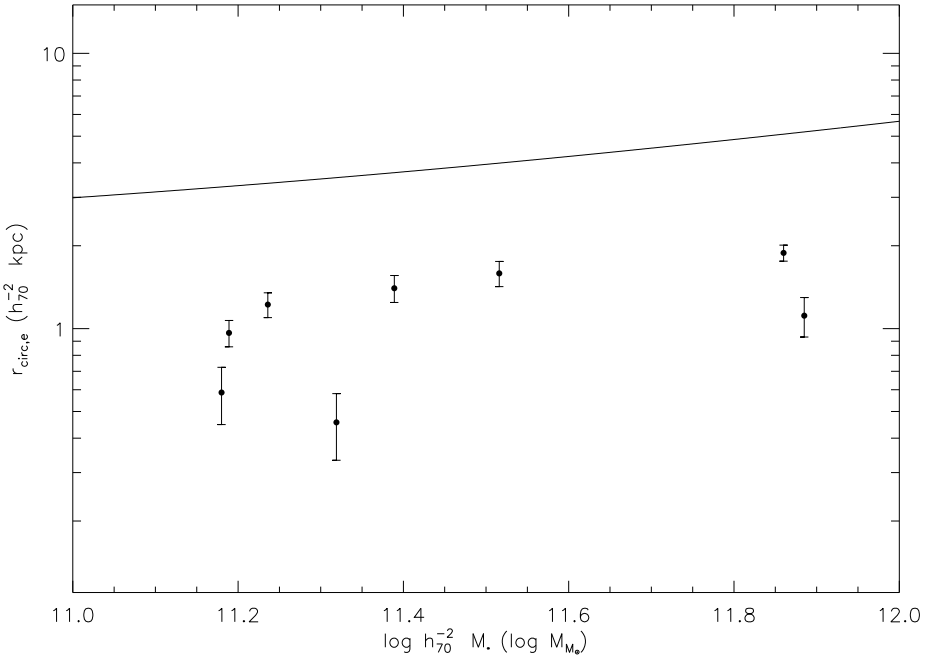

Figure 4.12: Size-mass relationship for disk-like ($n < 2.5$) massive galaxies at $z > 3$. Solid line represents the local size-mass relationship from SDSS (Shen et al. 2003). Error bars account for the standard deviation of the galaxy size measured with 5 different natural stars as PSF examples.

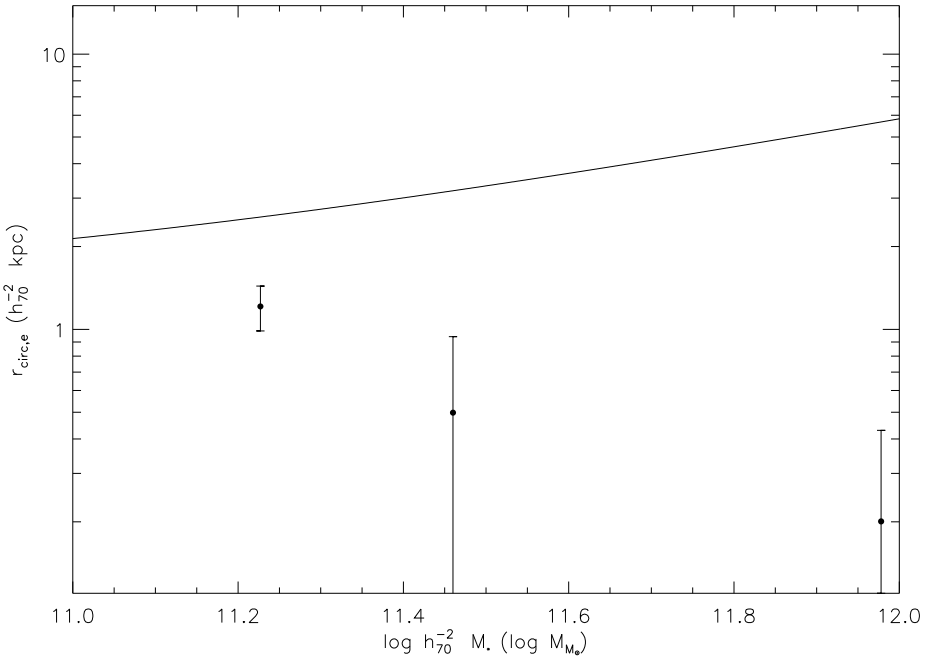

Figure 4.13: Size-mass relationship for spheroid-like ($n > 2.5$) massive galaxies at $z > 3$. Solid line represents the local size-mass relationship from SDSS (Shen et al. 2003). Error bars account for the standard deviation of the galaxy size measured with 5 different natural stars as PSF examples.

If, billions of years in the future, there is to be no life, no intelligence, no memory of the struggles of humanity, what point is there to existence? As a scientist and a human being, I have had to wrestle with this question... After a long period of indecision, I finally realized that the entire issue can be brought down to a simple problem – how will I act tomorrow? Given what I know about the future of the universe, how will I handle the everyday decisions that make up my life? What I finally came to see was this: It may be true that in a quadrillion years the universe will be a cold, expanding sea of radiation. There may be no one to know how I behave tomorrow, no one to remember what any of us did. But this is irrelevant. The point is that I will know tomorrow what I have done, I will know whether I was the best person I could be. And in the end, my friends, that is all that matters.

James Trefil in 'The dark side of the Universe'

Chapter 5

Conclusions & future work: exploring the ΛCDM galaxy formation using massive galaxies

5.1 Summary & conclusions of the thesis

In the epoch of high redshift galaxy detections, when multiwavelength all-sky and ultra-deep surveys are planned and conducted, we have a unique opportunity to understand galaxies in detail and thus the Universe as a whole by describing its basic components. This objective of this thesis was the study of the observational properties of massive ($M_{stellar} \geq 10^{11} h_{70}^{-2} M_{\odot}$) galaxies at $0 < z < 3$.

Admittedly, we have advanced greatly in the comprehension of galaxy formation having nowadays a framework to understand it: the ΛCDM Universe. According to this model, very high-z primeval gas-rich disks were the first formed, populating the most massive dark matter haloes and harbouring inside them the first stars. The lack of powerful enough telescopes prevent us from studying in detail the conditions of the galaxies in the primeval universe. Consequently, massive galaxies at moderate redshifts ($z = 2 - 3$) represent an unique test-bed to comprehend our ideas of galaxy formation and evolution, as their high luminosity allow us to track them through a very wide redshift range, and their often extreme properties are evidence for the physical

phenomena taking place there.

This thesis has benefited enormously from the possibility of utilising the GOODS NICMOS Survey. GNS was, at the time the student began the doctorate, the best (by far) NIR coverage of the premium GOODS fields. Its unprecedented depth and good resolution has permitted us to conduct a comprehensive series of studies to fully characterise the massive galaxy population, as it was especially designed to detect as many of these objects as possible.

The kick-off of our work consisted of the size determination of these massive galaxies. We had the largest compilation of massive galaxies at $z > 1.5$ observed with HST. This study helped solidify the picture that massive galaxies at high-z exhibit on average a factor of $\sim$3 and $\sim$5 smaller sizes than their local counterparts, depending whether they are disk-like ($n < 2.5$) or spheroid-like ($n > 2.5$), respectively. This fact implies mean stellar densities of the order of $\sim 2 \times 10^{10} \mathrm{M}_{\odot} \mathrm{kpc}^{-3}$, comparable to present day globular clusters.

It seems clear that these galaxies have suffered a profound transformation since $z \sim 2$. Hence their structural parameters have to reflect this change. In Chapter 2 we compare not only the size but the Sérsic index, axis ratios and their derived visual morphologies. We found a huge change in the dominant morphological class with cosmic time. The fraction of early-type galaxies among the massive galaxy population has changed from $\sim$20-30% at z$\sim$3 to $\sim$70% at z=0. Spheroid-like galaxies have been the predominant morphological massive class only since z$\sim$1.

To fully understand, however, the intrinsic nature of the morphological transformations, we need to explore ultimately the kinematics of the massive galaxies at high-z (see Chapter 3). 3D spectroscopy is a privileged tool to address this, as it provides access to spectral information spatially extended over the field-of-view of the observations. We utilised the SINFONI integral field spectrograph at VLT to analyse a set of ten massive galaxies at $z \sim 1.4$. Our results suggest this galaxy population is mainly rotationally supported. This is at odds with what happens in the local Universe, where the massive end of the galaxy mass function is dominated by a class of early-type galaxies defined as slow-rotators. We can also see in our images several merging examples. This fact, combined with the increasing number of peculiar galaxies with

redshift in the previous chapter, reaffirms that minor and major merging are suitable pathways for the evolution of the massive galaxy population.

In order to link the characteristics of massive galaxies with lower mass galaxies we constructed the size-mass relationship for the whole GNS sample in Chapter 4. It is not known whether the more massive galaxies have larger sizes in the high-z Universe (as at low-z) and how it fits with the strong size evolution found for the most massive galaxies. Our results concur with a similar statistical trend as at low-z where more massive galaxies have larger sizes. Nevertheless, most massive galaxies undergo a rapid change towards smaller radii at increasing redshift. The evolution of average mass galaxies is only moderate in this regard. Furthermore, massive galaxies at $z > 3$ also look very compact, with similar sizes as the ones found previously at $2 < z < 3$. Their morphologies and Sérsic indices show that most of them are better represented by a disk structure.

5.2 Future projects

An important conundrum that needs to be solved is the origin and formation of the extremely compact massive galaxies at high redshift. One way to look at this open question is to explore the submillimeter massive galaxy population at $z > 2$. Their high gas content and their number densities make them likely candidates of primordial objects. In the past, there was a dearth of optical-NIR HST imaging for these objects and hence few studies refer to their morphological properties (Dasyra *et al.*, 2008; Ricciardelli *et al.*, 2010; Swinbank *et al.*, 2010; Targett *et al.*, 2011). There is not an agreement about whether these objects are better represented by a disk or spheroidal population, and this is key to check the ΛCDM paradigm as the sub-mm galaxies should be progenitors of massive ($M_* \geq 10^{11} M_\odot$) compact high-z spheroids, due to their compatible star formation rates and number densities (Cimatti *et al.*, 2008). With the advent of HST WFC3 and its improved sensitivity and large field of view, studies about this topic will be performed much more efficiently. We propose to examine high resolution and deep imaging from public available CANDELS survey (Grogin *et al.*, 2011) attempting to characterize in UV and optical restframe on previously confirmed

50 sub-mm massive objects at $z > 2$.

The merging of two primordial massive gas-rich disk galaxies is expected to form a massive spheroidal object. A very compact remnant should be produced due to the enormous gas dissipation. This is another prediction within the ΛCDM scenario we are working in. In fact, we have found that these massive spheroids at high redshift have strikingly small sizes (~ 5 times smaller at a fixed stellar mass than their nearby Universe counterparts) and extreme surface mass densities. Recent theoretical renditions (Wuyts *et al.*, 2010) suggest that massive compact galaxies at high redshift should show redder cores than their external parts. Although the majority of the young stars would reside in the galaxy center, this age effect in the color profile would be compensated by the superposition of metallicity and extinction gradients. This color gradient prediction can be now tested using WFC3 HST public data looking at differences between Y and H filters, that correspond to U and V restframe bands respectively at $z = 2$. To date, color gradients have been only explored in a few galaxies at high-z (Gargiulo, Saracco & Longhetti, 2011) and we are in the perfect position to improve this situation.

In the last two years, research has attempted to understand how the massive ($M_* \geq 10^{11} M_\odot$) compact ($r_e = 1$ kpc) high-z ($z \geq 1.5$) galaxies end up as being the massive spheroids we observe in the nearby Universe. A number of astrophysical mechanisms have been advocated theoretically, such as major dry merging (Khochfar & Silk, 2006; Bluck *et al.*, 2009; López-Sanjuan *et al.*, 2010b,a) or AGN puffing-up(Fan *et al.*, 2008, 2010; Ragone-Figueroa & Granato, 2011). However, the most promising one following the ΛCDM scenario, is the continuous bombardment with minor objects which should surround the massive ones. These minor satellites should eventually merge with the massive galaxies, providing pristine gas that will feed the high star formation that has been recently found in these objects (Cava *et al.*, 2010; Bauer *et al.*, 2011; Viero *et al.*, 2012). Owing to the intrinsic faintness of these satellites, the best and possibly only way to carry out this project will be to have access to CANDELS data, as multi-wavelength data is necessary to derive reliable photometric redshifts for the possible galactic companions. Galactic outskirts of the massive galaxies will be characterized up to low surface brightness limits as well, unveiling whether they are consistent with

an inside-out formation scenario. To address the issue of massive galaxy growth we propose exploring the evolution in the number of satellites of these compact galaxies in the last 11 Gyr. To this aim we have already selected several catalogs in fields covered by CANDELS that will allow us to follow massive galaxy environment since redshift $z \sim 3$. These are the descriptions according to their locations:

- UDS — ~ 35 massive galaxies up to $z = 0.3$. With the expected depth we could reach extremely faint galactic companions at low redshift.
- EGS — ~ 170 massive objects from $0.2 < z < 2$.
- GNS GOODS — ~ 100 compact massive galaxies at $1.7 < z < 3$.

The depth of the above data assures we will be in position to follow homogeneously the evolution of the satellite population. Utilizing projected number densities of companions in certain apertures plus statistical corrections, and also magnitudes and color information will constrain the properties of the satellites with masses $\geq 10^9 M_{\odot}$. Moreover, the environment of the massive high-z galaxies will be fully understood for the first time. Previous deep HST observations have not inferred anything conclusive about it (Grützbauch *et al.*, 2011a). One expects these massive objects are related to primeval dark matter overdensities and as such they must be seeds for protocluster development. Questions about whether the so-called red sequence extends up to very high redshifts and about where the massive galaxies are preferentially located will be also addressed.

Most of the above tests to the ΛCDM model are based on pure photometric techniques. To fully understand, however, the intrinsic nature of the morphological transformations that this paradigm is suggesting, we need to explore ultimately the kinematics of the massive objects at high-z. In short term we will submit a series of VLT proposals we already prepared to extend my previous 3D spectroscopy sample of massive galaxies to high redshifts (up to $z \simeq 2.5$). All these new members have HST ACS and NICMOS (and eventually CANDELS) high resolution public imaging which improve the assessment in small feature recognition. For the first proposal, galaxies were selected to have high star formation rates – $200 - 400 M_{\odot} yr^{-1}$ from UV corrected estimations, Bauer *et al.* (2011) – and hence they will retrieve clear spectra even at these high redshift. Its partner proposal checks the possible AGN contribution to our

massive samples. The general idea we pursue is to disentangle whether these objects are rotationally or velocity dispersion supported.

An idea that will contribute very much to extragalactic studies in the future is the extensive use of 3D spectroscopy: With the advent of new NIR IFU and multi-IFU instruments (KMOS atVLT, IRIS at TMT, EAGLE at E-ELT), 3D spectroscopic surveys will become real in a short time. We need to be ready in order to capitalize on them, conducting simulations about their performance and also creating software capable of distinguishing clearly all the spectroscopic features. In addition to that, JWST will be equipped with an integral field unit (MIRI instrument). They will unveil many aspects of high redshift galaxy evolution and assembly. 3D spectroscopy will also allow us to describe the stellar populations of massive galaxies in detail and with local enhancements of metallicity and velocity dispersion we will discover merging histories. Above all, it will provide the astronomical community with a complementary method to parametrize morphologies, not only relying in the surface brightness profile fittings from the galaxies but also in their internal kinematics.

The series of projects we have already mentioned are direct tests of ΛCDM scenario, as they attempt to constrain the idea of high-redshift disks should become present-day spheroidal galaxies. We would like to drawn attention into the incredible wealth of both photometric and spectroscopic data that will arrive in the future: large space telescope programs such as the previously cited CANDELS or CLASH, plus huge ground-based surveys like Pan-STARRS or VISTA. My collaborators are co-Is in a number of these programs and we will access with them to these new resources. Our interest is based not only in observations but in the fact that nowadays, software construction in Astronomy research has been performed in most cases without any specific pattern and hence inefficiently. A computer-engineering framework in their development and life cycle is not only desirable but will become mandatory to deal with the future enormous amounts of information to be processed. Some interesting modifications have already been taken, for instance the Python language spreading in the community due to its free non-proprietary nature and computational speed, or the Virtual Observatory existence and its formatting style of archival imaging. Despite this progress, a step further is needed in professional database integration, reusability of the astronomical programs

and error handling coding. Beyond doubt, the synergy of these techniques and data mining will help greatly the future of astronomical computing. Robust software will retrieve accurate results, multi-purpose outcomes and the use of computer parallelization will optimize the performance. A Computer Science background (as the student's profile) will provide us with the tools to approach the data-mining problems we will face.

And we must not forget that the ultimate objective of all these current and future programs should be a contribution to our society. We are living in the extraordinary era of information, and in the world of globalization we are committed to return the beauty of Astronomy to the people, with public engagement and internet broadcasting. In our opinion, one of today's astronomer missions is showing to the public that beholding the Universe still fills our minds with awe and new questions.

Finally we would like to state that to conduct all these programs will represent a great step forward in galaxy formation and evolution. Ultimately, it will also be a valuable contribution to our society, as we will answer many enigmas about the farthest galaxies the human being can reach. Studying primordial massive disks and high redshift sub-millimeter galaxies, to gain a true knowledge on the ultracompact massive galaxy population and to look for massive relics in the nearby Universe will progressively introduce us into the revolutionary JWST era and, most importantly, it will improve our understanding of the Universe we live in.

Appendices

Appendix A

GNS parameters recovery simulations

The purpose of this Appendix is to explore the robustness of the structural parameters of the massive galaxies (1.7<z<3) in our GNS sample –H-band, F160W filter, HST NICMOS-3 camera, 3 orbits depth; Conselice *et al.* (2011a)–. As explained in the Chapter 2, a set of simulations similar to the ones presented here were already conducted for the ACS imaging used to analyze the galaxies in the redshift interval 0.2<z<2 (Trujillo *et al.*, 2007). To identity the ranges of the structural parameters to explore in our simulations, we use as a guide the ranges found in the quantitative morphological analysis based on GALFIT of the real GNS massive galaxies (Buitrago *et al.*, 2008). These were:

$$0.15 < r_e(arcsec) < 0.61$$

$$0.34 < n < 4.62$$

$$0.19 < ar < 0.92$$

$$-84.03 < pa < 85.28$$

$$20.5 < H_{AB} < 24$$

where r_e, n, ar, pa, H_{AB} stand for effective radius, Sérsic index, axis ratio, position angle and derived H_{AB}-band magnitude. The only exceptions where one galaxy with $n = 0.17$ and other two with $24 < H_{AB} < 24.5$. Taking these quantities into account, we simulated 16000 galaxies with the structural parameters randomized within these ranges:

$$0.15 < r_e(arcsec) < 2.0$$

$$0.25 < n < 8.0$$

$$0.1 < ar < 1.0$$

$$-89.99 < pa < 90.0$$

$$20 < H_{AB} < 25$$

The structural parameters of the mock galaxies were distributed linearly along the full parameter space, except for the effective radii where we did it logarithmically as we specially wanted to explore objects with small angular radii due to observed compactness of massive galaxies at high-z.

Images of every mock galaxy were created placing these objects randomly along the GNS pointings. We just place a mock galaxy on each GNS pointing at each time, to avoid altering the the typical density (i.e. number of neighbour galaxies) of the GNS data. Each model galaxy (i.e. the 2D surface brightness distribution following the Sérsic function) was convolved with a representative PSF, specifically we used one of the five natural stars which were utilised in Buitrago *et al.* (2008). To obtain errors in the same way as in that paper, we also ran GALFIT using these five different stars and then taking the mean values.

We have identified that the main source of uncertainty in the NICMOS data is the change of the PSF along the field of view of the camera. To illustrate how this affects the recovery of the structural parameters we first present in Figure A.1 and A.2 how our parameters are recovered when we use the same PSF for creating and recovering the mock galaxies and, in Figure A.3 and A.4, what are the effects on the parameters when we compare the input values with the average values obtained using the five different PSFs.

In Figure A.1 we show the relationship between the relative errors in the structural parameters (magnitude, effective radius and Sérsic index) versus the galaxy input magnitude. The relative errors are calculated as *(output-input)/input*, i. e., negative % refer to cases where the output is smaller than the input and viceversa. The left column of the plot displays the structural parameters of individual galaxies, whereas the right column

shows their means in bins of 0.5 mag. The mean values of the structural parameteres were derived using a robust method which removes the 5σ outliers. Error bars represent the standard deviation of the sample. To appreciate how the effect on the structural parameter is linked to the input Sérsic index of the mock galaxies we split the sample in four groups ($0 < n < 2$, $2 < n < 4$, $4 < n < 6$ and $6 < n < 8$). The results shown in Fig. A.1 are tabulated in the Table A.3. At increasing the valued of the Sérsic index, the recovery of the structural parameters are largely affected. We note that galaxies with low Sérsic index are well recovered down to our faintest magnitude. An average galaxy in our GNS sample (H=22.5 mag) and input Sérsic index of n=4 will have its effective radius biased only by a $\sim$10% and its Sérsic index around $\lesssim$20%.

In addition to the effect of the apparent magnitude of the objects on recovering their structural parameters, in Figure A.4 we explore what is the effect of the size (lower row) and intrinsic shape (upper row) for this matter. Galaxies are colour coded according to their magnitude. Combining the information contained in Fig. A.3 and A.4, we appreciate that the key parameters for retrieving accurate structural parameters are the apparent magnitude and the Sérsic index. The effective radius of the objects plays a minor role. The results show on Fig. A.4 are tabulated in the Table A.2.

The results presented so far assume that the PSF is known perfectly. However, the PSF is not very well behaved on the NICMOS 3 camera and it is important to quantify how this affects to the results presented here. To explore this issue we retrieve all the individual mock galaxies using the five different PSFs used in the Chapter 2. We obtain the mean values resulting from combining the results of these five different fits and we compare these values with input parameters. Thus, we created Figure A.3 and A.4 as the counterparts of Figure A.1 and A.2, playing Tables A.3 and A.4 the same role as Tables A.1 and A.2.

The most interested output of this test using the mean value from the fits of different PSFs is that the size of the source plays now a fundamental role at characterizing the error on the structural parameters. As expected large sources are less affected by the effect of changing the PSFs and the bias on the structural parameters remain basically the same than when we use just a single PSFs. However, at smaller sizes the effect of not knowing accurately the PSF affecting the source implies that the Sérsic

index uncertainty is large, although sizes are retrieve accurately. Summarizing, neither any effect nor a combination of effects is large enough to modify the main results of the Chapter 2. To illustrate this with the same example than before using an average galaxy in our GNS sample (H=22.5 mag) and input Sérsic index of n=4 will have its effective radius biased only by a $\sim$15% and its Sérsic index around $\sim$25%. Moreover, as stated on the text of Chapter 2, we use these simulations to correct, based on the observed (output) apparent magnitude, effective radius and Sérsic index, the structural parameters presented in this work.

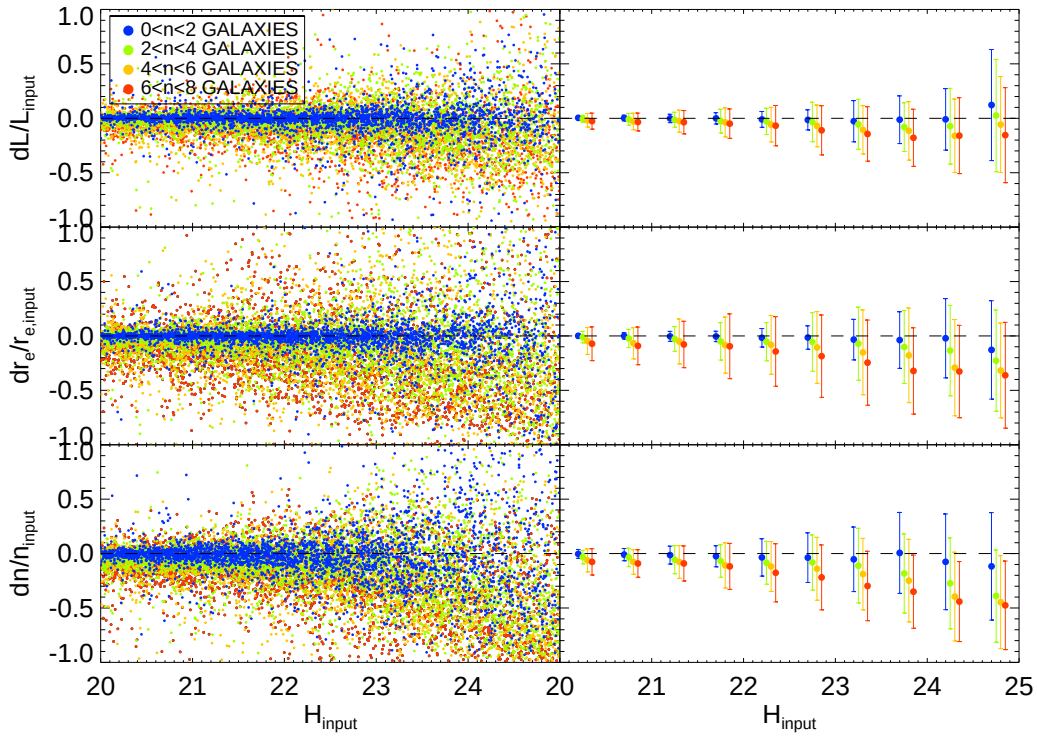

Figure A.1: Relative errors - *(output-input)/input* - of the structural parameters (magnitude, effective radius and Sérsic index) of our simulated GNS galaxies. The right column shows the means in bins of 0.5 mag (with a 5σ outlier-resistant determination), being the error bars the standard deviation of the sample. The information in this plot is tabulated in Table A.1.

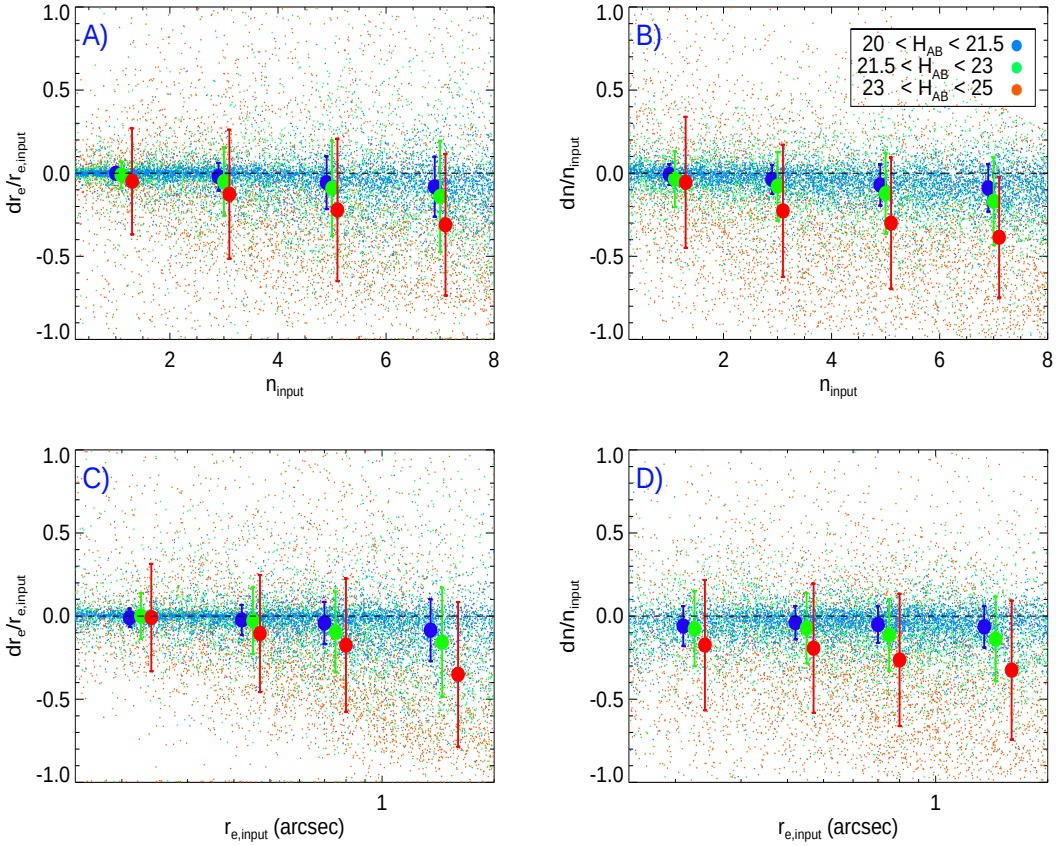

Figure A.2: Relative errors - *output-input/input* - of the effective radius (first column) and the Sérsic index (second column) as a function of the input Sérsic index (first row) and the input effective radius (second row). Galaxies are coloured according to their magnitude. For the sake of clarity, mean values (derived with a 5σ outlier-resistant determination) where added using 4 intervals in effective radius and Sérsic index, with the error bars being their standard deviation. Sérsic index intervals are $0 < n < 2$, $2 < n < 4$, $4 < n < 6$ and $6 < n < 8$. Effective radius intervals are $0.15" < r_e < 0.3"$, $0.3" < r_e < 0.6"$, $0.6" < r_e < 0.9"$ and $0.9" < r_e < 2"$. Note that the colour of these mean points is the same as the one of the galaxy individual points. The information in this plot is tabulated in Table A.2.

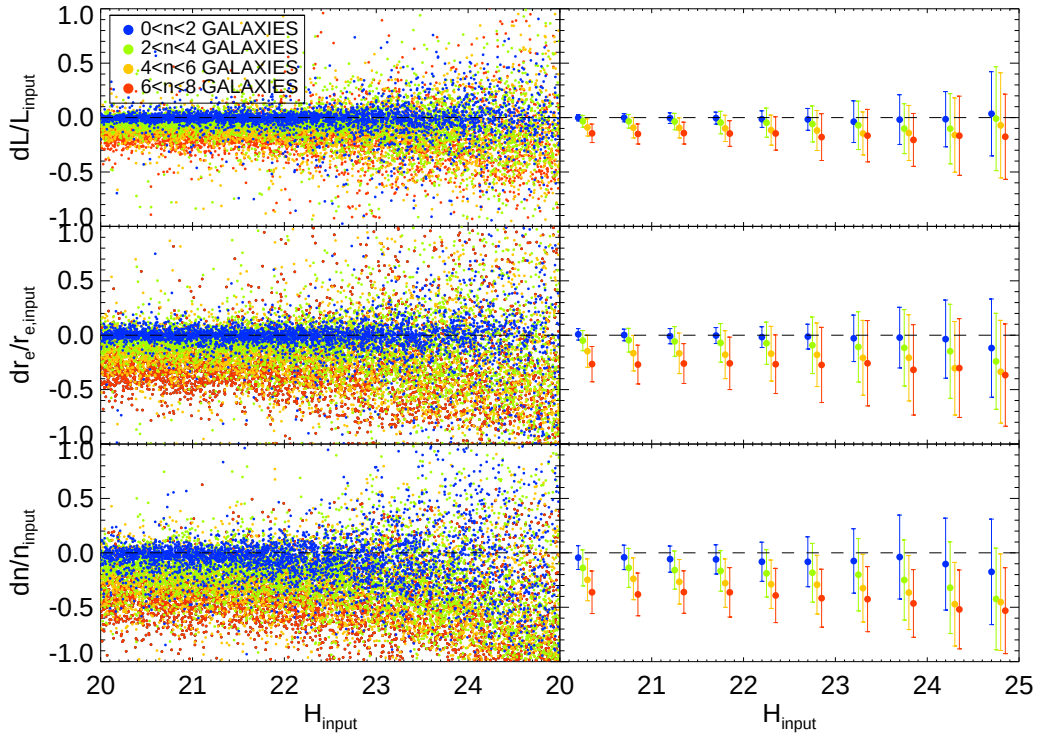

Figure A.3: Same as in Figure A.1, but using this time as the output parameters the mean values of the fits retrieved based on 5 different natural stars as PSFs. The results of this figure are tabulated in Table A.3.

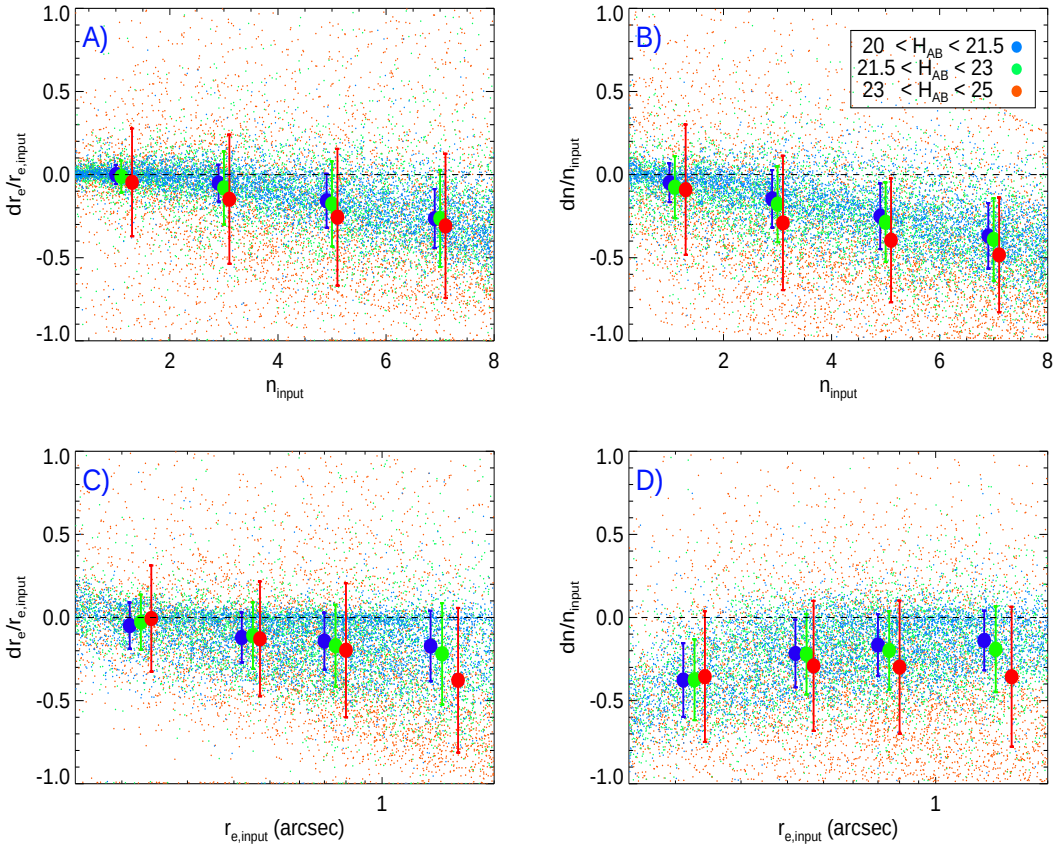

Figure A.4: Same as Figure A.2, but using this time as the output parameters the mean values of the fits retrieved based on 5 different natural stars as PSFs. The results of this figure are tabulated in Table A.4

Table A.1: Relative errors (%) on the structural parameters depending on the apparent magnitude (see Fig. A.1)

	$0 < n < 2$ galaxies	$2 < n < 4$ galaxies	$4 < n < 6$ galaxies	$6 < n < 8$ galaxies
$20.0 < H_{AB,input} < 20.5$				
$\delta L/L$	0.39 ± 1.75	-0.53 ± 3.21	-1.85 ± 6.24	-2.62 ± 7.36
$\delta r_e/r_e$	0.09 ± 2.03	-1.16 ± 5.27	-4.63 ± 12.35	-7.19 ± 15.54
$\delta n/n$	-0.34 ± 4.08	-3.22 ± 6.20	-6.25 ± 10.59	-7.62 ± 12.07
$20.5 < H_{AB,input} < 21.0$				
$\delta L/L$	0.21 ± 2.61	-0.99 ± 5.46	-2.95 ± 7.61	-3.43 ± 8.20
$\delta r_e/r_e$	0.01 ± 2.98	-2.33 ± 8.31	-6.78 ± 14.35	-9.16 ± 17.30
$\delta n/n$	-0.97 ± 5.63	-3.51 ± 8.48	-7.69 ± 11.25	-9.13 ± 12.68
$21.0 < H_{AB,input} < 21.5$				
$\delta L/L$	-0.12 ± 3.85	-1.34 ± 6.93	-2.60 ± 10.14	-3.62 ± 10.74
$\delta r_e/r_e$	-0.40 ± 4.58	-2.81 ± 11.39	-5.08 ± 20.67	-7.85 ± 21.32
$\delta n/n$	-1.42 ± 8.21	-5.65 ± 12.94	-7.72 ± 15.04	-9.08 ± 16.12
$21.5 < H_{AB,input} < 22.0$				
$\delta L/L$	-0.05 ± 5.17	-2.56 ± 10.93	-3.76 ± 13.39	-4.95 ± 13.55
$\delta r_e/r_e$	-0.50 ± 4.79	-4.98 ± 17.21	-8.46 ± 25.80	-9.54 ± 29.76
$\delta n/n$	-2.47 ± 9.68	-6.85 ± 14.97	-10.83 ± 20.77	-11.80 ± 21.14
$22.0 < H_{AB,input} < 22.5$				
$\delta L/L$	-1.03 ± 7.28	-2.87 ± 12.06	-5.83 ± 15.87	-6.79 ± 18.50
$\delta r_e/r_e$	-1.70 ± 8.48	-5.33 ± 17.56	-8.22 ± 27.02	-14.28 ± 32.00
$\delta n/n$	-3.55 ± 17.15	-8.50 ± 19.65	-11.86 ± 22.91	-17.65 ± 26.70
$22.5 < H_{AB,input} < 23.0$				
$\delta L/L$	-1.46 ± 9.27	-3.40 ± 18.16	-6.97 ± 19.19	-11.04 ± 22.58
$\delta r_e/r_e$	-1.48 ± 10.75	-5.55 ± 26.98	-10.61 ± 33.02	-18.60 ± 37.86
$\delta n/n$	-3.74 ± 22.80	-8.20 ± 25.31	-13.99 ± 28.88	-21.90 ± 29.83
$23.0 < H_{AB,input} < 23.5$				
$\delta L/L$	-2.70 ± 18.92	-5.54 ± 22.91	-10.57 ± 22.24	-14.38 ± 25.00
$\delta r_e/r_e$	-3.38 ± 18.65	-7.10 ± 33.57	-15.11 ± 38.94	-24.55 ± 39.17
$\delta n/n$	-5.29 ± 29.66	-11.14 ± 34.34	-18.92 ± 32.87	-29.79 ± 31.89
$23.5 < H_{AB,input} < 24.0$				
$\delta L/L$	-1.28 ± 21.90	-8.12 ± 22.41	-11.57 ± 26.88	-17.93 ± 26.23
$\delta r_e/r_e$	-3.81 ± 26.00	-10.21 ± 33.56	-17.86 ± 43.47	-32.17 ± 39.63
$\delta n/n$	0.61 ± 37.18	-18.35 ± 36.38	-24.90 ± 37.94	-35.02 ± 33.59
$24.0 < H_{AB,input} < 24.5$				
$\delta L/L$	-0.99 ± 28.30	-7.27 ± 34.80	-16.06 ± 33.78	-15.98 ± 34.87
$\delta r_e/r_e$	-2.13 ± 36.39	-13.48 ± 41.48	-29.16 ± 44.22	-32.70 ± 42.43
$\delta n/n$	-7.57 ± 43.98	-27.35 ± 41.82	-39.53 ± 40.77	-44.10 ± 36.75
$24.5 < H_{AB,input} < 25.0$				
$\delta L/L$	12.20 ± 51.04	2.50 ± 51.58	-5.73 ± 44.09	-15.50 ± 43.68
$\delta r_e/r_e$	-12.85 ± 45.18	-22.74 ± 46.45	-31.77 ± 43.55	-36.15 ± 48.64
$\delta n/n$	-11.73 ± 49.37	-38.99 ± 42.35	-44.67 ± 42.69	-47.58 ± 40.68

Table A.2: Relative errors (%) on the Structural Parameters (see Fig. A.2)

$\delta r_e/r_e$	$20 < H_{AB} < 21.5$	$21.5 < H_{AB} < 23$	$23 < H_{AB} < 25$
$0 < n < 2$	-0.04 ± 3.09	-1.00 ± 7.97	-4.89 ± 31.91
$2 < n < 4$	-2.14 ± 8.27	-5.13 ± 20.61	-12.66 ± 38.79
$4 < n < 6$	-5.71 ± 15.87	-9.08 ± 28.73	-22.12 ± 42.84
$6 < n < 8$	-8.16 ± 18.05	-13.98 ± 33.45	-31.04 ± 42.55
$0.15 < r_e(arcsec) < 0.3$	-0.94 ± 5.45	0.05 ± 13.79	-0.87 ± 32.27
$0.3 < r_e(arcsec) < 0.6$	-2.28 ± 9.02	-2.71 ± 20.11	-10.47 ± 35.21
$0.6 < r_e(arcsec) < 0.9$	-4.15 ± 12.67	-9.55 ± 24.26	-17.50 ± 40.12
$0.9 < r_e(arcsec) < 2.0$	-8.44 ± 18.68	-15.66 ± 32.69	-35.02 ± 43.53
$\delta n/n$	$20 < H_{AB} < 21.5$	$21.5 < H_{AB} < 23$	$23 < H_{AB} < 25$
$0 < n < 2$	-0.84 ± 6.23	-3.57 ± 16.86	-5.51 ± 39.42
$2 < n < 4$	-3.75 ± 8.71	-7.83 ± 20.63	-22.65 ± 39.74
$4 < n < 6$	-7.08 ± 12.33	-12.19 ± 24.38	-30.01 ± 39.47
$6 < n < 8$	-8.85 ± 14.25	-16.94 ± 26.32	-38.55 ± 36.30
$0.15 < r_e(arcsec) < 0.3$	-5.99 ± 12.04	-7.56 ± 22.54	-17.43 ± 39.18
$0.3 < r_e(arcsec) < 0.6$	-3.93 ± 10.03	-7.20 ± 21.14	-19.31 ± 38.89
$0.6 < r_e(arcsec) < 0.9$	-5.08 ± 11.05	-11.31 ± 21.56	-26.36 ± 39.79
$0.9 < r_e(arcsec) < 2.0$	-6.38 ± 12.51	-13.74 ± 25.47	-32.49 ± 41.78

Table A.3: Relative errors (%) on the Structural Parameters depending on the apparent magnitude using five different PSFs (see A.3)

	$0 < n < 2$ galaxies	$2 < n < 4$ galaxies	$4 < n < 6$ galaxies	$6 < n < 8$ galaxies
$20.0 < H_{AB,input} < 20.5$				
$\delta L/L$	-0.15 ± 2.95	-3.39 ± 5.48	-9.09 ± 7.90	-14.50 ± 8.47
$\delta r_e/r_e$	0.79 ± 5.25	-4.95 ± 9.28	-14.69 ± 14.79	-26.56 ± 16.21
$\delta n/n$	-4.39 ± 10.97	-13.84 ± 16.60	-24.76 ± 19.20	-36.22 ± 19.58
$20.5 < H_{AB,input} < 21.0$				
$\delta L/L$	-0.14 ± 3.82	-3.44 ± 6.32	-9.31 ± 9.39	-15.08 ± 9.23
$\delta r_e/r_e$	0.20 ± 5.36	-4.57 ± 10.89	-16.51 ± 16.28	-26.97 ± 17.87
$\delta n/n$	-4.16 ± 11.25	-13.82 ± 17.91	-23.84 ± 19.20	-38.19 ± 19.64
$21.0 < H_{AB,input} < 21.5$				
$\delta L/L$	-0.57 ± 4.92	-3.68 ± 7.55	-9.49 ± 9.25	-14.29 ± 10.06
$\delta r_e/r_e$	-0.86 ± 7.00	-5.73 ± 13.66	-16.66 ± 18.67	-26.05 ± 18.35
$\delta n/n$	-5.76 ± 12.02	-15.86 ± 17.54	-26.63 ± 20.50	-36.08 ± 19.52
$21.5 < H_{AB,input} < 22.0$				
$\delta L/L$	-0.49 ± 5.53	-4.59 ± 10.36	-9.94 ± 12.10	-14.68 ± 11.82
$\delta r_e/r_e$	-0.29 ± 7.33	-7.05 ± 17.72	-17.91 ± 22.02	-25.85 ± 24.09
$\delta n/n$	-6.04 ± 13.43	-16.61 ± 18.69	-27.84 ± 22.26	-36.30 ± 22.71
$22.0 < H_{AB,input} < 22.5$				
$\delta L/L$	-1.47 ± 7.60	-4.71 ± 13.41	-11.55 ± 13.82	-14.61 ± 15.32
$\delta r_e/r_e$	-1.75 ± 9.51	-7.38 ± 19.43	-16.97 ± 25.13	-26.68 ± 26.94
$\delta n/n$	-8.18 ± 17.99	-18.82 ± 21.73	-28.87 ± 22.24	-39.18 ± 24.90
$22.5 < H_{AB,input} < 23.0$				
$\delta L/L$	-1.67 ± 10.03	-5.89 ± 16.50	-11.89 ± 18.38	-17.96 ± 21.49
$\delta r_e/r_e$	-1.28 ± 11.40	-9.24 ± 26.02	-17.99 ± 29.22	-27.32 ± 34.57
$\delta n/n$	-8.25 ± 22.92	-18.29 ± 26.96	-29.25 ± 27.00	-41.66 ± 26.64
$23.0 < H_{AB,input} < 23.5$				
$\delta L/L$	-3.80 ± 19.13	-7.12 ± 22.24	-14.63 ± 19.75	-16.61 ± 24.12
$\delta r_e/r_e$	-2.84 ± 21.33	-10.78 ± 32.29	-20.79 ± 34.39	-25.78 ± 39.19
$\delta n/n$	-7.49 ± 29.62	-20.09 ± 33.28	-32.47 ± 31.11	-42.58 ± 29.90
$23.5 < H_{AB,input} < 24.0$				
$\delta L/L$	-1.89 ± 22.85	-10.19 ± 22.94	-14.19 ± 25.32	-20.52 ± 24.32
$\delta r_e/r_e$	-2.21 ± 27.87	-11.57 ± 35.12	-20.76 ± 39.58	-31.83 ± 41.51
$\delta n/n$	-3.87 ± 38.56	-24.95 ± 36.87	-36.53 ± 34.02	-46.46 ± 31.09
$24.0 < H_{AB,input} < 24.5$				
$\delta L/L$	-1.50 ± 25.40	-10.23 ± 32.27	-16.10 ± 34.15	-16.71 ± 36.33
$\delta r_e/r_e$	-3.60 ± 35.90	-14.78 ± 43.22	-30.37 ± 42.96	-30.21 ± 45.39
$\delta n/n$	-10.32 ± 42.23	-32.03 ± 42.13	-47.21 ± 38.40	-51.98 ± 36.24
$24.5 < H_{AB,input} < 25.0$				
$\delta L/L$	3.48 ± 38.67	-0.99 ± 47.79	-7.13 ± 48.32	-17.63 ± 39.12
$\delta r_e/r_e$	-11.83 ± 45.10	-24.02 ± 44.12	-33.58 ± 47.25	-36.64 ± 47.00
$\delta n/n$	-17.46 ± 48.50	-42.41 ± 46.73	-45.35 ± 44.40	-53.14 ± 39.50

Table A.4: Relative errors (%) on the Structural Parameters using five different PSFs (see A.4)

$\delta r_e/r_e$	$20 < H_{AB} < 21.5$	$21.5 < H_{AB} < 23$	$23 < H_{AB} < 25$
$0 < n < 2$	0.06 ± 5.77	-1.16 ± 9.59	-4.66 ± 32.39
$2 < n < 4$	-5.12 ± 11.07	-8.03 ± 21.95	-14.81 ± 38.86
$4 < n < 6$	-15.72 ± 16.22	-17.63 ± 25.57	-25.64 ± 41.12
$6 < n < 8$	-26.47 ± 17.73	-26.40 ± 29.20	-30.86 ± 43.40
$0.15 < r_e(arcsec) < 0.3$	-4.88 ± 13.91	-2.74 ± 16.53	-0.63 ± 31.95
$0.3 < r_e(arcsec) < 0.6$	-12.01 ± 15.03	-10.85 ± 19.95	-12.85 ± 34.54
$0.6 < r_e(arcsec) < 0.9$	-14.19 ± 17.17	-16.98 ± 24.64	-19.68 ± 40.32
$0.9 < r_e(arcsec) < 2.0$	-17.15 ± 21.19	-21.85 ± 30.48	-37.75 ± 43.51
$\delta n/n$	$20 < H_{AB} < 21.5$	$21.5 < H_{AB} < 23$	$23 < H_{AB} < 25$
$0 < n < 2$	-4.89 ± 11.68	-7.60 ± 18.65	-9.07 ± 39.19
$2 < n < 4$	-14.57 ± 17.28	-17.79 ± 22.82	-29.09 ± 40.43
$4 < n < 6$	-25.06 ± 19.75	-28.64 ± 23.92	-39.53 ± 37.22
$6 < n < 8$	-36.86 ± 19.70	-39.00 ± 24.87	-48.32 ± 34.49
$0.15 < r_e(arcsec) < 0.3$	-37.61 ± 22.17	-37.41 ± 24.34	-35.55 ± 39.30
$0.3 < r_e(arcsec) < 0.6$	-21.64 ± 20.35	-22.08 ± 24.19	-29.12 ± 39.11
$0.6 < r_e(arcsec) < 0.9$	-16.58 ± 18.55	-19.83 ± 23.63	-29.86 ± 40.01
$0.9 < r_e(arcsec) < 2.0$	-13.81 ± 17.93	-19.11 ± 25.80	-35.62 ± 42.06

Appendix B

Useful abbreviations

ACS	Advanced Camera for Surveys (Instrument aboard HST)
AO	Adaptive Optics
AGN	Active Galactic Nuclei
BCG	Brightest Cluster Galaxies
CANDELS	Cosmic Assembly Near-Infrared Deep Extragalactic Legacy Survey
CCD	Charge Coupled Device
CMB	Cosmic Microwave Background
DM	Dark Matter
FITS	Flexible Image Transport System (Standard format of astronomical images)
FWHM	Full Width at Half Maximum
GNS	GOODS NICMOS Survey
GOODS	Great Observatories Origins Deep Survey
GRB	Gamma-Ray Burst
HST	Hubble Space Telescope
IFU	Integral Field Unit
IGM	InterGalactic Medium
IMF	Initial Mass Function
IR	InfraRed
IRAC	Infrared Array Camera (Instrument aboard Spitzer telescope)
PSF	Point Spread Function
QSO	Quasi Stellar Objects or Quasars
NICMOS	Near Infrared Camera and Multi-Object Spectrometer (Instrument aboard HST)
NIR	Near InfraRed
SDSS	Sloan Digital Sky Survey
SED	Spectral Energy Distribution
SFR	Star Formation Rate
SSFR	Specific Star Formation Rate
SMBH	Super Massive Black Hole
SNe	Supernovae
UV	UltraViolet
WFC3	Wide Field Camera 3 (Instrument aboard HST)
ΛCDM	Λ Cold Dark Matter

Bibliography

Abazajian K. N., Adelman-McCarthy J. K., Agüeros M. A., Allam S. S., Allende Prieto C., An D., Anderson K. S. J., Anderson S. F., Annis J., Bahcall N. A., et al., 2009. ApJS, **182**, 543.

Abraham R. G., Tanvir N. R., Santiago B. X., Ellis R. S., Glazebrook K., van den Bergh S., 1996. MNRAS, **279**, L47.

Baldry I. K., Glazebrook K., Brinkmann J., Ivezić Ž., Lupton R. H., Nichol R. C., Szalay A. S., 2004. ApJ, **600**, 681.

Balestra I., Mainieri V., Popesso P., Dickinson M., Nonino M., Rosati P., Teimoorinia H., Vanzella E., Cristiani S., Cesarsky C., Fosbury R. A. E., Kuntschner H., Rettura A., 2010. *VizieR Online Data Catalog*, **3512**, 29012.

Bamford S. P., Aragón-Salamanca A., Milvang-Jensen B., 2006. MNRAS, **366**, 308.

Barden M., Rix H.-W., Somerville R. S., Bell E. F., Häußler B., Peng C. Y., Borch A., Beckwith S. V. W., Caldwell J. A. R., Heymans C., Jahnke K., Jogee S., McIntosh D. H., Meisenheimer K., Sánchez S. F., Wisotzki L., Wolf C., 2005. ApJ, **635**, 959.

Barden M., Jahnke K., Häußler B., 2008. ApJS, **175**, 105.

Barger A. J., Cowie L. L., Wang W.-H., 2008. ApJ, **689**, 687.

Barger A. J., Cowie L. L., Mushotzky R. F., Yang Y., Wang W.-H., Steffen A. T., Capak P., 2005. AJ, **129**, 578.

Barro G., Pérez-González P. G., Gallego J., Ashby M. L. N., Kajisawa M., Miyazaki S., Villar V., Yamada T., Zamorano J., 2011. ApJS, **193**, 13.

Bauer A. E., Conselice C. J., Pérez-González P. G., Grützbauch R., Bluck A. F. L., Buitrago F., Mortlock A., 2011. MNRAS, **417**, 289.

Baugh C. M., 2006. *Reports on Progress in Physics*, **69**, 3101.

Becker R. H., Fan X., White R. L., Strauss M. A., Narayanan V. K., Lupton R. H., Gunn J. E., Annis J., Bahcall N. A., Brinkmann J., Connolly A. J., Csabai I., Czarapata P. C., Doi M., Heckman T. M., Hennessy G. S., Ivezić Ž., Knapp G. R., Lamb D. Q., McKay T. A., Munn J. A., Nash T., Nichol R., Pier J. R., Richards G. T., Schneider D. P., Stoughton C., Szalay A. S., Thakar A. R., York D. G., 2001. AJ, **122**, 2850.

Beckwith S. V. W., Stiavelli M., Koekemoer A. M., Caldwell J. A. R., Ferguson H. C., Hook R., Lucas R. A., Bergeron L. E., Corbin M., Jogee S., Panagia N., Robberto M., Royle P., Somerville R. S., Sosey M., 2006. AJ, **132**, 1729.

Bedregal A. G., Aragón-Salamanca A., Merrifield M. R., 2006. MNRAS, **373**, 1125.

Bedregal A. G., Colina L., Alonso-Herrero A., Arribas S., 2009. ApJ, **698**, 1852.

Bell E. F., de Jong R. S., 2001. ApJ, **550**, 212.

Bell E. F., McIntosh D. H., Katz N., Weinberg M. D., 2003. ApJS, **149**, 289.

Bender R., Saglia R. P., Gerhard O. E., 1994. MNRAS, **269**, 785.

Benítez N., 2000. ApJ, **536**, 571.

Benson A. J., Bower R. G., Frenk C. S., Lacey C. G., Baugh C. M., Cole S., 2003. ApJ, **599**, 38.

Bernardi M., Sheth R. K., Nichol R. C., Miller C. J., Schlegel D., Frieman J., Schneider D. P., Subbarao M., York D. G., Brinkmann J., 2006. AJ, **131**, 2018.

Bertin E., Arnouts S., 1996. A&AS, **117**, 393.

Bezanson R., van Dokkum P. G., Tal T., Marchesini D., Kriek M., Franx M., Coppi P., 2009. ApJ, **697**, 1290.

Binney J., 2005. MNRAS, **363**, 937.

Blain A. W., Smail I., Ivison R. J., Kneib J.-P., Frayer D. T., 2002. Phys. Rep., **369**, 111.

Blanton M. R., Roweis S., 2007. AJ, **133**, 734.

Blanton M. R., Schlegel D. J., Strauss M. A., Brinkmann J., Finkbeiner D., Fukugita M., Gunn J. E., Hogg D. W., Ivezić Ž., Knapp G. R., Lupton R. H., Munn J. A., Schneider D. P., Tegmark M., Zehavi I., 2005. AJ, **129**, 2562.

Bluck A. F. L., Conselice C. J., Bouwens R. J., Daddi E., Dickinson M., Papovich C., Yan H., 2009. MNRAS, **394**, L51.

Bluck A. F. L., Conselice C. J., Almaini O., Laird E. S., Nandra K., Grützbauch R., 2011. MNRAS, **410**, 1174.

Böhm A., Ziegler B. L., Saglia R. P., Bender R., Fricke K. J., Gabasch A., Heidt J., Mehlert D., Noll S., Seitz S., 2004. A&A, **420**, 97.

Bolzonella M., Miralles J.-M., Pelló R., 2000. A&A, **363**, 476.

Bonnet H., Abuter R., Baker A., Bornemann W., Brown A., Castillo R., Conzelmann R., Damster R., Davies R., Delabre B., Donaldson R., Dumas C., Eisenhauer F., Elswijk E., Fedrigo E., Finger G., Gemperlein H., Genzel R., Gilbert A., Gillet G., Goldbrunner A., Horrobin M., Ter Horst R., Huber S., Hubin N., Iserlohe C., Kaufer

A., Kissler-Patig M., Kragt J., Kroes G., Lehnert M., Lieb W., Liske J., Lizon J.-L., Lutz D., Modigliani A., Monnet G., Nesvadba N., Patig J., Pragt J., Reunanen J., Röhrle C., Rossi S., Schmutzer R., Schoenmaker T., Schreiber J., Stroebele S., Szeifert T., Tacconi L., Tecza M., Thatte N., Tordo S., van der Werf P., Weisz H., 2004. *The Messenger*, **117**, 17.

Bouché N., Dekel A., Genzel R., Genel S., Cresci G., Förster Schreiber N. M., Shapiro K. L., Davies R. I., Tacconi L., 2010. ApJ, **718**, 1001.

Bournaud F., Chapon D., Teyssier R., Powell L. C., Elmegreen B. G., Elmegreen D. M., Duc P.-A., Contini T., Epinat B., Shapiro K. L., 2011. ApJ, **730**, 4.

Bournaud F., Jog C. J., Combes F., 2007. A&A, **476**, 1179.

Bouwens R. J., Illingworth G. D., Blakeslee J. P., Broadhurst T. J., Franx M., 2004. ApJ, **611**, L1.

Bouwens R. J., Illingworth G. D., Labbe I., Oesch P. A., Trenti M., Carollo C. M., van Dokkum P. G., Franx M., Stiavelli M., González V., Magee D., Bradley L., 2011. Nature, **469**, 504.

Boylan-Kolchin M., Springel V., White S. D. M., Jenkins A., Lemson G., 2009. MNRAS, **398**, 1150.

Boylan-Kolchin M., Ma C.-P., Quataert E., 2006. MNRAS, **369**, 1081.

Bruzual G., Charlot S., 2003. MNRAS, **344**, 1000.

Buitrago F., Trujillo I., Conselice C. J., Bouwens R. J., Dickinson M., Yan H., 2008. ApJ, **687**, L61.

Bundy K., Ellis R. S., Conselice C. J., Taylor J. E., Cooper M. C., Willmer C. N. A., Weiner B. J., Coil A. L., Noeske K. G., Eisenhardt P. R. M., 2006. ApJ, **651**, 120.

Bundy K., Fukugita M., Ellis R. S., Targett T. A., Belli S., Kodama T., 2009. ApJ, **697**, 1369.

Butcher H., Oemler, Jr. A., 1984. ApJ, **285**, 426.

Calura F., Menci N., 2011. MNRAS, **413**, L1.

Calzetti D., Armus L., Bohlin R. C., Kinney A. L., Koornneef J., Storchi-Bergmann T., 2000. ApJ, **533**, 682.

Cappellari M., Emsellem E., Bacon R., Bureau M., Davies R. L., de Zeeuw P. T., Falcón-Barroso J., Krajnović D., Kuntschner H., McDermid R. M., Peletier R. F., Sarzi M., van den Bosch R. C. E., van de Ven G., 2007. MNRAS, **379**, 418.

Cappellari M., di Serego Alighieri S., Cimatti A., Daddi E., Renzini A., Kurk J. D., Cassata P., Dickinson M., Franceschini A., Mignoli M., Pozzetti L., Rodighiero G., Rosati P., Zamorani G., 2009. ApJ, **704**, L34.

Cappellari M., Emsellem E., Krajnović D., McDermid R. M., Scott N., Verdoes Kleijn G. A., Young L. M., Alatalo K., Bacon R., Blitz L., Bois M., Bournaud F., Bureau M., Davies R. L., Davis T. A., de Zeeuw P. T., Duc P.-A., Khochfar S., Kuntschner H., Lablanche P.-Y., Morganti R., Naab T., Oosterloo T., Sarzi M., Serra P., Weijmans A.-M., 2011. MNRAS, **413**, 813.

Carrasco E. R., Conselice C. J., Trujillo I., 2010. MNRAS, **405**, 2253.

Cassata P., Giavalisco M., Guo Y., Ferguson H., Koekemoer A. M., Renzini A., Fontana A., Salimbeni S., Dickinson M., Casertano S., Conselice C. J., Grogin N., Lotz J. M., Papovich C., Lucas R. A., Straughn A., Gardner J. P., Moustakas L., 2010. ApJ, **714**, L79.

Cassata P., Giavalisco M., Guo Y., Renzini A., Ferguson H., Koekemoer A. M., Salimbeni S., Scarlata C., Grogin N. A., Conselice C. J., Dahlen T., Lotz J. M., Dickinson M., Lin L., 2011. ApJ, **743**, 96.

Cava A., Rodighiero G., Pérez-Fournon I., Buitrago F., Trujillo I., other authors in alphabetical order, 2010. MNRAS, **409**, L19.

Cenarro A. J., Trujillo I., 2009. ApJ, **696**, L43.

Ceverino D., Dekel A., Bournaud F., 2010. MNRAS, **404**, 2151.

Chabrier G., 2003. PASP, **115**, 763.

Cimatti A., Cassata P., Pozzetti L., Kurk J., Mignoli M., Renzini A., Daddi E., Bolzonella M., Brusa M., Rodighiero G., Dickinson M., Franceschini A., Zamorani G., Berta S., Rosati P., Halliday C., 2008. A&A, **482**, 21.

Coil A. L., Davis M., Madgwick D. S., Newman J. A., Conselice C. J., Cooper M., Ellis R. S., Faber S. M., Finkbeiner D. P., Guhathakurta P., Kaiser N., Koo D. C., Phillips A. C., Steidel C. C., Weiner B. J., Willmer C. N. A., Yan R., 2004a. ApJ, **609**, 525.

Coil A. L., Newman J. A., Kaiser N., Davis M., Ma C.-P., Kocevski D. D., Koo D. C., 2004b. ApJ, **617**, 765.

Cole S., Norberg P., Baugh C. M., Frenk C. S., other authors in alphabetical order, 2001. MNRAS, **326**, 255.

Collister A. A., Lahav O., 2004. PASP, **116**, 345.

Conselice C. J., Blackburne J. A., Papovich C., 2005. ApJ, **620**, 564.

Conselice C. J., Bershady M. A., Dickinson M., Papovich C., 2003. AJ, **126**, 1183.

Conselice C. J., Bundy K., Ellis R. S., Brichmann J., Vogt N. P., Phillips A. C., 2005. ApJ, **628**, 160.

Conselice C. J., Bundy K., Trujillo I., Coil A., Eisenhardt P., Ellis R. S., Georgakakis A., Huang J., Lotz J., Nandra K., Newman J., Papovich C., Weiner B., Willmer C., 2007. MNRAS, **381**, 962.

Conselice C. J., Bluck A. F. L., Buitrago F., Bauer A. E., Grützbauch R., Bouwens R. J., Bevan S., Mortlock A., Dickinson M., Daddi E., Yan H., Scott D., Chapman S. C., Chary R.-R., Ferguson H. C., Giavalisco M., Grogin N., Illingworth G., Jogee S., Koekemoer A. M., Lucas R. A., Mobasher B., Moustakas L., Papovich C., Ravindranath S., Siana B., Teplitz H., Trujillo I., Urry M., Weinzirl T., 2011a. MNRAS, **413**, 80.

Conselice C. J., Bluck A. F. L., Ravindranath S., Mortlock A., Koekemoer A. M., Buitrago F., Grützbauch R., Penny S. J., 2011b. MNRAS, **417**, 2770.

Conselice C. J., Yang C., Bluck A. F. L., 2009. MNRAS, **394**, 1956.

Conselice C. J., 2006. ApJ, **638**, 686.

Cooper M. C., Aird J. A., Coil A. L., Davis M., Faber S. M., Juneau S., Lotz J. M., Nandra K., Newman J. A., Willmer C. N. A., Yan R., 2011. *VizieR Online Data Catalog*, **2193**, 30014.

Cowie L. L., Songaila A., Hu E. M., Cohen J. G., 1996. AJ, **112**, 839.

Cresci G., Hicks E. K. S., Genzel R., Schreiber N. M. F., Davies R., Bouché N., Buschkamp P., Genel S., Shapiro K., Tacconi L., Sommer-Larsen J., Burkert A., Eisenhauer F., Gerhard O., Lutz D., Naab T., Sternberg A., Cimatti A., Daddi E., Erb D. K., Kurk J., Lilly S. L., Renzini A., Shapley A., Steidel C. C., Caputi K., 2009. ApJ, **697**, 115.

Croton D. J., Springel V., White S. D. M., De Lucia G., Frenk C. S., Gao L., Jenkins A., Kauffmann G., Navarro J. F., Yoshida N., 2006. MNRAS, **365**, 11.

Daddi E., Cimatti A., Renzini A., Fontana A., Mignoli M., Pozzetti L., Tozzi P., Zamorani G., 2004. ApJ, **617**, 746.

Daddi E., Renzini A., Pirzkal N., Cimatti A., Malhotra S., Stiavelli M., Xu C., Pasquali A., Rhoads J. E., Brusa M., di Serego Alighieri S., Ferguson H. C., Koekemoer A. M., Moustakas L. A., Panagia N., Windhorst R. A., 2005. ApJ, **626**, 680.

Daddi E., Dickinson M., Morrison G., Chary R., Cimatti A., Elbaz D., Frayer D., Renzini A., Pope A., Alexander D. M., Bauer F. E., Giavalisco M., Huynh M., Kurk J., Mignoli M., 2007. ApJ, **670**, 156.

Damjanov I., McCarthy P. J., Abraham R. G., Glazebrook K., Yan H., Mentuch E., Le Borgne D., Savaglio S., Crampton D., Murowinski R., Juneau S., Carlberg R. G., Jørgensen I., Roth K., Chen H.-W., Marzke R. O., 2009. ApJ, **695**, 101.

Damjanov I., Abraham R. G., Glazebrook K., McCarthy P. J., Caris E., Carlberg R. G., Chen H.-W., Crampton D., Green A. W., Jørgensen I., Juneau S., Le Borgne D., Marzke R. O., Mentuch E., Murowinski R., Roth K., Savaglio S., Yan H., 2011. ApJ, **739**, L44.

Dasyra K. M., Yan L., Helou G., Surace J., Sajina A., Colbert J., 2008. ApJ, **680**, 232.

Davies R. I., 2007. MNRAS, **375**, 1099.

Davis T. A., Bureau M., Young L. M., Alatalo K., Blitz L., Cappellari M., Scott N., Bois M., Bournaud F., Davies R. L., de Zeeuw P. T., Emsellem E., Khochfar S., Krajnović D., Kuntschner H., Lablanche P.-Y., McDermid R. M., Morganti R., Naab T., Oosterloo T., Sarzi M., Serra P., Weijmans A.-M., 2011. MNRAS, **414**, 968.

De Lucia G., Springel V., White S. D. M., Croton D., Kauffmann G., 2006. MNRAS, **366**, 499.

de Ravel L., Le Fèvre O., Tresse L., Bottini D., Garilli B., Le Brun V., Maccagni D., Scaramella R., Scodeggio M., Vettolani G., Zanichelli A., Adami C., Arnouts S., Bardelli S., Bolzonella M., Cappi A., Charlot S., Ciliegi P., Contini T., Foucaud S., Franzetti P., Gavignaud I., Guzzo L., Ilbert O., Iovino A., Lamareille F., McCracken H. J., Marano B., Marinoni C., Mazure A., Meneux B., Merighi R., Paltani S., Pellò R., Pollo A., Pozzetti L., Radovich M., Vergani D., Zamorani G., Zucca E., Bondi M., Bongiorno A., Brinchmann J., Cucciati O., de La Torre S., Gregorini L., Memeo P., Perez-Montero E., Mellier Y., Merluzzi P., Temporin S., 2009. A&A, **498**, 379.

de Vaucouleurs G., 1948. *Annales d'Astrophysique*, **11**, 247.

de Zeeuw P. T., Bureau M., Emsellem E., Bacon R., Carollo C. M., Copin Y., Davies R. L., Kuntschner H., Miller B. W., Monnet G., Peletier R. F., Verolme E. K., 2002. MNRAS, **329**, 513.

Dekel A., Birnboim Y., Engel G., Freundlich J., Goerdt T., Mumcuoglu M., Neistein E., Pichon C., Teyssier R., Zinger E., 2009. Nature, **457**, 451.

Delgado-Serrano R., Hammer F., Yang Y. B., Puech M., Flores H., Rodrigues M., 2010. A&A, **509**, A78+.

Dib S., Bell E., Burkert A., 2006. ApJ, **638**, 797.

Dickinson M., Giavalisco M., GOODS Team, 2003. In: *The Mass of Galaxies at Low and High Redshift*, p. 324, ed. R. Bender & A. Renzini.

Dressler A., 1980. ApJ, **236**, 351.

Efstathiou G., Jones B. J. T., 1979. MNRAS, **186**, 133.

Eggen O. J., Lynden-Bell D., Sandage A. R., 1962. ApJ, **136**, 748.

Eisenhauer F., Abuter R., Bickert K., Biancat-Marchet F., Bonnet H., Brynnel J., Conzelmann R. D., Delabre B., Donaldson R., Farinato J., Fedrigo E., Genzel R., Hubin N. N., Iserlohe C., Kasper M. E., Kissler-Patig M., Monnet G. J., Roehrle C., Schreiber J., Stroebele S., Tecza M., Thatte N. A., Weisz H., 2003. In: *Society of Photo-Optical Instrumentation Engineers (SPIE) Conference Series*, p. 1548, ed. M. Iye & A. F. M. Moorwood.

Eliche-Moral M. C., Prieto M., Gallego J., Barro G., Zamorano J., López-Sanjuan C., Balcells M., Guzmán R., Muñoz-Mateos J. C., 2010. A&A, **519**, A55+.

Elmegreen D. M., Elmegreen B. G., Rubin D. S., Schaffer M. A., 2005. ApJ, **631**, 85.

Emsellem E., Cappellari M., Krajnović D., Alatalo K., Blitz L., Bois M., Bournaud F., Bureau M., Davies R. L., Davis T. A., de Zeeuw P. T., Khochfar S., Kuntschner H., Lablanche P.-Y., McDermid R. M., Morganti R., Naab T., Oosterloo T., Sarzi M., Scott N., Serra P., van de Ven G., Weijmans A.-M., Young L. M., 2011. MNRAS, **414**, 888.

Epinat B., Contini T., Le Fèvre O., Vergani D., Garilli B., Amram P., Queyrel J., Tasca L., Tresse L., 2009. A&A, **504**, 789.

Epinat B., Amram P., Balkowski C., Marcelin M., 2010. MNRAS, **401**, 2113.

Erb D. K., Steidel C. C., Shapley A. E., Pettini M., Reddy N. A., Adelberger K. L., 2006. ApJ, **647**, 128.

Faber S. M., Jackson R. E., 1976. ApJ, **204**, 668.

Faber S. M., Phillips A. C., Kibrick R. I., Alcott B., Allen S. L., Burrous J., Cantrall T., Clarke D., Coil A. L., Cowley D. J., Davis M., Deich W. T. S., Dietsch K., Gilmore D. K., Harper C. A., Hilyard D. F., Lewis J. P., McVeigh M., Newman J., Osborne J., Schiavon R., Stover R. J., Tucker D., Wallace V., Wei M., Wirth G., Wright C. A., 2003. In: *Society of Photo-Optical Instrumentation Engineers (SPIE) Conference Series*, p. 1657, ed. M. Iye & A. F. M. Moorwood.

Faber S. M., Willmer C. N. A., Wolf C., Koo D. C., Weiner B. J., Newman J. A., Im M., other authors in alphabetical order, 2007. ApJ, **665**, 265.

Fan L., Lapi A., De Zotti G., Danese L., 2008. ApJ, **689**, L101.

Fan L., Lapi A., Bressan A., Bernardi M., De Zotti G., Danese L., 2010. ApJ, **718**, 1460.

Fantin D. S. M., Merrifield M. R., Green A. M., 2008. MNRAS, **390**, 1055.

Feldmann R., Carollo C. M., Mayer L., 2011. ApJ, **736**, 88.

Fernández Lorenzo M., Cepa J., Bongiovanni A., Castañeda H., Pérez García A. M., Lara-López M. A., Pović M., Sánchez-Portal M., 2009. A&A, **496**, 389.

Fernández Lorenzo M., Cepa J., Bongiovanni A., Pérez García A. M., Lara-López M. A., Pović M., Sánchez-Portal M., 2010. A&A, **521**, A27+.

Ferrarese L., Merritt D., 2000. ApJ, **539**, L9.

Ferreras I., Lisker T., Pasquali A., Khochfar S., Kaviraj S., 2009. MNRAS, **396**, 1573.

Ferreras I., Pasquali A., Rogers B. *Does Environment Affect the Star Formation Histories of Early-Type Galaxies?*, 103. 2011.

Fioc M., Rocca-Volmerange B., 1997. A&A, **326**, 950.

Flores H., Hammer F., Puech M., Amram P., Balkowski C., 2006. A&A, **455**, 107.

Fontanot F., De Lucia G., Monaco P., Somerville R. S., Santini P., 2009. MNRAS, **397**, 1776.

Förster Schreiber N. M., Genzel R., Bouché N., Cresci G., Davies R., Buschkamp P., Shapiro K., Tacconi L. J., Hicks E. K. S., Genel S., Shapley A. E., Erb D. K., Steidel C. C., Lutz D., Eisenhauer F., Gillessen S., Sternberg A., Renzini A., Cimatti A., Daddi E., Kurk J., Lilly S., Kong X., Lehnert M. D., Nesvadba N., Verma A., McCracken H., Arimoto N., Mignoli M., Onodera M., 2009. ApJ, **706**, 1364.

Förster Schreiber N. M., Shapley A. E., Erb D. K., Genzel R., Steidel C. C., Bouché N., Cresci G., Davies R., 2011a. ApJ, **731**, 65.

Förster Schreiber N. M., Shapley A. E., Genzel R., Bouché N., Cresci G., Davies R., Erb D. K., Genel S., Lutz D., Newman S., Shapiro K. L., Steidel C. C., Sternberg A., Tacconi L. J., 2011b. ApJ, **739**, 45.

Freeman K. C., 1970. ApJ, **160**, 811.

Freese K., Ilie C., Spolyar D., Valluri M., Bodenheimer P., 2010. ApJ, **716**, 1397.

Gargiulo A., Saracco P., Longhetti M., 2011. MNRAS, **412**, 1804.

Geach J. E., Smail I., Best P. N., Kurk J., Casali M., Ivison R. J., Coppin K., 2008. MNRAS, **388**, 1473.

Genzel R., Burkert A., Bouché N., Cresci G., Förster Schreiber N. M., Shapley A., Shapiro K., Tacconi L. J., Buschkamp P., Cimatti A., Daddi E., Davies R., Eisenhauer F., Erb D. K., Genel S., Gerhard O., Hicks E., Lutz D., Naab T., Ott T., Rabien S., Renzini A., Steidel C. C., Sternberg A., Lilly S. J., 2008. ApJ, **687**, 59.

Giavalisco M., Ferguson H. C., Koekemoer A. M., Dickinson M., other authors in alphabetical order., 2004. ApJ, **600**, L93.

Giovanelli R., Haynes M. P., Herter T., Vogt N. P., Wegner G., Salzer J. J., da Costa L. N., Freudling W., 1997. AJ, **113**, 22.

Gnerucci A., Marconi A., Cresci G., Maiolino R., Mannucci F., Calura F., Cimatti A., Cocchia F., Grazian A., Matteucci F., Nagao T., Pozzetti L., Troncoso P., 2011. A&A, **528**, A88+.

Granato G. L., De Zotti G., Silva L., Bressan A., Danese L., 2004. ApJ, **600**, 580.

Gray M. E., Wolf C., Barden M., Peng C. Y., Häußler B., Bell E. F., McIntosh D. H., Guo Y., Caldwell J. A. R., Bacon D., Balogh M., Barazza F. D., Böhm A., Heymans C., Jahnke K., Jogee S., van Kampen E., Lane K., Meisenheimer K., Sánchez S. F., Taylor A., Wisotzki L., Zheng X., Green D. A., Beswick R. J., Saikia D. J., Gilmour R., Johnson B. D., Papovich C., 2009. MNRAS, **393**, 1275.

Greif T. H., Bromm V., 2006. MNRAS, **373**, 128.

Grogin N. A., Kocevski D. D., Faber S. M., Ferguson H. C., Koekemoer A. M., Riess, other authors by alphabetical order, 2011. ApJS, **197**, 35.

Grützbauch R., Chuter R. W., Conselice C. J., Bauer A. E., Bluck A. F. L., Buitrago F., Mortlock A., 2011a. MNRAS, **412**, 2361.

Grützbauch R., Conselice C. J., Varela J., Bundy K., Cooper M. C., Skibba R., Willmer C. N. A., 2011b. MNRAS, **411**, 929.

Gunn J. E., Gott, III J. R., 1972. ApJ, **176**, 1.

Guo Y., McIntosh D. H., Mo H. J., Katz N., van den Bosch F. C., Weinberg M., Weinmann S. M., Pasquali A., Yang X., 2009. MNRAS, **398**, 1129.

Guth A. H., 1981. Phys. Rev. D, **23**, 347.

Gutiérrez C. M., Trujillo I., Aguerri J. A. L., Graham A. W., Caon N., 2004. ApJ, **602**, 664.

Häring N., Rix H.-W., 2004. ApJ, **604**, L89.

Häussler B., McIntosh D. H., Barden M., Bell E. F., Rix H.-W., Borch A., Beckwith S. V. W., Caldwell J. A. R., Heymans C., Jahnke K., Jogee S., Koposov S. E., Meisenheimer K., Sánchez S. F., Somerville R. S., Wisotzki L., Wolf C., 2007. ApJS, **172**, 615.

Hogg D. W., 1999. *ArXiv Astrophysics e-prints*.

Hopkins P. F., Hernquist L., Cox T. J., Dutta S. N., Rothberg B., 2008. ApJ, **679**, 156.

Hopkins P. F., Bundy K., Murray N., Quataert E., Lauer T. R., Ma C.-P., 2009a. MNRAS, **398**, 898.

Hopkins P. F., Hernquist L., Cox T. J., Keres D., Wuyts S., 2009b. ApJ, **691**, 1424.

Hopkins P. F., Murray N., Quataert E., Thompson T. A., 2010. MNRAS, **401**, L19.

Hoyle F., 1948. MNRAS, **108**, 372.

Hubble E., Humason M. L., 1931. ApJ, **74**, 43.

Hubble E. P., 1926. ApJ, **64**, 321.

Huertas-Company M., Rouan D., Tasca L., Soucail G., Le Fèvre O., 2008. A&A, **478**, 971.

Huertas-Company M., Aguerri J. A. L., Bernardi M., Mei S., Sánchez Almeida J., 2011. A&A, **525**, A157+.

Hughes D. H., Serjeant S., Dunlop J., Rowan-Robinson M., Blain A., Mann R. G., Ivison R., Peacock J., Efstathiou A., Gear W., Oliver S., Lawrence A., Longair M., Goldschmidt P., Jenness T., 1998. Nature, **394**, 241.

Illingworth G., 1977. ApJ, **218**, L43.

Kassin S. A., Weiner B. J., Faber S. M., Koo D. C., Lotz J. M., Diemand J., Harker J. J., Bundy K., Metevier A. J., Phillips A. C., Cooper M. C., Croton D. J., Konidaris N., Noeske K. G., Willmer C. N. A., 2007. ApJ, **660**, L35.

Kauffmann G., White S. D. M., Guiderdoni B., 1993. MNRAS, **264**, 201.

Kaviraj S., 2010. MNRAS, **406**, 382.

Kereš D., Katz N., Weinberg D. H., Davé R., 2005. MNRAS, **363**, 2.

Khochfar S., Silk J., 2006. ApJ, **648**, L21.

Khochfar S., Silk J., 2009. MNRAS, **397**, 506.

Komatsu E., Smith K. M., Dunkley J., Bennett C. L., Gold B., Hinshaw G., Jarosik N., Larson D., Nolta M. R., Page L., Spergel D. N., Halpern M., Hill R. S., Kogut A., Limon M., Meyer S. S., Odegard N., Tucker G. S., Weiland J. L., Wollack E., Wright E. L., 2011. ApJS, **192**, 18.

Kormendy J., Richstone D., 1995. ARA&A, **33**, 581.

Kormendy J., 1977. ApJ, **218**, 333.

Krajnović D., Bacon R., Cappellari M., Davies R. L., de Zeeuw P. T., Emsellem E., Falcón-Barroso J., Kuntschner H., McDermid R. M., Peletier R. F., Sarzi M., van den Bosch R. C. E., van de Ven G., 2008. MNRAS, **390**, 93.

Kriek M., van Dokkum P. G., Franx M., Quadri R., Gawiser E., Herrera D., Illingworth G. D., Labbé I., Lira P., Marchesini D., Rix H.-W., Rudnick G., Taylor E. N., Toft S., Urry C. M., Wuyts S., 2006. ApJ, **649**, L71.

Kriek M., van Dokkum P. G., Franx M., Illingworth G. D., Magee D. K., 2009. ApJ, **705**, L71.

Larson R. B., Tinsley B. M., Caldwell C. N., 1980. ApJ, **237**, 692.

Laureijs R., Amiaux J., Arduini S., Augueres J. ., Brinchmann J., Cole R., Cropper M., Dabin C., Duvet L., Ealet A., et al., 2011. *ArXiv e-prints*.

Law D. R., Steidel C. C., Erb D. K., Larkin J. E., Pettini M., Shapley A. E., Wright S. A., 2007. ApJ, **669**, 929.

Law D. R., Steidel C. C., Erb D. K., Larkin J. E., Pettini M., Shapley A. E., Wright S. A., 2009. ApJ, **697**, 2057.

Lehnert M. D., Nesvadba N. P. H., Cuby J.-G., Swinbank A. M., Morris S., Clément B., Evans C. J., Bremer M. N., Basa S., 2010. Nature, **467**, 940.

Lemaître G., 1927. *Annales de la Societe Scietifique de Bruxelles*, **47**, 49.

Lemoine-Busserolle M., Lamareille F., 2010. MNRAS, **402**, 2291.

Liddle A., 2003. *An Introduction to Modern Cosmology, Second Edition*.

Lilly S. J., Le Fevre O., Hammer F., Crampton D., 1996. ApJ, **460**, L1+.

Lintott C., Schawinski K., Bamford S., Slosar A., Land K., Thomas D., Edmondson E., Masters K., Nichol R. C., Raddick M. J., Szalay A., Andreescu D., Murray P., Vandenberg J., 2011. MNRAS, **410**, 166.

Longhetti M., Saracco P., Severgnini P., Della Ceca R., Mannucci F., Bender R., Drory N., Feulner G., Hopp U., 2007. MNRAS, **374**, 614.

López-Sanjuan C., Balcells M., García-Dabó C. E., Prieto M., Cristóbal-Hornillos D., Eliche-Moral M. C., Abreu D., Erwin P., Guzmán R., 2009a. ApJ, **694**, 643.

López-Sanjuan C., Balcells M., Pérez-González P. G., Barro G., García-Dabó C. E., Gallego J., Zamorano J., 2009b. A&A, **501**, 505.

López-Sanjuan C., Balcells M., Pérez-González P. G., Barro G., Gallego J., Zamorano J., 2010a. A&A, **518**, A20+.

López-Sanjuan C., Balcells M., Pérez-González P. G., Barro G., García-Dabó C. E., Gallego J., Zamorano J., 2010b. ApJ, **710**, 1170.

López-Sanjuan C., Le Fèvre O., de Ravel L., Cucciati O., Ilbert O., Tresse L., Bardelli S., Bolzonella M., Contini T., Garilli B., Guzzo L., Maccagni D., McCracken H. J., Mellier Y., Pollo A., Vergani D., Zucca E., 2011. A&A, **530**, A20+.

Madau P., Ferguson H. C., Dickinson M. E., Giavalisco M., Steidel C. C., Fruchter A., 1996. MNRAS, **283**, 1388.

Magee D. K., Bouwens R. J., Illingworth G. D., 2007. In: *Astronomical Data Analysis Software and Systems XVI*, p. 261, ed. R. A. Shaw, F. Hill, & D. J. Bell.

Magorrian J., Tremaine S., Richstone D., Bender R., Bower G., Dressler A., Faber S. M., Gebhardt K., Green R., Grillmair C., Kormendy J., Lauer T., 1998. AJ, **115**, 2285.

Maltby D. T., Aragón-Salamanca A., Gray M. E., Barden M., Häußler B., Wolf C., Peng C. Y., Jahnke K., McIntosh D. H., Böhm A., van Kampen E., 2010. MNRAS, **402**, 282.

Mancini C., Daddi E., Renzini A., Salmi F., McCracken H. J., Cimatti A., Onodera M., Salvato M., Koekemoer A. M., Aussel H., Le Floc'h E., Willott C., Capak P., 2010. MNRAS, **401**, 933.

Maraston C., 2005. MNRAS, **362**, 799.

Markwardt C. B., 2009. In: *Astronomical Data Analysis Software and Systems XVIII*, p. 251, ed. D. A. Bohlender, D. Durand, & P. Dowler.

Martinez-Manso J., Guzman R., Barro G., Cenarro J., Perez-Gonzalez P., Sanchez-Blazquez P., Trujillo I., Balcells M., Cardiel N., Gallego J., Hempel A., Prieto M., 2011. ApJ, **738**, L22.

Masters K. L., Mosleh M., Romer A. K., Nichol R. C., Bamford S. P., Schawinski K., Lintott C. J., Andreescu D., Campbell H. C., Crowcroft B., Doyle I., Edmondson E. M., Murray P., Raddick M. J., Slosar A., Szalay A. S., Vandenberg J., 2010. MNRAS, **405**, 783.

Masters K. L., Springob C. M., Huchra J. P., 2008. AJ, **135**, 1738.

Matteucci F., 1994. A&A, **288**, 57.

McIntosh D. H., Bell E. F., Rix H.-W., Wolf C., Heymans C., Peng C. Y., Somerville R. S., Barden M., Beckwith S. V. W., Borch A., Caldwell J. A. R., Häußler B., Jahnke K., Jogee S., Meisenheimer K., Sánchez S. F., Wisotzki L., 2005. ApJ, **632**, 191.

McLure R. J., Dunlop J. S., Cirasuolo M., Koekemoer A. M., Sabbi E., Stark D. P., Targett T. A., Ellis R. S., 2010. MNRAS, **403**, 960.

Meurer G. R., Carignan C., Beaulieu S. F., Freeman K. C., 1996. AJ, **111**, 1551.

Michałowski M., Hjorth J., Watson D., 2010. A&A, **514**, A67+.

Milgrom M., 1983. ApJ, **270**, 365.

Mirny K., Modigliani A., Neeser M. J., Nürnberger D., 2010. In: *Society of Photo-Optical Instrumentation Engineers (SPIE) Conference Series*.

Mo H., van den Bosch F. C., White S., 2010. *Galaxy Formation and Evolution*.

Modigliani A., Hummel W., Abuter R., Amico P., Ballester P., Davies R., Dumas C., Horrobin M., Neeser M., Kissler-Patig M., Peron M., Rehunanen J., Schreiber J., Szeifert T., 2007. *ArXiv Astrophysics e-prints*.

Moore B., Lake G., Quinn T., Stadel J., 1999. MNRAS, **304**, 465.

Mortlock A., Conselice C. J., Bluck A. F. L., Bauer A. E., Grützbauch R., Buitrago F., Ownsworth J., 2011. MNRAS, **413**, 2845.

Muzzin A., Marchesini D., van Dokkum P. G., Labbé I., Kriek M., Franx M., 2009. ApJ, **701**, 1839.

Naab T., Trujillo I., 2006. MNRAS, **369**, 625.

Naab T., Johansson P. H., Ostriker J. P., 2009. ApJ, **699**, L178.

Nesvadba N. P. H., Lehnert M. D., Davies R. I., Verma A., Eisenhauer F., 2008. A&A, **479**, 67.

Newman A. B., Ellis R. S., Treu T., Bundy K., 2010. ApJ, **717**, L103.

Newman J. A., Cooper M. C., Davis M., Faber S. M., Coil A. L., Guhathakurta P., Koo D. C., Phillips A. C., Conroy C., Dutton A. A., Finkbeiner D. P., Gerke B. F., Rosario D. J., Weiner B. J., Willmer C. N. A., Yan R., Harker J. J., Kassin S. A., Konidaris N. P., Lai K., Madgwick D. S., Noeske K. G., Wirth G. D., Connolly A. J., Kaiser N., Kirby E. N., Lemaux B. C., Lin L., Lotz J. M., Luppino G. A., Marinoni C., Matthews D. J., Metevier A., Schiavon R. P., 2012. *ArXiv e-prints*.

Onodera M., Daddi E., Gobat R., Cappellari M., Arimoto N., Renzini A., Yamada Y., McCracken H. J., Mancini C., Capak P., Carollo M., Cimatti A., Giavalisco M., Ilbert O., Kong X., Lilly S., Motohara K., Ohta K., Sanders D. B., Scoville N., Tamura N., Taniguchi Y., 2010. ApJ, **715**, L6.

Oosterloo T., Morganti R., Crocker A., Jütte E., Cappellari M., de Zeeuw T., Krajnović D., McDermid R., Kuntschner H., Sarzi M., Weijmans A.-M., 2010. MNRAS, **409**, 500.

Oser L., Ostriker J. P., Naab T., Johansson P. H., Burkert A., 2010. ApJ, **725**, 2312.

Papovich C., Moustakas L. A., Dickinson M., Le Floc'h E., Rieke G. H., Daddi E., Alexander D. M., Bauer F., Brandt W. N., Dahlen T., Egami E., Eisenhardt P., Elbaz D., Ferguson H. C., Giavalisco M., Lucas R. A., Mobasher B., Pérez-González P. G., Stutz A., Rieke M. J., Yan H., 2006. ApJ, **640**, 92.

Patton D. R., Carlberg R. G., Marzke R. O., Pritchet C. J., da Costa L. N., Pellegrini P. S., 2000. ApJ, **536**, 153.

Peebles P. J. E., 1982. ApJ, **263**, L1.

Peng C. Y., Ho L. C., Impey C. D., Rix H.-W., 2002. AJ, **124**, 266.

Peng C. Y., Ho L. C., Impey C. D., Rix H.-W., 2010. AJ, **139**, 2097.

Penzias A. A., Wilson R. W., 1965. ApJ, **142**, 419.

Pérez-González P. G., Rieke G. H., Villar V., Barro G., Blaylock M., Egami E., Gallego J., Gil de Paz A., Pascual S., Zamorano J., Donley J. L., 2008a. ApJ, **675**, 234.

Pérez-González P. G., Trujillo I., Barro G., Gallego J., Zamorano J., Conselice C. J., 2008b. ApJ, **687**, 50.

Perlmutter S., Aldering G., Goldhaber G., Knop R. A., Nugent P., Castro P. G., Deustua S., Fabbro S., Goobar A., Groom D. E., Hook I. M., Kim A. G., Kim M. Y., Lee J. C., Nunes N. J., Pain R., Pennypacker C. R., Quimby R., Lidman C., Ellis R. S., Irwin M., McMahon R. G., Ruiz-Lapuente P., Walton N., Schaefer B., Boyle B. J., Filippenko A. V., Matheson T., Fruchter A. S., Panagia N., Newberg H. J. M., Couch W. J., The Supernova Cosmology Project, 1999. ApJ, **517**, 565.

Poggianti B. M., Fasano G., Bettoni D., Cava A., Dressler A., Vanzella E., Varela J., Couch W. J., D'Onofrio M., Fritz J., Kjaergaard P., Moles M., Valentinuzzi T., 2009. ApJ, **697**, L137.

Popesso P., Dickinson M., Nonino M., Vanzella E., Daddi E., Fosbury R. A. E., Kuntschner H., Mainieri V., Cristiani S., Cesarsky C., Giavalisco M., Renzini A., GOODS Team, 2009. A&A, **494**, 443.

Press W. H., Schechter P., 1974. ApJ, **187**, 425.

Pritchard J., Loeb A., 2010. Nature, **468**, 772.

Puech M., Flores H., Hammer F., Yang Y., Neichel B., Lehnert M., Chemin L., Nesvadba N., Epinat B., Amram P., Balkowski C., Cesarsky C., Dannerbauer H., di Serego Alighieri S., Fuentes-Carrera I., Guiderdoni B., Kembhavi A., Liang Y. C., Östlin G., Pozzetti L., Ravikumar C. D., Rawat A., Vergani D., Vernet J., Wozniak H., 2008. A&A, **484**, 173.

Queyrel J., Contini T., Pérez-Montero E., Garilli B., Le Fèvre O., Kissler-Patig M., Epinat B., Vergani D., Tresse L., Amram P., Lemoine-Busserolle M., 2009. A&A, **506**, 681.

Ragone-Figueroa C., Granato G. L., 2011. MNRAS, **414**, 3690.

Ravindranath S., Ferguson H. C., Conselice C., Giavalisco M., Dickinson M., Chatzichristou E., de Mello D., Fall S. M., Gardner J. P., Grogin N. A., Hornschemeier A., Jogee S., Koekemoer A., Kretchmer C., Livio M., Mobasher B., Somerville R., 2004. ApJ, **604**, L9.

Retzlaff J., Rosati P., Dickinson M., Vandame B., Rité C., Nonino M., Cesarsky C., GOODS Team, 2010. A&A, **511**, A50+.

Ricciardelli E., Trujillo I., Buitrago F., Conselice C. J., 2010. MNRAS, **406**, 230.

Riess A. G., Filippenko A. V., Challis P., Clocchiatti A., Diercks A., Garnavich P. M., Gilliland R. L., Hogan C. J., Jha S., Kirshner R. P., Leibundgut B., Phillips M. M., Reiss D., Schmidt B. P., Schommer R. A., Smith R. C., Spyromilio J., Stubbs C., Suntzeff N. B., Tonry J., 1998. AJ, **116**, 1009.

Robertson B. E., Ellis R. S., Dunlop J. S., McLure R. J., Stark D. P., 2010. Nature, **468**, 49.

Rousselot P., Lidman C., Cuby J.-G., Moreels G., Monnet G., 2000. A&A, **354**, 1134.

Rubin V. C., Thonnard N., Ford, Jr. W. K., 1978. ApJ, **225**, L107.

Rudnick G., Rix H.-W., Franx M., Labbé I., Blanton M., Daddi E., Förster Schreiber N. M., Moorwood A., Röttgering H., Trujillo I., van der Wel A., van der Werf P., van Dokkum P. G., van Starkenburg L., 2003. ApJ, **599**, 847.

Ryan, Jr. R. E., McCarthy P. J., Cohen S. H., Yan H., Hathi N. P., Koekemoer A. M., Rutkowski M. J., Mechtley M. R., Windhorst R. A., O'Connell R. W., other authors in alphabetical order, 2012. ApJ, **749**, 53.

Ryden B. S., Forbes D. A., Terlevich A. I., 2001. MNRAS, **326**, 1141.

Ryden B. S., 2004. ApJ, **601**, 214.

Salpeter E. E., 1955. ApJ, **121**, 161.

Sánchez S. F., Kennicutt R. C., Gil de Paz A., van de Ven G., Vílchez J. M., Wisotzki L., Walcher C. J., Mast D., Aguerri J. A. L., other authors in alphabetical order, 2012. A&A, **538**, A8.

Saracco P., Longhetti M., Andreon S., 2009. MNRAS, **392**, 718.

Schawinski K., Lintott C., Thomas D., Sarzi M., Andreescu D., Bamford S. P., Kaviraj S., Khochfar S., Land K., Murray P., Nichol R. C., Raddick M. J., Slosar A., Szalay A., Vandenberg J., Yi S. K., 2009. MNRAS, **396**, 818.

Scoville N., Aussel H., Brusa M., Capak P., Carollo C. M., Elvis M., Giavalisco M., Guzzo L., Hasinger G., Impey C., Kneib J.-P., LeFevre O., Lilly S. J., Mobasher B., Renzini A., Rich R. M., Sanders D. B., Schinnerer E., Schminovich D., Shopbell P., Taniguchi Y., Tyson N. D., 2007. ApJS, **172**, 1.

Sérsic J. L., 1968. *Atlas de galaxias australes*.

Shankar F., Marulli F., Bernardi M., Mei S., Meert A., Vikram V., 2011. *ArXiv e-prints*.

Shapiro K. L., Genzel R., Quataert E., Förster Schreiber N. M., Davies R., Tacconi L., Armus L., Bouché N., Buschkamp P., Cimatti A., Cresci G., Daddi E., Eisenhauer F., Erb D. K., Genel S., Hicks E. K. S., Lilly S. J., Lutz D., Renzini A., Shapley A., Steidel C. C., Sternberg A., 2009. ApJ, **701**, 955.

Shen S., Mo H. J., White S. D. M., Blanton M. R., Kauffmann G., Voges W., Brinkmann J., Csabai I., 2003. MNRAS, **343**, 978.

Shih H.-Y., Stockton A., 2011. ApJ, **733**, 45.

Silich S., Tenorio-Tagle G., Muñoz-Tuñón C., Hueyotl-Zahuantitla F., Wünsch R., Palouš J., 2010. ApJ, **711**, 25.

Smoot G. F., Bennett C. L., Kogut A., Wright E. L., Aymon J., Boggess N. W., Cheng E. S., de Amici G., Gulkis S., Hauser M. G., Hinshaw G., Jackson P. D., Janssen M., Kaita E., Kelsall T., Keegstra P., Lineweaver C., Loewenstein K., Lubin P., Mather J., Meyer S. S., Moseley S. H., Murdock T., Rokke L., Silverberg R. F., Tenorio L., Weiss R., Wilkinson D. T., 1992. ApJ, **396**, L1.

Sobral D., Best P. N., Smail I., Geach J. E., Cirasuolo M., Garn T., Dalton G. B., 2011. MNRAS, **411**, 675.

Spolyar D., Freese K., Gondolo P., 2008. *Physical Review Letters*, **100(5)**, 051101.

Steidel C. C., Giavalisco M., Pettini M., Dickinson M., Adelberger K. L., 1996. ApJ, **462**, L17+.

Steinhardt P. J., Turok N., 2002. *Science*, **296**, 1436.

Swinbank A. M., Smail I., Chapman S. C., Borys C., Alexander D. M., Blain A. W., Conselice C. J., Hainline L. J., Ivison R. J., 2010. MNRAS, **405**, 234.

Szomoru D., Franx M., van Dokkum P. G., 2012. ApJ, **749**, 121.

Tacconi L. J., Genzel R., Neri R., Cox P., Cooper M. C., Shapiro K., Bolatto A., Bouché N., Bournaud F., Burkert A., Combes F., Comerford J., Davis M., Schreiber N. M. F., Garcia-Burillo S., Gracia-Carpio J., Lutz D., Naab T., Omont A., Shapley A., Sternberg A., Weiner B., 2010. Nature, **463**, 781.

Targett T. A., Dunlop J. S., McLure R. J., Best P. N., Cirasuolo M., Almaini O., 2011. MNRAS, **412**, 295.

Taylor E. N., Franx M., Glazebrook K., Brinchmann J., van der Wel A., van Dokkum P. G., 2010. ApJ, **720**, 723.

Tegmark M., Silk J., Rees M. J., Blanchard A., Abel T., Palla F., 1997. ApJ, **474**, 1.

Thomas D., Maraston C., Bender R., Mendes de Oliveira C., 2005. ApJ, **621**, 673.

Toft S., van Dokkum P., Franx M., Labbe I., Förster Schreiber N. M., Wuyts S., Webb T., Rudnick G., Zirm A., Kriek M., van der Werf P., Blakeslee J. P., Illingworth G., Rix H.-W., Papovich C., Moorwood A., 2007. ApJ, **671**, 285.

Tonini C., Maraston C., Ziegler B., Böhm A., Thomas D., Devriendt J., Silk J., 2011. MNRAS, **415**, 811.

Toomre A., Toomre J., 1972. ApJ, **178**, 623.

Toomre A., 1977. ARA&A, **15**, 437.

Tresse L., Maddox S. J., Le Fèvre O., Cuby J.-G., 2002. MNRAS, **337**, 369.

Trujillo I., Carrasco E. R., Ferre-Mateu A., 2012. *ArXiv e-prints*.

Trujillo I., Feulner G., Goranova Y., Hopp U., Longhetti M., Saracco P., Bender R., Braito V., Della Ceca R., Drory N., Mannucci F., Severgnini P., 2006a. MNRAS, **373**, L36.

Trujillo I., Förster Schreiber N. M., Rudnick G., Barden M., Franx M., Rix H.-W., Caldwell J. A. R., McIntosh D. H., Toft S., Häussler B., Zirm A., van Dokkum P. G., Labbé I., Moorwood A., Röttgering H., van der Wel A., van der Werf P., van Starkenburg L., 2006b. ApJ, **650**, 18.

Trujillo I., Conselice C. J., Bundy K., Cooper M. C., Eisenhardt P., Ellis R. S., 2007. MNRAS, **382**, 109.

Trujillo I., Cenarro A. J., de Lorenzo-Cáceres A., Vazdekis A., de la Rosa I. G., Cava A., 2009. ApJ, **692**, L118.

Trujillo I., Ferreras I., de La Rosa I. G., 2011. MNRAS, **415**, 3903.

Trujillo I., Graham A. W., Caon N., 2001. MNRAS, **326**, 869.

Tully R. B., Fisher J. R., 1977. A&A, **54**, 661.

Twite J. W., Conselice C. J., Buitrago F., Noeske K., Weiner B. J., Acosta-Pulido J. A., Bauer A. E., 2012. MNRAS, **420**, 1061.

Ueda Y., Akiyama M., Ohta K., Miyaji T., 2003. ApJ, **598**, 886.

Valentinuzzi T., Fritz J., Poggianti B. M., Cava A., Bettoni D., Fasano G., D'Onofrio M., Couch W. J., Dressler A., Moles M., Moretti A., Omizzolo A., Kjærgaard P., Vanzella E., Varela J., 2010a. ApJ, **712**, 226.

Valentinuzzi T., Poggianti B. M., Saglia R. P., Aragón-Salamanca A., Simard L., Sánchez-Blázquez P., D'onofrio M., Cava A., Couch W. J., Fritz J., Moretti A., Vulcani B., 2010b. ApJ, **721**, L19.

van de Sande J., Kriek M., Franx M., van Dokkum P. G., Bezanson R., Whitaker K. E., Brammer G., Labbé I., Groot P. J., Kaper L., 2011. ApJ, **736**, L9+.

van den Bosch F. C., 2000. ApJ, **530**, 177.

van der Wel A., Rix H.-W., Wuyts S., McGrath E. J., Koekemoer A. M., Bell E. F., Holden B. P., Robaina A. R., McIntosh D. H., 2011. ApJ, **730**, 38.

van Dokkum P. G., Franx M., Kriek M., Holden B., Illingworth G. D., Magee D., Bouwens R., Marchesini D., Quadri R., Rudnick G., Taylor E. N., Toft S., 2008. ApJ, **677**, L5.

van Dokkum P. G., Whitaker K. E., Brammer G., Franx M., Kriek M., Labbé I., Marchesini D., Quadri R., Bezanson R., Illingworth G. D., Muzzin A., Rudnick G., Tal T., Wake D., 2010. ApJ, **709**, 1018.

van Dokkum P. G., Brammer G., Fumagalli M., Nelson E., Franx M., Rix H.-W., Kriek M., Skelton R. E., Patel S., Schmidt K. B., Bezanson R., Bian F., da Cunha E., Erb D. K., Fan X., Förster Schreiber N., Illingworth G. D., Labbé I., Lundgren B., Magee D., Marchesini D., McCarthy P., Muzzin A., Quadri R., Steidel C. C., Tal T., Wake D., Whitaker K. E., Williams A., 2011. ApJ, **743**, L15.

van Dokkum P. G., 2005. AJ, **130**, 2647.

Viero M. P., Moncelsi L., Mentuch E., Buitrago F., Bauer A. E., Chapin E. L., Conselice C. J., Devlin M. J., Halpern M., Marsden G., Netterfield C. B., Pascale E., Pérez-González P. G., Rex M., Scott D., Smith M. W. L., Truch M. D. P., Trujillo I., Wiebe D. V., 2012. MNRAS, **421**, 2161.

Vogt N. P., Forbes D. A., Phillips A. C., Gronwall C., Faber S. M., Illingworth G. D., Koo D. C., 1996. ApJ, **465**, L15.

Vogt N. P., Phillips A. C., Faber S. M., Gallego J., Gronwall C., Guzman R., Illingworth G. D., Koo D. C., Lowenthal J. D., 1997. ApJ, **479**, L121.

Weinzirl T., Jogee S., Conselice C. J., Papovich C., Chary R.-R., Bluck A., Grützbauch R., Buitrago F., Mobasher B., Lucas R. A., Dickinson M., Bauer A. E., 2011. ApJ, **743**, 87.

White S. D. M., Frenk C. S., 1991. ApJ, **379**, 52.

Wiklind T., Dickinson M., Ferguson H. C., Giavalisco M., Mobasher B., Grogin N. A., Panagia N., 2008. ApJ, **676**, 781.

Williams R. J., Quadri R. F., Franx M., van Dokkum P., Toft S., Kriek M., Labbé I., 2010. ApJ, **713**, 738.

Willott C. J., McLure R. J., Hibon P., Bielby R., McCracken H. J., Kneib J.-P., Ilbert O., Bonfield D. G., Bruce V. A., Jarvis M. J., 2012. *ArXiv e-prints*.

Wright S. A., Larkin J. E., Barczys M., Erb D. K., Iserlohe C., Krabbe A., Law D. R., McElwain M. W., Quirrenbach A., Steidel C. C., Weiss J., 2007. ApJ, **658**, 78.

Wright S. A., Larkin J. E., Law D. R., Steidel C. C., Shapley A. E., Erb D. K., 2009. ApJ, **699**, 421.

Wuyts S., Labbé I., Schreiber N. M. F., Franx M., Rudnick G., Brammer G. B., van Dokkum P. G., 2008. ApJ, **682**, 985.

Wuyts S., Cox T. J., Hayward C. C., Franx M., Hernquist L., Hopkins P. F., Jonsson P., van Dokkum P. G., 2010. ApJ, **722**, 1666.

Yan H., Dickinson M., Eisenhardt P. R. M., Ferguson H. C., Grogin N. A., Paolillo M., Chary R.-R., Casertano S., Stern D., Reach W. T., Moustakas L. A., Fall S. M., 2004. ApJ, **616**, 63.

Zackrisson E., Rydberg C.-E., Schaerer D., Östlin G., Tuli M., 2011. ApJ, **740**, 13.

Ziegler B. L., Böhm A., Fricke K. J., Jäger K., Nicklas H., Bender R., Drory N., Gabasch A., Saglia R. P., Seitz S., Heidt J., Mehlert D., Möllenhoff C., Noll S., Sutorius E., 2002. ApJ, **564**, L69.

Zirm A. W., van der Wel A., Franx M., Labbé I., Trujillo I., van Dokkum P., Toft S., Daddi E., Rudnick G., Rix H.-W., Röttgering H. J. A., van der Werf P., 2007. ApJ, **656**, 66.

Zwicky F., 1933. *Helvetica Physica Acta*, **6**, 110.